



*ugr* | **Universidad  
de Granada**

**THERMODYNAMIC FORMULATION FOR NON-LINEAR  
FINITE ELEMENT APPLIED TO MULTI-COUPLED MATERIALS**

BY:

**Roberto Palma Guerrero**

A PHD THESIS SUBMITTED TO:

**University of Granada**

ADVISORS:

**José Luis Pérez Aparicio & Rafael Gallego Sevilla**

Department of Structural Mechanics & Hydraulic Engineering ,  
University of Granada  
Granada (Spain)

November 2011

Editor: Editorial de la Universidad de Granada  
Autor: Roberto Palma Guerrero  
D.L.: GR 1708-2012  
ISBN: 978-84-9028-045-4

**Thermodynamic Formulation for Non-linear Finite Element  
Applied to Multicoupled Materials**  
Copyright © 2012 by Roberto Palma Guerrero

# Summary



This thesis presents a non-linear finite element formulation for non-equilibrium interactions that couple up to four fields: mechanical, thermal, electric and magnetic.

From a theoretical point of view, the multi-coupled governing equations are obtained using the Extended Non-Equilibrium Thermodynamic formalism. This formalism permits to study thermodynamic systems for which local equilibrium hypothesis is not valid, introducing dissipative fluxes, which are closely related with empirical parameters, in the entropy balance. These empirical parameters represent thermal and electric viscosities and are denominated relaxation times.

Numerically, the governing equations are developed into a variational formulation within the finite element framework to permit the implementation of the multi-coupled problem into the computer code FEAP. Standard isoparametric eight-node elements with six degrees of freedom (displacements, temperature, voltage and magnetic scalar potential) per node are used. Non-linearities are addressed with the *Newton-Rhapson* algorithm. For the dynamic problem, HHT and *Newmark- $\beta$*  algorithms are compared to obtain accurate results, since numerical oscillations (*Gibbs* phenomena) are present when relaxation times are considered. The last algorithm, which is regularized by relating time steps and element sizes, provides the best results.

Finally, the finite element implementation is validated and the time integration algorithm is tested using practical applications:

- ▷ Research on the propagation of temperatures, voltages and heat fluxes due to thermal relaxation time or second sound
- ▷ Simulation of the elasto-thermo-electric responses in materials subjected to electric pulses
- ▷ Study of the hysteretic behavior in photovoltaic materials due to the coupling between relaxation times
- ▷ Analysis of galvanomagnetic and thermo-magnetic interactions, which improve the efficiency of commercial electronic devices such as *Peltier* cells



# Agradecimientos / Acknowledgements

En primer lugar, quiero agradecer a mi director, Dr. José Luis Pérez Aparicio, por su paciencia, confianza y excelente orientación durante este trabajo. Además, agradezco su amistad y hospitalidad durante todas mis estancias en la Universidad Politécnica de Valencia. También agradezco a mi codirector, Dr. Rafael Gallego Sevilla, y al director del departamento, Dr. Javier Suárez Medina, por todo el apoyo recibido durante esta etapa. Agradezco a los profesores Antolino Gallego, por hacer posible que comenzara en el mundo de la investigación, y Guillermo Rus, por su forma de ver la investigación que ha marcado y, creo, marcará toda mi carrera investigadora.

El trabajo desarrollado en esta tesis no hubiera sido posible sin el apoyo económico de la beca del Ministerio de Educación con referencia FPU AP-2006-02372.

A todos mis compañeros del Departamento de Mecánica de Estructuras e Ingeniería Hidráulica de la Universidad de Granada y especialmente a mis grandes amigos Rafa Bravo, Inas y Miguel Ángel. No quiero olvidarme de mis compañeros del Departamento de Física Aplicada donde realicé la última etapa de esta tesis. Liliana, Elisabeth, Cristobal y Leandro, muchas gracias por vuestra ayuda y sincera amistad.

Personalmente, quiero dedicar esta tesis a mis padres porque siempre han apoyado mis decisiones y me han ayudado a lograr esta meta. A mis fabulosos hermanos, Tony y Manolo, a Manoli y a mis sobrinos, Tony y Dani, por los que siempre ha merecido la pena dejar la tesis a un lado cuando era necesario.

Finalmente, quiero agradecer todo el apoyo y ánimo que he recibido de mi esposa, Ana. Gracias Ana: por lograr que nunca me rindiera, por tantas horas de soledad que has pasado y espero saber recompensar algún día y por ser la piedra angular de éste que suscribe.

Santa Cruz del Comercio, 17 de Noviembre de 2011

Roberto Palma Guerrero



# Abbreviations

ET	Equilibrium Thermodynamics
NET	Non–Equilibrium Thermodynamics
ENET	Extended Non–Equilibrium Thermodynamics
FE	Finite Element
FEM	Finite Element Method
d.o.f.	Degree of freedom
TE	ThermoElement
PT	Pulsed Thermoelectric
COP	Coefficient–Of–Performance
SA	Sensitivity Analysis
IP	Inverse Problem
GA	Genetic Algorithm
MCT	Monte Carlo Technique
PDF	Probability Distribution Function
CDF	Cumulative Distribution Function
SRC	Standardized Regression Coefficients
UA	Uncertainty Analysis
CF	Cost Function





# List of Symbols

Symbol	Description
$\Omega$	Domain
$\Gamma$	Boundary
$\Omega^\infty$	Surrounding
$\mathcal{E}$	Set of extensive variables
$\mathcal{I}$	Set of intensive variables
$\delta$	Inexact differential
$d$	Exact differential
$\mathcal{S}$	Set of classical state variables
$\mathcal{F}$	Set of classical fluxes
$(\cdot)^t$	Transpose
$\mathbf{Y}$	Thermodynamic force
$\mathcal{P}$	<i>Lagrangian</i> continuum property
$\mathcal{p}$	<i>Eulerian</i> continuum property
$\mathbf{n}$	Outward pointing unit normal boundary field
$L^{kl}$	Phenomenological coefficients
$\Omega_e$	Element subdomain
$\mathcal{R}$	Residual
$A, B$	Global numbering of elements
$k$	<i>Newton–Rhapson</i> counter
$\mathbf{g}$	Derivatives of degrees of freedom
$\mathcal{K}$	Tangent stiffness matrix
$\mathcal{C}$	Tangent capacity matrix
$\mathcal{M}$	Tangent mass matrix
$c_1, c_2, c_3$	Finite element matrix parameters
$\bar{\beta}, \bar{\gamma}$	<i>Newmark–<math>\beta</math></i> standard parameters
$\bar{\alpha}$	HHT standard parameter
$\mathbf{U} = a^U, a^T, a^V, a^\varphi$	Degrees of freedom
$\bar{\rho}$	Spectral radius
$\hat{T}$	Undamped natural period
$C$	<i>Courant</i> number
$P$	Amplification factor
$N$	Number of measurement points
$\mathbf{I}$	Identity matrix
$\varepsilon$	<i>Levi–Civita</i> symbol
$n_{el}$	Number of elements
$n_{pe}$	Number of nodes per element

Symbol	Description
$\mathcal{N}$	Shape functions
$\mathcal{B}^s$	Discretized mechanical matrix gradient
$\mathcal{B}$	Discretized matrix gradients
$c$	Scalar factor for <i>Poynting</i> theorems
$\dot{r}$	Residual term for <i>Poynting</i> theorems
$\phi$	Observable variable
$\xi$	Random variable
$M_d$	Mathematical model
$N_\xi$	Number of random variables
$\mu$	Mean
$\sigma$	Standard deviation
$m$	Number of executions or sample size
$\theta_r$	Regression coefficient
$\Psi$	Approximation error
$R$	Correlation coefficient
$\Theta$	Standardized regression coefficient
$\Psi^{EXP}$	Experimental measurement
$\Psi^{NUM}$	Simulated measurement
$f$	Cost function
$f^L$	Logarithmic cost function
$\epsilon$	Non-dimensional constant
$\mathbf{p}$	Set of parameters
$\eta_c$	Ratio of <i>a</i> -spot model
$m_r$	Ratio of convergence

Symbol	SI	Description
$\rho_m$	[Kg/m <sup>3</sup> ]	Mass density
$U$	[J]	Internal energy
$Q$	[J]	Heat
$W$	[J]	Work
$S$	[J/K]	Entropy
$T$	[K]	Temperature
$\mathbf{T}$	[N/m <sup>2</sup> ]	<i>Cauchy</i> stress tensor
$E$	[V/m]	Electric field
$B$	[T]	Magnetic induction
$S$	[-]	Small strain tensor
$P$	[C/m <sup>2</sup> ]	Polarization
$M$	[A/m]	Magnetization
$X$	[m]	<i>Lagrangian</i> coordinates
$x$	[m]	<i>Eulerian</i> coordinates

Symbol	SI	Description
$t$	[s]	Time
$\mathbf{U}$	[m]	<i>Lagrangian</i> displacements vector
$\mathbf{u}$	[m]	<i>Eulerian</i> displacements vector
$\mathbf{v}$	[m/s]	<i>Eulerian</i> velocity
$\rho_q$	[C/m <sup>3</sup> ]	Charge density
$Kn$	[-]	<i>Knudsen</i> number
$De$	[-]	<i>Deborah</i> number
$L_K$	[m]	Experiment length
$T_D$	[s]	Experiment duration
$l_K$	[m]	Mean free path
$t_D$	[s]	Equilibration time
$u$	[J/m <sup>3</sup> ]	Internal energy density
$s$	[J/Km <sup>3</sup> ]	Entropy density
$e$	[J/m <sup>3</sup> ]	Total energy density
$\mathbf{j}_e$	[A/m <sup>2</sup> ]	Total energy flux
$\dot{W}_T$	[J/s]	Thermal power
$\mathbf{q}$	[W/m <sup>2</sup> ]	Thermal flux
$\mathbf{j}_s$	[J/Ksm <sup>2</sup> ]	Entropy flux
$\sigma^s$	[J/Km <sup>3</sup> ]	Entropy production
$s_{NE}$	[J/Km <sup>3</sup> ]	Non-equilibrium entropy density
$\mathbf{f}$	[N/m <sup>3</sup> ]	Body forces
$\mathbf{t}$	[Pa]	Tractions or surface forces
$\dot{W}_M$	[J/s]	Mechanical power
$\dot{k}$	[J/s]	Total derivative of kinetic energy
$\epsilon_0$	[F/m]	Vacuum permittivity
$\mu_0$	[Vs/Am]	Vacuum permeability
$\rho_q^f$	[C/m <sup>3</sup> ]	Density of <i>free</i> electric charge
$\rho_q^b$	[C/m <sup>3</sup> ]	Density of <i>bound</i> electric charge
$\mathbf{j}$	[A/m <sup>2</sup> ]	<i>Free</i> electric flux
$\mathbf{j}^b$	[A/m <sup>2</sup> ]	<i>Bound</i> electric flux
$\mathbf{D}$	[C/m <sup>2</sup> ]	Electric displacement or induction
$\mathbf{H}$	[A/m]	Magnetic field
$\epsilon$	[F/m]	Material permittivity
$\mu$	[Vs/Am]	Material permeability
$A$	[Vs/m]	Magnetic vector potential
$\varphi$	[A/m <sup>2</sup> ]	Magnetic scalar potential
$V$	[C/m]	Electric vector potential
$V$	[V]	Voltage
$\mathbf{S}_P$	[J/sm <sup>2</sup> ]	<i>Poynting</i> vector
$u_{EM}$	[J/m <sup>3</sup> ]	Density of electromagnetic internal energy
$\mathbf{G}^M$	[CV/m]	<i>Minkowski</i> momentum density
$\mathbf{G}^A$	[CV/m]	<i>Abraham</i> momentum density
$p$	[Cm/Kg]	Specific polarization
$\mathbf{m}$	[Am <sup>2</sup> /Kg]	Specific magnetization
$T_0$	[K]	Temperature reference

Symbol	SI	Description
$h$	[J/K]	Specific heat capacity
$\pi^E$	[C/Km <sup>2</sup> ]	Pyroelectric properties
$\pi^M$	[A/Km]	Pyromagnetic properties
$T^{eq}$	[Pa]	Equilibrium stress tensor
$E^{eq}$	[V/m]	Equilibrium electric field
$B^{eq}$	[T]	Equilibrium magnetic induction
$T^{neq}$	[Pa]	Non-equilibrium stress tensor
$E^{neq}$	[V/m]	Non-equilibrium electric field
$B^{neq}$	[T]	Non-equilibrium magnetic induction
$L_s, L_p, L_m$		Phenomenological coefficients
$\dot{Q}$	[W/sm <sup>2</sup> ]	Dissipative thermal flux
$\dot{J}$	[A/sm <sup>2</sup> ]	Dissipative electric flux
$C_i$	[-]	Constants
$\Pi$	[J]	Electromagnetic enthalpy
$\kappa$	[W/mK]	Thermal conductivity
$C$	[Pa]	Elastic stiffness
$e^E$	[C/m <sup>2</sup> ]	Piezoelectric properties
$e^M$	[N/Am]	Piezomagnetic properties
$\beta$	[K <sup>-1</sup> ]	Thermal expansion coefficients
$\nu$	[Tm/V]	Magnetolectric properties
$T^R$	[Pa]	Residual stress
$P^R$	[C/m <sup>2</sup> ]	Residual polarization
$\bar{u}$	[m]	Prescribed displacements
$\bar{T}$	[K]	Prescribed temperature
$\bar{V}$	[V]	Prescribed voltage
$\bar{\varphi}$	[A/m <sup>2</sup> ]	Prescribed magnetic scalar potential
$q_c$	[W/m <sup>2</sup> ]	Prescribed thermal flux
$j_c$	[A/m <sup>2</sup> ]	Prescribed electric flux
$B_c$	[T]	Prescribed magnetic flux
$\tau_{\{q,j,jq,qj\}}$	[s]	Relaxation times
$\alpha$	[V/K]	<i>Seebeck</i> coefficient
$\gamma$	[A/mV]	Electric conductivity
$q_b$	[W/m <sup>2</sup> ]	Boundary heat flux
$h$	[W/m <sup>2</sup> K]	Convection heat transfer coefficient
$T_\infty$	[K]	Temperature reference for convection and radiation
$q^c$	[W/m <sup>2</sup> ]	Convection heat flux
$q^r$	[W/m <sup>2</sup> ]	Radiation heat flux
$e_{EM}$	[A/m <sup>2</sup> ]	Electromotive force
$t_h$	[V/K]	<i>Thomson</i> coefficient
$\pi$	[V/K]	Absolute <i>Peltier</i> coefficient
$L_{x_i}$	[m]	Thermoelement length
$T_c$	[K]	Temperature at cold face
$T_h$	[K]	Temperature at hot face
$T_m$	[K]	Average temperature
$\Delta t$	[s]	Time step
$h$	[m]	Finite element length

Symbol	SI	Description
$I_{app}^{max}$	[A]	Maximum applied intensity in steady-state
$I_{app}$	[A]	Applied intensity
$t_p$	[s]	Pulse duration
$\Delta T_{max}$	[K]	Maximum temperature difference
$\Delta T_p$	[K]	Maximum transient temperature difference
$\Delta T_{pp}$	[K]	Maximum post-pulse temperature difference
$K_{emp}$	[s]	Empirical magnitude
$T_{ob}$	[s]	Observation time
$freq$	[s <sup>-1</sup> ]	Frequency
$\bar{N}$	[m <sup>2</sup> /Ks]	<i>Nernst</i> coefficient
$\bar{M}$	[m <sup>2</sup> /Vs]	<i>Righi-Leduc</i> coefficient
$\bar{R}$	[m <sup>3</sup> /As]	<i>Hall</i> coefficient
$\kappa$	[WK/m]	Tensor of thermal conductivities
$\alpha$	[V/K]	Tensor of <i>Seebeck</i> coefficients
$\gamma$	[A/mV]	Tensor of electric conductivities
$\rho$	[Ωm]	Tensor of electric resistivities
$V_{af}$	[V]	Voltage source
$I_{tec}$	[A]	Thermocouple intensity
$Q_c$	[J]	Total heat at cold face
$Q_h$	[J]	Total heat at hot face
$Z$	[-]	Figure-of-merit
$\kappa_c$	[WKm]	Thermal contact conductivity
$\gamma_c$	[Am/V]	Electric contact conductivity
$\kappa_{Cu}$	[WKm]	Thermal contact conductivity of copper
$\gamma_{Cu}$	[Am/V]	Electric contact conductivity of copper
$\kappa_{eff}^{Sn}$	[WKm]	Effective thermal contact conductivity of tin
$\gamma_{eff}^{Sn}$	[Am/V]	Effective electric contact conductivity of tin
$A_c$	[m <sup>2</sup> ]	Connection area
$I_\Omega$	[a/m <sup>3</sup> ]	Volumetric intensity
$T_{max}$	[K]	Maximum temperature
$T_{min}$	[K]	Minimum temperature
$V_{fe}$	[V]	FE potential drop
$V_{tec}$	[V]	Potential drop in <i>Peltier</i> coolers
$Q_{cfe}$	[J]	FE heat taken from cold face
$Q_{ctec}$	[J]	Heat taken from cold face in <i>Peltier</i> coolers
$\theta$	[°]	Angle



# Contents

Summary	i
Agradecimientos / Acknowledgements	iii
Abbreviations	v
List of Symbols	vii
Chapter 1 Introduction	1
1.1 Multi-coupled formulation . . . . .	3
1.1.1 Equilibrium interactions . . . . .	6
1.1.2 Non-equilibrium interactions . . . . .	8
1.2 Literature review . . . . .	11
1.2.1 Theoretical formulation . . . . .	11
1.2.2 Finite element formulation . . . . .	12
1.3 Objectives . . . . .	15
1.4 Outline of thesis . . . . .	15
<b>I THEORETICAL FORMULATION</b>	<b>17</b>
Chapter 2 Outline of Continuum Physics	19
2.1 Thermodynamics . . . . .	19
2.1.1 Equilibrium thermodynamics . . . . .	21
2.1.2 Non-Equilibrium Thermodynamics . . . . .	23
2.1.3 Extended Non-Equilibrium Thermodynamics . . . . .	27
2.2 Classical Continuum Mechanics . . . . .	27
2.2.1 Momentum balance . . . . .	28
2.2.2 Energy balance . . . . .	28
2.3 Classical Electrodynamics . . . . .	29
2.3.1 Maxwell equations . . . . .	29
2.3.2 Compatibility equations . . . . .	31
2.3.3 Energy balance: Poynting theorem . . . . .	31



2.3.4	Momentum balance . . . . .	33
Chapter 3	Multi-coupled governing equations	35
3.1	Multi-coupled balance equations . . . . .	35
3.1.1	Energy balance . . . . .	36
3.1.2	Momentum balance . . . . .	37
3.1.3	Entropy balance . . . . .	37
3.1.4	Energy balance: thermal conduction temperature . . . . .	41
3.2	Multi-coupled governing equations for equilibrium interactions . . . . .	43
3.2.1	Balance equations . . . . .	43
3.2.2	Constitutive equations . . . . .	44
3.3	Multi-coupled governing equations for non-equilibrium interactions . . . . .	45
3.3.1	Balance equations . . . . .	45
3.3.2	Transport equations . . . . .	46
3.3.3	Interpretation of the relaxation times . . . . .	48
 <b>II FINITE ELEMENT FORMULATION</b>		 <b>51</b>
Chapter 4	Finite element formulation	53
4.1	Outline of the Finite Element Method . . . . .	53
4.1.1	Non-linear transient solutions . . . . .	54
4.1.2	Stability of the time integration algorithms . . . . .	56
4.2	Finite element formulation for non-equilibrium interactions . . . . .	57
4.2.1	Weak forms . . . . .	57
4.2.2	Residuals . . . . .	59
4.2.3	Tangent stiffness matrices . . . . .	63
4.2.4	Capacity matrices . . . . .	66
4.2.5	Mass matrices . . . . .	67
4.3	Interface finite element . . . . .	68
 <b>III RESULTS</b>		 <b>71</b>
Chapter 5	Thermoelectric interactions	73
5.1	Review of basic thermoelectric effects . . . . .	74
5.2	Finite element equations . . . . .	76
5.3	Results . . . . .	76
5.3.1	Analytical solutions . . . . .	77
5.3.2	Numerical solutions for cases I to III . . . . .	80
5.3.3	Numerical solutions for case IV . . . . .	82
5.4	A complete three-dimensional simulation . . . . .	86

5.5	Conclusions . . . . .	89
Chapter 6	Elasto–thermoelectric interactions	91
6.1	Experimental procedure . . . . .	92
6.2	Finite element equations . . . . .	94
6.3	Numerical results . . . . .	94
6.3.1	Electric current for maximum cooling . . . . .	95
6.3.2	Maximum transient temperature difference . . . . .	96
6.3.3	Effects of the pulse shape on the pulsed thermoelectric variables . . . . .	98
6.3.4	Effect of the thermoelement geometry on the pulsed thermoelectric variables . . . . .	100
6.3.5	Effect of the relaxation time on the pulsed thermoelectric variables . . . . .	102
6.4	Conclusions . . . . .	103
Chapter 7	Hysteretic behavior in thin–film photovoltaic materials	105
7.1	Physical interpretation of the hysteretic behavior . . . . .	106
7.1.1	Experimental procedure . . . . .	107
7.1.2	Theoretical explanation . . . . .	108
7.2	Finite element equations . . . . .	109
7.3	Calibration of the numerical model: inverse problem . . . . .	109
7.3.1	Sensitivity Analysis . . . . .	110
7.3.2	Inverse problem . . . . .	111
7.4	Design of experiments for the validation of the theoretical explanation . . . . .	113
7.5	Conclusions . . . . .	117
Chapter 8	Galvanomagnetic and thermo–magnetic interactions	119
8.1	Physical interpretation of galvanomagnetic and thermo–magnetic interactions	120
8.2	Finite element equations . . . . .	124
8.3	Results . . . . .	125
8.3.1	Hall and Righi–Leduc effects . . . . .	125
8.3.2	<i>Ettingshausen</i> and <i>Nernst</i> effects . . . . .	128
8.4	Conclusions . . . . .	131
Chapter 9	Elasto–magneto–thermo–electric study of commercial Peltier coolers	133
9.1	<i>Peltier</i> coolers . . . . .	135
9.1.1	Carnot equivalence . . . . .	137
9.2	Finite element equations . . . . .	138
9.3	Finite element model . . . . .	138
9.3.1	Modeling thermal and electrical contacts . . . . .	142
9.4	Results . . . . .	143
9.4.1	Study of thermoelectric interactions . . . . .	144

9.4.2	Comparison between numerical and experimental results . . . . .	148
9.4.3	Study of galvanomagnetic and thermo–magnetic interactions . . . . .	149
9.4.4	Study of thermal stresses . . . . .	151
9.5	Sensitivity Analysis . . . . .	154
9.5.1	Problem definition . . . . .	154
9.5.2	SA Results . . . . .	155
9.6	Study of the temperature–dependency of material properties on the <i>Peltier</i> cooler performance . . . . .	159
9.7	Conclusions . . . . .	162
Chapter 10	Conclusions and future works	163
10.1	Conclusions . . . . .	163
10.2	Future works . . . . .	164
Appendix A	Outline of the sensitivity analysis and inverse problem techniques	165
A.1	Sensitivity Analysis . . . . .	165
A.2	Inverse Problem . . . . .	167
A.2.1	Cost function . . . . .	168
A.2.2	Parametrization . . . . .	169
A.2.3	Search algorithm . . . . .	169
A.3	Genetic Algorithm . . . . .	169
Appendix B	Material properties	171
References		175

## List of Figures

1.1	Piezoelectric sensor, picture taken from <i>vortexelectricaz.blogspot.com</i> . . . . .	1
1.2	Magnetostrictive actuator, picture taken from <i>cedrat.com</i> . . . . .	2
1.3	Top-left, <i>Peltier</i> cooler composed of thermoelements also shown in picture bottom-left. Top-right, photovoltaic cell. Bottom-right, a photovoltaic-like behavior has recently been observed in the <i>Vespa orientalis</i> hornet. The hornet picture is taken from <i>hornissenschutz.de</i> and the others from several manufacturers. . . . .	3
1.4	Great scientists who observed some of the interactions present in this thesis. <i>Carl von Linné</i> (1707–1778) was a Swedish botanist, physician, and zoologist who discovered the pyroelectric effect. <i>Jean-Baptiste-Joseph Fourier</i> (1768–1830) was a French physicist. <i>Thomas Johann Seebeck</i> (1770–1831) was a physicist who in 1821 discovered the thermoelectric effect. <i>Jean Charles Athanase Peltier</i> (1785–1845) was a French physicist. <i>Georg Simon Ohm</i> (1789–1854) was a German physicist. <i>James Prescott Joule</i> (1818–1889) was an English physicist. <i>Adolf Eugen Fick</i> (1829–1901) was a German physiologist. He started to study mathematics and physics, but after realized he was more interested in medicine. <i>Edwin Herbert Hall</i> (1855–1938) was an American physicist who conducted thermoelectric research at Harvard. <i>Pierre Curie</i> (1859–1906) was a French physicist. <i>Walther Hermann Nernst</i> (1864–1941) was a German physical chemist and physicist who is known for the third law of thermodynamics. All these pictures and references have been taken from <i>Wikipedia</i> . . . . .	4
1.5	Cause and effect. First- and second-order material properties (higher-order terms are neglected). . . . .	5
1.6	Experimental response of a pair of variables showing regions: linear, non-linear and hysteresis branch. . . . .	5
1.7	Modified equilibrium <i>Heckmann</i> diagram taking into account four fields. Intensive variables are represented by rectangles, extensive ones by circles and first-order properties by triangles (for notation, see Tables 1.1 and 1.2). For clarity, the four principal and only 12 coupled interactions are represented. . . . .	6

1.8	Non–equilibrium diagram taking into account the three fluxes. Driving forces (intensive variables) are represented by rectangles, and fluxes (extensive ones) by circles. Magnetic field, mechanical stress and coupled conductivities are not included for clarity. For notation, see Tables 1.3 and 1.4. . . . .	9
2.1	<i>Josiah Willard Gibbs</i> (1839–1903), American physicist who was awarded with the first American Ph.D. in engineering in 1863. . . . .	20
2.2	Thermodynamic universe composed of the thermodynamic system $\Omega$ and of its surrounding $\Omega^\infty$ . . . . .	21
2.3	<i>Leonhard Paul Euler</i> (1707–1783) was born in Switzerland and was the best mathematician in the XVIII Century. <i>Giuseppe Lodovico Lagrangia</i> or <i>Lagrange</i> (1736–1813) was born in Italy and succeeded <i>Euler</i> as the director of mathematics at the <i>Prussian Academy of Science</i> in <i>Berlin</i> . . . . .	22
2.4	Reference system showing the <i>Lagrangian</i> and <i>Eulerian</i> descriptions. . . . .	23
2.5	Mass density versus volume, picture taken from <i>Eringen</i> [1980]. . . . .	24
2.6	<i>Martin Hans Christian Knudsen</i> was a Danish physicist who was renowned for his work on kinetic molecular theory. . . . .	25
2.7	<i>Lars Onsager</i> (1903–1976) was a theoretical physicist, winner of the 1968 <i>Nobel Prize</i> in Chemistry. . . . .	26
2.8	System or body in the <i>Continuum Mechanics</i> framework subjected to: volume forces, essential and natural boundary conditions. . . . .	28
2.9	<i>Johann Carl Friedrich Gauss</i> (1777–1855) was a German scientist. <i>Michael Faraday</i> (1791–1867) was an English natural philosopher, in the terminology of the time. <i>James Clerk Maxwell</i> (1831–1879) was a Scottish physicist author of the denominated <i>second great unification in physics</i> . . . . .	29
2.10	<i>John Henry Poynting</i> (1852–1914), English physicist. . . . .	31
2.11	<i>Hermann Minkowski</i> (1864–1909) was a German mathematician of Ashkenazi Jewish descent. <i>Max Abraham</i> (1875–1922) was a German physicist who was born to a family of Jewish merchants. . . . .	33
3.1	The total energy contained in the thermodynamic system is the sum of the mechanical, thermal and electromagnetic energies. . . . .	36
3.2	The entropy balance is composed of entropy flux and of entropy production. On one hand, the entropy flux is closely related with the thermal flux. On the other, there are five entropy sources that arise from thermal conduction, from <i>Joule</i> heating and from mechanical, electric and magnetic irreversibilities. . . .	39
3.3	<i>Petrus Josephus Wilhelmus Debye</i> (1884–1966), Dutch physicist. . . . .	40
3.4	Outline of simplifications and particularization of governing equations for equilibrium and non–equilibrium interactions. . . . .	42
3.5	One–dimensional <i>Maxwell</i> model for the interpretation of relaxation times. . .	48
4.1	Continuum domain discretized by the finite element method. Each 3–D element is composed of eight nodes. . . . .	54

4.2	<i>Boris Grigoryevich Galerkin</i> (1871–1945) was a Russian/Soviet mathematician and engineer. . . . .	61
4.3	Non-linear isoparametric 3-D finite element (left). Special 2-D interface finite element (right). . . . .	69
4.4	FEAP (Finite Element Analysis Program) is the computer code used for the implementation of the finite element formulation in the present thesis. . . . .	70
5.1	Basic thermocouple probe used for the measurement of temperatures, picture taken from <i>www.thermocouples.com/</i> . . . . .	74
5.2	Heat power due to <i>Peltier</i> effect in two thermoelectric materials. . . . .	75
5.3	p-type thermoelement geometry, applied boundary conditions, dimensions, fluxes and coordinates. . . . .	77
5.4	Voltage (left) and temperature (right) distributions along thermoelement for cases I (top row) and II (bottom row) and for three time instants. Analytical results with different line types, finite element with circles. . . . .	81
5.5	Thermal fluxes in cases I (top) and II (bottom) and for three times. Analytical results represented with different line types, finite element with circles. . . . .	82
5.6	Analytical temperature solution for $t = 0.06$ , $\tau_q = 0.02$ [s], $C = 1/6$ (top). Different Newmark- $\beta$ and HHT parameters to study <i>Gibbs</i> phenomena (middle), see Table 5.2. Adjusting by trial and error the <i>Courant</i> number in Test b to avoid oscillations (bottom). . . . .	83
5.7	Voltage (top) and temperature (bottom) versus thermoelement length for several time instants. For voltage, only finite element results. For temperature, analytical results are shown with different line types and corresponding finite element results with circles. . . . .	85
5.8	Thermal flux versus thermoelement length at $t = 0.06$ . Semi-analytical result represented by solid line and finite element by circles. . . . .	86
5.9	Thermal flux versus thermoelement length for several time instants with $\tau_q = 0.02$ (top) and relaxation time influence in the wave shape (bottom) at $t = 0.06$ . Only finite element results represented. . . . .	87
5.10	Truncated pyramid thermoelement dimensions for three-dimensional simulation. At hot face, surface $1.96$ [mm <sup>2</sup> ] and $T_h = 50$ [°C]; at cold $1.58$ , $T_c = 30$ with constant prescribed vertical flux $j_{x_3} = 2.65 \times 10^6$ [A/m <sup>2</sup> ]. . . . .	88
5.11	Temperature distribution inside the truncated pyramid thermoelement for the parabolic (left) and hyperbolic (right) models and for several time instants. For parabolic model $\tau_q = 0$ , for hyperbolic $\tau_q = 0.02$ [s] are assumed. Boundary conditions and geometry shown in Figure 5.10. . . . .	89
6.1	Pulsed thermoelectrics are included in electronic devices such as the gas sensor, shown in this figure. Picture taken from <i>http://www.tdlsensors.co.uk</i> . . . . .	91

6.2	Main variables involved in a pulsed thermoelectric. Measured temperature at the cold face (top) and applied electric pulse (bottom) versus time for the experiment developed in Snyder et al. [2002]. . . . .	93
6.3	Model and boundary conditions used to simulate a pulsed thermoelectric. Only a thermoelement is used to reduce the calculation time. . . . .	94
6.4	Temperature at the cold face versus prescribed electric flux for the determination of the electric current for maximum cooling under steady-state situations. Two simulations are represented considering constant and variable properties. Only finite element results are shown. . . . .	95
6.5	Strain along vertical $x_3$ direction versus applied electric flux. Two simulations are represented considering constant and variable properties. Only finite element results are shown. . . . .	96
6.6	Evolution of the temperature at the cold face when a square pulse of electric current is prescribed. Temperature at the hot face is fixed to be $T_h = 25$ [°C]. Two simulations are represented considering constant and variable properties. Only finite element results. . . . .	96
6.7	Maximum transient temperature difference versus pulse amplification. Finite element results using constant and variables properties (circles) and empirical ones (lines) are compared. . . . .	97
6.8	Electric pulse influence on elastic response of a thermoelement: strain along vertical $x_3$ direction versus time. Only finite element results are shown. . . . .	98
6.9	Stress distribution along $x_3$ direction inside the thermoelement at $t = 56$ [s]. At this time instant, the maximum stress is reached since the maximum post-pulse temperature is achieved. . . . .	98
6.10	Effects of different current pulse shapes on pulsed thermoelectric variables. Temperature at the cold face (top), strain along vertical direction $x_3$ (middle) and applied voltage (bottom) versus time. Only finite element results using variable properties are shown. . . . .	99
6.11	Three different geometries used to study the influence of thermoelement shape on pulsed thermoelectric variables. . . . .	101
6.12	Temperature at the cold face (top) and strain along vertical direction $x_3$ (bottom) versus time for the three geometries shown in Figure 6.11. For all the geometries the same square pulse of electric current is applied. Only finite element results using variable properties are shown. . . . .	101
6.13	Maximum transient (top) and post-pulse (bottom) temperature differences versus the relaxation time $\tau_{qj}$ . Only finite element results using variable properties are shown. . . . .	102
7.1	Experimental configuration for the measurement of the <i>Seebeck</i> coefficient. . .	106

7.2	Experimental results reported in Ferrer et al. [2006] for FeS <sub>2</sub> (left) and Ti-doped FeS <sub>2</sub> (right) thin films. Top: applied temperature difference $\Delta T(t)$ ; middle: measured voltage $\Delta V$ ; bottom: $\Delta V$ versus $\Delta T$ . . . . .	107
7.3	Standardized regression coefficient in absolute value, see notation in Table 7.1.	110
7.4	Genetic algorithm convergence. Cost function versus number of generations.	113
7.5	Experimental (solid line) and finite element (circles) results obtained for a n-type sample of Ti-doped FeS <sub>2</sub> . Top: measured voltage versus time, bottom: measured voltage versus applied temperature. . . . .	114
7.6	Measured voltage versus applied temperature. Experimental (solid line) and finite element (circles) results obtained for a p-type sample of Ti-doped FeS <sub>2</sub> .	114
7.7	Numerical experiment consisting of the application of a linear temperature signal (top) and of the calculation of the generated voltage. Calculated voltage versus applied temperature (bottom). Only finite element results are shown. . . . .	115
7.8	Numerical experiment consisting of the application of two sinusoidal temperature signals with different frequencies (top) and of the calculation of the generated voltages. Calculated voltage versus applied temperature (bottom). Again, finite element results are only shown. . . . .	116
7.9	Numerical experiment consisting of the application of an exponentially increasing sinusoidal temperature signal (top) and of the calculation of the generated voltage. Calculated voltage versus applied temperature (bottom). Again, finite element results are only shown. . . . .	117
8.1	Biosensor based on the <i>Hall</i> effect and used for molecule recognition. Picture taken from <a href="http://bme240.eng.uci.edu/">http://bme240.eng.uci.edu/</a> . . . . .	120
8.2	Physical magnitudes involved in the galvanomagnetic and thermo-magnetic interactions. . . . .	121
8.3	Sketch of the four transverse galvanomagnetic and thermo-magnetic interactions. Following the convection of Figure 1.5, causes are represented by rectangles and effects by circles. . . . .	122
8.4	Geometry, boundary conditions and prescribed fluxes for the validation of the: <i>Hall</i> (left) and <i>Righi-Leduc</i> (right) effects. . . . .	126
8.5	Voltage distribution (left) and gradient of voltage along the $x_2$ direction (right) for the validation of the <i>Hall</i> effect. The vertical length of the thermoelement is magnified 100 times ( $L_{x_3} = 11.4$ [mm]): semi-infinite domain. . . . .	127
8.6	Voltage distributions with (left) and without (right) magnetic field applied. A finite domain $L_{x_3} = 1.14$ [mm] is considered. Magnetic field disturbs the voltage distribution due to the <i>Hall</i> effect. . . . .	128
8.7	Gradient of voltage along the $x_2$ direction (left) and electric flux along the $x_3$ direction (right) due to the <i>Hall</i> effect. A finite domain $L_{x_3} = 1.14$ [mm] is considered. . . . .	128



8.8	Temperature distribution (left) and gradient of temperature along the $x_2$ direction (right) for the validation of the <i>Righi-Leduc</i> effect. The vertical length of the thermoelement is magnified 100 times ( $L_{x_3} = 11.4$ [mm]): semi-infinite domain. . . . .	129
8.9	Geometry, boundary conditions and prescribed fluxes for the validation of the <i>Ettingshausen</i> (left) and <i>Nernst</i> (right) effects. . . . .	130
8.10	Voltage (left) and temperature (right) gradients along $x_2$ for the validation of the <i>Ettingshausen</i> and the <i>Nernst</i> effects, respectively. The vertical length of the thermoelement is magnified 100 times ( $L_{x_3} = 11.4$ [mm]): semi-infinite domain. . . . .	131
9.1	<i>Peltier</i> cooling thermocouple, thermal fluxes and electric magnitudes. Hot and cold faces temperatures. . . . .	136
9.2	Simplified $T$ - $s$ diagram of a charge carrier in thermoelectric materials (top). Balance of energies per unit volume (bottom). The non-physical term $I_\Omega$ is included for numerical procedures. . . . .	137
9.3	Top view scheme of the CP1.4-127-045 thermoelectric cell. Periodicity (top) and symmetry (bottom). . . . .	139
9.4	Dimensions [mm] of a CP1.4-127-045 thermocouple, materials and origin of coordinates. Symmetry represented by flags, periodicity by sawed lines. . . .	140
9.5	Mesh of 12,670 elements for half thermocouple. Prescribed voltage, temperature, magnetic field and electric flux. . . . .	141
9.6	Convergence of normalized voltage drop and extracted heat versus number of elements. . . . .	141
9.7	Contour plot distributions from the finite element analyses, electric magnitudes in left and thermal in right column. Top: Voltage and temperature. Middle: Horizontal fluxes. Bottom: Vertical fluxes, all for $I_{tec} = 8,7$ [A], $T_c = T_h = 50$ [°C]. . . . .	145
9.8	Vertical temperature and voltage distributions for $T_h = 50$ [°C] and several $T_c$ . Origin at the thermoelement bottom-left. . . . .	146
9.9	Three-dimensional view of the vertical heat flux $q_{x_2}$ for $I_{tec} = 8,7$ [A], $T_c = T_h = 50$ [°C]. . . . .	147
9.10	Comparison of analytical formulae (Rowe [1995]), current finite element and manufacturer (MELCOR [2000]). Heat extracted and voltage drop for the functioning range of $I_{tec}$ , $T_c$ and for $T_h = 50$ [°C]. . . . .	148
9.11	Coefficient-of-performance versus magnetic field along the $x_3$ direction, maintaining $T_h = 50$ [°C], $I_{tec} = 7.5$ [A]. . . . .	149
9.12	Voltage (left) and temperature (right) distributions without (top) and with (bottom) applied magnetic field $B_{x_3} = 0.55$ [T]. $T_h = 50$ , $T_c = 50$ [°C] and $I_{tec} = 7.5$ [A]. . . . .	150

9.13	Coefficient-of-performance versus angle between magnetic field and electric and thermal fluxes, maintaining $T_h = 50$ [°C], $I_{tec} = 7.5$ [A] and $B = 0.55$ [T]. Note that electric and thermal fluxes are prescribed along the $x_2$ direction. . .	151
9.14	Contour plot distributions of the displacements along the $x_1$ (top-left), $x_2$ (top-right) and $x_3$ (bottom) directions for $I_{tec} = 7.5$ [A], $T_c = T_h = 50$ [°C]. . .	152
9.15	Two views of the <i>Von Mises</i> stresses for $I_{tec} = 7.5$ [A], $T_c = T_h = 50$ [°C]. . . . .	153
9.16	Undeformed mesh (red line) and deformed one due to the thermal stresses. For clarity, the deformed mesh is magnified by a factor 200. . . . .	153
9.17	View of the <i>Von Mises</i> stresses for $I_{tec} = 7.5$ [A], $T_c = T_h = 50$ [°C] and $B_{x_3} = 0.55$ [T]. . . . .	154
9.18	Maximum <i>Von Mises</i> stresses inside the thermoelement versus prescribed magnetic field along the $x_3$ direction, maintaining $T_h = 50$ [°C] and $I_{tec} = 7.5$ [A].	154
9.19	Probability distribution function for potential drop, extracted heat and coefficient-of-performance for $T_c = T_h = 50$ [°C], $I_{tec} = 8.7$ [A]. Mean and standard deviation indicated in each figure. . . . .	157
9.20	Standardized regression coefficients in absolute value for $T_c = T_h = 50$ [°C], $I_{tec} = 8.7$ [A]. Notation in Table 9.3. . . . .	158
9.21	Standardized regression coefficients in absolute value for $T_h = 50$ [°C], $I_{tec} = 8.7$ [A] and two values of $T_c$ . Notation in Table 9.3. . . . .	159
9.22	Effect of thermal and electric conductivities reduction due to contact in soldering. Coefficient-of-performance versus ratio between real and total contact surfaces. $T_h = 50$ [°C], $I_{tec} = 1.7$ [A]. . . . .	160
9.23	Coefficient-of-performance versus extracted heat for increasing electric intensity, $T_h = 50$ [°C], $T_c = 15$ [°C]. Thermal conductivity $\kappa$ temperature dependent. . . . .	161
A.1	Flowchart to compute the probability distribution function (PDF), cumulative distribution function (CDF) and standardized regression coefficients (SRC) using the Monte Carlo technique. . . . .	166
A.2	Flowchart of the model-based inverse problem. . . . .	168
A.3	Flowchart of the inverse problem solution by genetic algorithms. Gener., Fitts., Mr, Cr, Ps and Ng denote generations, cost function, mutation ratio, crossover ratio, population size and number of generations, respectively. . . .	170
B.1	Thermoelectric material property variations with temperature for the bismuth telluride material. . . . .	172



*Those who are weak don't fight. Those who are stronger might fight for an hour. Those who are stronger still might fight for many years. The strongest fight their whole life. They are the indispensable ones.*

**Bertolt Brecht** (1898–1956)

# 1

## Introduction



Modern technological devices, in particular electronics, use extensively multi-coupled materials, that are characterized by coupling up to four fields: thermal, mechanical, electric and magnetic. These materials are increasingly subjected to sophisticated manufacturing processes that include miniaturization for application in micro-devices. In addition, they are also submitted to applications with fast phenomena as ultrasound waves or pulsed operation modes.

Before exposing the objectives of the present thesis and to provide an idea of the importance of these materials, the following paragraphs list some interactions and their applications in modern technologies.

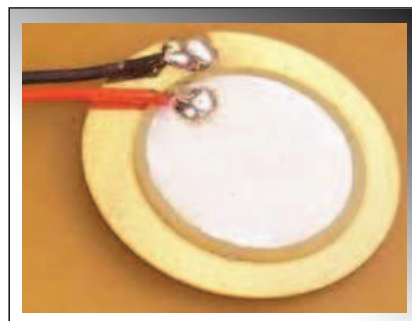


Figure 1.1: Piezoelectric sensor, picture taken from [vortexelectricaz.blogspot.com](http://vortexelectricaz.blogspot.com).

**Piezoelectricity**, electro–mechanical interaction, was discovered by the brothers *Pierre* and *Jacks Curie* in 1880 (direct effect) and by *Lipmann* in 1881 (inverse effect). Piezoelectric

materials are used as sensors (pressure sensors), as actuators (high precision positioning devices), in sonar applications (ultrasonic applications, hydrophones), in energy conversion (piezotransformers, energy harvesters); see Lahmer [2008] for more applications. Figure 1.1 shows a piezoelectric sensor fabricated with polarized ceramics. Currently, a new generation of piezo-elastomers is being used in many applications.

**Magnetostriction**, magneto-mechanical interaction, was first reported by *Joule* in the early 1840's, observing the change in length of iron particles when their magnetization was changed. The first application of magnetostrictive materials was during *World War II*, when they were employed in building transducers for sonar applications. Currently, these materials are used in active vibration control, control surface deployment and energy harvesting, see Atulasimha and Flatau [2011] for a full revision on applications. Figure 1.2 shows a magnetostrictive actuator composed of a magnetostrictive material (Terfenol-D) inside a solenoid that generates a magnetic field.



Figure 1.2: Magnetostrictive actuator, picture taken from *cedrat.com*.

**Thermoelectricity**, interaction of heat and electricity, was observed by *Seebeck* and *Peltier* in 1821 and 1835, respectively, even earlier than the quantitative formulation of *Ohm's* law in 1855. Three separated transport effects are present in thermoelectricity: *Seebeck*, *Peltier* and *Thomson*. In addition, the *Ohm* and *Fourier* laws that are inherent to electric and thermal fluxes are also present. Thermoelectric devices are used as coolers (cooling electronic devices, refrigeration and air conditioning), for power generation (energy harvesters, photovoltaic cells), as energy sensors (detection of water condensation and fluid flow, infrared thin film, cryogenic heat flux sensors), see Riffat and Ma [2003] for more applications. Curiously, a thermoelectric behavior has recently been observed in the Oriental hornet (*Vespa orientalis*) along its cuticular surface, see Galushko et al. [2005]. Figure 1.3 shows several devices composed of thermoelectric materials and the *Vespa orientalis* hornet.

The previous are just samples of interactions that can occur in a material subjected to four fields. Therefore, it is important to show the magnitude of the problem by means of an introduction on multi-coupled formulation.



Figure 1.3: Top-left, *Peltier* cooler composed of thermoelements also shown in picture bottom-left. Top-right, photovoltaic cell. Bottom-right, a photovoltaic-like behavior has recently been observed in the *Vespa orientalis* hornet. The hornet picture is taken from *hornissenschutz.de* and the others from several manufacturers.

### 1.1 Multi-coupled formulation

Every cause has an effect. In *Physics*, cause and effect are represented by intensive and extensive variables, respectively. The interaction of both types of variables is expressed through phenomenological equations, generally non-linear and written in terms of certain coefficients denominated material properties: observables that can be measured.

Figure 1.5 shows a conceptualization of the phenomenological equations, mathematically representing interactions. Traditionally, these interactions have been classified into two groups:

- ▷ Equilibrium
- ▷ Non-equilibrium



Figure 1.4: Great scientists who observed some of the interactions present in this thesis. *Carl von Linné* (1707–1778) was a Swedish botanist, physician, and zoologist who discovered the pyroelectric effect. *Jean-Baptiste-Joseph Fourier* (1768–1830) was a French physicist. *Thomas Johann Seebeck* (1770–1831) was a physicist who in 1821 discovered the thermoelectric effect. *Jean Charles Athanase Peltier* (1785–1845) was a French physicist. *Georg Simon Ohm* (1789–1854) was a German physicist. *James Prescott Joule* (1818–1889) was an English physicist. *Adolf Eugen Fick* (1829–1901) was a German physiologist. He started to study mathematics and physics, but after realized he was more interested in medicine. *Edwin Herbert Hall* (1855–1938) was an American physicist who conducted thermoelectric research at Harvard. *Pierre Curie* (1859–1906) was a French physicist. *Walther Hermann Nernst* (1864–1941) was a German physical chemist and physicist who is known for the third law of thermodynamics. All these pictures and references have been taken from *Wikipedia*.

In turn, material properties, which are mathematically tensors whose ranks related those of intensive and extensive variables, describe linear or non-linear interactions and can be classified into three groups, see *Tinder* [2008], *Newnham* [2005]:

- ▷ First-order
- ▷ Second-order
- ▷ Domain-wall

Since the interaction between fields is never perfect, the properties become time dependent from a macroscopic point of view in a way that is not reversible, that is, dissipation sources that produce domain-wall properties are present. Therefore, the effect associated to a given cause is not only dependent on the cause itself, but also on the whole history of

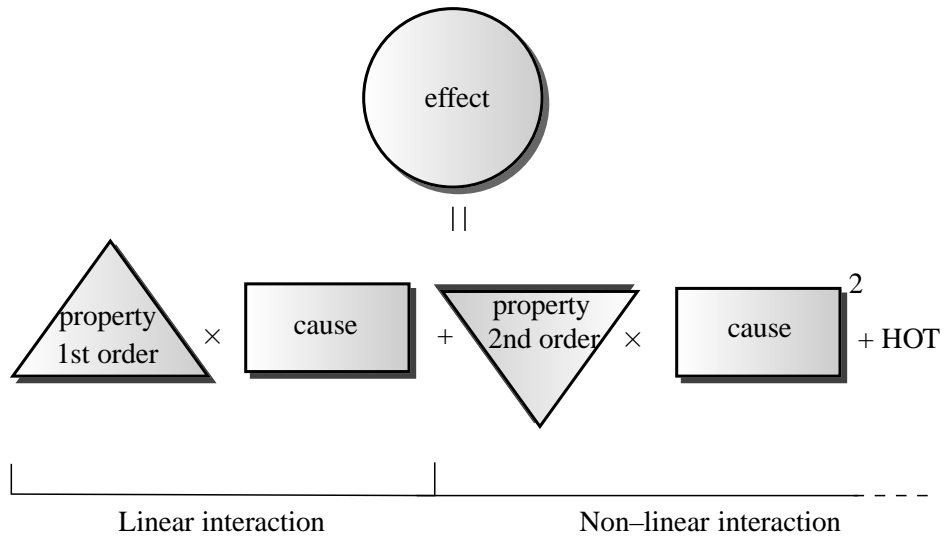


Figure 1.5: Cause and effect. First- and second-order material properties (higher-order terms are neglected).

states that the material has undergone to reach the current state: there are important memory effects in the definition of the phenomenological equations.

Figure 1.6 shows a schematic representation of the interaction between an extensive and an intensive variable, distinguishing three regions:

- a) Linear and reversible; first-order material properties can be used to describe the interaction
- b) Non-linear, but still reversible; the region can be described with second-order material properties
- c) Non-linear and irreversible due to domain-wall effects, represented as a hysteresis branch

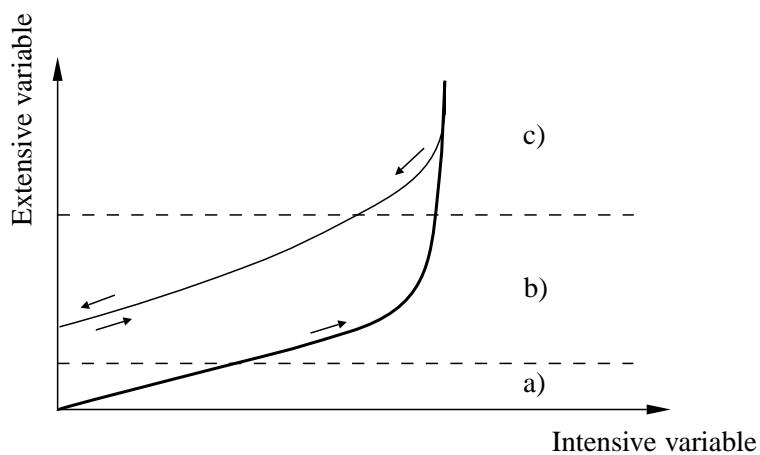


Figure 1.6: Experimental response of a pair of variables showing regions: linear, non-linear and hysteresis branch.



The following subsections introduce the equilibrium and non-equilibrium interactions and the related material properties.

### 1.1.1 Equilibrium interactions

The equilibrium interactions are formulated in thermodynamically reversible processes, which are processes that can be approximated by a succession of equilibrium states. Therefore, the equilibrium interactions are studied by equilibrium thermodynamics.

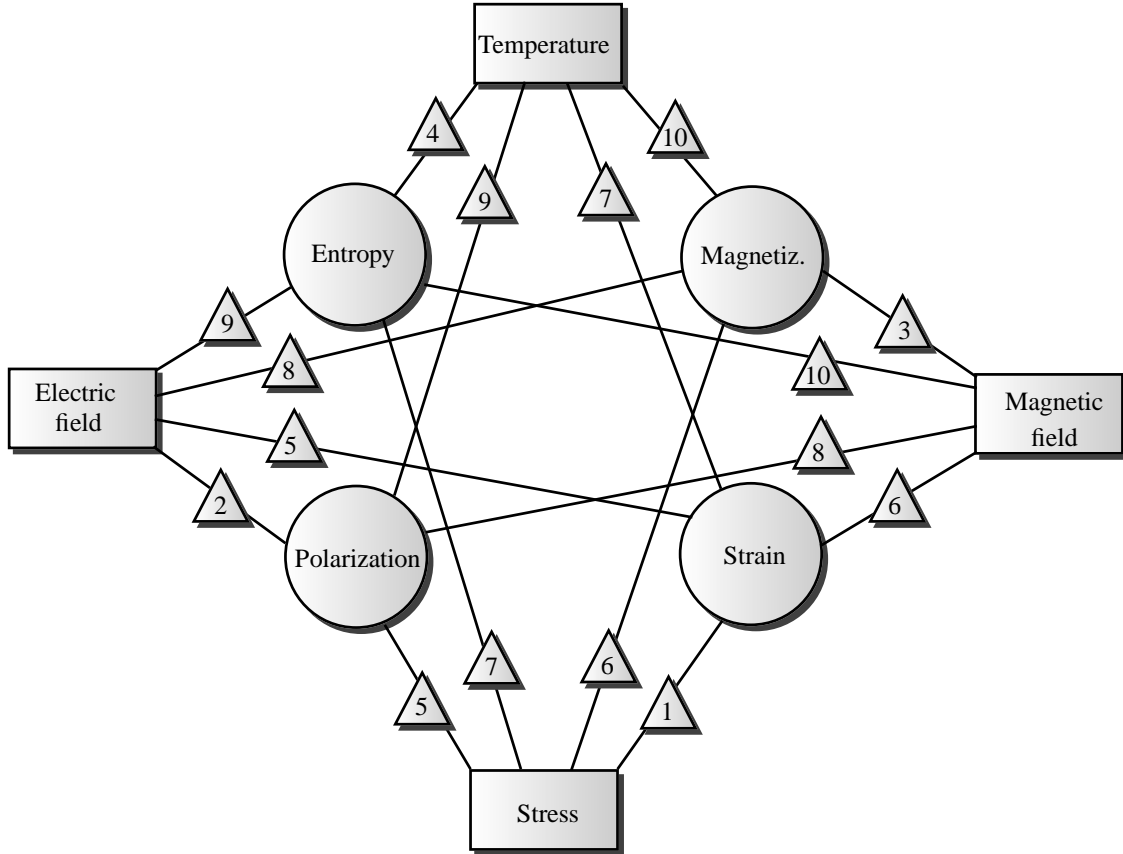


Figure 1.7: Modified equilibrium *Heckmann* diagram taking into account four fields. Intensive variables are represented by rectangles, extensive ones by circles and first-order properties by triangles (for notation, see Tables 1.1 and 1.2). For clarity, the four principal and only 12 coupled interactions are represented.

The intensive and extensive variables to study the equilibrium interactions are (stress, temperature, electric and magnetic fields) and (strain, entropy, polarization, magnetization), respectively. Following the convection of Figure 1.5, these variables are represented by rectangles (intensive) and circles (extensive) in Figure 1.7.

First-order properties are usually represented by the *Heckmann* diagram of field interactions, see Thurston [1994], Ballato [1995], Baoyuan et al. [2003] and Tinder [2008]. This diagram shows mechanical, thermal, electrical fields and their interactions. In the present





Notation	Conjugate variables	Property
	Stress - Strain	Elasticity
	Electric field - Polarization	Electric susceptibility
	Magnetic field - Magnetization	Magnetic susceptibility
	Temperature - Entropy	Heat capacity

Table 1.1: First-order equilibrium principal properties. The numbers in the first column refer to Figure 1.7.

thesis, in addition, the magnetic field is considered. Therefore, four pairs of conjugate variables, each pair with an intensive and an extensive variable, directly relate each of the fields. According to Tinder [2008] and Newnham [2005], there are in total 28 interactions:

- ▷ 4 principal interactions that relate conjugate variables
- ▷ 24 coupled interactions that relate all intensive and extensive variables

The modified *Heckmann* diagram including the four fields is shown in Figure 1.7. Again, following the convection of Figure 1.5, the first-order properties are represented by triangles. The notation of properties is given in Tables 1.1 and 1.2 for the principal and coupled interactions, respectively. For clarity, the four principal and only 12 coupled interactions are represented.

Second-order properties represent reversible but non-linear interactions and their addition in general allows for an almost exact modeling of the phenomenological equations. Generally, these properties are weak correction terms to the first-order interactions but in some cases they may be dominating, for instance under higher field strengths, e.g. electrostriction or magnetostriction.







Notation	Fields	Property
	Mechanic - Electric	Direct and converse piezoelectric
	Mechanic - Magnetic	Direct and converse piezomagnetic
	Mechanic - Thermal	Thermal expansion and piezocaloric
	Electric - Magnetic	Direct and converse magnetoelectric
	Electric - Thermal	Direct and converse pyroelectric
	Magnetic - Thermal	Direct and converse pyromagnetic

Table 1.2: First-order equilibrium coupled properties. Each row includes the two coupled interactions including the fields listed. The numbers in the first column refer to Figure 1.7.

### 1.1.2 Non-equilibrium interactions

Non-equilibrium interactions are studied by non-equilibrium thermodynamics or, in other words, thermodynamics of irreversible processes. In the framework of this formalism, the intensive (temperature, voltage and concentration gradients) and extensive (thermal, electric and mass fluxes) variables are denominated driving forces and fluxes, respectively. Again, they are represented by rectangles and circles in Figure 1.8.

The properties are again classified into first-order, second-order and domain-wall, being valid the three regions shown in Figure 1.6. However, now all processes are irreversible since the entropy of a system out of equilibrium always increases, see Chapter 2. In addition, the interpretation of domain-wall properties requires extended non-equilibrium thermodynamics and, according to Hernández-Lemus and Orgaz [2002], still represents a challenge for the theoretical physicists.

For the first-order properties, there are three pairs of conjugate variables, with a total of 15 interactions:

- ▷ 9 conductivities that relate fluxes and gradients
- ▷ 3 power properties that relate gradients
- ▷ 3 interactions between fluxes

Tables 1.3 and 1.4 list the three principal conductivities and the three power properties, respectively. The interaction between fluxes does not require any additional material property since they will be included in the balance equations, see Chapter 3. For example, an electric flux increases the thermal flux due to the *Joule* effect without the necessity of introducing additional properties.

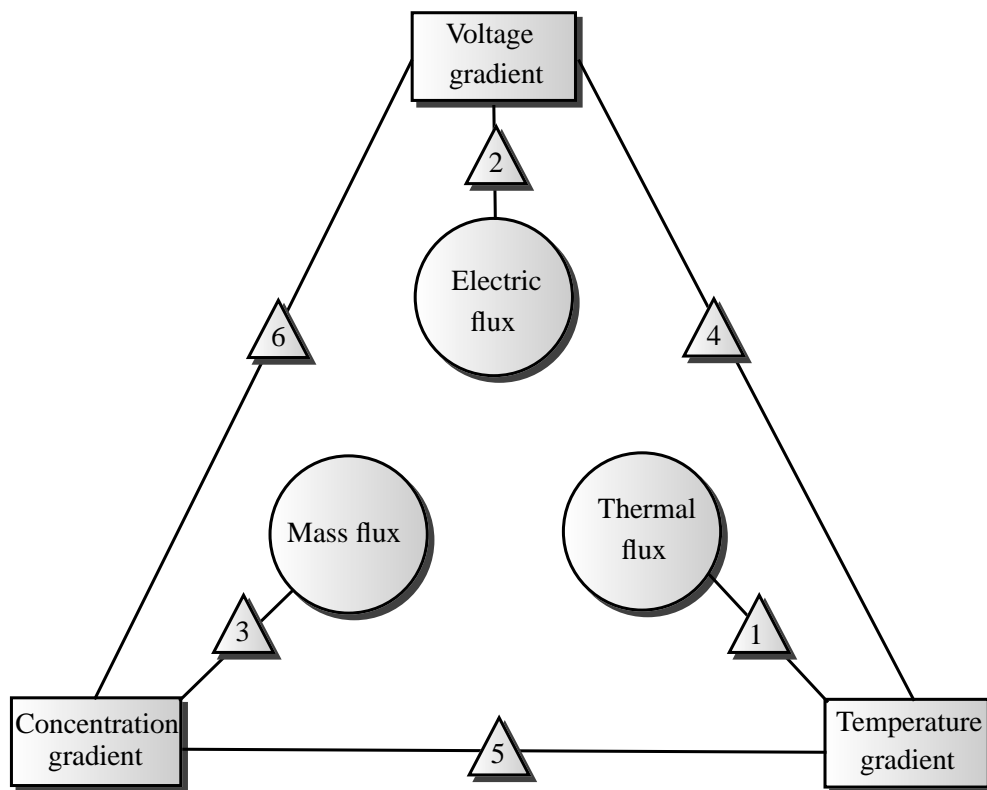


Figure 1.8: Non-equilibrium diagram taking into account the three fluxes. Driving forces (intensive variables) are represented by rectangles, and fluxes (extensive ones) by circles. Magnetic field, mechanical stress and coupled conductivities are not included for clarity. For notation, see Tables 1.3 and 1.4.

The presence of magnetic fields or mechanical stresses will affect the non-equilibrium interactions, inducing changes in the material properties and leading to new interactions such as piezoresistance, magnetoresistance, thermomagnetism, galvanomagnetism or thermogalvanomagnetism.

Figure 1.8 shows a *Heckmann* diagram analogous to the one shown in Figure 1.7 for first-order non-equilibrium interactions. Again, the first-order properties are represented by




Notation	Conjugate variables	Conductivity
	Thermal flux - Temperature gradient	Thermal
	Electric flux - Voltage gradient	Electrical
	Mass flux - Concentration gradient	Diffusivity

Table 1.3: First-order principal conductivities. Numbers on first column refer to Figure 1.8.




Notation	Gradients	Power property
	Temperature - Voltage	Thermoelectricity
	Temperature - Concentration	Thermodiffusivity
	Voltage - Concentration	Electrodiffusivity

Table 1.4: First-order power properties relating gradients. Numbers on first column refer to Figure 1.8.

triangles, see Tables 1.3 and 1.4 for notation. For clarity, the interactions caused by magnetic fields and mechanical stresses and the six coupled conductivities are not represented.

Summarizing, an active material simultaneously affected by thermal, mechanical, electric and magnetic fields can be subjected to 43 interactions requiring 40 first-order material properties to describe them. Additional complications exist: some of these properties can be dependent on the magnitude of some of the fields and, if domain-wall effects are present, these properties will be time dependent with an important memory effect.

## 1.2 Literature review

This literature review has been divided into two blocks: theoretical and Finite Element (FE) formulations. In addition, an specific state of the art appears at the beginning of each chapter in the Part III of the work.

### 1.2.1 Theoretical formulation

There are basically two theoretical procedures to study the multi-coupled formulation from a thermodynamic point of view:

**Non-equilibrium thermodynamics** was used in Callen [1948], Callen [1985] and Landau and Lifshitz [1984] considering only thermal, electric and magnetic fields and for non-polarizable/non-magnetizable materials. These works were extended in de Groot [1961] and de Groot and Mazur [1984] incorporating the mechanic field and taking into account the polarization/magnetization of the materials. However, dielectric/magnetic relaxations, known as *Debye* relaxations and interpreted as irreversibilities due to microscopic polarization/magnetization interactions, are not fully studied in these works. On one hand, the dielectric relaxation was investigated for isotropic, Restuccia and Kluitenberg [1988]), and for anisotropic, Restuccia and Kluitenberg [1992], materials; on the other, the magnetic relaxation was reported in Restuccia [2010] using the internal variables procedure.

**Rational thermodynamics**, which transforms the thermodynamic concepts into a *Continuum Mechanics* framework, was stated by Coleman [1964] and Truesdell [1968]. Several authors have used this procedure to obtain a multi-coupled formulation, see Ersoy [1984], Eringen and Maugin [1990] and Nour et al. [1990] for example.

As discussed at the beginning of this chapter, miniaturized devices and high-frequency processes are increasingly applied in modern technologies. For these applications the local equilibrium hypothesis, which will be stated in Chapter 2, is not valid, requiring new and advanced theoretical procedures. According to Lebon et al. [2008], four procedures are possible:

**Extended non-equilibrium thermodynamics** that introduces state variables and fluxes as independent variables (mixed formulation)

**Rational extended thermodynamics** that develops evolution equations for fluxes, introducing supplementary *Lagrange* multipliers

**Internal variables** that are macroscopic representations of microscopic internal structures, and are incorporated to the state variables

**Hamiltonian formalisms** that are a generalization of the *Poisson* bracket formalism, Landau and Lifshitz [1982], expressing the evolution equations by means of two thermodynamic potentials (total energy and dissipation) denominated generators

Using the first procedure, an extended approach considering thermal and electric fields without polarization was developed in Llebot et al. [1983]. The polarization effects were investigated in del Castillo and García-Colín [1986]. The mechanic field was incorporated to the previous thermal and electric ones in Maruszewski and Lebon [1986] and Lu and Hanagud [2004]. A full revision of extended non-equilibrium thermodynamics, applications and theoretical developments, can be found in Nettleton and Sobolev [1995a], Nettleton and Sobolev [1995b] and Nettleton and Sobolev [1996].

Examples of multi-coupled formulations using rational extended thermodynamics and internal variables are Ersoy [1986] and Restuccia [2010], respectively.

### 1.2.2 *Finite element formulation*

To the best of our knowledge, there has been no attempt to propose a unified formulation for the multi-physics problem of active materials using the Finite Element Method (FEM). Most advanced publications study single interactions or phenomena. Only very recently, the issues of multi-physics and multi-coupling have been addressed in Tang and Yu [2009], but considering micro-mechanical models. Therefore, their computational cost is very elevated and the application for optimization and design of devices is very expensive if not impossible. A separate state of art for each interaction will be developed in the following sections.

#### PIEZOELECTRIC INTERACTION

In the literature there are two alternative FE formulations for the piezoelectric problem: scalar and vector.

The scalar formulation uses four degrees of freedom (d.o.f.) per node: three displacement and a scalar potential or voltage. A monolithic or fully coupled (coupling at the stiffness matrix) formulation was developed by Allik and Hughes [1970]; an iterative or stagger formulation was proposed by Gaudenzi and Bathe [1995]. Starting from the Allik and Hughes [1970] formulation, several modifications have been introduced in the last decades: the assembled matrix was rescaled in Qi et al. [1997] to avoid its ill-conditionality, the remanent strain and polarization were included in Zeng and Rajapakse [2004]. The latter work could be considered the first step to model the hysteretic behavior inherent to ferroelectric materials. According to Kaltenbacher et al. [2010], there are three different approaches to model this behavior:

- ▷ Thermodynamically consistent models, Kamlah and Bohle [2001]

- ▷ Micromechanical models, McMeeking et al. [2007]
- ▷ Models with hysteresis operator, Kaltenbacher et al. [2010]

The vector formulation, developed by Landis [2002], uses six d.o.f. per node: three displacements and three components of the vector potential. The main difference between both formulations arises from the choice of the constitutive equations: the electric displacement has to be chosen as an independent variable for the vector formulation. A problem related to the vector formulation is the loss of uniqueness. For this reason, some gauging procedures were investigated in Semenov et al. [2006], incorporating the *Coulomb* gauge to the formulation developed in Landis [2002] by means of the penalty method. The main drawback of the vector formulation is the increase of CPU time, however, this disadvantage can be offset by the rapid convergence in non-linear problems.

#### MAGNETOSTRICTIVE INTERACTION

As in the piezoelectric interaction, there are two FE formulations, based on the scalar (four d.o.f.) and vector (six d.o.f.) magnetic potentials. Furthermore, fully coupled and staggered formulations are reported in the literature.

For the scalar formulation, a fully coupled, 2-D and non-linear FE formulation was developed in Benbouzid et al. [1993], extending it by incorporating the dynamic response in Benbouzid et al. [1995a] and the *eddy* currents in Benbouzid et al. [1995b]. An alternative 2-D staggered formulation was proposed in Hirsinger and Billardon [1995], assuming the non-linear problem only for the magnetic field and solving it by *Newton* methods. A fully coupled 3-D and dynamic FE was formulated in Kannan and Dasgupta [1997]. The hysteretic behavior was modeled using thermodynamically consistent models in Linnemann and Klinkel [2006], Klinkel and Linnemann [2008], Linnemann et al. [2009] and Kaltenbacher et al. [2009].

For the vector formulation, a fully coupled, 3-D, non-linear and steady-state FE was developed in Reng et al. [1995], solving the non-linearities by the *Newton-Rhapson* algorithm and symmetrizing the whole matrix. Similar 2-D FE models were reported in Besbes et al. [1996], Yan et al. [2004] and Gros et al. [1998]. The latter included experimental magnetostrictive curves into the tangent stiffness matrix. An alternative fully 3-D and non-linear FE formulation, including the *Maxwell* stress tensor, was reported in Pérez-Aparicio and Sosa [2004]. This formulation was extended in Yoo et al. [2008] and Kiang and Tong [2010], including the non-linearities of the material, i.e. the dependence of the properties with the magnetic field.

#### THERMOELASTIC INTERACTION

For the thermoelastic interaction state of art description, it is necessary to develop a brief historical introduction about the theoretical methods.



In principle, the classical thermoelasticity is not compatible with the physical observations since intrinsically has two shortcomings:

- i) There is only one way coupling: the mechanical field does not interact with the thermal one
- ii) The heat equation states infinity speeds of propagation for the heat waves (parabolic model)

The first shortcoming was solved in Biot [1956], introducing the theory of coupled thermoelasticity. For this purpose, the entropy was balanced by introducing a dissipative or entropy production term, which fully coupled the governing equations. The second shortcoming was addressed in Cattaneo [1938], modifying the *Fourier* law by means of an empirical parameter: the relaxation time. For the *Continuum Mechanics* community, the *Cattaneo* or hyperbolic model is denominated second sound.

Numerically, the uncoupled thermoelasticity was addressed by means of staggered FE formulations, e.g. Nowacki [1962]. These formulations use two steps: temperature distributions are obtained solving the heat conduction problem and thermal stresses solving the elastic problem from the strains caused by the temperature distribution previously calculated.

In order to solve the coupled thermoelasticity proposed by Biot [1956], several FE works have been reported in the literature. For example, Carter and Booker [1989] and Serra and Bonaldi [2008] developed 3-D isoparametric formulation and an eight-node element based on the *Reissner-Mindlin* plate theory, respectively.

The influence of the second sound in the thermoelasto-dynamic behavior of continuum bodies has been studied by several authors using the FEM. The difficulty of the second sound model is the time integration scheme, since numerical oscillations appear. Explicit finite differences were used in Tamma and Namburu [1992], enabling a better physical interpretation. In Bargmann and Steinmann [2005], this temporal discretization was solved using discontinuous and continuous *Galerkin* methods (mixed method for the time integration). However, numerical oscillations appeared and a stabilization method was developed by the same authors in Bargmann and Steinmann [2006] and Bargmann and Steinmann [2008]. The *Newmark- $\beta$*  algorithm, with optimized time steps and algorithm parameters, was proposed in Yu et al. [2006], Zhou et al. [2006] and Tian et al. [2006].

#### *THERMOELECTRIC INTERACTION*

A steady-state and non-linear 3-D FE formulation, considering temperature-dependence properties, was reported in Gavela and Pérez-Aparicio [1998], Pérez-Aparicio and Gavela [1998] and Pérez-Aparicio et al. [2007] and implemented into the research code FEAP. Dynamic thermoelectric elements were implemented into the FE commercial softwares ANSYS and COMSOL in Antonova and Looman [2005] and Ebling et al. [2009], respectively. These

implementations did not consider temperature–dependent properties, but included a standard interface element to model heat convection. In addition, the commercial softwares permit the study of the mechanical responses; feature that was used by Huang et al. [2008], Clin et al. [2009] and Gao et al. [2011]. The elasto–termoelectric interaction, considering temperature–dependence properties, was implemented into the commercial FE software COMSOL in Jaegle et al. [2008] and Jaegle [2008].

### 1.3 Objectives

The design of electronic devices is often based on laborious experiments in which different alternatives are built and tested. Only recently, numerical models that can predict accurately the behavior of some of these materials have been developed, allowing prototyping in the numerical laboratory, prior to the building and testing in the electronics laboratory. This numerical prototyping, although faster than the experimental one, is still applied to particular problems one by one. On this basis, the objectives of the present thesis are:

- ◇ To develop an unified thermodynamic formulation applied to multi–coupled materials jointly subjected to mechanical, thermal, electric and magnetic fields. For this purpose, the extended non–equilibrium thermodynamics is used.
- ◇ To use the FEM to transform the multi–coupled formulation into a matrix form amenable for the implementation into a computer code. Due to the complexity of the targeted problem, only the non–equilibrium interactions have been transformed into a FE formulation. In addition, concentration gradients and mass fluxes are assumed to be zero
- ◇ To implement the non–equilibrium FE formulation into the research code FEAP, see Taylor [2010], and to validate it by means of several practical applications

### 1.4 Outline of thesis

In order to separate the theoretical and numerical developments and the results, the thesis is divided into three parts:

Part I introduces the notation and obtains the multi–coupled governing equations. **Chapter 2** presents an outline of *Continuum Physics* to clarify ideas about *Thermodynamics*, *Continuum Mechanics* and *Electromagnetism*. From the extended non–equilibrium formalism, the governing equations composed of balance and of transport or constitutive equations are obtained in **Chapter 3**.

Part II extracts the residual forms from the governing equations using the FEM, see **Chapter 4**. Then, the fully coupled assembled matrix is obtained and all its terms are

commented. In addition, non-linear and time-integration algorithms are presented. As mentioned, the FE formulation is applied only for non-equilibrium interactions. For equilibrium interactions, the author of the thesis and his advisor have several publications in international journals.

Part III obtains results from the FE code using relevant applications, validating and testing the numerical algorithms. Five different applications (five chapters) are developed:

- ▷ **Chapter 5** studies the thermoelectric interaction taking into account the relaxation time or second sound for the thermal field. Numerical results are validated using four analytical 1-D solutions and calibrating and testing the time-integration algorithms. In addition, a more complete 3-D example is included, obtaining interesting conclusions for future works
- ▷ **Chapter 6** investigates the elasto-thermo-electric interactions studying the stresses in a thermoelectric cooler under electric current pulses (pulsed thermoelectric). This is a novel application used in micro-electronics to cool devices
- ▷ **Chapter 7** studies the hysteretic behavior of the thermoelectric interaction. This behavior was experimentally observed in Ferrer et al. [2006], but no physical explanation was given in the publication. We believe that this behavior is due to the coupled relaxation times. In order to validate our explanation, the experiment is calibrated solving an inverse problem. For this purpose, a cost function is defined and minimized by genetic algorithm. Once calibrated, the FE results agrees with the experimental ones and several additional numerical experiments are performed
- ▷ **Chapter 8** studies the magneto-thermo-electric coupling (thermomagnetic and galvanomagnetic interactions) using simple analytical solutions. The presence of a magnetic field alters the 3-D voltage and temperature distributions
- ▷ **Chapter 9** investigates the elasto-magneto-thermo-electric interaction on a commercial *Peltier* cooler. The obtained results permit to extract important conclusions for the design and optimization of these coolers

## **Part I**

# **THEORETICAL FORMULATION**



*Truth in science can be defined  
as the working hypothesis best  
suited to open the way to the  
next better one.*

**Konrad Zacharias Lorenz**  
(1903–1989)

# 2

## Outline of Continuum Physics



This chapter presents an outline of *Continuum Physics* to introduce the necessary equations for obtaining the multi-coupled governing equations. Note that governing equations are composed of balance equations, of transport or constitutive equations and of boundary conditions. Section 2.1 reviews the *Thermodynamics* formalisms from *Classical Thermodynamics* or *Thermostatistics* to the formalism used in the present thesis: *Extended Non-Equilibrium Thermodynamics*. Section 2.2 and 2.3 introduce the basic concepts on *Continuum Mechanics* and *Electromagnetism*, respectively. Furthermore, Section 2.3 presents the *Minkowski–Abraham* controversy, which still represents a challenge for theoretical physicists.

### 2.1 Thermodynamics

*Thermodynamics* is a physical science that studies the transformations of energy in all their forms. The term “thermodynamics” was born in 1854 when the Scottish physicist *Kelvin* stated a concise definition of thermodynamics:

*Thermo–dynamics is the subject of the relation of heat to forces acting between contiguous parts of bodies, and the relation of heat to electrical agency.*

However, one of the founding papers in thermodynamics was a 300–page paper published by *Gibbs* in 1876: *On the Equilibrium of Heterogeneous Substances*.

Before discussing the thermodynamic formalism and in order to clarify the formulations developed in this section, several definitions are introduced.

A thermodynamic system is a portion of matter with domain  $\Omega$  and boundary  $\Gamma$ . The union of the system and its surrounding  $\Omega^\infty$  constitutes the thermodynamic universe, which is shown in Figure 2.2. There are three types of thermodynamics systems:

- ▷ *Open system*: Exchanges matter and energy with its surrounding
- ▷ *Closed system*: Exchanges energy but not matter
- ▷ *Isolated system*: Does not exchange neither energy nor matter

State variables are a set of path-independent variables that describe the “state” of the thermodynamic system. There are two types of state variables:

- ▷ *Extensive variables ( $\mathcal{E}$ )*: Depend on the amount of matter in the system
- ▷ *Intensive variables ( $\mathcal{I}$ )*: Depend on the external conditions imposed on the system

As mentioned in the Chapter 1, extensive and intensive variables represent causes and effects, respectively.

A thermodynamic process represents the energetic evolution of a thermodynamic system from an initial state to a final state. There are two types of processes:

- ▷ *Reversible process*: Continuum sequence of equilibrium states (idealized process)
- ▷ *Irreversible process*: Any non-reversible process

*Thermodynamics* usually refers to a discipline that encompasses different formalisms. According to Lebon et al. [2008], three thermodynamic formalisms can be defined:

- ▷ **Equilibrium Thermodynamics (ET)**, Callen [1985], studies macroscopic properties of systems that are in mechanical, thermal, electric, magnetic and chemical equilibrium. This formalism should be denominated thermostatic, since it studies time-independent and spatially homogeneous systems. However and for historical reasons, it is denominated thermodynamics

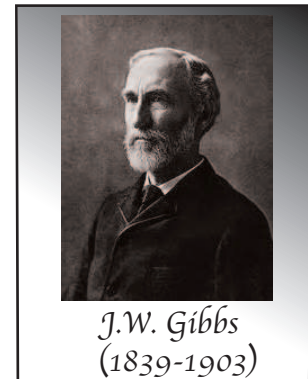


Figure 2.1: *Josiah Willard Gibbs* (1839–1903), American physicist who was awarded with the first American Ph.D. in engineering in 1863.

- ▷ **Non–Equilibrium Thermodynamics (NET)** or thermodynamics of irreversible processes, de Groot and Mazur [1984], deals with processes that depend on time and on spatial coordinates. This formalism is based on the local equilibrium hypothesis, which will be stated in the following sections.
- ▷ **Extended Non–Equilibrium Thermodynamics (ENET)**, Jou and Lebon [1996], studies systems where the local equilibrium hypothesis is not valid using thermodynamic mixed formulations

These formalisms are described in the following subsections.

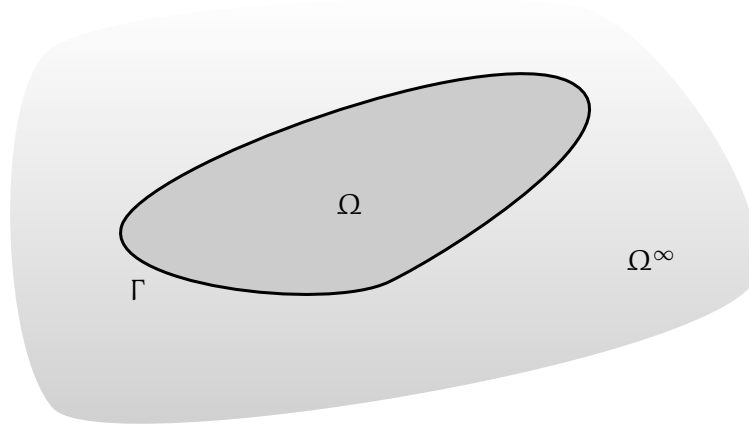


Figure 2.2: Thermodynamic universe composed of the thermodynamic system  $\Omega$  and of its surrounding  $\Omega^\infty$ .

### 2.1.1 *Equilibrium thermodynamics*

ET is based on two fundamental laws (zero and third laws are omitted in the present thesis). The first principle or energy conservation law states that the energy of the universe is a constant. Mathematically:

$$dU = \delta Q + \delta W \quad (2.1)$$

where  $U$ ,  $Q$  and  $W$  denote internal energy, heat and work performed by the system, respectively. Furthermore, the symbol  $\delta$  denotes that  $\delta Q$  and  $\delta W$  depend on the path: they are not state variables but path variables. The symbol “d” represents exact differentials and is used to represent state variables.

The second principle or entropy law states that the entropy  $S$  of the universe never decrease. Representing the entropy as the sum of two terms:

$$dS = d^s S + d^i S \geq 0 \quad (2.2)$$



where  $d^s S$  and  $d^i S$  are the entropy variations due to reversible exchanges of matter and energy with the surrounding and due to internal irreversible processes, respectively. The first term on the right side in (2.2) can be expressed as:

$$d^s S = \frac{\delta Q}{T} \quad (2.3)$$

where  $T$  is the temperature. In conclusion, the second law permits to define a new state variable  $d^s S$  from a path variable  $\delta Q$ .

Considering reversible processes:  $d^i S = 0$ , the Gibbs equation is obtained by combining the first and the second laws:

$$TdS = dU - \sum_{i=1}^3 \mathcal{I}_i d\mathcal{E}_i \quad (2.4)$$

where the reversible work  $dW$  is the sum of the products of extensive and intensive variables. Table 2.1 shows these variables for equilibrium interactions.

Intensives	$\mathcal{I}$	Extensives	$\mathcal{E}$
Stress	$T$	Strain	$S$
Electric field	$E$	Polarization	$P$
Magnetic induction	$B$	Magnetization	$M$

Table 2.1: Intensive and extensive variables for equilibrium interactions.

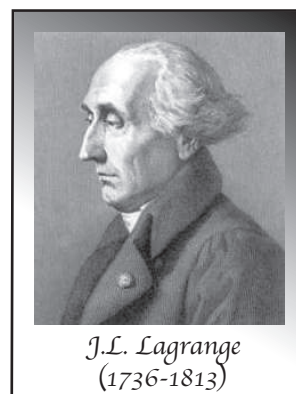
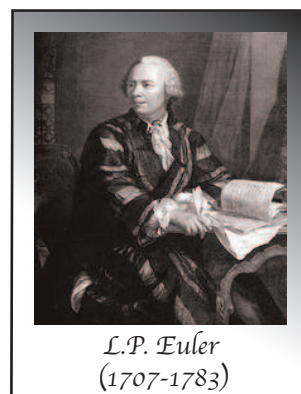


Figure 2.3: *Leonhard Paul Euler* (1707–1783) was born in Switzerland and was the best mathematician in the XVIII Century. *Giuseppe Lodovico Lagrangia* or *Lagrange* (1736–1813) was born in Italy and succeeded *Euler* as the director of mathematics at the *Prussian Academy of Science* in *Berlin*.

### 2.1.2 Non-Equilibrium Thermodynamics

NET transforms the thermodynamic laws into continuum or local forms (balance equations) by assuming the continuum and the local equilibrium hypotheses. In this sense, NET may be interpreted as *Continuum Physics* formalism: its state variables depend on time and on spatial coordinates. Before expressing the laws in continuum forms, the reference system and the mentioned hypotheses are defined.

#### REFERENCE SYSTEM

Two descriptions to study the motion of the system are shown in Figure 2.4: *Lagrangian* and *Eulerian*, Eringen [1980] and Bonet and Wood [1997]. The material or *Lagrangian*  $X$  description refers to the behavior of a material point (used in *Solid Mechanics*); the spatial or *Eulerian*  $x$  one to spatial positions (used in *Fluid Mechanics*).

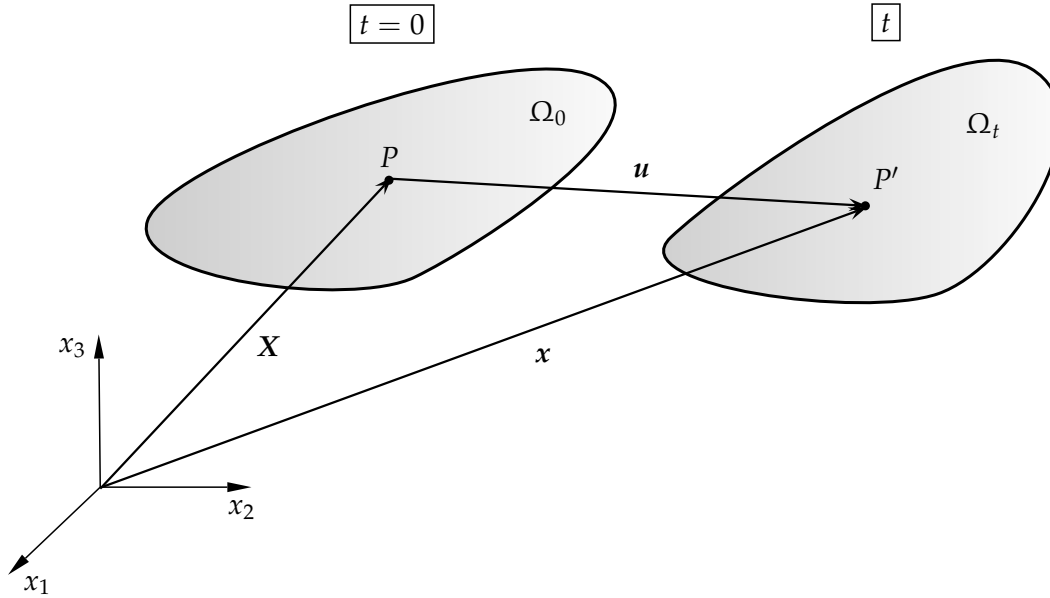


Figure 2.4: Reference system showing the *Lagrangian* and *Eulerian* descriptions.

The consideration of the two different descriptions implies the definition of two: position vectors ( $X, x$ ), displacement vectors ( $U, u$ ) and time derivatives. The latter are related by:

$$\frac{d_p(x, t)}{dt} = \frac{\partial_p(x, t)}{\partial t} + \mathbf{v} \cdot \nabla_p(x, t) \quad (2.5)$$

where  $t$  denotes time,  $p(x, t)$  represents a continuum property in *Eulerian* description and  $\mathbf{v}$  is the *Eulerian* velocity. The last term on the right side in (2.5) is denominated convective derivative, since it is closely related to the particle motion inside the system.

In the rest of the present thesis the *Lagrangian* description is used. Therefore and according to Oliver and Agelet [2000],  $x = X$ ,  $u = U$  and the convective term is avoided. An obvious advantage of the *Lagrangian* formulation is that the convective term disappears.

## HYPOTHESES

The continuum hypothesis, Eringen [1980], assumes that the matter in the system  $\Omega$  is continuously distributed and fills the entire system. Mathematically:

$$\rho_m = \lim_{\Delta\Omega \rightarrow 0} \frac{\Delta m}{\Delta\Omega} \geq 0 \quad ; \quad (2.6)$$

$$\rho_q = \lim_{\Delta\Omega \rightarrow 0} \frac{\Delta q}{\Delta\Omega} \geq 0$$

where  $\rho_m, \rho_q$  denote the mass and electric charge (either positive or negative) densities, respectively, and  $\Delta m, \Delta q$  the total mass and electric charge contained in  $\Delta\Omega$ . When  $\Delta\Omega$  is greater than a certain critical  $\Delta\Omega^*$ , the *Continuum Mechanics* is a good mathematical model since  $\rho_m$  and  $\rho_q$  depend only on the spatial coordinates and on the time and not on the  $\Delta\Omega$ , see Figure 2.5. Note that the validity of this hypothesis is closely related to  $\Delta\Omega^*$  and, therefore, to a critical length  $L_k$  that will be introduced in the equation (2.7).

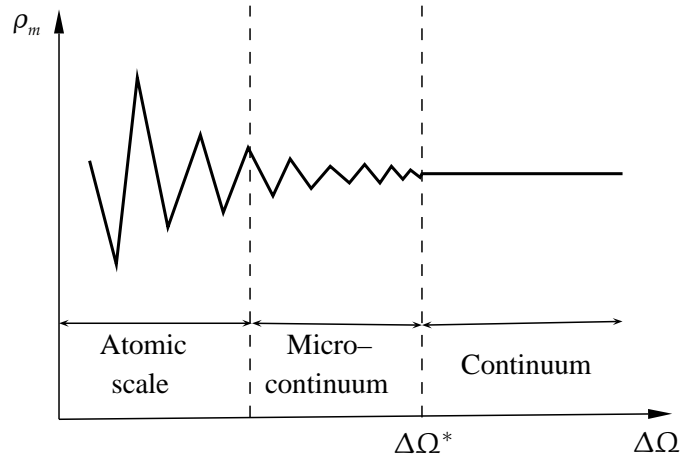


Figure 2.5: Mass density versus volume, picture taken from Eringen [1980].

The local equilibrium hypothesis, Lebon et al. [2008], assumes that the state variables out of equilibrium are the same that those used at equilibrium. This hypothesis permits to rewrite the *Gibbs* equation (2.4) locally for any time and for any material point, solving the restriction imposed by the ET that stated the time-independency of the state variables. A physical interpretation of this hypothesis may be that each *Lagrangian* point is in a different equilibrium state. Exchange of physical quantities between different points (states) is possible. Furthermore, the equilibrium state of each point changes over time.

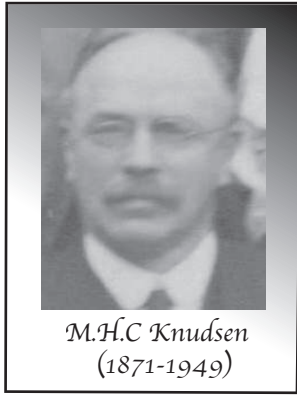


Figure 2.6: *Martin Hans Christian Knudsen* was a Danish physicist who was renowned for his work on kinetic molecular theory.

The validity of these hypotheses is closely related with the *Knudsen* ( $Kn$ ) and the *Deborah* ( $De$ ) numbers, respectively:

$$Kn = \frac{l_K}{L_K} ; \quad De = \frac{t_D}{T_D} \quad (2.7)$$

where  $L_K, T_D$  are two macroscopic parameters, representing the length and duration of the experiment, respectively, and  $l_K, t_D$  are two microscopic parameters: mean free path and equilibration or relaxation time inside each point, respectively. The previous hypotheses are valid when  $Kn, De \ll 1$ . There are several applications for which they are not valid:

▷  $Kn \geq 1$ , for example: micro- and nano-systems, thin films, superlattices, porous media

▷  $De \geq 1$ , for example: ultrasound propagation in dilute gases, polymers, superconductors, etc

Assuming the validity of these hypotheses, the thermodynamic variables may be expressed in continuum forms by integrating in  $\Omega$ . For example:

$$U = \int_{\Omega} \rho_m u \, d\Omega ; \quad S = \int_{\Omega} \rho_m s \, d\Omega \quad (2.8)$$

where  $u$  and  $s$  denote energy and entropy densities.

### BALANCE EQUATIONS

The mass balance states that the mass inside the system will remain constant over time. According to Eringen [1980]:

$$\dot{\rho}_m = -\rho_m \nabla \cdot \mathbf{v} \quad (2.9)$$

The energy balance may be understood as a continuum form of the first law. Applying to it the *divergence* theorem and denoting  $j_e$  to the energy flux and  $e$  to the total energy density (including all energy forms):

$$\frac{\partial}{\partial t} \int_{\Omega} \rho_m e \, d\Omega = \int_{\Omega} \rho_m \frac{de}{dt} \, d\Omega = - \int_{\Gamma} j_e \cdot \mathbf{n} \, d\Gamma = - \int_{\Omega} \nabla \cdot j_e \, d\Omega \quad (2.10)$$

Finally, the local form of the energy balance, de Groot and Mazur [1984], is given by:

$$\rho_m \dot{e} = -\nabla \cdot j_e \quad (2.11)$$

The entropy balance is the second law rewritten in a continuum form taking into account the *divergence* theorem:

$$\int_{\Omega} \rho_m \frac{ds}{dt} d\Omega = - \int_{\Omega} \nabla \cdot \mathbf{j}_s d\Omega + \int_{\Omega} \sigma^s d\Omega \quad (2.12)$$

where  $\mathbf{j}_s$  and  $\sigma^s$  are the entropy flux and entropy production, respectively. Finally, the local entropy balance is given by:

$$\rho_m \dot{s} = -\nabla \cdot \mathbf{j}_s + \sigma^s \quad (2.13)$$

where, according to the second law, the entropy production must be:

$$\sigma^s \geq 0 \Rightarrow \begin{cases} \sigma^s > 0 & \rightarrow \text{Irreversible process} \\ \sigma^s = 0 & \rightarrow \text{Reversible process} \end{cases} \quad (2.14)$$

### TRANSPORT EQUATIONS

The transport equations (constitutive equations in the framework of the ET) are obtained by expressing the entropy production as:

$$\sigma^s = \sum_k \mathbf{j}_s^k \cdot \mathbf{Y}^k \quad (2.15)$$

where  $\mathbf{j}_s^k$  are the  $k$  fluxes (extensive variables) and  $\mathbf{Y}^k$  the driving forces (intensive variables). As mentioned in Chapter 1, fluxes and forces are linearly related in a first and most times a good approximation by the phenomenological equations:

$$\mathbf{j}_s^k = \sum_l L^{kl} \mathbf{Y}^l \quad (2.16)$$

where  $L^{kl}$  are the first-order material properties.

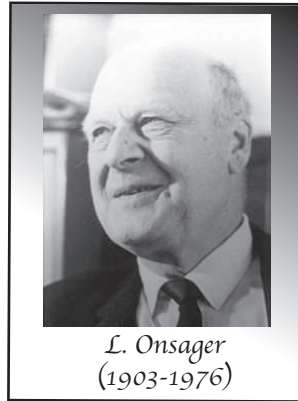


Figure 2.7: *Lars Onsager* (1903–1976) was a theoretical physicist, winner of the 1968 *Nobel Prize* in Chemistry.

According to de Groot and Mazur [1984], these material properties have three restrictions:

- i) Due to material symmetry and according to the *Curie* law, the fluxes cannot have more elements of symmetry than the driving forces they produce. Note that this restriction is not valid for the non-linear regime according to Lebon et al. [2008].
- ii) Due to the second law, the sign of the entropy production must be:

$$\sigma^s = \sum_{kl} L^{kl} \mathbf{Y}_k \cdot \mathbf{Y}_L \geq 0 \Rightarrow \begin{cases} L^{kk} \geq 0 \\ L^{kk}L^{ll} \geq \frac{1}{4}(L^{kl} + L^{lk})^2 \end{cases} \quad (2.17)$$

- iii) Due to the time reversal of the microscopic governing equations, the *Onsager–Casimir’s* reciprocal equations state:

$$L^{kl} = \pm(L^{lk})^t \quad (2.18)$$

### 2.1.3 Extended Non-Equilibrium Thermodynamics

The ENET assumes the existence of a non-equilibrium entropy density  $s_{NE}$ , that depends on the NET state variables  $\mathcal{S}$  and on the dissipative fluxes  $\dot{\mathcal{F}}$ . For the multi-coupled formulation,  $\mathcal{S}$  and  $\dot{\mathcal{F}}$  will be enumerated in the next chapter. Finally, the *Gibbs* equation is represented using a thermodynamic mixed formulation:

$$s_{NE} = s_{NE}(\mathcal{S}, \dot{\mathcal{F}}) \quad (2.19)$$

The procedure to obtain the transport equations is the same than that used in NET. Therefore, the main difference between ENET and NET is the complementation of the classical variables by dissipative fluxes. Then, ENET permits the study of thermodynamic systems in which the local equilibrium hypothesis is not valid.

## 2.2 Classical Continuum Mechanics

The present thesis assumes the small deformation theory that is based on two assumptions, Oliver and Agelet [2000]:

- i) Small displacements:  $\|\mathbf{u}\| \ll \|\mathbf{X}\|$ , see Figure 2.4. This assumption implies that there is no distinction between *Lagrangian* and *Eulerian* descriptions
- ii) Higher-order effects are neglected, implying that the mechanical compatibility equation is given by:

$$\nabla \times (\mathbf{S} \times \nabla) = 0 \Rightarrow \mathbf{S} = \nabla^s \mathbf{u} \quad (2.20)$$

where  $(.)^s$  denotes the symmetric part of the small strain tensor  $\mathbf{S}$

### 2.2.1 Momentum balance

Consider a continuum system (or body in the *Continuum Mechanics* framework, see Figure 2.8) subjected to volume  $\mathbf{f}$  and boundary  $\bar{\mathbf{t}}$  forces. Furthermore, it is bounded by essential  $\Gamma_u$  and natural  $\Gamma_p$  boundary conditions:

$$\text{Natural or } \textit{Newmann} \quad \Gamma_p : \quad \bar{\mathbf{t}} = \mathbf{T} \cdot \mathbf{n}$$

$$\text{Essential or } \textit{Dirichlet} \quad \Gamma_u : \quad \bar{\mathbf{u}} = \mathbf{u}$$

where  $\mathbf{n}$  and  $\bar{\mathbf{u}}$  denote the outward-pointing normal and the prescribed displacements, respectively.

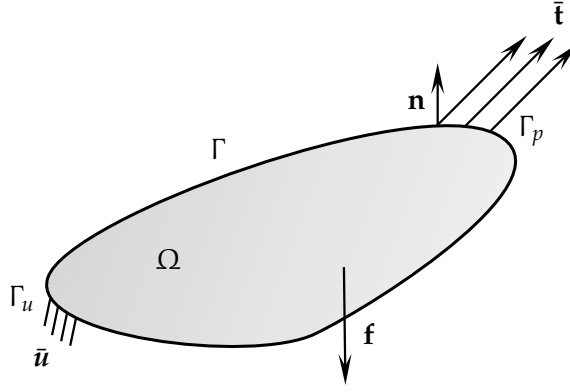


Figure 2.8: System or body in the *Continuum Mechanics* framework subjected to: volume forces, essential and natural boundary conditions.

The momentum balance is obtained by integrating both types of forces in  $\Omega$  and by applying the *divergence* theorem:

$$\int_{\Omega} \rho_m \ddot{\mathbf{u}} \, d\Omega = \int_{\Omega} \mathbf{f} \, d\Omega + \int_{\Gamma} \bar{\mathbf{t}} \, d\Gamma = \int_{\Omega} \mathbf{f} \, d\Omega + \int_{\Omega} \nabla \cdot \mathbf{T} \, d\Omega \quad (2.21)$$

and rewriting (2.21) in local form:

$$\rho_m \ddot{\mathbf{u}} = \nabla \cdot \mathbf{T} + \mathbf{f} \quad (2.22)$$

### 2.2.2 Energy balance

The energy balance is obtained using the theorem of live forces that states that the power carried out by the forces acting on the continuum body is equal to its kinetic energy. Therefore, the mechanical power  $\dot{W}_M$  is given by:

$$\dot{W}_M = \int_{\Omega} \mathbf{f} \cdot \mathbf{v} \, d\Omega + \int_{\Gamma} \mathbf{t} \cdot \mathbf{v} \, d\Gamma = \frac{d}{dt} \int_{\Omega} \frac{1}{2} \rho_m v^2 \, d\Omega + \int_{\Omega} \mathbf{T} : \dot{\mathbf{S}} \, d\Omega \quad (2.23)$$

The first and second terms on the right side represent the mechanical power due to the kinetic energy and the stresses, respectively. This thesis considers only the second term. Therefore, assuming an adiabatic process (no exchange of thermal energy between the system and its surrounding), the balance of mechanical energy  $u_M$  in local form is given by:

$$\rho_m \dot{u}_M = \mathbf{T} : \dot{\mathbf{S}} \quad (2.24)$$

## 2.3 Classical Electrodynamics

*Classical Electrodynamics* or *Classical Electromagnetism* is a physical theory that studies the interactions between electric charges and currents. It was developed over the course of the 19th century, most prominently by *Maxwell*.

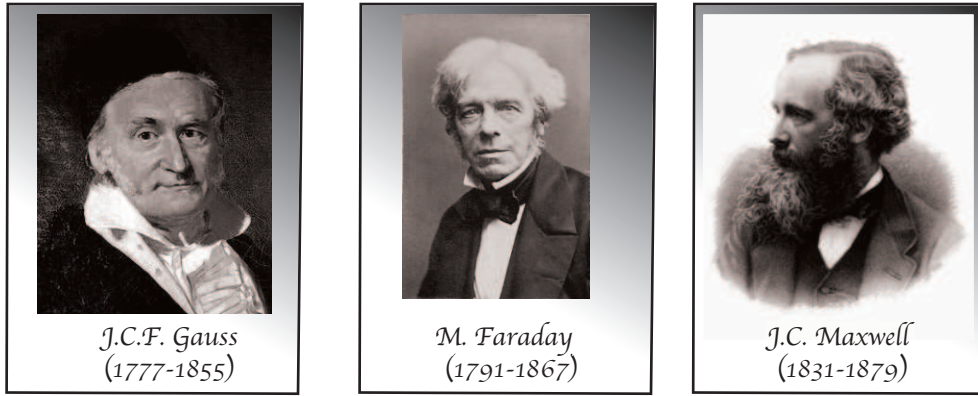


Figure 2.9: *Johann Carl Friedrich Gauss* (1777–1855) was a German scientist. *Michael Faraday* (1791–1867) was an English natural philosopher, in the terminology of the time. *James Clerk Maxwell* (1831–1879) was a Scottish physicist author of the denominated *second great unification in physics*.

### 2.3.1 Maxwell equations

*Maxwell* equations are a set of four empirical and macroscopical equations that couple the electric and magnetic fields:

$$\begin{aligned}
 \text{Gauss electric :} & \quad \nabla \cdot \mathbf{E} &= \frac{1}{\epsilon_0} (\rho_q^f + \rho_q^b) & ; \\
 \text{Gauss magnetic :} & \quad \nabla \cdot \mathbf{B} &= 0 & ; \\
 \text{Faraday :} & \quad \nabla \times \mathbf{E} + \frac{\partial \mathbf{B}}{\partial t} &= \mathbf{0} & ; \\
 \text{Ampère :} & \quad \nabla \times \mathbf{B} - \mu_0 \epsilon_0 \frac{\partial \mathbf{E}}{\partial t} &= \mu_0 (\mathbf{j} + \mathbf{j}^b) & 
 \end{aligned} \quad (2.25)$$



where  $\epsilon_0$  and  $\mu_0$  denote the permittivity and permeability of the vacuum, respectively;  $\rho_q^f, \mathbf{j}$  and  $\rho_q^b, \mathbf{j}^b$  are the *free* and *bound* sources (electric charge density, electric flux), respectively. The *free* sources may exist inside the material, while the *bound* are generated by the interaction of an external field on the system.

*Gauss* electric law relates the electric field  $\mathbf{E}$  and its sources  $\rho_q = \rho_q^f + \rho_q^b$ ; *Ampère* law the magnetic induction  $\mathbf{B}$  and  $\mathbf{j}, \mathbf{j}^b$ . *Gauss* magnetic and *Faraday* laws couple  $\mathbf{E}$  and  $\mathbf{B}$ . Note that, for these equations, the right side is zero since there are no magnetic monopoles: the magnetic field is solenoidal.

The *bound* sources characterize the response of the material by means of two new fields: polarization  $\mathbf{P}$  and magnetization  $\mathbf{M}$ . Mathematically, see Jiménez and Campos [1996] and Kinsler et al. [2009]:

$$\begin{aligned}\rho_\Omega^b &= -\nabla \cdot \mathbf{P} & ; \\ \mathbf{j}^b &= \nabla \times \mathbf{M} + \frac{\partial \mathbf{P}}{\partial t}\end{aligned}\tag{2.26}$$

Introducing (2.26) in (2.25) and taking into account the electromagnetic constitutive equations:

$$\begin{aligned}\mathbf{D} &= \epsilon_0 \mathbf{E} + \mathbf{P} & ; \\ \mathbf{H} &= \frac{1}{\mu_0} \mathbf{B} - \mathbf{M}\end{aligned}\tag{2.27}$$

the *Maxwell* equations may be rewritten as:

$$\begin{aligned}\nabla \cdot \mathbf{D} &= \rho_q^f & ; \\ \nabla \cdot \mathbf{B} &= 0 & ; \\ \nabla \times \mathbf{E} + \frac{\partial \mathbf{B}}{\partial t} &= \mathbf{0} & ; \\ \nabla \times \mathbf{H} - \frac{\partial \mathbf{D}}{\partial t} &= \mathbf{j}\end{aligned}\tag{2.28}$$

where  $\mathbf{D}$  and  $\mathbf{H}$  are the electric displacement or induction and magnetic field, respectively. For quasi-static conditions and according to Jackson [1962], Reitz and Milford [1960] and Griffiths [1999], equation (2.27) may be expressed by:

$$\begin{aligned}\mathbf{D} &= \boldsymbol{\epsilon} \cdot \mathbf{E} & ; \\ \mathbf{H} &= \boldsymbol{\mu}^{-1} \cdot \mathbf{B}\end{aligned}\tag{2.29}$$

where  $\boldsymbol{\epsilon}$  and  $\boldsymbol{\mu}$  are the material permittivity and permeability, respectively, that depend on many factors: mechanical and thermal states, frequency in dissipative media, field strength

in non-linear media and history in hysteretic materials.

The *Maxwell* equations are linear, non-linearities may be emerged from the constitutive equations and/or the electromagnet-mechanical interactions.

The equation of electric charge balance is obtained by manipulating the *Ampère* and electric *Gauss* laws:

$$\frac{\partial \rho_q^f}{\partial t} = -\nabla \cdot \mathbf{j} \Rightarrow \nabla \cdot \left( \mathbf{j} + \frac{\partial \mathbf{D}}{\partial t} \right) = 0 \quad (2.30)$$

### 2.3.2 Compatibility equations

According to the field theory, see Reitz and Milford [1960] for example, the electric and the magnetic fields may be obtained from scalar or vectorial potentials:

$$\begin{aligned} \nabla \cdot \mathbf{B} = 0 & \Rightarrow \mathbf{B} = \nabla \times \mathbf{A} & ; \\ \nabla \times \mathbf{H} = \mathbf{0} & \Rightarrow \mathbf{H} = -\nabla \varphi & ; \\ \nabla \cdot \mathbf{D} = 0 & \Rightarrow \mathbf{D} = \nabla \times \mathbf{V} & ; \\ \nabla \times \mathbf{E} = -\frac{\partial \mathbf{B}}{\partial t} & \Rightarrow \mathbf{E} = -\nabla V - \frac{\partial \mathbf{A}}{\partial t} \end{aligned} \quad (2.31)$$

where  $\mathbf{A}$ ,  $\varphi$ ,  $\mathbf{V}$ ,  $V$  are the magnetic vector potential, magnetic scalar potential, electric vector potential and electric scalar potential or voltage, respectively.

### 2.3.3 Energy balance: Poynting theorem

The electromagnetic energy balance is given by the *Poynting* theorem, Jackson [1962].

There are four *Poynting* theorems depending on the choice of the *Poynting* vector  $\mathbf{S}_P$  (see Table 2.2), which points in the propagation direction of an electromagnetic wave and has dimensions of power per area.

According to Kinsler et al. [2009], this theorem is easily interpreted for non-dispersive or non-dissipative linear materials. However, for dispersive materials (material non-linearity in the *Electromagnetism* framework) the choice of the flux vector may be decisive.

The four *Poynting* theorems may be expressed in the general form, Kinsler et al. [2009]:

$$\frac{\partial u_{EM}}{\partial t} = -c \nabla \cdot \mathbf{S}_P - \dot{r} \quad (2.32)$$

where  $c$ ,  $u_{EM} = \frac{1}{2}\epsilon_0 \mathbf{E} \cdot \mathbf{E} + \mu_0 \mathbf{H} \cdot \mathbf{H}$  and  $\dot{r}$  denote a scalar factor, the density of electromagnetic internal energy and a residual term, respectively. The last term takes into account the power

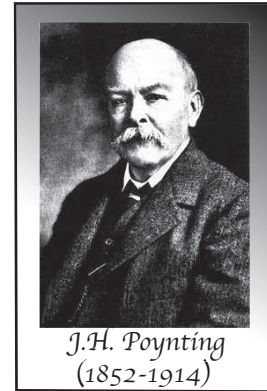


Figure 2.10: John Henry Poynting (1852–1914), English physicist.

density and the dispersive terms. Table 2.3 shows the expressions of  $c$  and of  $\dot{r}$  for the four theorems.

Representation	$S_{\mathcal{P}}$
Abraham [1910]	$\mathbf{E} \times \mathbf{H}$
Electric current, Kinsler et al. [2009]	$\mathbf{E} \times \mathbf{B}$
Magnetic current, Kinsler et al. [2009]	$\mathbf{D} \times \mathbf{H}$
Minkowski [1908]	$\mathbf{D} \times \mathbf{B}$

Table 2.2: Summary of *Poynting* vectors.

$S_{\mathcal{P}}$	$c$	$\dot{r}$
$\mathbf{E} \times \mathbf{H}$	1	$\mathbf{j} \cdot \mathbf{E} + \mathbf{E} \cdot \frac{\partial \mathbf{P}}{\partial t} + \mu_0 \mathbf{H} \cdot \frac{\partial \mathbf{M}}{\partial t}$
$\mathbf{E} \times \mathbf{B}$	$\mu_0^{-1}$	$\mathbf{j} \cdot \mathbf{E} + \mathbf{E} \cdot \frac{\partial \mathbf{P}}{\partial t} + \mathbf{E} \cdot (\nabla \times \mathbf{M})$
$\mathbf{D} \times \mathbf{H}$	$\epsilon_0^{-1}$	$\frac{1}{\epsilon_0} \mathbf{j} \cdot \mathbf{D} + \mu_0 \mathbf{H} \cdot \frac{\partial \mathbf{M}}{\partial t} + \frac{1}{\epsilon_0} \mathbf{H} \cdot (\nabla \times \mathbf{P})$
$\mathbf{D} \times \mathbf{B}$	$(\epsilon_0 \mu_0)^{-1}$	$\frac{1}{\epsilon_0} \mathbf{j} \cdot \mathbf{D} + \frac{1}{\epsilon_0} \mathbf{D} \cdot (\nabla \times \mathbf{M}) + \frac{1}{\mu_0 \epsilon_0} \mathbf{H} \cdot (\nabla \times \mathbf{P})$

Table 2.3: Summary of *Poynting* theorems.

In the *Abraham* representation the residual depends on temporal derivatives of the material response (temporal description); in *Minkowski*, it depends on spatial derivatives (spatial description). Note that the cross product represents a dispersive response in spatial description. The others representations are mixed forms.

### 2.3.4 Momentum balance

The total momentum for an electromagnetic field interacting with the matter is unique. However, its division into matter and electromagnetic parts may be described by two different ways due to the corpuscle–wave duality of the light. In the last century physicists and mathematicians have been debating about this duality. The two main theories were proposed by Minkowski [1908] and by Abraham [1910], causing the *Minkowski–Abraham* controversy. In addition, several theories have emerged in the last years, see Bowyer [2005] for a full review.



Figure 2.11: *Hermann Minkowski* (1864–1909) was a German mathematician of Ashkenazi Jewish descent. *Max Abraham* (1875–1922) was a German physicist who was born to a family of Jewish merchants.

*Minkowski* and *Abraham* theories are closely related to the choice of the *Poynting* vector for the representation of the momentum density. The *Minkowski*  $G^M$  and *Abraham*  $G^A$  momentum densities are shown in Table 2.4. Note that both momentum densities are equal in vacuum but not inside matter.

Representation	Momentum density
Abraham [1910]	$G^A = \epsilon_0 \mu_0 (\mathbf{E} \times \mathbf{H})$
Minkowski [1908]	$G^M = \mathbf{D} \times \mathbf{B}$

Table 2.4: Summary of electrodynamic momentum densities.

The *Minkowski momentum balance* is obtained by operating the *Maxwell* equations, Kinsler et al. [2009]:

$$\frac{\partial}{\partial t} \mathbf{G}^M = \nabla \cdot \mathbf{T}^M + \mathbf{f}^{EM} \quad (2.33)$$

where:

$$\mathbf{T}^M = \mathbf{D} \otimes \mathbf{E} + \mathbf{B} \otimes \mathbf{H} - \left( \frac{1}{2} \mathbf{E}^2 + \frac{1}{2} \mathbf{B}^2 - \mathbf{M} \cdot \mathbf{B} \right) \mathbf{I} \quad ; \quad (2.34)$$

$$\mathbf{f}^{EM} = -(\nabla \otimes \mathbf{E}) \cdot \mathbf{P} - (\nabla \otimes \mathbf{B}) \cdot \mathbf{M} - \rho_q^f \mathbf{E} - \mathbf{j} \times \mathbf{B}$$

The *Abraham momentum balance* is obtained by introducing the relation  $\epsilon_0 \mu_0 (\mathbf{E} \times \mathbf{H}) = \mathbf{D} \times \mathbf{B} - \epsilon_0 \mu_0 (\mathbf{E} \times \mathbf{M}) - \mathbf{P} \times \mathbf{B}$  into (2.33) and taking into account the second expression of Table 2.4:

$$\frac{\partial}{\partial t} \mathbf{G}^A = \nabla \cdot \mathbf{T}^M + \mathbf{f}^{EM} + \epsilon_0 \mu_0 \frac{\partial}{\partial t} (\mathbf{M} \times \mathbf{E}) - \frac{\partial}{\partial t} (\mathbf{P} \times \mathbf{B}) \quad (2.35)$$

The last two terms on the right side in (2.35) are denominated *Abraham force* in Jiménez and Campos [1996]. According to Hinds [2009], this force can be interpreted as the difference between the canonical (wave vector) and kinetic momentum densities:

$$\epsilon_0 \mu_0 \frac{\partial}{\partial t} (\mathbf{M} \times \mathbf{E}) - \frac{\partial}{\partial t} (\mathbf{P} \times \mathbf{B}) = \mathbf{G}_{can} - \mathbf{G}_{kin} \quad (2.36)$$

Recently, in Barnett [2010] has been concluded that  $\mathbf{G}^M$  represents the canonical momentum and  $\mathbf{G}^A$  the kinetic one. In addition, according to Hinds [2009],  $\mathbf{G}^M$ ,  $\mathbf{G}^A$  describe the wave-like and particle-like phenomena, respectively. Indeed,  $\mathbf{G}^M$  is a pseudo-momentum, which is conserved in homogeneous and isotropic media, Jiménez and Campos [1996]. Also,  $\mathbf{G}^M$  is asymmetric: the moment of momentum is not conserved. In the vacuum, kinetic and pseudo-momentum or canonical momentum are equal.

The present work studies the particle-like phenomena associated with forces and kinetic momenta. Therefore, the *Abraham energy-momentum* description is considered in the remainder.

*Insanity: doing the same thing  
over and over again and expect-  
ing different results.*

Albert Einstein (1879–1955)

# 3

## Multi-coupled governing equations



The aim of this chapter is to obtain the multi-coupled governing equations from the equations described in Chapter 2. Nevertheless and as discussed in Chapter 1, a distinction between equilibrium and non-equilibrium interactions must be performed. Otherwise, complex interactions such as viscosity or electromagnetic relaxations must be included in the formulation, which is beyond the scope of the present thesis.

Multi-coupled governing equations are composed of the balance equations, of the transport or constitutive equations and of the boundary conditions. For this reason and for a proper understanding, this chapter is structured as follows: Section 3.1 obtains the multi-coupled balance equations considering the mechanical, thermal, electric and magnetic fields. Furthermore, the multi-coupled entropy balance equations are formulated using the three thermodynamic formalisms in order to develop a comprehensible formulation. Once obtained the multi-coupled balance equations, two completely different sections are developed: Sections 3.2 and 3.3 obtain the multi-coupled governing equations for equilibrium and for non-equilibrium interactions, respectively.

### 3.1 Multi-coupled balance equations

The multi-coupled balance equations are composed of the energy and of momentum balances. In addition, the entropy balance is considered to obtain the constitutive and transport equations using the procedure described in Chapter 2.

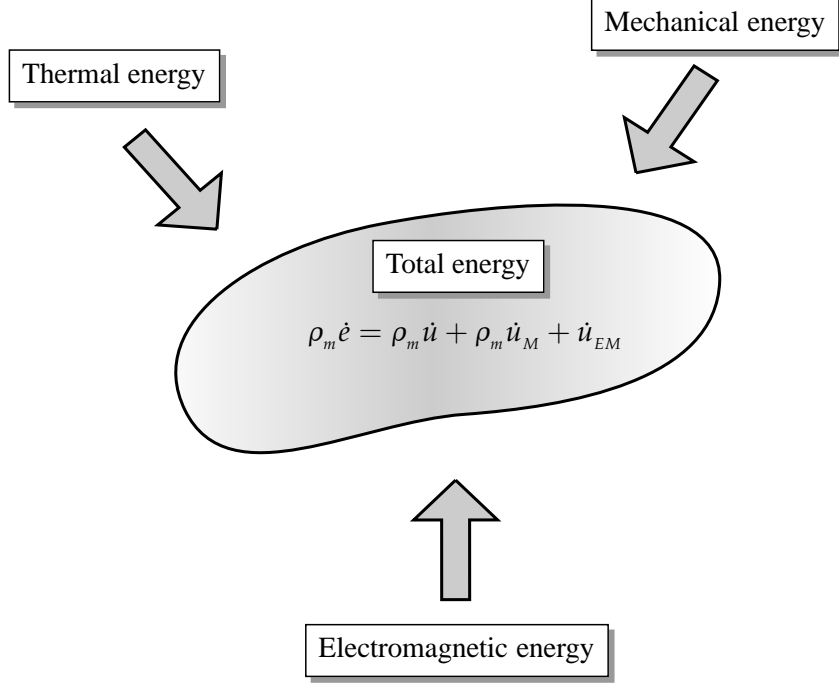


Figure 3.1: The total energy contained in the thermodynamic system is the sum of the mechanical, thermal and electromagnetic energies.

### 3.1.1 Energy balance

Consider a thermodynamic universe consisting of a system and its surrounding as that shown in Figure 2.2. The total energy of the universe is the sum of the mechanical  $u_M$ , thermal  $u$  and electromagnetic  $u_{EM}$  energies, see Figure 3.1. According to the first thermodynamic principle (2.11), the total energy is unique and can be expressed by:

$$\rho_m \dot{e} = -\nabla \cdot \mathbf{j}_e \Rightarrow \begin{cases} \rho_m \dot{e} = \rho_m \dot{u}_M + \rho_m \dot{u} + \dot{u}_{EM} ; \\ \mathbf{j}_e = \mathbf{q} + \mathbf{S}_P \end{cases} \quad (3.1)$$

The total energy flux  $\mathbf{j}_e$  is composed of thermal  $\mathbf{q}$  and of electromagnetic  $\mathbf{S}_P$  fluxes. Note that this work uses the *Abraham* representation of the electromagnetic energy balance. The mechanical flux is not included since viscous interactions are not considered, see de Groot and Mazur [1984] for further details.

The multi-coupled energy balance is obtained solving for  $\rho_m \dot{u}$  in (3.1):

$$\rho_m \dot{u} = -\nabla \cdot (\mathbf{q} + \mathbf{S}_P) - \rho_m \dot{u}_M - \dot{u}_{EM} \quad (3.2)$$

and introducing the balance of mechanical energy (2.24) and of *Abraham* electromagnetic energy (2.32):

$$\rho_m \dot{u} = -\nabla \cdot (\mathbf{q} + \mathbf{S}_P) + \mathbf{T} : \dot{\mathbf{S}} + \nabla \cdot \mathbf{S}_P + \mathbf{j} \cdot \mathbf{E} + \mathbf{E} \cdot \frac{\partial \mathbf{P}}{\partial t} + \mathbf{B} \cdot \frac{\partial \mathbf{M}}{\partial t} \quad (3.3)$$

Simplifying and expressing the partial differentials in total form, since there is no distinction between *Eulerian* and *Lagrangian* descriptions:

$$\rho_m \dot{u} = -\nabla \cdot \mathbf{q} + \mathbf{T} : \dot{\mathbf{S}} + \mathbf{E} \cdot \dot{\mathbf{P}} + \mathbf{B} \cdot \dot{\mathbf{M}} + \mathbf{j} \cdot \mathbf{E} \quad (3.4)$$

This balance equation agrees with that given in Restuccia and Kluitenberg [1992] and does not satisfy the requirements of the relativity theory. However, in the present thesis it is assumed that the velocity of the medium with respect to the observer is small compared with the light velocity. An exact relativistic formulation is developed in de Groot and Mazur [1984].

### 3.1.2 Momentum balance

According to de Groot and Mazur [1984], the conservation of total momentum takes into account the mechanical and electromagnetic momenta and may be expressed by:

$$\rho_m \ddot{\mathbf{u}} + \frac{\partial \mathbf{G}^A}{\partial t} = \nabla \cdot (\mathbf{T} + \mathbf{T}^M) \quad (3.5)$$

This conservation equation could have been stated differently. However, the amount  $(\mathbf{T} + \mathbf{T}^M)$  should always be considered. The multi-coupled momentum balance is obtained solving for  $\nabla \cdot \mathbf{T}^M$  in the *Abraham* momentum balance (2.35) and by subtracting the result in (3.5):

$$\begin{aligned} \rho_m \ddot{\mathbf{u}} = & \nabla \cdot \mathbf{T} + \rho_q^f \mathbf{E} + \mathbf{j} \times \mathbf{B} + (\nabla \otimes \mathbf{E}) \cdot \mathbf{P} + (\nabla \otimes \mathbf{B}) \cdot \mathbf{M} \\ & - \epsilon_0 \mu_0 \frac{\partial}{\partial t} (\mathbf{M} \times \mathbf{E}) + \frac{\partial}{\partial t} (\mathbf{P} \times \mathbf{B}) \end{aligned} \quad (3.6)$$

The terms (from second to fifth) on the right side in (3.6) are the *Lorentz* forces; sixth and seventh the *ponderomotive* forces that are highly non-linear and may be considered as second-order terms of the first ones.

An important advantage of the form of the total momentum conservation given by (3.5) is the elimination of the *Maxwell* stress tensor. Using other forms, the *Maxwell* stresses are maintained, but removing other terms in (3.6).

### 3.1.3 Entropy balance

The multi-coupled entropy balance is obtained using the ET, NET and ENET formalisms in order to develop a comprehensive derivation.

## EQUILIBRIUM THERMODYNAMICS

From the ET framework, the *Gibbs* equation is given by (2.4), in which the reversible work was expressed as the sum of the products of the extensive and intensive variables given



in Table 2.1. Denoting the reversible variables by the superscripts  $(.)^{eq}$ , the multi-coupled *Gibbs* equation can be written as:

$$ds = \frac{1}{T} du - \frac{1}{\rho_m T} T^{eq} : dS - \frac{1}{T} E^{eq} \cdot dp - \frac{1}{T} B^{eq} \cdot dm \quad (3.7)$$

where  $p$  and  $m$  are the specific polarization and magnetization, i.e.:  $P = \rho_m p$ ,  $M = \rho_m m$ , respectively. According to Restuccia and Kluitenberg [1992], the initial states are assumed to be:

$$T^{eq} = E^{eq} = B^{eq} = \mathbf{0} \quad \text{if} \quad S = p = m = \mathbf{0} \quad \text{and} \quad T = T_0$$

where  $T_0$  is the reference temperature.

The *Helmholtz* free energy  $f$  is obtained introducing (3.7) in the relation  $f = u - T s$  to give:

$$df = -sdT + \frac{1}{\rho_m} T^{eq} : dS + E^{eq} \cdot dp + B^{eq} \cdot dm \quad (3.8)$$

From the free energy, the multi-coupled entropy at equilibrium may be extracted, Restuccia and Kluitenberg [1992]:

$$\rho_m \dot{s} = \frac{c}{T_0} \dot{T} + \boldsymbol{\beta} : \dot{S} + \boldsymbol{\pi}^E \cdot \dot{P} + \boldsymbol{\pi}^M \cdot \dot{M} \quad (3.9)$$

where  $c$ ,  $\boldsymbol{\pi}^E$  and  $\boldsymbol{\pi}^M$  denote heat capacity, pyroelectric and pyromagnetic properties, respectively.

#### NON-EQUILIBRIUM THERMODYNAMICS

From the NET framework and assuming the continuum and local equilibrium hypotheses, the multi-coupled *Gibbs* equation (3.7) is rewritten in a continuum form using the multi-coupled energy balance (3.4):

$$\begin{aligned} \rho_m \dot{s} = & -\nabla \cdot \left( \frac{\boldsymbol{q}}{T} \right) + \boldsymbol{q} \cdot \nabla \left( \frac{1}{T} \right) + \frac{1}{T} \boldsymbol{j} \cdot \boldsymbol{E} \\ & + \frac{1}{T} (T - T^{eq}) : \dot{S} + \frac{1}{T} (\boldsymbol{E} - \boldsymbol{E}^{eq}) \cdot \dot{P} + \frac{1}{T} (\boldsymbol{B} - \boldsymbol{B}^{eq}) \cdot \dot{M} \end{aligned} \quad (3.10)$$

Furthermore, the following vectorial identity has been used:

$$\frac{\nabla \cdot \boldsymbol{q}}{T} = \nabla \cdot \left( \frac{\boldsymbol{q}}{T} \right) - \boldsymbol{q} \cdot \nabla \left( \frac{1}{T} \right)$$

The entropy flux and entropy production terms are calculated by comparing (3.10) and (2.13):

$$j_s = \frac{q}{T} \quad ;$$

$$\sigma^s = q \cdot \nabla \left( \frac{1}{T} \right) + \frac{1}{T} j \cdot E + \frac{1}{T} (T - T^{eq}) : \dot{S} + \frac{1}{T} (E - E^{eq}) \cdot \dot{P} + \frac{1}{T} (B - B^{eq}) \cdot \dot{M} \quad (3.11)$$

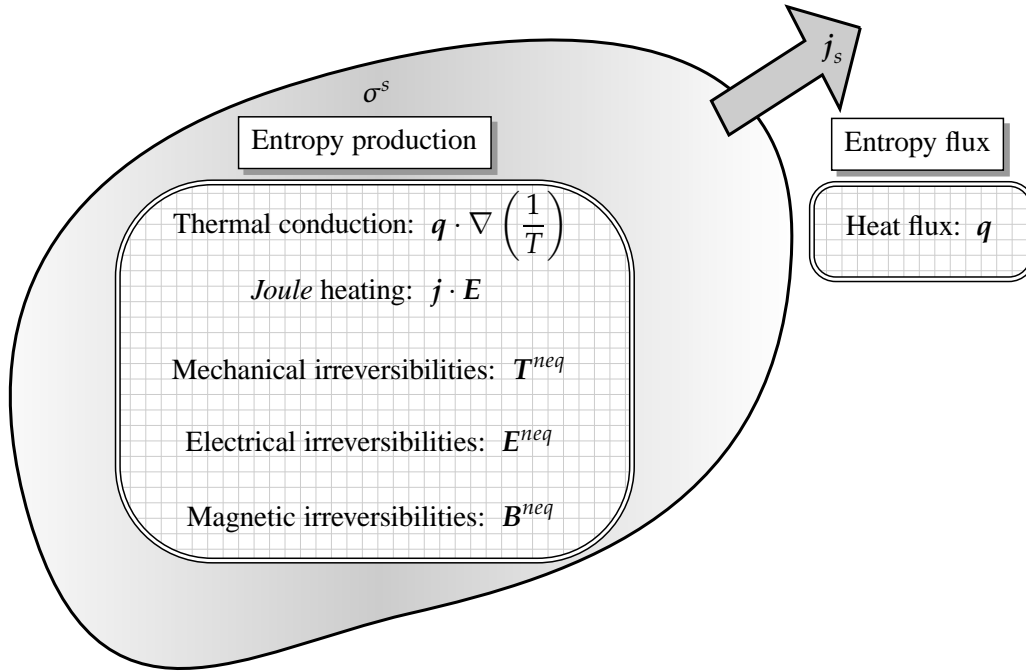


Figure 3.2: The entropy balance is composed of entropy flux and of entropy production. On one hand, the entropy flux is closely related with the thermal flux. On the other, there are five entropy sources that arise from thermal conduction, from *Joule* heating and from mechanical, electric and magnetic irreversibilities.

From (3.11), the entropy flux is closely related to the heat flux, see Figure 3.2. For the entropy production, the first two terms on the right side arise from the thermal conduction and from the *Joule* heating, respectively. The rest of terms from:

- ▷ Non-equilibrium stress tensor:  $T^{neq} = T - T^{eq}$
- ▷ Non-equilibrium electric field:  $E^{neq} = E - E^{eq}$
- ▷ Non-equilibrium magnetic induction:  $B^{neq} = B - B^{eq}$

The contribution of the last three terms to the entropy production (irreversibilities) are due to viscous interactions (de Groot and Mazur [1984]), dielectric relaxations (Debye [1913]) and magnetic relaxations (Restuccia [2010]), respectively.

The dielectric relaxation was discovered by *Debye* in 1913 and represents the momentary delay in the permittivity of a material due to the lag in molecular polarization. This delay between applied electric field and molecular polarization implies irreversible interactions, resulting in hysteretic behavior. An analogous interpretation of the magnetic relaxation may be performed replacing electric by magnetic field and permittivity by permeability.

Neglecting cross effect for simplicity, the transport or phenomenological equations that relate equilibrium and non-equilibrium terms are deduced in Restuccia and Kluitenberg [1992]:

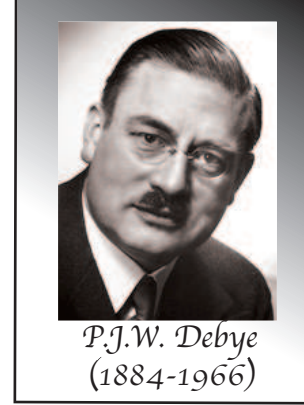


Figure 3.3: *Petrus Josephus Wilhelmus Debye* (1884–1966), Dutch physicist.

$$\begin{aligned} \mathbf{T} &= \mathbf{T}^{eq} + L_s \dot{\mathbf{S}} \quad ; \\ \mathbf{E} &= \mathbf{E}^{eq} + L_p \dot{\mathbf{P}} \quad ; \\ \mathbf{B} &= \mathbf{B}^{eq} + L_m \dot{\mathbf{M}} \end{aligned} \quad (3.12)$$

where  $L_s, L_p, L_m$  represent material properties or phenomenological coefficients.

**Simplification 1:** Transport interactions due to non-equilibrium stresses, electric and magnetic fields are neglected. Therefore,  $L_s, L_p, L_m$  are assumed to be zero and  $\mathbf{T}^{neq} = \mathbf{E}^{neq} = \mathbf{B}^{neq} = \mathbf{0}$ . This simplification uncouples the governing equations, permitting the developing of formulations for equilibrium and for non-equilibrium interactions.

Assuming this simplification, the multi-coupled entropy balance, entropy flux and entropy production are given by:

$$\rho_m \dot{s} = -\nabla \cdot \left( \frac{\mathbf{q}}{T} \right) + \mathbf{q} \cdot \nabla \left( \frac{1}{T} \right) + \frac{1}{T} \mathbf{j} \cdot \mathbf{E} \Rightarrow \begin{cases} \mathbf{j}_s = \frac{\mathbf{q}}{T} \\ \sigma^s = \mathbf{q} \cdot \nabla \left( \frac{1}{T} \right) + \frac{1}{T} \mathbf{j} \cdot \mathbf{E} \end{cases} \quad ; \quad (3.13)$$

where the irreversibilities arise from the heat flux and from the *Joule* heating.

### EXTENDED NON-EQUILIBRIUM THERMODYNAMICS

As has been reported, the ENET assumes the existence of a non-equilibrium entropy density  $s_{NE}$  and a *Gibbs* equation that depends on state variables  $\mathcal{S}$  and on dissipative fluxes  $\dot{\mathcal{F}}$ . The state variables are those used by the NET; the dissipative fluxes are  $\dot{\mathcal{F}} = \{\dot{\mathbf{Q}}, \mathbf{j}\}$ . Thermal  $\dot{\mathbf{Q}}$  and electric  $\mathbf{j}$  dissipative fluxes can be expressed by:

$$\dot{\mathbf{Q}} = f(\nabla \dot{T}) \quad ; \quad (3.14)$$

$$\mathbf{j} = f(\nabla \dot{V})$$

Note that there are no mechanical and no magnetic dissipative fluxes for simplicity. Assuming the **Simplification 1** and using the procedure given in Llebot et al. [1983], a mixed form of the *Gibbs* equation is calculated. The multi-coupled entropy balance is obtained combining this mixed *Gibbs* equation and (3.4):

$$\begin{aligned} \rho_m \dot{s} &= -\nabla \cdot \left( \frac{\mathbf{q}}{T} \right) + \mathbf{q} \cdot \left[ \nabla \left( \frac{1}{T} \right) + \frac{C_1}{T} \dot{\mathbf{Q}} + \frac{C_3}{T} \mathbf{j} \right] + \mathbf{j} \cdot \left[ \frac{1}{T} \mathbf{E} + \frac{C_2}{T} \dot{\mathbf{Q}} + \frac{C_4}{T} \mathbf{j} \right] \Rightarrow \\ \Rightarrow \left\{ \begin{array}{l} j_s &= \frac{\mathbf{q}}{T} \\ \sigma^s &= \mathbf{q} \cdot \left[ \nabla \left( \frac{1}{T} \right) + \frac{C_1}{T} \dot{\mathbf{Q}} + \frac{C_3}{T} \mathbf{j} \right] + \mathbf{j} \cdot \left[ \frac{1}{T} \mathbf{E} + \frac{C_2}{T} \dot{\mathbf{Q}} + \frac{C_4}{T} \mathbf{j} \right] \end{array} \right. \quad ; \quad (3.15) \end{aligned}$$

where  $C_1, C_2, C_3$  and  $C_4$  are constants to be determined.

The ENET incorporates four terms or irreversibilities to the entropy production respects to that obtained from the NET and given in (3.13). These new terms emerge from the dissipative fluxes and are closely related with the relaxation times, see Section 3.3.

#### 3.1.4 Energy balance: thermal conduction temperature

Mechanical, polarization and magnetization interactions are avoided due to the **Simplification 1**. For this reason and to take into account these interactions, the multi-coupled energy balance (3.4) must be modified. However, there are two temperatures: equilibrium and non-equilibrium or thermal conduction temperatures. The first temperature is an intensive variable and is closely related with the entropy; the gradient of the last one is a driving force: its conjugate force is the heat flux. In the literature there are “two” temperature theories to study the fully-coupled thermoelastic coupling, see Youssef [2006], Youssef and El-Bary [2010]. However, in the present thesis a unique temperature is considered.

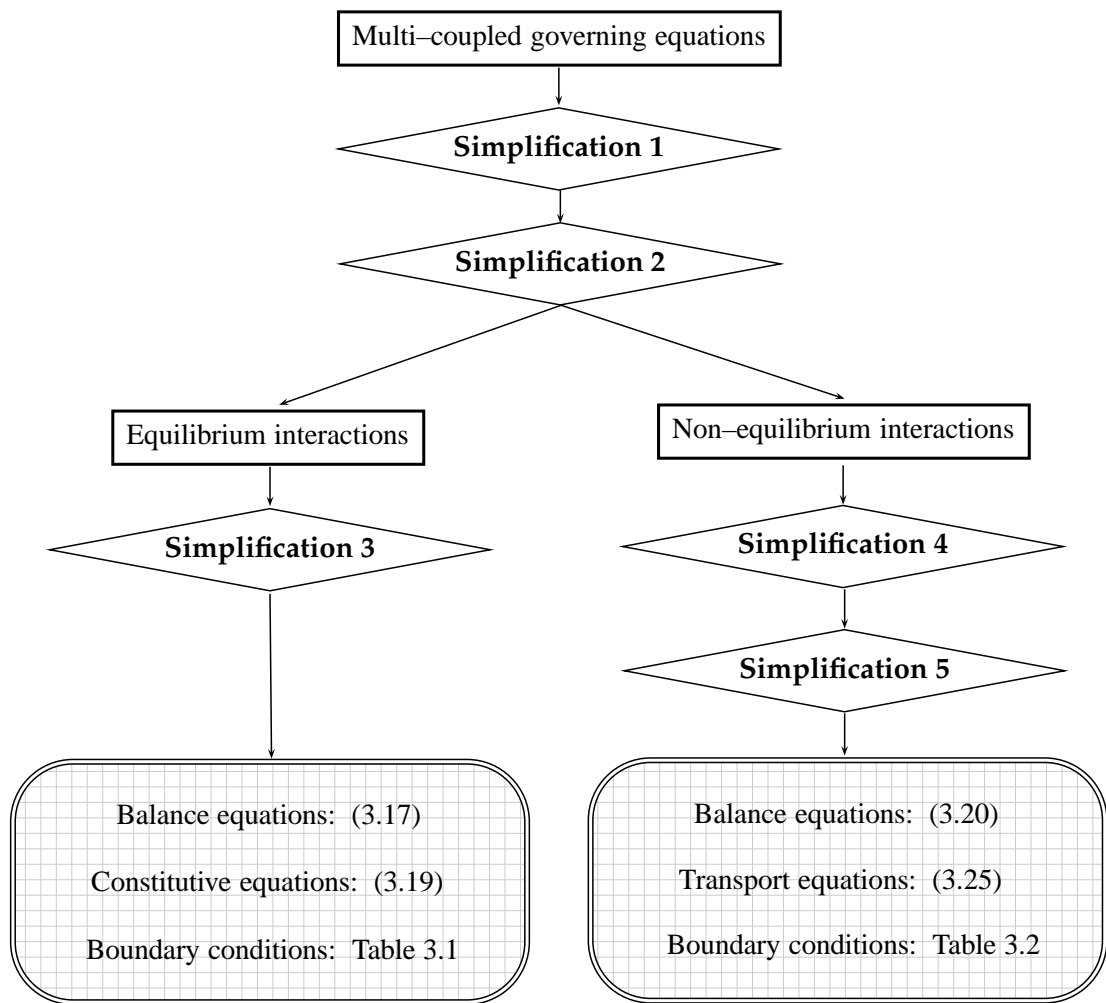


Figure 3.4: Outline of simplifications and particularization of governing equations for equilibrium and non-equilibrium interactions.

**Simplification 2:** Equilibrium and non-equilibrium or conduction temperatures are assumed to be equals, permitting to develop a fully-coupled formulation without the definition of “two” temperatures.

Finally, the modified multi-coupled energy balance is obtained assuming the **Simplification 2** and comparing the entropy balance (3.13) and the *Helmholtz* free energy (3.9):

$$\rho_m c \dot{T} = -\nabla \cdot \mathbf{q} + \mathbf{j} \cdot \mathbf{E} - T_0 \boldsymbol{\beta} : \dot{\mathbf{S}} - T_0 \boldsymbol{\pi}^E \cdot \dot{\mathbf{P}} - T_0 \boldsymbol{\pi}^M \cdot \dot{\mathbf{M}} \quad (3.16)$$

The obtained multi-coupled balance equations are particularized for equilibrium and non-equilibrium interactions, taking into account five simplifications. Figure 3.4 shows these particularizations and simplifications.

### 3.2 Multi-coupled governing equations for equilibrium interactions

This section presents the multi-coupled governing equation for equilibrium interactions, which are obtained introducing a new simplification:

**Simplification 3:** For equilibrium interactions, there are no electric flux  $\mathbf{j} = \mathbf{0}$ ; no free electric charge density  $\rho_q^f = 0$ . From the last assumption, the term  $\partial D / \partial t$  into the *Ampère* law is assumed to be zero.

#### 3.2.1 Balance equations

The balance equations for equilibrium interactions are the momentum balance (3.6), the energy balance (3.16), the *Gauss* electric and the *Gauss* magnetic laws (2.28):

$$\begin{aligned} \rho_m \ddot{\mathbf{u}} &= \nabla \cdot \mathbf{T} + (\nabla \otimes \mathbf{E}) \cdot \mathbf{P} + \mu_0 (\nabla \otimes \mathbf{H}) \cdot \mathbf{M} - \epsilon_0 \mu_0 \frac{\partial}{\partial t} (\mathbf{M} \times \mathbf{E}) + \mu_0 \frac{\partial}{\partial t} (\mathbf{P} \times \mathbf{H}) \quad ; \\ \rho_m c \dot{T} &= -\nabla \cdot \mathbf{q} - T_0 \boldsymbol{\beta} : \dot{\mathbf{S}} - T_0 \boldsymbol{\pi}^E \cdot \dot{\mathbf{P}} - T_0 \boldsymbol{\pi}^M \cdot \dot{\mathbf{M}} \quad ; \\ \nabla \cdot \mathbf{D} &= 0 \quad ; \\ \nabla \cdot \mathbf{B} &= 0 \end{aligned}$$

(3.17)

Note that the choice of the *Gauss* electric and magnetic laws implies a formulation based on the scalar potential.

### 3.2.2 Constitutive equations

According to Soh and Liu [2005], eight sets of multi-coupled constitutive equations can be stated, depending on the independent variables chosen. In this thesis, the independent variables are  $S, E, H$ :  $S = \nabla^S u$ ,  $E = -\nabla V$  and  $H = -\nabla \varphi$ , permitting a displacement-based FE formulation.

The multi-coupled constitutive equations are obtained from the electromagnetic enthalpy  $\Pi$ :

$$\Pi = \frac{1}{2} (T : S - D \cdot E - B \cdot H - \rho_m s T) \quad (3.18)$$

giving:

$$\begin{aligned} T &= \mathbf{C} : S - \mathbf{e}^E \cdot E - \mathbf{e}^M \cdot H - \beta (T - T_0) + T^R ; \\ q &= -\kappa \nabla T ; \\ D &= \mathbf{e}^E : S + \epsilon \cdot E + \nu \cdot H + \pi^E (T - T_0) + P^R ; \\ B &= \mathbf{e}^M : S + \nu \cdot E + \mu \cdot H + \pi^M (T - T_0) \end{aligned} \quad (3.19)$$

where  $\kappa$ ,  $\mathbf{C}$ ,  $\mathbf{e}^E$ ,  $\mathbf{e}^M$ ,  $\beta$ ,  $\epsilon$ ,  $\nu$  and  $\mu$  denote thermal conductivity, stiffness, piezoelectric properties, piezomagnetic properties, coefficients of thermal expansion, permittivity tensor, magnetoelectric properties and permeability tensor, respectively. For more information on these properties and their measurement techniques, see the piezoelectric (IEE [1987]) and magnetostrictive (IEE [1990]) standards. Residual stresses  $T^R$  and polarizations  $P^R$ , which emerge from manufacturing processes and can be relevant in some applications, have been incorporated to the multi-coupled constitutive equations.

The incorporation of the constitutive equations (3.19) into the momentum and energy balance equations (3.17) is performed solving for  $\mathbf{P}$ ,  $\mathbf{M}$  in (2.27).

Finally, the *Dirichlet* and *Newmann* boundary conditions are shown in Table 3.1, where  $\bar{u}$ ,  $\bar{T}$ ,  $\bar{V}$  and  $\bar{\varphi}$  are the prescribed: displacements, temperature, voltage and scalar magnetic potential, respectively. Furthermore,  $\mathbf{t}$ ,  $q_c$  and  $B_c$  denote traction, prescribed thermal and magnetic fluxes. The last condition has not physical sense, however it is incorporated to prescribe magnetic fields from a numerical point of view.

<i>Dirichlet</i> boundary conditions	<i>Newmann</i> boundary conditions
$u = \bar{u}$	$T^{eq} \cdot \mathbf{n} = \mathbf{t}$
$T = \bar{T}$	$\mathbf{q} \cdot \mathbf{n} = q_c$
$V = \bar{V}$	$D \cdot \mathbf{n} = 0$
$\varphi = \bar{\varphi}$	$B \cdot \mathbf{n} = B_c$

Table 3.1: Summary of *Dirichlet* and *Newmann* boundary conditions for equilibrium interactions.

### 3.3 Multi-coupled governing equations for non-equilibrium interactions

Before obtaining the multi-coupled governing equations, two simplifications are introduced:

**Simplification 4:** For non-equilibrium interactions, non-polarizable ( $\mathbf{P} = \mathbf{0}$ ) and non-magnetizable ( $\mathbf{M} = \mathbf{0}$ ) materials are assumed. These assumptions are good approximations in conductor materials, Landau and Lifshitz [1984].

**Simplification 5:** For non-equilibrium interactions, there are no free electric charge densities:  $\rho_q^f = 0$ . Again, this assumption implies that  $\partial D / \partial t \approx 0$ , which is a good approximation for the most of applications according to Landau and Lifshitz [1984].

#### 3.3.1 Balance equations

Considering the previous simplifications, the balance equations for non-equilibrium interactions are the momentum (3.6), energy (3.16) and electric charge (2.30) balance equations. In addition, the magnetic *Gauss* law (2.28) is also included. Again, this inclusion implies a scalar potential formulation:

$$\begin{aligned}
 \rho_m \ddot{\mathbf{u}} &= \nabla \cdot \mathbf{T} + \mathbf{j} \times \mathbf{B} && ; \\
 \rho_m c \dot{T} &= -\nabla \cdot \mathbf{q} - T_0 \boldsymbol{\beta} : \dot{\mathbf{S}} + \mathbf{j} \cdot \mathbf{E} && ; \\
 \nabla \cdot \mathbf{j} &= 0 && ; \\
 \nabla \cdot \mathbf{B} &= 0 && 
 \end{aligned}
 \tag{3.20}$$



### 3.3.2 Transport equations

According to the NET and ENET formalisms, the transport equations are obtained expressing the entropy production (3.15) in the form of linear relations between fluxes and forces:

$$\begin{aligned} -\nabla \left( \frac{1}{T} \right) &= \frac{1}{T} C_1 \dot{\mathbf{Q}} - L^{11} \mathbf{q} + \frac{1}{T} C_3 \dot{\mathbf{J}} - L^{12} \mathbf{j} ; \\ \frac{1}{T} \nabla V &= \frac{1}{T} C_2 \dot{\mathbf{Q}} - L^{21} \mathbf{q} + \frac{1}{T} C_4 \dot{\mathbf{J}} - L^{22} \mathbf{j} \end{aligned} \quad (3.21)$$

where  $L^{kl}$  are the material properties or phenomenological coefficients that must satisfy the thermodynamic restrictions given in (2.17) and (2.18). Finally and according to Llebot et al. [1983], the transport equations are:

$$\begin{aligned} \mathbf{q} + \tau_q \dot{\mathbf{Q}} &= -\kappa \nabla T + \alpha T \mathbf{j} + \tau_{qj} \alpha T \dot{\mathbf{J}} ; \\ \mathbf{j} + \tau_j \dot{\mathbf{J}} &= -\gamma \nabla V - \alpha \gamma \nabla T + \tau_{jq} \frac{\alpha \gamma}{\kappa} \dot{\mathbf{Q}} \end{aligned} \quad (3.22)$$

On one hand,  $\alpha$ ,  $\gamma$  and  $\kappa$  are the *Seebeck* coefficient, electric and thermal conductivities, which will be tensor entities in presence of magnetic field as will be reported in Chapter 8. On the other,  $\tau_q$ ,  $\tau_j$ ,  $\tau_{jq}$  and  $\tau_{qj}$  are the relaxation times: empirical parameters that are defined as the time-interval between two successive collisions at the microscopic level of either holes or electrons. Each term in (3.22) represents a physical effect:

- ▷  $\tau_q \dot{\mathbf{Q}}$ ,  $\tau_j \dot{\mathbf{J}}$  represent the hyperbolic models for propagation of heat and of electric fluxes, respectively. The first term is closely related with the *Cattaneo* or *Maxwell–Cattaneo* model; the second one with the *Drude* relaxation model, see Jou and Lebon [1996]. Note that the *Cattaneo* model is denominated second sound in the *Continuum Mechanics* framework
- ▷  $\kappa \nabla T$ ,  $\gamma \nabla V$  are the heat and electric laws that were stated by *Fourier* and *Ohm*, respectively
- ▷  $\alpha T \mathbf{j}$  expresses the *Peltier* and *Thomson* effects that will be described in Chapter 5
- ▷  $\tau_{qj} \alpha T \dot{\mathbf{J}}$ ,  $\tau_{jq} \frac{\alpha \gamma}{\kappa} \dot{\mathbf{Q}}$  represent dissipative interactions and are responsible for the hysteretic behavior, see Chapters 6 and 7
- ▷  $\alpha \gamma \nabla T$  is closely related with the *Seebeck* effect, see Chapter 5

The relaxation time  $\tau_j$  is assumed to be zero due to the **Simplification 5**. This assumption can be verified introducing the electric transport equations (3.22) in the balance of electric charge (3.20), giving:

$$\nabla \cdot \left( -\gamma \nabla V - \alpha \gamma \nabla T + \tau_{jq} \frac{\alpha \gamma}{\kappa} \dot{\mathbf{Q}} \right) - \tau_j \nabla \cdot \dot{\mathbf{J}} = 0 \quad (3.23)$$

The last term on the left side must be zero to satisfy the balance of electric charge:  $\tau_j = 0$ . This mathematical manipulation is used in analytical works (Youssef [2006], for example) to include the  $\tau_q \dot{\mathbf{Q}}$  term into the energy balance equation and will be used in the Chapter 4 to facilitate the FE implementation.

In a first and good approximation, the dissipative fluxes  $\dot{\mathbf{Q}}$  and  $\dot{\mathbf{J}}$  may be expressed by:

$$\dot{\mathbf{Q}} = -\kappa \nabla \dot{T} \quad ; \quad (3.24)$$

$$\dot{\mathbf{j}} = -\gamma \nabla \dot{V}$$

Considering the transport equations (3.22), the mechanical and magnetic constitutive equations (3.19) and taking into account (3.23) and (3.24), the transport and constitutive equations for the non-equilibrium interactions are:

$\mathbf{T} = \mathbf{C} : \mathbf{S} - \boldsymbol{\beta} (T - T_0) \quad ;$	(3.25)
$\mathbf{q} = -\kappa \nabla T + \alpha T \dot{\mathbf{j}} - \tau_{qj} \alpha T \gamma \nabla \dot{V} + \tau_q \kappa \nabla \dot{T} \quad ;$	
$\dot{\mathbf{j}} = -\gamma \nabla V - \alpha \gamma \nabla T - \tau_{jq} \alpha \gamma \nabla \dot{T} \quad ;$	
$\mathbf{B} = \mu_0 \mathbf{H}$	

where the permeability for conductor materials is assumed to be  $\mu_0$  since magnetization interactions are not present.

Finally, the *Dirichlet* and *Newmann* boundary conditions are shown in Table 3.2, where  $j_c$  denotes the prescribed electric flux.

<i>Dirichlet</i> boundary conditions	<i>Newmann</i> boundary conditions
$u = \bar{u}$	$\mathbf{T} \cdot \mathbf{n} = \mathbf{t}$
$T = \bar{T}$	$\mathbf{q} \cdot \mathbf{n} = q_c$
$V = \bar{V}$	$\dot{\mathbf{j}} \cdot \mathbf{n} = j_c$
$\varphi = \bar{\varphi}$	$\mathbf{B} \cdot \mathbf{n} = B_c$

Table 3.2: Summary of *Dirichlet* and *Newmann* boundary conditions for non-equilibrium interactions.

### 3.3.3 Interpretation of the relaxation times

An interpretation of the relaxation times using the one-dimensional *Maxwell* viscoelastic model is developed in this section. The *Maxwell* model is used by the *Continuum Mechanics* community to model the constitutive equations of viscoelastic materials and can be extrapolated for the interpretation of the relaxation times.

Consider the one-dimensional *Maxwell* model represented in Figure 3.5, consisting of a spring and of a dashpot. The spring and dashpot constants are denoted by  $\mathcal{L}$  and  $\eta$ , respectively. In addition, the fluxes (stresses)  $\mathcal{F}$  and driving forces (strains)  $\Xi$  are also represented.

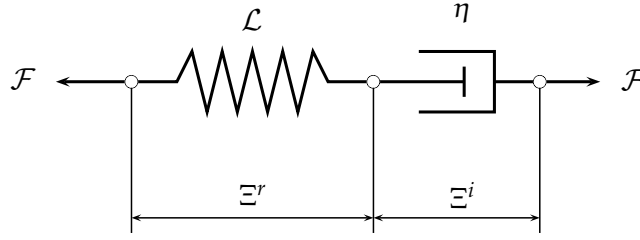


Figure 3.5: One-dimensional *Maxwell* model for the interpretation of relaxation times.

From the *Maxwell* model and according to Simo and Hughes [1998], fluxes and driving forces satisfies:

$$\mathcal{F} = \mathcal{F}^r = \mathcal{F}^i \quad ; \quad (3.26)$$

$$\Xi = \Xi^r + \Xi^i$$

where superscripts  $(.)^r$ ,  $(.)^i$  denote reversible and irreversible magnitudes, respectively. From these relationships, the transport equation is:

$$\mathcal{F} = \mathcal{L} \Xi - \mathcal{L} \Xi^i \quad (3.27)$$

In addition, the irreversible driving force can be expressed by, see Simo and Hughes [1998]:

$$\dot{\Xi}^i + \frac{1}{\tau} \Xi^i = \frac{1}{\tau} \Xi \quad (3.28)$$

where  $\tau = \eta/\mathcal{L}$  is the relaxation time. Integrating (3.28) and assuming  $\Xi^i(t) = 0$  as  $t \rightarrow -\infty$ :

$$\Xi^i = \frac{1}{\tau} \int_{-\infty}^t e^{-(t-t')/\tau} \Xi(t') dt \quad (3.29)$$

For instance, considering  $\Xi = -\partial T/\partial x$ ,  $\mathcal{F} = q$ ,  $\mathcal{L} = \kappa$ ,  $\tau = \tau_q$ , the hyperbolic or *Cattaneo* thermal transport equations can be formulated as:

$$q = -\kappa \frac{\partial T}{\partial x} + \frac{\kappa}{\tau_q} \int_{-\infty}^t e^{-(t-t')/\tau_q} \frac{\partial T}{\partial x}(t') dt \quad (3.30)$$

This representation of the transport or constitutive equations by means of convolution integrals is commonly used by the *Continuum Mechanics* community. In addition, numerical

techniques for the solution of these convolution equations are reported in Simo and Hughes [1998].

Summarizing, the relaxation times are magnitudes that represent viscous interactions:

- ▷  $\tau_q, \tau_j$  represent thermal and electric viscosities, respectively
- ▷  $\tau_{qj}, \tau_{jq}$  are coupling relaxation times that represent thermal and electric viscosities due to the presence of voltage and of temperature gradients, respectively

Finally, the thermal and transport equations give in (3.25) can be rewritten using the convolution integrals:

$$\begin{aligned}
 \mathbf{q} &= -\kappa \nabla T + \alpha T \mathbf{j} + \frac{\kappa}{\tau_q} \int_{-\infty}^t e^{-(t-t')/\tau_q} \nabla T(t') dt + \frac{\alpha T \gamma}{\tau_{qj}} \int_{-\infty}^t e^{-(t-t')/\tau_{qj}} \nabla V(t') dt ; \\
 \mathbf{j} &= -\gamma \nabla V - \alpha \gamma \nabla T + \frac{\alpha \gamma}{\tau_{jq}} \int_{-\infty}^t e^{-(t-t')/\tau_{jq}} \nabla T(t') dt
 \end{aligned}
 \tag{3.31}$$

This representation of the transport equations could be the starting point to develop a FE formulation using the numerical techniques applied to viscoelastic materials in Simo and Hughes [1998]. In the present thesis, the transport equations are those given in (3.25), nevertheless the representation (3.31) will be used in future works.



## **Part II**

# **FINITE ELEMENT FORMULATION**



*Every honest researcher I know admits he's just a professional amateur. He's doing whatever he's doing for the first time. That makes him an amateur. He has sense enough to know that he's going to have a lot of trouble, so that makes him a professional.*

**Charles Franklin Kettering**  
(1876–1958)

# 4

## Finite element formulation



A variational formulation, within the FEM, is developed in the present chapter to permit the implementation of the multi-coupled governing equations for non-equilibrium interaction into a computer code. In addition, a special interface element is formulated to prescribe fluxes and to simulate radiation and convection phenomena. Both FE's are implemented into the research code FEAP, Taylor [2010], belonging to the University of California at Berkeley (USA). Note that the FE formulation is only for non-equilibrium interactions; for equilibrium interactions the author of the present thesis and his advisor have published several articles in international journals. However, the inclusion of this element for equilibrium interaction is beyond the scope of this thesis.

Section 4.1 presents an outline of the FEM, introducing non-linear and time integration algorithms. Sections 4.2 and 4.3 develop the FE formulations for non-equilibrium interactions and for the interface element, respectively.

### 4.1 Outline of the Finite Element Method

The FEM is a numerical technique used to model many problem in science and engineering. This is the most advanced method for the solution of multi-coupled problems. However, it involves complex mathematical concepts, see Zienkiewicz et al. [2005] or Hughes [1987] for further studies.

Considering the continuum system of domain  $\Omega$  and boundary  $\Gamma$  shown in Figure 4.1, the FEM implies the following steps:



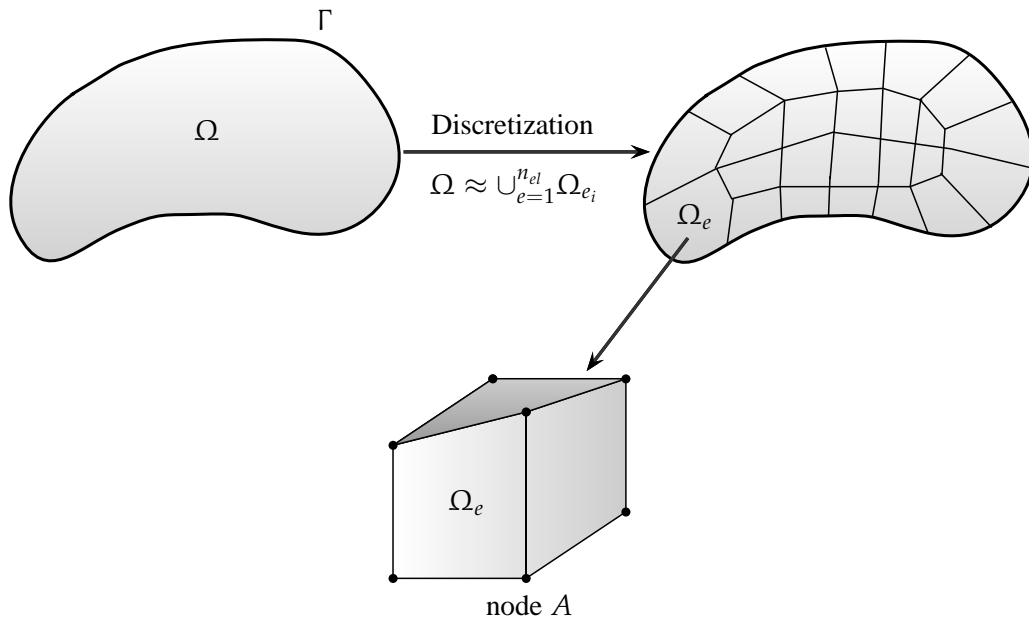


Figure 4.1: Continuum domain discretized by the finite element method. Each 3-D element is composed of eight nodes.

- i) The continuum domain  $\Omega$  is divided into subdomains or elements  $\Omega_e$ , which are interconnected at the nodal points
- ii) The nodal values of d.o.f. are assumed to be the unknown parameters of the problem
- iii) A set of functions or shape functions are chosen to interpolate the solution within each finite element in terms of their nodal values
- iv) The principle of virtual work is applied to the governing equations to obtain the weak form of the problem
- iv) The solution is calculated by solving a set of linear or non-linear equations:
  - ▷ Non-linearities are solved by algorithms such as *Newton-Raphson*, Zienkiewicz et al. [2005]
  - ▷ Dynamic equations are computed by time integration algorithms, see Fung [2003] for a full review of these algorithms

#### 4.1.1 Non-linear transient solutions

The multi-coupled formulation for non-equilibrium interactions is a non-linear transient problem, from a mathematical point of view. Therefore, its solution requires non-linear and time integration algorithms:

- ▷ Non-linearities are solved by the *Newton-Raphson* algorithm

▷ Time integration is performed by *Newmark-β* or HHT, Hilber et al. [1977], algorithms

These algorithms have been widely used in structural and solid mechanics and will not be described in detail here.

The resolution of non-linear transient problems imply three steps:

- i) The time interval is divided into small time increments  $\Delta t$
- ii) The analytical time derivatives are replaced by discrete forms using *Newmark-β* or HHT algorithms
- iii) The non-linear algebraic problem for each time increment is solved using the *Newton-Raphson* algorithm

The assembled non-linear FE equations are written in a residual form  $\mathcal{R}$  and linearized by:

$$\mathcal{R}_A^k = - \left. \frac{\partial \mathcal{R}_A}{\partial \mathbf{g}_B} \right|^k \mathbf{d}\mathbf{g}_A^k \quad (4.1)$$

where  $A, B$  are the global numbering of two nodes,  $k$  the *Newton-Raphson* iteration counter and  $\mathbf{g}_A$  the derivatives of the d.o.f. at node  $A$ . The algorithm for time integration is written as:

$$- \left. \frac{\partial \mathcal{R}_A}{\partial \mathbf{g}_B} \right|^k = c_1 \mathcal{K}_{AB} + c_2 \mathcal{C}_{AB} + c_3 \mathcal{M}_{AB} \quad (4.2)$$

where the parameters  $c_1, c_2$  and  $c_3$  are given in Table 4.1 in terms of the standard parameters  $\bar{\beta}, \bar{\gamma}$  for the *Newmark-β* algorithm and, in addition,  $\bar{\alpha}$  for the HHT algorithm.

Method	$c_1$	$c_2$	$c_3$
<i>Newmark-β</i>	1	$\frac{\bar{\gamma}}{\bar{\beta}\Delta t}$	$\frac{1}{\bar{\beta}\Delta t^2}$
HHT	$\bar{\alpha}$	$\frac{\bar{\alpha}\bar{\gamma}}{\bar{\beta}\Delta t}$	$\frac{1}{\bar{\beta}\Delta t^2}$

Table 4.1: Finite element matrix parameters for *Newmark-β* and for HHT algorithms.

The consistent tangent  $\mathcal{K}$ , capacity  $\mathcal{C}$  and mass  $\mathcal{M}$  matrices are derived for each iteration:

$$\begin{aligned}\mathcal{K}_{AB} &= -\frac{\partial \mathcal{R}_A}{\partial \mathbf{U}_B} \quad ; \\ \mathcal{C}_{AB} &= -\frac{\partial \mathcal{R}_A}{\partial \dot{\mathbf{U}}_B} \quad ; \\ \mathcal{M}_{AB} &= -\frac{\partial \mathcal{R}_A}{\partial \ddot{\mathbf{U}}_B}\end{aligned}\tag{4.3}$$

where  $\mathbf{g}_B = \mathbf{U}_B$ ,  $\mathbf{g}_B = \dot{\mathbf{U}}_B$ ,  $\mathbf{g}_B = \ddot{\mathbf{U}}_B$  represent the zero-, first- and second-derivative, respectively.

Finally, the solution is updated using  $\mathbf{g}_B^{k+1} = \mathbf{g}_B^k + d\mathbf{g}_B^k$ . Note that the *Newton-Raphson* should exhibit a quadratic asymptotic rate of convergence to ensure a correct derivation of the tangent matrices.

#### 4.1.2 Stability of the time integration algorithms

A time integration algorithm is unconditionally stable if the size of the time step  $\Delta t$  does not affect the stability of the solution. For linear problems, *Newmark- $\beta$*  and HHT algorithms are unconditionally stable if, see Hughes [1987]:

$$\begin{aligned}\underline{\text{Newmark} - \beta} : \quad & \bar{\gamma} \leq 0.5 \quad ; \quad \bar{\beta} \leq (2\bar{\gamma} + 1)^2/16 \quad ; \quad - \\ \underline{\text{HHT}} : \quad & \bar{\gamma} = 0.5 - \bar{\alpha} \quad ; \quad \bar{\beta} \leq (2\bar{\gamma} + 1)^2/16 \quad ; \quad -1/3 < \bar{\alpha} < 0\end{aligned}\tag{4.4}$$

Algorithm	$\bar{\rho}$	$\bar{\beta}$	$\bar{\gamma}$	$\bar{\alpha}$
<i>Newmark-<math>\beta</math></i>	1	1/4	1/2	-
	3/2	9/14	16/49	-
	1/2	4/9	5/6	-
	0	1	3/2	-
HHT	3/2	9/14	16/49	6/7
	1/2	4/9	5/6	2/3

Table 4.2: Typical *Newmark- $\beta$*  and HHT parameters that guarantee the stability of the dynamic algorithms.

For linear problems, Table 4.2 shows the unconditionally stable parameters for different spectral radii  $\bar{\rho}$ . According to Fung [2003],  $\bar{\rho}$  should stay close to unity for small to intermediate time steps and decrease to  $\bar{\rho} \approx 0.5$  only when  $\Delta t/\hat{T} \rightarrow \infty$ , where  $\hat{T}$  is the undamped natural period.

For non-linear problems, the algorithm stability must be studied, requiring spectral analyses. However, they are beyond the scope of the present thesis. For this reason, the time integration algorithms are regularized by relating time steps and element sizes using the *Courant* number, Courant et al. [2007]. This regularization is adjusted by trial and error numerical experiments in order to avoid numerical oscillations (*Gibbs* phenomena).

## 4.2 Finite element formulation for non-equilibrium interactions

Consider the system shown in Figure 4.1. The non-equilibrium interactions of this system are fully defined by (3.20) and (3.25). Nevertheless, a modification will be imposed to facilitate the FE implementation: the dissipative flux  $\mathbf{Q}$  is introduced in the energy balance (3.20) using the procedure described in (3.23). Finally, the multi-coupled balance and transport equations are:

$$\begin{aligned}
 \rho_m \ddot{\mathbf{u}} &= \nabla \cdot \mathbf{T} + \mathbf{j} \times \mathbf{B} && ; \\
 \tau_q \rho_m c \ddot{T} + \rho_m c \dot{T} &= -\nabla \cdot \mathbf{q} - T_0 \boldsymbol{\beta} : \dot{\mathbf{S}} - \mathbf{j} \cdot \nabla V - \tau_q \frac{\partial}{\partial t} (\mathbf{j} \cdot \nabla V) - \tau_q \frac{\partial}{\partial t} (T_0 \boldsymbol{\beta} : \dot{\mathbf{S}}) && ; \\
 \nabla \cdot \mathbf{j} &= 0 && ; \\
 \nabla \cdot \mathbf{B} &= 0 && ;
 \end{aligned}
 \tag{4.5}$$

$$\begin{aligned}
 \mathbf{T} &= \mathbf{C} : \mathbf{S} - \boldsymbol{\beta} (T - T_0) && ; \\
 \mathbf{q} &= -\kappa \nabla T + \alpha T \mathbf{j} - \tau_{qj} \alpha T \gamma \nabla \dot{V} && ; \\
 \mathbf{j} &= -\gamma \nabla V - \alpha \gamma \nabla T - \tau_{jq} \alpha \gamma \nabla \dot{T} && ; \\
 \mathbf{B} &= \mu_0 \mathbf{H} && ;
 \end{aligned}
 \tag{4.6}$$

Note that the compatibility equation  $\mathbf{E} = -\nabla V$  has been introduced. Furthermore, the boundary conditions are those given in Table 3.2.

### 4.2.1 Weak forms

According to standard variational methods reported in Zienkiewicz et al. [2005], the weak forms are obtained by multiplying the balance equations by variations of the d.o.f.  $\delta \mathbf{u}$ ,  $\delta T$ ,  $\delta V$ ,  $\delta \varphi$  and by integrating in  $\Omega$ :

$$\int_{\Omega} \delta \mathbf{u} \cdot \nabla \cdot \mathbf{T} \, d\Omega + \int_{\Omega} \delta \mathbf{u} \cdot (\mathbf{j} \times \mathbf{B}) \, d\Omega - \int_{\Omega} \delta \mathbf{u} \cdot \rho_m \ddot{\mathbf{u}} \, d\Omega = 0 \quad ;$$

$$\int_{\Omega} \delta T \nabla \cdot \mathbf{q} \, d\Omega + \int_{\Omega} \delta T T_0 \boldsymbol{\beta} : \dot{\mathbf{S}} \, d\Omega + \int_{\Omega} \delta T \mathbf{j} \cdot \nabla V \, d\Omega + \tau_q \int_{\Omega} \delta T \frac{\partial}{\partial t} (T_0 \boldsymbol{\beta} : \dot{\mathbf{S}}) \, d\Omega +$$

$$\tau_q \int_{\Omega} \delta T \frac{\partial}{\partial t} (\mathbf{j} \cdot \nabla V) \, d\Omega + \tau_q \int_{\Omega} \delta T \rho_m c \ddot{T} \, d\Omega + \int_{\Omega} \delta T \rho_m c \dot{T} \, d\Omega = 0 \quad ;$$

$$\int_{\Omega} \delta V \nabla \cdot \mathbf{j} \, d\Omega = 0 \quad ;$$

$$\int_{\Omega} \delta \varphi \nabla \cdot \mathbf{B} \, d\Omega = 0 \quad (4.7)$$

Finally, the weak forms are obtained by applying the divergence theorem to the first term on the left side of all equations and by introducing the *Newmann* boundary conditions:

$$\begin{aligned} & - \int_{\Omega} \nabla \delta \mathbf{u} : \mathbf{T} \, d\Omega + \int_{\Gamma} \delta \mathbf{u} \cdot \mathbf{t} \, d\Gamma + \int_{\Omega} \delta \mathbf{u} \cdot (\mathbf{j} \times \mathbf{B}) \, d\Omega - \int_{\Omega} \delta \mathbf{u} \cdot \rho_m \ddot{\mathbf{u}} \, d\Omega = 0 \quad ; \\ & - \int_{\Omega} \nabla \delta T \cdot \mathbf{q} \, d\Omega + \int_{\Gamma} \delta T q_c \, d\Gamma + \int_{\Omega} \delta T T_0 \boldsymbol{\beta} : \dot{\mathbf{S}} \, d\Omega + \int_{\Omega} \delta T \mathbf{j} \cdot \nabla V \, d\Omega + \\ & \tau_q \int_{\Omega} \delta T \frac{\partial}{\partial t} (T_0 \boldsymbol{\beta} : \dot{\mathbf{S}}) \, d\Omega + \tau_q \int_{\Omega} \delta T \frac{\partial}{\partial t} (\mathbf{j} \cdot \nabla V) \, d\Omega + \tau_q \int_{\Omega} \delta T \rho_m c \ddot{T} \, d\Omega + \\ & \int_{\Omega} \delta T \rho_m c \dot{T} \, d\Omega = 0 \quad ; \quad (4.8) \\ & - \int_{\Omega} \nabla \delta V \cdot \mathbf{j} \, d\Omega + \int_{\Gamma} \delta V j_c \, d\Gamma = 0 \quad ; \\ & - \int_{\Omega} \nabla \delta \varphi \cdot \mathbf{B} \, d\Omega + \int_{\Gamma} \delta \varphi B_c \, d\Gamma = 0 \end{aligned}$$

#### 4.2.2 Residuals

The continuum domain  $\Omega$  is discretized with elements  $\Omega_e$ , as shown in Figure 4.1, to obtain the residuals. Therefore,  $\Omega = \cup_{e=1}^{n_{el}} \Omega_e$ , where  $n_{el}$  is the total number of elements, each one delimited by  $n_{pe} = 8$  nodes. In turn, there are six d.o.f. (three displacements, temperature, voltage and magnetic scalar potential) per node.

For an element  $e$ , d.o.f. and spatial coordinates  $x$  are approximated using 3-D isoparametric shape functions  $\mathcal{N}_e$ :

$$\begin{aligned}
\mathbf{u} &\approx \mathbf{u}^h = \mathcal{N}_e \mathbf{a}_e^U & ; & & \dot{\mathbf{u}} &\approx \dot{\mathbf{u}}^h = \mathcal{N}_e \dot{\mathbf{a}}_e^U & ; & & \ddot{\mathbf{u}} &\approx \ddot{\mathbf{u}}^h = \mathcal{N}_e \ddot{\mathbf{a}}_e^U & ; \\
T &\approx T^h = \mathcal{N}_e \mathbf{a}_e^T & ; & & \dot{T} &\approx \dot{T}^h = \mathcal{N}_e \dot{\mathbf{a}}_e^T & ; & & \ddot{T} &\approx \ddot{T}^h = \mathcal{N}_e \ddot{\mathbf{a}}_e^T & ; \\
V &\approx V^h = \mathcal{N}_e \mathbf{a}_e^V & ; & & \dot{V} &\approx \dot{V}^h = \mathcal{N}_e \dot{\mathbf{a}}_e^V & ; & & & & (4.9) \\
\varphi &\approx \varphi^h = \mathcal{N}_e \mathbf{a}_e^\varphi & ; & & & & & & & & \\
\mathbf{x} &\approx \mathbf{x}^h = \mathcal{N}_e \mathbf{a}_e^x & & & & & & & & & 
\end{aligned}$$

where:

$$\begin{aligned}
\mathbf{a}_e^U &= \{a_{e_1}^{u,v,w}, \dots, a_{e_{n_{pe}}}^{u,v,w}\}^t & ; \\
\mathbf{a}_e^T &= \{a_{e_1}^T, \dots, a_{e_{n_{pe}}}^T\}^t & ; \\
\mathbf{a}_e^V &= \{a_{e_1}^V, \dots, a_{e_{n_{pe}}}^V\}^t & ; \\
\mathbf{a}_e^\varphi &= \{a_{e_1}^\varphi, \dots, a_{e_{n_{pe}}}^\varphi\}^t
\end{aligned}$$

are the nodal unknowns.

The discretized matrix gradients of the element are given by:

$$\begin{aligned}
\nabla^s \mathbf{u} &\approx \nabla^s \mathcal{N}_e \mathbf{a}_e^U = \mathcal{B}_e^s \mathbf{a}_e^U & ; & & \nabla^s \dot{\mathbf{u}} &\approx \nabla^s \mathcal{N}_e \dot{\mathbf{a}}_e^U = \mathcal{B}_e^s \dot{\mathbf{a}}_e^U & ; \\
\nabla T &\approx \nabla \mathcal{N}_e \mathbf{a}_e^T = \mathcal{B}_e \mathbf{a}_e^T & ; & & \nabla \dot{T} &\approx \nabla \mathcal{N}_e \dot{\mathbf{a}}_e^T = \mathcal{B}_e \dot{\mathbf{a}}_e^T & ; \\
\nabla V &\approx \nabla \mathcal{N}_e \mathbf{a}_e^V = \mathcal{B}_e \mathbf{a}_e^V & ; & & \nabla \dot{V} &\approx \nabla \mathcal{N}_e \dot{\mathbf{a}}_e^V = \mathcal{B}_e \dot{\mathbf{a}}_e^V & ; \\
\nabla \varphi &\approx \nabla \mathcal{N}_e \mathbf{a}_e^\varphi = \mathcal{B}_e \mathbf{a}_e^\varphi & & & & & & & & & (4.10)
\end{aligned}$$

and they can be expressed in matrix form as:

$$[\mathcal{B}_e^s] = \begin{bmatrix} N_{1,x_1} & \dots & N_{8,x_1} \\ N_{1,x_2} & \dots & N_{8,x_2} \\ N_{1,x_3} & \dots & N_{8,x_3} \\ N_{1,x_3} + N_{1,x_2} & \dots & N_{8,x_3} + N_{8,x_2} \\ N_{1,x_3} + N_{1,x_1} & \dots & N_{8,x_1} + N_{8,x_2} \\ N_{1,x_2} + N_{1,x_1} & \dots & N_{8,x_2} + N_{8,x_1} \end{bmatrix} \quad (4.11)$$

$$[\mathcal{B}_e] = \begin{bmatrix} N_{1,x_1} & \dots & N_{8,x_1} \\ N_{1,x_2} & \dots & N_{8,x_2} \\ N_{1,x_3} & \dots & N_{8,x_3} \end{bmatrix} \quad (4.12)$$

where  $N_{1,x_1}$  denotes the derivative of  $N_1$  with respect to  $x_1$ . Similarly, the variations are discretized as:

$$\begin{aligned} \delta u &\approx \delta u^h = \mathcal{N}_e \mathbf{a}_e^U & ; & & \nabla^s \delta u &\approx \nabla^s \mathcal{N}_e \mathbf{a}_e^U = \mathcal{B}_e^s \mathbf{a}_e^U & ; \\ \delta T &\approx \delta T^h = \mathcal{N}_e \mathbf{a}_e^T & ; & & \nabla \delta T &\approx \nabla \mathcal{N}_e \mathbf{a}_e^T = \mathcal{B}_e \mathbf{a}_e^T & ; \\ \delta V &\approx \delta V^h = \mathcal{N}_e \mathbf{a}_e^V & ; & & \nabla \delta V &\approx \nabla \mathcal{N}_e \mathbf{a}_e^V = \mathcal{B}_e \mathbf{a}_e^V & ; \\ \delta \varphi &\approx \delta \varphi^h = \mathcal{N}_e \mathbf{a}_e^\varphi & ; & & \nabla \delta \varphi &\approx \nabla \mathcal{N}_e \mathbf{a}_e^\varphi = \mathcal{B}_e \mathbf{a}_e^\varphi & \end{aligned} \quad (4.13)$$

Introducing these discretization forms in the transport and constitutive equations (4.6):

$$\begin{aligned} T_e &= \mathbf{C} \mathcal{B}_e^s \mathbf{a}_e^U - \beta (\mathcal{N}_e \mathbf{a}_e^T - T_0) & ; \\ q_e &= -\kappa \mathcal{B}_e \mathbf{a}_e^T - \alpha \gamma \mathcal{N}_e \mathbf{a}_e^T \mathcal{B}_e \mathbf{a}_e^V - \alpha^2 \gamma \mathcal{N}_e \mathcal{B}_e (\mathbf{a}_e^T)^2 - \tau_{qj} \alpha \mathcal{N}_e \mathbf{a}_e^T \gamma \mathcal{B}_e \dot{\mathbf{a}}_e^V & ; \\ j_e &= -\gamma \mathcal{B}_e \mathbf{a}_e^V - \alpha \gamma \mathcal{B}_e \mathbf{a}_e^T - \tau_{jq} \alpha \gamma \mathcal{B}_e \dot{\mathbf{a}}^T & ; \\ B_e &= -\mu_0 \mathcal{B}_e \mathbf{a}_e^\varphi & \end{aligned} \quad (4.14)$$

The *Galerkin* approach permits to convert the continuous formulation given in (4.8) into discrete formulation as that given in (4.15), which is amenable for numerical analysis. This approach was stated by the Russian mathematician and engineer *B. Galerkin*.

The *Galerkin* forms are obtained by introducing the discretization (4.9), (4.10) and (4.13) in the weak forms (4.8):

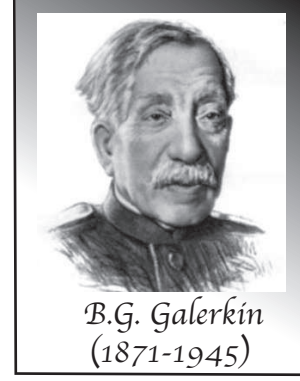


Figure 4.2: *Boris Grigoryevich Galerkin* (1871–1945) was a Russian/Soviet mathematician and engineer.

$$\begin{aligned}
& - \int_{\Omega} (\mathbf{B}_e^s)^t \mathbf{T} \, d\Omega + \int_{\Gamma} \mathcal{N}_e^t \mathbf{t} \, d\Gamma + \int_{\Omega} \mathcal{N}_e^t (\mathbf{j} \times \mathbf{B}) \, d\Omega - \int_{\Omega} \mathcal{N}_e^t \rho_m \mathcal{N}_e \ddot{\mathbf{a}}_e^U \, d\Omega = 0 \quad ; \\
& - \int_{\Omega} \mathbf{B}_e^t \mathbf{q} \, d\Omega + \int_{\Gamma} \mathcal{N}_e^t q_c \, d\Gamma + \int_{\Omega} \mathcal{N}_e^t T_0 \boldsymbol{\beta} \mathbf{B}_m^s \dot{\mathbf{a}}_e^U \, d\Omega + \int_{\Omega} \mathcal{N}_e^t \mathbf{j} \mathbf{B}_e \mathbf{a}_e^V \, d\Omega + \\
& \tau_q \int_{\Omega} \mathcal{N}_e^t \frac{\partial}{\partial t} (T_0 \boldsymbol{\beta} \mathbf{B}_t^s \dot{\mathbf{a}}_e^U) \, d\Omega + \tau_q \int_{\Omega} \mathcal{N}_e^t \frac{\partial}{\partial t} (\mathbf{j} \mathbf{B}_e \mathbf{a}_e^V) \, d\Omega + \tau_q \int_{\Omega} \mathcal{N}_e^t \rho_m c \mathcal{N}_e \ddot{\mathbf{a}}_e^T \, d\Omega + \\
& \int_{\Omega} \mathcal{N}_e^t \rho_m c \mathcal{N}_e \dot{\mathbf{a}}_e^T \, d\Omega = 0 \quad ; \\
& - \int_{\Omega} \mathbf{B}_e^t \mathbf{j} \, d\Omega + \int_{\Gamma} \mathcal{N}_e^t j_c \, d\Gamma = 0 \quad ; \\
& - \int_{\Omega} \mathbf{B}_e^t \mathbf{B} \, d\Omega + \int_{\Gamma} \mathcal{N}_e B_c \, d\Gamma = 0
\end{aligned} \tag{4.15}$$



Finally, the assembled residuals for each d.o.f. at each global node  $A$  are obtained from (4.15):

$$\begin{aligned}
\mathcal{R}_A^U &= - \int_{\Omega} (\mathcal{B}^s)^t_A T_A \, d\Omega + \int_{\Gamma} \mathcal{N}_A^t \mathbf{t} \, d\Gamma + \int_{\Omega} \mathcal{N}_A^t (\mathbf{j} \times \mathbf{B})_A \, d\Omega - \\
&\quad \int_{\Omega} \mathcal{N}_A^t \rho_m \mathcal{N}_A \ddot{\mathbf{u}}_A^U \, d\Omega = \mathbf{0} \quad ; \\
\mathcal{R}_A^T &= - \int_{\Omega} \mathcal{B}_A^t q_A \, d\Omega + \int_{\Gamma} \mathcal{N}_A q_c \, d\Gamma + \int_{\Omega} \mathcal{N}_A T_0 \boldsymbol{\beta} \mathcal{B}_A^s \dot{\mathbf{a}}_A^U \, d\Omega + \\
&\quad \int_{\Omega} \mathcal{N}_A \mathbf{j}_A \mathcal{B}_A \mathbf{a}_A^V \, d\Omega + \tau_q \int_{\Omega} \mathcal{N}_A \frac{\partial}{\partial t} (T_0 \boldsymbol{\beta} \mathcal{B}^s \dot{\mathbf{a}}^U)_A \, d\Omega + \\
&\quad \tau_q \int_{\Omega} \mathcal{N}_A \frac{\partial}{\partial t} (\mathbf{j} \mathcal{B} \mathbf{a}^V)_A \, d\Omega + \tau_q \int_{\Omega} \mathcal{N}_A \rho_m c \mathcal{N}_A \ddot{\mathbf{a}}_A^T \, d\Omega + \\
&\quad \int_{\Omega} \mathcal{N}_A \rho_m c \mathcal{N}_A \dot{\mathbf{a}}_A^T \, d\Omega = 0 \quad ; \\
\mathcal{R}_A^V &= - \int_{\Omega} \mathcal{B}_A^t \mathbf{j}_A \, d\Omega + \int_{\Gamma} \mathcal{N}_A j_c \, d\Gamma = 0 \quad ; \\
\mathcal{R}_A^{\varphi} &= - \int_{\Omega} \mathcal{B}_A^t B_A \, d\Omega + \int_{\Gamma} \mathcal{N}_A B_c \, d\Gamma = 0
\end{aligned} \tag{4.16}$$

Note that there are four residuals and six d.o.f. However, the mechanical residual  $\mathcal{R}_A^U$  is a matrix entity since there are three mechanical d.o.f or displacements. Therefore, the shape functions for the mechanical residual are also matrix entities.

### 4.2.3 Tangent stiffness matrices

The tangent stiffness matrices are obtained by deriving the residuals with respect to the d.o.f, as it has been shown in (4.3):

$$\begin{aligned}
 \mathcal{K}_{AB}^{UU} &= -\frac{\partial \mathcal{R}_A^U}{\partial \mathbf{a}_B^U} = \int_{\Omega} (\mathbf{B}^s)^t_A \frac{\partial \mathbf{T}}{\partial \mathbf{a}_B^U} d\Omega & ; \\
 \mathcal{K}_{AB}^{UT} &= -\frac{\partial \mathcal{R}_A^U}{\partial \mathbf{a}_B^T} = \int_{\Omega} (\mathbf{B}^s)^t_A \frac{\partial \mathbf{T}}{\partial \mathbf{a}_B^T} d\Omega - \int_{\Omega} \mathcal{N}_A^t \frac{\partial}{\partial \mathbf{a}_B^T} (\mathbf{j} \times \mathbf{B}) d\Omega & ; \\
 \mathcal{K}_{AB}^{UV} &= -\frac{\partial \mathcal{R}_A^U}{\partial \mathbf{a}_B^V} = - \int_{\Omega} \mathcal{N}_A^t \frac{\partial}{\partial \mathbf{a}_B^V} (\mathbf{j} \times \mathbf{B}) d\Omega & ; \\
 \mathcal{K}_{AB}^{U\varphi} &= -\frac{\partial \mathcal{R}_A^U}{\partial \mathbf{a}_B^\varphi} = - \int_{\Omega} \mathcal{N}_A^t \frac{\partial}{\partial \mathbf{a}_B^\varphi} (\mathbf{j} \times \mathbf{B}) d\Omega & ;
 \end{aligned} \tag{4.17}$$

Beyond the principal interaction  $\mathcal{K}_{AB}^{UU}$ , the mechanical field interacts with the thermal, electric and magnetic fields through the *Lorentz* forces. In addition, mechanical and thermal fields are also coupled by thermal stresses.

$$\begin{aligned}
 \mathcal{K}_{AB}^{TU} &= -\frac{\partial \mathcal{R}_A^T}{\partial \mathbf{a}_B^U} = 0 & ; \\
 \mathcal{K}_{AB}^{TT} &= -\frac{\partial \mathcal{R}_A^T}{\partial \mathbf{a}_B^T} = \int_{\Omega} \mathbf{B}_A^t \frac{\partial \mathbf{q}}{\partial \mathbf{a}_B^T} d\Omega - \int_{\Omega} \mathcal{N}_A \frac{\partial \mathbf{j}}{\partial \mathbf{a}_B^T} \mathbf{B} a_B^V d\Omega - \\
 & \quad \tau_q \int_{\Omega} \mathcal{N}_A \frac{\partial \mathbf{j}}{\partial \mathbf{a}_B^T} \mathbf{B} \dot{a}_B^V d\Omega & ; \\
 \mathcal{K}_{AB}^{TV} &= -\frac{\partial \mathcal{R}_A^T}{\partial \mathbf{a}_B^V} = \int_{\Omega} \mathbf{B}_A^t \frac{\partial \mathbf{q}}{\partial \mathbf{a}_B^V} d\Omega - \int_{\Omega} \mathcal{N}_A \frac{\partial \mathbf{j}}{\partial \mathbf{a}_B^V} \mathbf{B} a_B^V d\Omega - \\
 & \quad \int_{\Omega} \mathcal{N}_A \mathbf{j}_B \mathbf{B}_B d\Omega - \tau_q \int_{\Omega} \mathcal{N}_A \frac{\partial \mathbf{j}_B}{\partial t} \mathbf{B}_B d\Omega - \\
 & \quad \tau_q \int_{\Omega} \mathcal{N}_A \frac{\partial \mathbf{j}}{\partial \mathbf{a}_B^V} \mathbf{B}_B \dot{a}_B^V d\Omega & ; \\
 \mathcal{K}_{AB}^{T\varphi} &= -\frac{\partial \mathcal{R}_A^T}{\partial \mathbf{a}_B^\varphi} = 0
 \end{aligned} \tag{4.18}$$

On one hand, the thermal and electric fields are coupled by several thermoelectric interactions that will be described in the next chapter. On the other, there are no thermo-

mechanical no thermo–magnetic interactions. However and as will be reported in Chapter 8, the thermo–magnetic interaction modifies the term  $\mathcal{K}_{AB}^{T\varphi}$ . Note that thermo–magnetic and galvanomagnetic interactions are not included in the present chapter for clarity but they will be introduced in Chapter 8.

$$\begin{aligned}
\mathcal{K}_{AB}^{VU} &= -\frac{\partial \mathcal{R}_A^V}{\partial \mathbf{a}_B^U} = 0 & ; & \quad \mathcal{K}_{AB}^{\varphi U} = -\frac{\partial \mathcal{R}_A^\varphi}{\partial \mathbf{a}_B^U} = 0 & ; \\
\mathcal{K}_{AB}^{VT} &= -\frac{\partial \mathcal{R}_A^V}{\partial \mathbf{a}_B^T} = \int_{\Omega} \mathbf{B}_A^t \frac{\partial \mathbf{j}}{\partial \mathbf{a}_B^T} d\Omega & ; & \quad \mathcal{K}_{AB}^{\varphi T} = -\frac{\partial \mathcal{R}_A^\varphi}{\partial \mathbf{a}_B^T} = 0 & ; \\
\mathcal{K}_{AB}^{VV} &= -\frac{\partial \mathcal{R}_A^V}{\partial \mathbf{a}_B^V} = \int_{\Omega} \mathbf{B}_A^t \frac{\partial \mathbf{j}}{\partial \mathbf{a}_B^V} d\Omega & ; & \quad \mathcal{K}_{AB}^{\varphi V} = -\frac{\partial \mathcal{R}_A^\varphi}{\partial \mathbf{a}_B^V} = 0 & ; \\
\mathcal{K}_{AB}^{V\varphi} &= -\frac{\partial \mathcal{R}_A^V}{\partial \mathbf{a}_B^\varphi} = 0 & ; & \quad \mathcal{K}_{AB}^{\varphi\varphi} = -\frac{\partial \mathcal{R}_A^\varphi}{\partial \mathbf{a}_B^\varphi} = \int_{\Omega} \mathbf{B}_A^t \frac{\partial \mathbf{B}}{\partial \mathbf{a}_B^\varphi} d\Omega
\end{aligned}$$

(4.19)

For the electric d.o.f, the thermoelectric  $\mathcal{K}_{AB}^{VT}$  interactions are observed again. The term  $\mathcal{K}_{AB}^{\varphi V}$  represents the galvanomagnetic interaction and will be modified in the Chapter 8. For the magnetic d.o.f, the non–zero term is only the principal interaction.  $\mathcal{K}_{AB}^{\varphi T}$  and  $\mathcal{K}_{AB}^{\varphi V}$  are zero due to the **Simplification 1** and **Simplification 3**, respectively. Finally, the derivatives are obtained using (4.14) and the chain rule:

$$\frac{\partial T}{\partial \mathbf{a}_B^U} = \mathbf{C} \mathbf{B}_B^s \quad ; \quad \frac{\partial T}{\partial \mathbf{a}_B^T} = -\beta \mathcal{N}_B \quad ; \quad \frac{\partial T}{\partial \mathbf{a}_B^V} = 0 \quad ; \quad \frac{\partial T}{\partial \mathbf{a}_B^\varphi} = 0 \quad ; \quad (4.20)$$

$$\frac{\partial \mathbf{q}}{\partial \mathbf{a}_B^U} = 0 \quad ;$$

$$\frac{\partial \mathbf{q}}{\partial \mathbf{a}_B^T} = \alpha \mathcal{N}_B \mathbf{a}_B^T \frac{\partial \mathbf{j}}{\partial \mathbf{a}_B^T} + \alpha \mathbf{j}_B \mathcal{N}_B - \kappa \mathbf{B}_B + \frac{\partial \alpha}{\partial T} \mathcal{N}_B \mathbf{a}_B^T \mathbf{j}_B \mathcal{N}_B - \frac{\partial \kappa}{\partial T} \mathbf{B}_B \mathbf{a}_B^T \mathcal{N}_B -$$

$$\tau_{qj} \left( \frac{\partial \alpha}{\partial T} \mathcal{N}_B \mathcal{N}_B \mathbf{a}_B^T \gamma \mathbf{B}_B \dot{\mathbf{a}}_B^V + \alpha \mathcal{N}_B \gamma \mathbf{B}_B \dot{\mathbf{a}}_B^V + \alpha \mathcal{N}_B \mathbf{a}_B^T \frac{\partial \gamma}{\partial T} \mathcal{N}_B \mathbf{B}_B \dot{\mathbf{a}}_B^V \right) \quad ;$$

$$\frac{\partial \mathbf{q}}{\partial \mathbf{a}_B^V} = \alpha \mathcal{N}_B \mathbf{a}_B^T \frac{\partial \mathbf{j}}{\partial \mathbf{a}_B^V} \quad ;$$

$$\frac{\partial \mathbf{q}}{\partial \mathbf{a}_B^\varphi} = 0$$

(4.21)

$$\begin{aligned}
\frac{\partial j}{\partial \mathbf{a}_B^U} &= 0 && ; \\
\frac{\partial j}{\partial \mathbf{a}_B^T} &= -\alpha \gamma \mathbf{B}_B - \frac{\partial \alpha}{\partial T} \mathcal{N}_B \gamma \mathbf{B}_B \mathbf{a}_B^T - \frac{\partial \gamma}{\partial T} \left( \mathbf{B}_B^V \mathbf{a}_B^V + \alpha \mathbf{B}_B^T \mathbf{a}_B^T \right) \mathcal{N}_B - \\
&\quad \tau_{jq} \mathcal{N}_B \mathbf{B}_B^T \dot{\mathbf{a}}_B^T \left( \frac{\partial \alpha}{\partial T} \gamma + \frac{\partial \gamma}{\partial T} \alpha \right) && ; \quad (4.22)
\end{aligned}$$

$$\frac{\partial j}{\partial \mathbf{a}_B^V} = -\gamma \mathbf{B}_B \quad ;$$

$$\frac{\partial j}{\partial \mathbf{a}_B^g} = 0$$

The derivatives  $\partial \alpha / \partial T$ ,  $\partial \kappa / \partial T$ ,  $\partial \gamma / \partial T$  are due to the temperature-dependency of the *Seebeck* coefficient (*Thomson* effect), thermal and electric conductivities, respectively. These dependencies will be fitted to quadratic polynomials in Appendix A. Therefore, the derivatives are linear relationships, which will be introduced in the numerical code.

$$\frac{\partial \mathbf{B}}{\partial \mathbf{a}_B^U} = 0 \quad ; \quad \frac{\partial \mathbf{B}}{\partial \mathbf{a}_B^T} = 0 \quad ; \quad \frac{\partial \mathbf{B}}{\partial \mathbf{a}_B^V} = 0 \quad ; \quad \frac{\partial \mathbf{B}}{\partial \mathbf{a}_B^g} = -\mu_0 \mathbf{B}_B \quad ; \quad (4.23)$$

$$\frac{\partial}{\partial \mathbf{a}_B^U} (\mathbf{j} \times \mathbf{B}) = 0 \quad ;$$

$$\frac{\partial}{\partial \mathbf{a}_B^T} (\mathbf{j} \times \mathbf{B}) = \frac{\partial \mathbf{j}}{\partial \mathbf{a}_B^T} \times \mathbf{B}_B \quad ; \quad (4.24)$$

$$\frac{\partial}{\partial \mathbf{a}_B^V} (\mathbf{j} \times \mathbf{B}) = \frac{\partial \mathbf{j}}{\partial \mathbf{a}_B^V} \times \mathbf{B}_B \quad ;$$

$$\frac{\partial}{\partial \mathbf{a}_B^g} (\mathbf{j} \times \mathbf{B}) = \mathbf{j}_B \times \frac{\partial \mathbf{B}}{\partial \mathbf{a}_B^g}$$

The last derivatives are consequence of the *Lorentz* forces due to the presence of magnetic fields.

#### 4.2.4 Capacity matrices

The capacity matrices are obtained deriving the residuals with respect to the first-derivative of d.o.f:

$$\begin{aligned}
 \mathbf{c}_{AB}^{UU} &= \mathbf{c}_{AB}^{UT} = \mathbf{c}_{AB}^{UV} = \mathbf{c}_{AB}^{U\varphi} = \mathbf{0} & ; \\
 \mathbf{c}_{AB}^{TU} &= -\frac{\partial \mathcal{R}_A^T}{\partial \dot{\mathbf{a}}_B^U} = -\int_{\Omega} \mathcal{N}_A T_0 \boldsymbol{\beta} \mathbf{B}_B^s \, d\Omega & ; \\
 \mathbf{c}_{AB}^{TT} &= -\frac{\partial \mathcal{R}_A^T}{\partial \dot{\mathbf{a}}_B^T} = -\tau_q \int_{\Omega} \mathcal{N}_A \frac{\partial^2 \mathbf{j}}{\partial t \partial \dot{\mathbf{a}}_B^T} \mathbf{B}_B \mathbf{a}_B^V \, d\Omega - \int_{\Omega} \mathcal{N}_A \rho_m c \mathcal{N}_B \, d\Omega & ; \\
 \mathbf{c}_{AB}^{TV} &= -\frac{\partial \mathcal{R}_A^T}{\partial \dot{\mathbf{a}}_B^V} = -\tau_q \int_{\Omega} \mathcal{N}_A \frac{\partial^2 \mathbf{j}}{\partial t \partial \dot{\mathbf{a}}_B^V} \mathbf{B}_B \mathbf{a}_B^V \, d\Omega - \tau_q \int_{\Omega} \mathcal{N}_A \mathbf{j}_B \mathbf{B}_B \, d\Omega + \\
 &\quad \int_{\Omega} \mathbf{B}_A \frac{\partial \mathbf{q}}{\partial \dot{\mathbf{a}}_B^V} \, d\Omega & ; \\
 \mathbf{c}_{AB}^{T\varphi} &= -\frac{\partial \mathcal{R}_A^T}{\partial \dot{\mathbf{a}}_B^\varphi} = 0 & ; \\
 \mathbf{c}_{AB}^{VU} &= \mathbf{c}_{AB}^{VV} = \mathbf{c}_{AB}^{V\varphi} = \mathbf{0}; \quad \mathbf{c}_{AB}^{VT} = -\frac{\partial \mathcal{R}_A^V}{\partial \dot{\mathbf{a}}_B^T} = \int_{\Omega} \mathbf{B}_A^t \frac{\partial \mathbf{j}}{\partial \dot{\mathbf{a}}_B^T} \, d\Omega & ; \\
 \mathbf{c}_{AB}^{\varphi U} &= \mathbf{c}_{AB}^{\varphi T} = \mathbf{c}_{AB}^{\varphi V} = \mathbf{c}_{AB}^{\varphi\varphi} = \mathbf{0} & 
 \end{aligned}$$

(4.25)

For the capacity matrices, four terms are only no-zero.  $\mathbf{c}_{AB}^{TU}$  represents the thermoelastic damping that was introduced in Biot [1956] to study the thermo-mechanical interactions. This term arises from the irreversible entropy flux due to the thermal fluxes that have been originated from the volumetric strain variations. The heat capacity is represented by the second term on the right side in  $\mathbf{c}_{AB}^{TT}$ . The rest of terms in  $\mathbf{c}_{AB}^{TT}$ ,  $\mathbf{c}_{AB}^{TV}$ ,  $\mathbf{c}_{AB}^{VT}$  are closely related with the relaxation times (viscous terms).

Again, the derivatives are obtained applying the chain rule:

$$\begin{aligned}
\frac{\partial T}{\partial t} &= \mathbf{C} \mathbf{B}^s \dot{\mathbf{a}}^U - \beta \mathcal{N} \dot{\mathbf{a}}^T ; & \frac{\partial j}{\partial t} &= -\gamma \mathbf{B} \dot{\mathbf{a}}^V - \alpha \gamma \mathbf{B} \dot{\mathbf{a}}^T ; \\
\frac{\partial^2 T}{\partial t \partial \dot{\mathbf{a}}_B^U} &= \mathbf{C} \mathbf{B}_B^s ; & \frac{\partial^2 j}{\partial t \partial \dot{\mathbf{a}}_B^V} &= -\gamma \mathbf{B}_B ; \\
\frac{\partial^2 T}{\partial t \partial \dot{\mathbf{a}}_B^T} &= -\beta \mathcal{N}_B ; & \frac{\partial^2 j}{\partial t \partial \dot{\mathbf{a}}_B^V} &= -\alpha \gamma \mathbf{B}_B ; \\
\frac{\partial q}{\partial \dot{\mathbf{a}}_B^V} &= -\tau_{qj} \alpha T_B \gamma \mathbf{B}_B ; & \frac{\partial j}{\partial \dot{\mathbf{a}}_B^T} &= -\tau_{jq} \alpha \gamma \mathbf{B}_B
\end{aligned} \tag{4.26}$$

#### 4.2.5 Mass matrices

The mass matrices are obtained deriving the residuals with respect to the second-derivative of the d.o.f:

$$\begin{aligned}
\mathcal{M}_{AB}^{UU} &= -\frac{\partial \mathcal{R}_A^U}{\partial \ddot{\mathbf{a}}_B^U} = \int_{\Omega} \mathcal{N}_A^t \rho_m \mathcal{N}_B \, d\Omega ; & \mathcal{M}_{AB}^{UT} &= \mathcal{M}_{AB}^{UV} = \mathcal{M}_{AB}^{U\varphi} = \mathbf{0} ; \\
\mathcal{M}_{AB}^{TU} &= -\frac{\partial \mathcal{R}_A^T}{\partial \ddot{\mathbf{a}}_B^U} = -\tau_q \int_{\Omega} \mathcal{N}_A T_0 \mathbf{B}_B^s \, d\Omega ; & \mathcal{M}_{AB}^{TV} &= \mathbf{0} ; \\
\mathcal{M}_{AB}^{TT} &= -\frac{\partial \mathcal{R}_A^T}{\partial \ddot{\mathbf{a}}_B^T} = -\tau_q \int_{\Omega} \mathcal{N}_A \rho_m c \mathcal{N}_B \, d\Omega ; & \mathcal{M}_{AB}^{T\varphi} &= \mathbf{0} ; \\
\mathcal{M}_{AB}^{VU} &= \mathcal{M}_{AB}^{VT} = \mathcal{M}_{AB}^{VV} = \mathcal{M}_{AB}^{V\varphi} = \mathbf{0} ; \\
\mathcal{M}_{AB}^{\varphi U} &= \mathcal{M}_{AB}^{\varphi T} = \mathcal{M}_{AB}^{\varphi V} = \mathcal{M}_{AB}^{\varphi\varphi} = \mathbf{0}
\end{aligned} \tag{4.27}$$

The non-zero terms are the classical mass matrix  $\mathcal{M}_{AB}^{UU}$  and those terms  $\mathcal{M}_{AB}^{TU}$ ,  $\mathcal{M}_{AB}^{TT}$  that emerge from the relaxation time  $\tau_q$ . The latter represents a hyperbolic propagation of the temperature denominated second sound, as has been commented.

The final assembled matrix problem is given by

$$\begin{array}{c}
 \left[ \begin{array}{cccc}
 c_1 \mathcal{K}^{UU} + c_3 \mathcal{M}^{UU} & c_1 \mathcal{K}^{UT} & c_1 \mathcal{K}^{UV} & c_1 \mathcal{K}^{U\varphi} \\
 c_2 \mathbf{c}^{TU} + c_3 \mathcal{M}^{TU} & c_1 \mathcal{K}^{TT} + c_2 \mathbf{c}^{TT} + c_3 \mathcal{M}^{TT} & c_1 \mathcal{K}^{TV} + c_2 \mathbf{c}^{TV} & \mathbf{0} \\
 \mathbf{0} & c_1 \mathcal{K}^{VT} + c_2 \mathbf{c}^{VT} & c_1 \mathcal{K}^{VV} & \mathbf{0} \\
 \mathbf{0} & \mathbf{0} & \mathbf{0} & c_1 \mathcal{K}^{\varphi\varphi}
 \end{array} \right] \\
 \\
 \left. \begin{array}{c}
 \left( \mathbf{da}^U \right)^k \\
 \mathbf{da}^T \\
 \mathbf{da}^V \\
 \mathbf{da}^\varphi
 \end{array} \right\} = \left. \begin{array}{c}
 \left( \mathcal{R}^U \right)^k \\
 \mathcal{R}^T \\
 \mathcal{R}^V \\
 \mathcal{R}^\varphi
 \end{array} \right\}
 \end{array}
 \tag{4.28}$$

where:

$$\left. \begin{array}{c}
 \left( \mathbf{a}^U \right)^{k+1} \\
 \mathbf{a}^T \\
 \mathbf{a}^V \\
 \mathbf{a}^\varphi
 \end{array} \right\} = \left. \begin{array}{c}
 \left( \mathbf{a}^U \right)^k \\
 \mathbf{a}^T \\
 \mathbf{a}^V \\
 \mathbf{a}^\varphi
 \end{array} \right\} + \left. \begin{array}{c}
 \mathbf{da}^U \\
 \mathbf{da}^T \\
 \mathbf{da}^V \\
 \mathbf{da}^\varphi
 \end{array} \right\}
 \tag{4.29}$$

From (4.28), the multi-coupled assembled matrix is asymmetric. Note that this assembled matrix will change in Chapter 8 due to the inclusion of the galvanomagnetic and thermo-magnetic interactions. However, the matrix will remain asymmetric. Therefore and from a numerical point of view, asymmetric equation solvers must be used to guarantee quadratic rates of convergence. This problem is solved using the FEAP command UTAN, see Taylor [2010].

### 4.3 Interface finite element

Radiation and convection phenomena are very important in electronic devices due to the trend towards miniaturization in micro-electronic: temperatures can also reach very high values not usual in traditional mesoscale applications.

For this reason, a special interface 2-D FE (see Figure 4.3) is developed and implemented to prescribe fluxes and to study radiation and convection heat fluxes through the air, avoiding the expensive FE meshing of this gas. To facilitate the assembly process, this new element has the same d.o.f. in each node that the 3-D FE for non-equilibrium interactions.

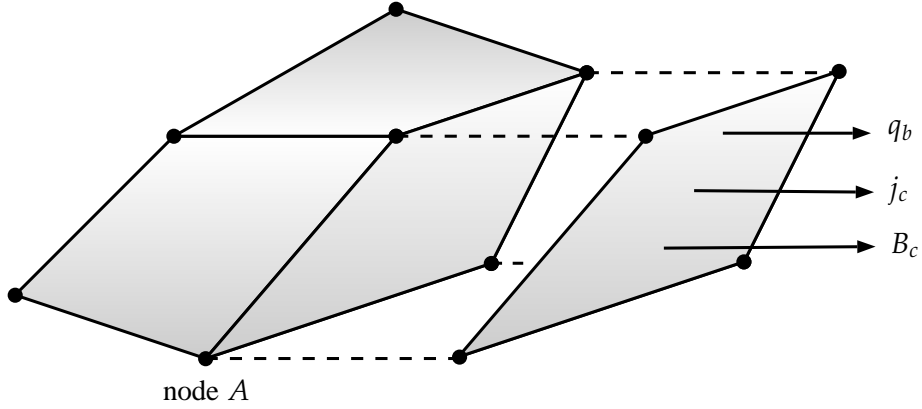


Figure 4.3: Non-linear isoparametric 3-D finite element (left). Special 2-D interface finite element (right).

The interface finite element does not represent any physical continuum, therefore it is uncoupled but non-linear since the radiation phenomena depends on the function  $T^4$ . From a FE point of view, the *Newton-Raphson* scheme is used to solve this non-linearity. The governing equations are written in residual form:

$$\begin{array}{l}
 \mathcal{R}_A^U = \mathbf{0} \quad ; \\
 \mathcal{R}_A^T = \int_{\Gamma} q_b \, d\Gamma \quad ; \\
 \mathcal{R}_A^V = \int_{\Gamma} j_c \, d\Gamma \quad ; \\
 \mathcal{R}_A^{\varphi} = \int_{\Gamma} B_c \, d\Gamma
 \end{array}
 \tag{4.30}$$

Note that  $B_c$  has not physical sense, however it is incorporated for the prescription of magnetic flux from a numerical point of view. Furthermore, the boundary heat flux  $q_b$  is composed of the prescribed  $q_c$ , the convection  $q^c$  and the radiation  $q^r$  heat fluxes:

$$q_b = q_c + \underbrace{h (T - T_{\infty})}_{q^c} + \underbrace{\epsilon_{emis} \sigma (T^4 - T_{\infty}^4)}_{q^r}
 \tag{4.31}$$

where  $h$  is the convection heat transfer coefficient that depends on the physical properties of the surrounding fluid (such as temperature and speed) and on the physical situation in which convection occurs,  $\epsilon_{emis}$  is the emissivity and  $T_{\infty}$  is the temperature reference for convection and radiation phenomena.



The final assembled matrix is divided into 16 submatrices, corresponding to the negative derivatives of (4.30) with respect to the discretization of the six d.o.f:

$$\boxed{\begin{bmatrix} 0 & 0 & 0 & 0 \\ 0 & \mathcal{K}^{TT} & 0 & 0 \\ 0 & 0 & 0 & 0 \\ 0 & 0 & 0 & 0 \end{bmatrix} \begin{Bmatrix} \mathbf{da}^U \\ \mathbf{da}^T \\ \mathbf{da}^V \\ \mathbf{da}^\varphi \end{Bmatrix}^k = \begin{Bmatrix} \mathcal{R}^U \\ \mathcal{R}^T \\ \mathcal{R}^V \\ \mathcal{R}^\varphi \end{Bmatrix}^k} \quad (4.32)$$

Solely, the consistent tangent sub-matrix corresponding to the direct thermal field is non-zero:

$$\boxed{\mathcal{K}_{AB}^{TT} = \int_{\Gamma} \mathcal{N}_A \left( h + 4 \epsilon_{emis} \sigma T^3 \right) \mathcal{N}_B d\Gamma} \quad (4.33)$$

due to the presence of convection and radiation phenomena.

As has been reported, both FE formulations have been implemented into the research code FEAP, Taylor [2010], which has been developed by the Professor *R.L. Taylor* in the University of California at *Berkeley, California (USA)*. This code has several dummy routines (user elements) that can be used for the implementation of new modular elements using the programming code Fortran.



Figure 4.4: FEAP (Finite Element Analysis Program) is the computer code used for the implementation of the finite element formulation in the present thesis.

**Part III**

**RESULTS**



*All truths are easy to understand once they are discovered; the point is to discover them.*

**Galileo Galilei** (1564–1642)

# 5

## Thermoelectric interactions



Thermoelectric materials are solid state semiconductors that couple electric and thermal energies by means of three separated thermoelectric effects: *Seebeck*, *Peltier* and *Thomson*. In addition, the *Ohm* and *Fourier* laws, which are inherent to electric and thermal fluxes, are also present. Thermoelectric materials are used as heat pumps (heating and cooling) and generators, see Riffat and Ma [2003] for a full revision on thermoelectric applications. In the last decade, miniaturized thermoelectric devices and high-frequency processes are increasingly applied for the cooling of micro-electronic devices, see Chapter 6.

According to the ENET, the *Ohm* and *Fourier* laws are incorrect from a physical point of view since they lead a parabolic energy propagation: parabolic model. In order to obtain a hyperbolic or *Cattaneo* model, relaxation times must be introduced in the formulation. Note that both models agree in steady-state situations.

The objectives of the present chapter are:

- ▷ To simulate the thermoelectric effects under the hyperbolic model
- ▷ To calibrate the time-integration algorithm

For the first objective, only the thermal relaxation time  $\tau_q$  is considered. As mentioned, this effect is denominated second sound. Note that  $\tau_j = 0$  due to the **Simplification 5**. For the second objective, HHT and *Newmark- $\beta$*  algorithms are compared and regularized relating time steps and element sizes. As discussed in Chapter 4, the calibration is performed by

trial and error numerical experiments since spectral analyses are beyond of the scope of the present thesis.

Section 5.1 reviews the *Seebeck*, *Peltier* and *Thomson* effects; Section 5.2 extracts the FE equations from the multi-coupled FE assembled matrix; Section 5.3 compares four 1-D analytical solutions with numerical results to validate the FE implementation and to calibrate the time-integration algorithm; Section 5.4 presents a 3-D simulation and, finally, Section 5.5 reports the conclusions.

## 5.1 Review of basic thermoelectric effects

This section presents an overview of the basic thermoelectric effects: *Seebeck*, *Peltier* and *Thomson*, most of the related formulation has been published in Pérez-Aparicio et al. [2007].

From (3.23) and considering  $\tau_{jq} = \tau_{qj} = 0$ , the transport equations to study the thermoelectric effects under the hyperbolic or second sound model are:

$$\mathbf{q} = -\kappa \nabla T - \alpha T \mathbf{j} - \tau_q \dot{\mathbf{Q}} \quad ; \quad (5.1)$$

$$\mathbf{j} = -\gamma \nabla V - \alpha \gamma \nabla T$$

where the first terms on the right hand side in (5.1) represent the *Fourier* (top) and *Ohm* (bottom) laws; the second terms the *Peltier* and *Thomson* effects (top) and the *Seebeck* effect (bottom); the third term (top) the thermal hyperbolicity or second sound.

### SEEBECK EFFECT

The *Seebeck* effect is due to the presence of an electromotive force  $\epsilon_{EM}$  when the temperature distribution  $T$  varies inside a thermoelectric material:

$$\epsilon_{EM} = -\alpha \nabla T|_{j=0} \quad (5.2)$$

This electromotive force is considered as a voltage gradient and incorporated into the *Ohm* law, obtaining (5.1)–bottom. The *Seebeck* effect has been traditionally used to measure temperatures by means of basic thermocouples as that shown in Figure 5.1.



Figure 5.1: Basic thermocouple probe used for the measurement of temperatures, picture taken from [www.thermocouples.com/](http://www.thermocouples.com/).

### PELTIER EFFECT

A similar description holds for the heat transfer field: the charges (either electrons or holes) from the electric current can transport thermal energy through the material in a sort of convection phenomena that is superimposed to that of *Fourier* law:

$$\mathbf{q} = \alpha T \mathbf{j} \quad (5.3)$$

### THOMSON EFFECT

The *Thomson* effect is closely related to the temperature-dependency of the *Seebeck* coefficient. From (5.3), it can be appreciated that this heat flux will change from one point to other if  $\alpha$  also changes, in particular if it is a function of the varying temperature field. Generally, in the literature the *Thomson* coefficient  $t_h$  is defined by:

$$t_h = T \left[ \frac{\partial \alpha(T)}{\partial T} \right] \quad (5.4)$$

In order to clarify the previous effects, Figure 5.2 shows an electric flux  $\mathbf{j}$  passing through the union of two thermoelectric materials with different *Seebeck* coefficients:  $\alpha_1$  and  $\alpha_2$ . This flux is taken constant through the interface of area  $A_i$  by the hypothesis of conservation of charge. Ignoring the thermal conduction influence and assuming constant the temperature at the interface, the coupled heat flux will be  $\mathbf{q} = \alpha T \mathbf{j}$ . Since the two materials have different *Seebeck* coefficients, a jump of  $\mathbf{q}$  will appear at the interface, inducing the presence of a heat power  $Q = (\mathbf{q}_1 - \mathbf{q}_2) \cdot \mathbf{n} A_i = (\alpha_1 - \alpha_2) T \mathbf{j} \cdot \mathbf{n} A_i$ , where  $\pi_{12} = \alpha_1 - \alpha_2$  is the absolute *Peltier* coefficient. If  $\alpha_1 > \alpha_2$  there will be a release of heat, otherwise an absorption. This phenomenon is called *Peltier*, and in reality is more complicated than the one described here, due to the temperature high non-linearity at the interphase, Pérez-Aparicio et al. [2007];  $T$  reduces/increases at the center of this interphase in order to “absorb” also by conduction the *Peltier* heat, creating a strong gradient.

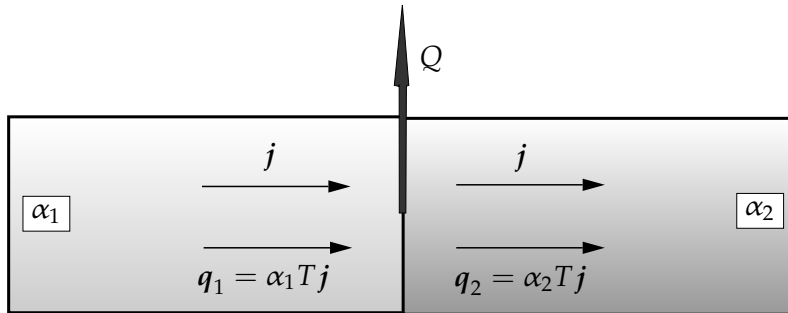


Figure 5.2: Heat power due to *Peltier* effect in two thermoelectric materials.

## 5.2 Finite element equations

The multi-coupled FE formulation only requires two degrees of freedom (temperature and voltage) to model the thermoelectric effects under the hyperbolic model. Therefore and from (4.28) the assembled matrix is:

$$\begin{bmatrix} c_1 \mathcal{K}^{TT} + c_2 \mathcal{C}^{TT} + c_3 \mathcal{M}^{TT} & c_1 \mathcal{K}^{TV} + c_2 \mathcal{C}^{TV} \\ c_1 \mathcal{K}^{VT} + c_2 \mathcal{C}^{TV} & c_1 \mathcal{K}^{VV} \end{bmatrix} \quad (5.5)$$

where the term  $\mathcal{M}^{TT}$  is due to the relaxation time  $\tau_q$  and permits a hyperbolic propagation of temperature, of voltage and of thermal flux.

## 5.3 Results

The FE formulation is validated by means of four cases for which analytical solutions are found in the literature, modified or developed. These solutions are 1-D simplifications of the thermoelectric governing equations and are summarized in Table 5.1. Due to difficulty in developing analytical solutions, the temperature dependence of the electric and thermal conductivities is not included in the validations. Nevertheless, this dependency will be verified in Chapter 9 using experimental results.

Case	Simplifications					Effects
I	$\tau_q = 0$	$j = 0$	$\alpha = cte$	$\gamma = cte$	$\kappa = cte$	F, S
II	$\tau_q = 0$	$j \neq 0$	$\alpha = cte$	$\gamma = cte$	$\kappa = cte$	F, S, J
III	$\tau_q = 0$	$j \neq 0$	$\alpha(T)$	$\gamma = cte$	$\kappa = cte$	F, S, J, Th
IV	$\tau_q \neq 0$	$j \neq 0$	$\alpha(T)$	$\gamma = cte$	$\kappa = cte$	F, S, J, Th, ss

Table 5.1: 1-D validation cases, simplifications and included effects: F - Fourier, S - Seebeck, J - Joule, Th - Thomson, ss - second sound.

For all cases, a p-type ThermoElement (TE) device manufactured by MELCOR [2010] with properties given in Appendix B is modeled. The TE is a parallelepiped of dimensions  $L_{x_1} = L_{x_2} = 1.4$ ,  $L_{x_3} = 1.14$  [mm]. For a p-type TE, the electric flux direction is co-linear with the heat flux. The boundary conditions are discontinuous: initially the temperature is  $T = 0$  everywhere. For  $t > 0$  the boundary temperatures are set to  $T_c = 30$  at the cold face and to  $T_h = 50$  [°C] at the hot face. The boundary voltage is set to  $V = 0$  [V] at the cold face. Figure 5.3 shows the geometric dimensions and the boundary conditions.

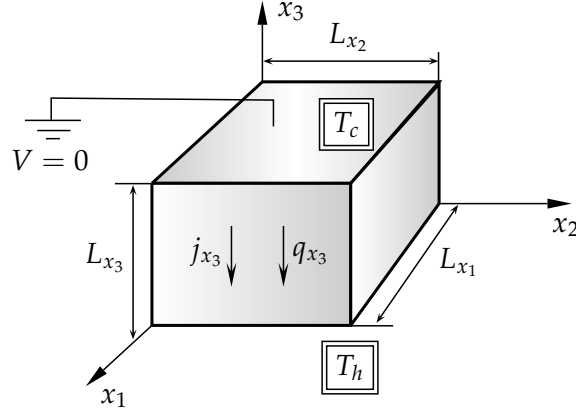


Figure 5.3: p-type thermoelement geometry, applied boundary conditions, dimensions, fluxes and coordinates.

For cases II, III and IV, an electric flux in the  $x_3$  direction is prescribed using the special interface element developed in Chapter 4. The applied intensity is 5.2 [A], an average of the ones specified by the manufacturer and corresponds to an electric flux  $j_3 = 2.65 \times 10^6$  [A/m<sup>2</sup>].

The constant properties for  $\alpha$ ,  $\gamma$ ,  $\kappa$  are obtained from Appendix B using an average temperature  $T_m = (T_h + T_c)/2$ . The thermal strong forms for each case are given by:

$$\begin{aligned}
 \text{I : } & \kappa \frac{\partial^2 T}{\partial x_3^2} = \rho_m c \frac{\partial T}{\partial t} & ; \\
 \text{II : } & \kappa \frac{\partial^2 T}{\partial x_3^2} = \rho_m c \frac{\partial T}{\partial t} - \frac{j_{x_3}^2}{\gamma} & ; \\
 \text{III : } & \kappa \frac{\partial^2 T}{\partial x_3^2} = \rho_m c \frac{\partial T}{\partial t} - \frac{j_{x_3}^2}{\gamma} + t_h j_{x_3} \frac{\partial T}{\partial x_3} & ; \\
 \text{IV : } & \kappa \frac{\partial^2 T}{\partial x_3^2} = \rho_m c \frac{\partial T}{\partial t} - \frac{j_{x_3}^2}{\gamma} + t_h j_{x_3} \frac{\partial T}{\partial x_3} + \tau_q \frac{\partial}{\partial t} \left[ j_{x_3} \left( \frac{\partial V}{\partial x_3} \right) \right] + \tau_q \rho_m c \frac{\partial^2 T}{\partial t^2} & ;
 \end{aligned} \tag{5.6}$$

where the fourth and fifth terms on the right side of case IV represent the second sound effects: irreversibility or dissipation and hyperbolicity, respectively.

### 5.3.1 Analytical solutions

For cases I to III,  $\tau_q = 0$  and the thermal strong forms (5.6) are diffusive: second order parabolic partial differential equations. For I, the situation is linear and homogeneous; for II linear and non-homogeneous and for III non-linear and non-homogeneous. Case IV is a non-linear and non-homogeneous hyperbolic problem, since  $\tau_q \neq 0$ .

Analytical solutions for the thermal field in cases I and II are given in Polyanin [2002], while the voltage distributions and thermal fluxes are calculated in the present thesis. For



III, the thermal and electrical solutions are given in Seiffert et al. [2002]. For IV, the analytical solution for the temperature is given in Alata et al. [2003] and is based on a *Laplace* transform solution technique. However, several differences between this solution and the numerical results are found, thus, a new corrected comparison solution is deduced in the present thesis. Furthermore, the heat flux is calculated using a semi-analytical procedure that combines the analytical temperature solution with finite differences to obtain the gradient of temperature. Analytical results for voltage are not generated due to the necessity of using numerical techniques in all steps.

#### ANALYTICAL SOLUTION FOR CASE I

$$\begin{aligned}
 V(x_3, t) &= -\alpha \left[ \frac{\Delta T}{L_{x_3}} x_3 - \Delta T + \sum_{n=1}^{\infty} c_n \sin \left( \frac{n\pi x_3}{L_{x_3}} \right) e^{-\Lambda t} \right] ; \\
 T(x_3, t) &= T_c + \frac{\Delta T}{L_{x_3}} x_3 + \sum_{n=1}^{\infty} c_n \sin \left( \frac{n\pi x_3}{L_{x_3}} \right) e^{-\Lambda t} ; \\
 q_3(x_3, t) &= -\kappa \left[ \frac{\Delta T}{L_{x_3}} + \sum_{n=1}^{\infty} c_n \cos \left( \frac{n\pi x_3}{L_{x_3}} \right) \frac{n\pi}{L_{x_3}} e^{-\Lambda t} \right]
 \end{aligned} \tag{5.7}$$

where:

$$\begin{aligned}
 \Delta T &= T_h - T_c ; \\
 \Lambda &= \beta \left( \frac{n\pi}{L} \right)^2 ; \\
 \beta &= \frac{\kappa}{\rho_m c} ; \\
 c_n &= \frac{2}{L_{x_3}} \int_0^{L_{x_3}} \left( T_c - \frac{\Delta T}{L_{x_3}} x_3 \right) \sin \left( \frac{n\pi x_3}{L_{x_3}} \right) dx_3
 \end{aligned} \tag{5.8}$$

ANALYTICAL SOLUTION FOR CASE II

$$\begin{aligned}
 V(x_3, t) &= \frac{j_{x_3}}{\gamma} (L_{x_3} - x_3) + \\
 &\quad \alpha \left[ \left( \frac{\Delta T}{L_{x_3}} - A_1 x_3 \right) (L_{x_3} - x_3) - \sum_{n=1}^{\infty} c_n \sin \left( \frac{n\pi x_3}{L_{x_3}} \right) e^{-\Lambda t} \right] \quad ; \\
 T(x_3, t) &= \frac{A_2}{L_{x_3}} x_3 + T_c - A_3 x_3^2 + \sum_{n=1}^{\infty} c_n \sin \left( \frac{n\pi x_3}{L_{x_3}} \right) e^{-\Lambda t} \quad ; \\
 q_3(x_3, t) &= -\kappa \left[ \frac{A_2}{L_{x_3}} - 2A_3 x_3 + \sum_{n=1}^{\infty} c_n \cos \left( \frac{n\pi x_3}{L_{x_3}} \right) \frac{n\pi}{L_{x_3}} e^{-\Lambda t} \right] + \alpha T(x_3, t) j_{x_3}
 \end{aligned} \tag{5.9}$$

where:

$$\begin{aligned}
 A_1 &= \frac{j_{x_3}}{2\kappa \gamma} \quad ; \\
 A_2 &= \Delta T + \frac{(j_{x_3} L_{x_3})^2}{2\beta \rho_m c \gamma} \quad ; \\
 A_3 &= \frac{j_{x_3}^2}{2\beta \rho_m c \gamma} \quad ; \\
 c_n &= \frac{2}{L_{x_3}} \int_0^{L_{x_3}} \left( \frac{A_2}{L_{x_3}} x_3 + T_c - A_3 x_3^2 \right) \sin \left( \frac{n\pi x_3}{L_{x_3}} \right) dx_3
 \end{aligned} \tag{5.10}$$

ANALYTICAL SOLUTION FOR CASE IV

From Alata et al. [2003], the dimensionless parameters  $\xi = x_3/L_{x_3}$  and  $\eta = t\kappa/\rho c L_{x_3}^2$  are used to rewrite (5.7)–bottom in an amenable form to be solved by the *Laplace* technique:

$$\frac{\partial T}{\partial \xi^2} + F_1 \frac{T}{\xi} + F_2 - \frac{\partial T}{\partial \eta} - \tau_q F_3 \frac{\partial T}{\partial \eta^2} + \tau_q F_4 \frac{\partial}{\partial \eta} \left[ F_2 \frac{A\kappa}{L_{x_3}^2} - \frac{\alpha\kappa A}{t_h L_{x_3}^2} F_1 \left( \frac{\partial T}{\partial \xi} \right) \right] = 0 \quad ; \tag{5.11}$$

$$T(\xi, 0) = 0 \quad ; \quad T(0, \eta) = T_h \quad ; \quad T(1, \eta) = T_c$$

Note that the boundary conditions have been included. Regarding Alata et al. [2003],  $F_1 = -t_h I L_{x_3} / \kappa A$ ,  $F_2 = I^2 L_{x_3}^2 / \kappa \gamma A^2$  have been modified and  $F_3 = \kappa / \rho_m c L_{x_3}^2$ ,  $F_4 = 1 / \rho_m c A$  are incorporated. Applying the *Laplace* transform

$$\boxed{\begin{aligned} W(\xi, s) &= P_{11} e^{\lambda_{11}\xi} + P_{12} e^{\lambda_{12}\xi} + \frac{F_2}{s(\tau_q F_3 s^2 + s)} ; \\ W(\xi) &= 0 ; \quad W(0) = \frac{T_c}{s} ; \quad W(1) = \frac{T_h}{s} \end{aligned}} \quad (5.12)$$

where  $s$  is time in the *Laplace* domain. The boundary conditions in (5.12) are different from those in Alata et al. [2003]: in this reference they are not transformed. Then, the following parameters are modified

$$\begin{aligned} P_{11} &= \frac{\frac{T_h}{s} + e^{\lambda_{12}} \left( \frac{F_2}{s(\tau_q F_3 s^2 + s)} - \frac{T_c}{s} \right) - \frac{F_2}{s(\tau_q F_3 s^2 + s)}}{e^{\lambda_{11}} - e^{\lambda_{12}}} ; \\ P_{12} &= \frac{T_c}{s} - P_{11} - \frac{F_2}{s(\tau_q F_3 s^2 + s)} ; \\ \left\{ \begin{array}{l} \lambda_{11} \\ \lambda_{12} \end{array} \right\} &= \frac{1}{2} \left( -A_1 \mp \sqrt{A_1^2 - 4B_1} \right) ; \end{aligned} \quad (5.13)$$

$$A_1 = F_1 (t_h L^2 + A \alpha \kappa \tau_q s F_4) ; \quad B_1 = -t_h^2 L^4 (s + \tau_q F_3 s^2)$$

Finally, equations (5.12) are inverted using the *Riemann*-sum approximation as in Alata et al. [2003].

### 5.3.2 Numerical solutions for cases I to III

Numerical solutions are obtained using a structured (coarse) mesh of 11 elements in the  $x_3$  direction. Only one element is used in the  $x_1$  and  $x_2$  directions since the problem is fundamentally 1-D. A time step of  $\Delta t = 0.1$  and the standard *Newmark*- $\beta$  parameters, see Chapter 4,  $\bar{\beta} = 0.25$ ,  $\bar{\gamma} = 0.5$  are used.

Figure 5.4 shows the voltage (left) and temperature (right) distributions along the  $x_3$  direction for case I (top), and for cases II and III (bottom). Solutions at  $t = 0.05, 0.3, 5$  [s] are represented: the analytical ones with lines and the FE results with circles. For case I, the temperature distributions are quadratic in nature during the initial transient response due to the boundary conditions. At near steady-state (e.g.,  $t = 5$ ) they become nearly linear, since this problem is of the *Laplace*-type: the lack of electric current implies the absence of a

*Joule* effect. The voltage distributions are proportional to the temperature, with the *Seebeck* coefficient being the slope.

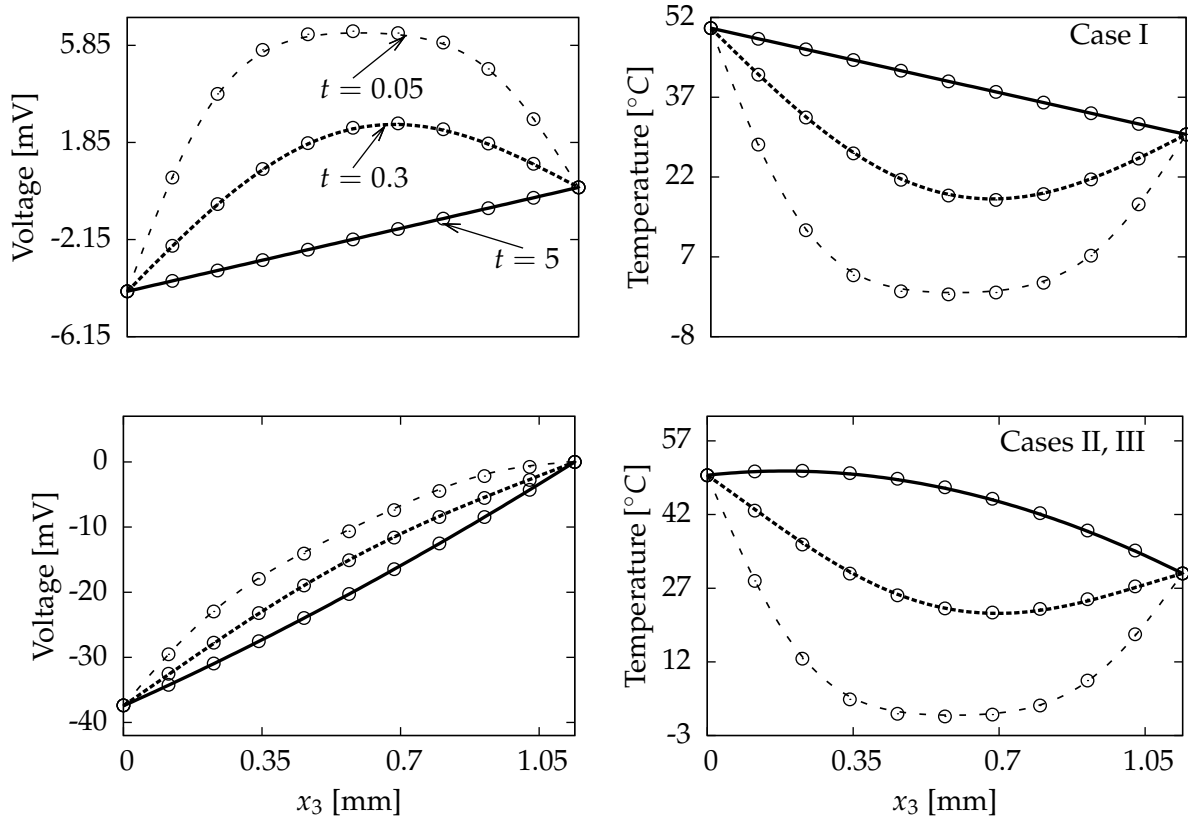


Figure 5.4: Voltage (left) and temperature (right) distributions along thermoelement for cases I (top row) and II (bottom row) and for three time instants. Analytical results with different line types, finite element with circles.

For case II, near quadratic distributions appear for the steady–state situation due to the *Joule* effect: this is a *Poisson*–type problem. Now, voltage distributions are not proportional to temperature ones, since the potential drop increases due to electric energy being converted into thermal energy. Results for case III are very similar, since the *Thomson* effect is not relevant under the applied intensity, see Chapter 9. As expected for these simple cases, the agreement between analytical and FEM distributions is very good.

Figure 5.5 shows the thermal flux along the  $x_3$  direction versus the TE length. Analytical and FE results differ slightly at the edges, since the mesh is not highly refined to capture the *Newmann* boundary condition. For short times, the flux distributions are very similar in both cases, since the temperature distributions have the same shape. Near steady–state, a constant distribution is obtained for case I (from the linear temperature distribution) and a linear for case II (from a quadratic temperature). In addition, for case II the heat flux changes sign due to the second term on the right–face of (5.1)–top prevailing over the first one. Note that the prescribed electric flux is negative, according to the flux direction into the p–type TE. Again, case III is similar to case II and is not shown.

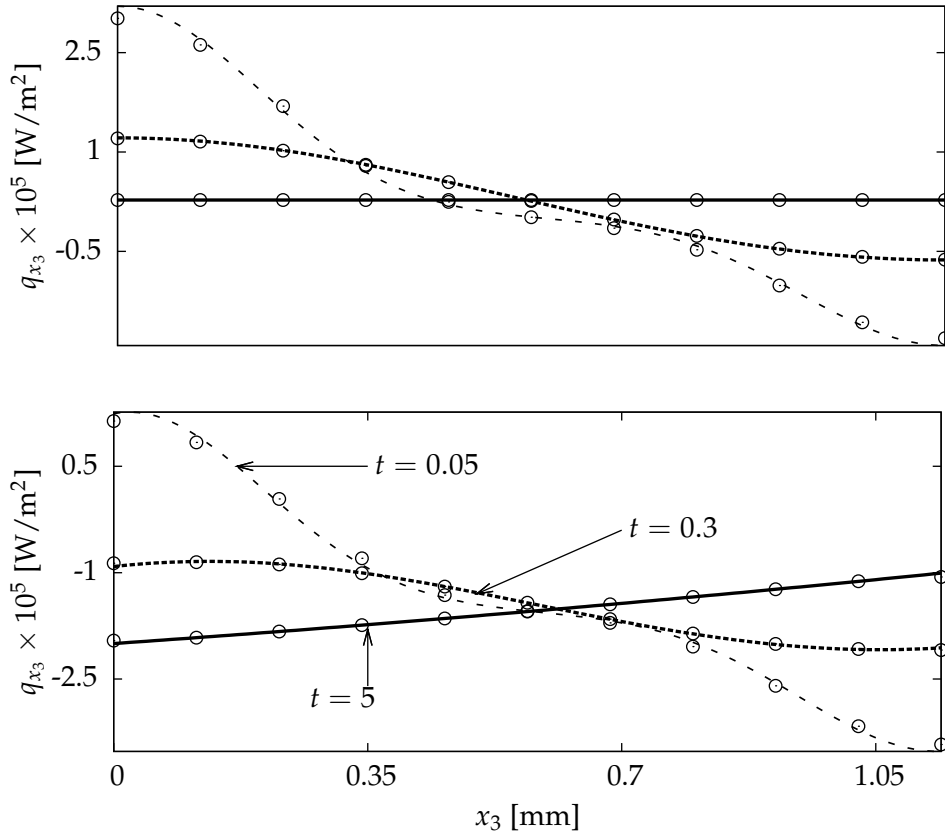


Figure 5.5: Thermal fluxes in cases I (top) and II (bottom) and for three times. Analytical results represented with different line types, finite element with circles.

### 5.3.3 Numerical solutions for case IV

Differences between the parabolic and the hyperbolic models appear in the early times where the voltage and temperature distributions appear as piecewise functions with sharp discontinuities near the edges. This occurs since both energies travel as finite velocity waves, see Figure 5.6. In addition, strong changes of temperature occur when discontinuous initial boundary conditions are used, inducing *Gibbs* phenomena. For larger times, the parabolic model dominates and, therefore, the numerical algorithm must be:

- ▷ robust and efficient to automatically solve both parabolic and hyperbolic models depending on the time instant
- ▷ able to have controllable numerical dissipation to mitigate the *Gibbs* phenomena

For a linear problem and according to Ciegis [2009], no numerical oscillations will appear if the dynamic algorithm is regularized by the relationship  $\Delta t \leq C h/v$ , where  $C$  is the Courant number, Courant et al. [2007], and  $v = \sqrt{\kappa/\rho c \tau_q}$ , the linear wave velocity. The cases considered in the present thesis are highly non-linear, therefore the spectrum of the algorithm is not evident enough for a good estimation of the ratio  $\Delta t/h$ . In the analyses a structured mesh of 200 elements ( $h = 8.1429 \times 10^{-6}$ ) in the  $x_3$  direction is used. Since a

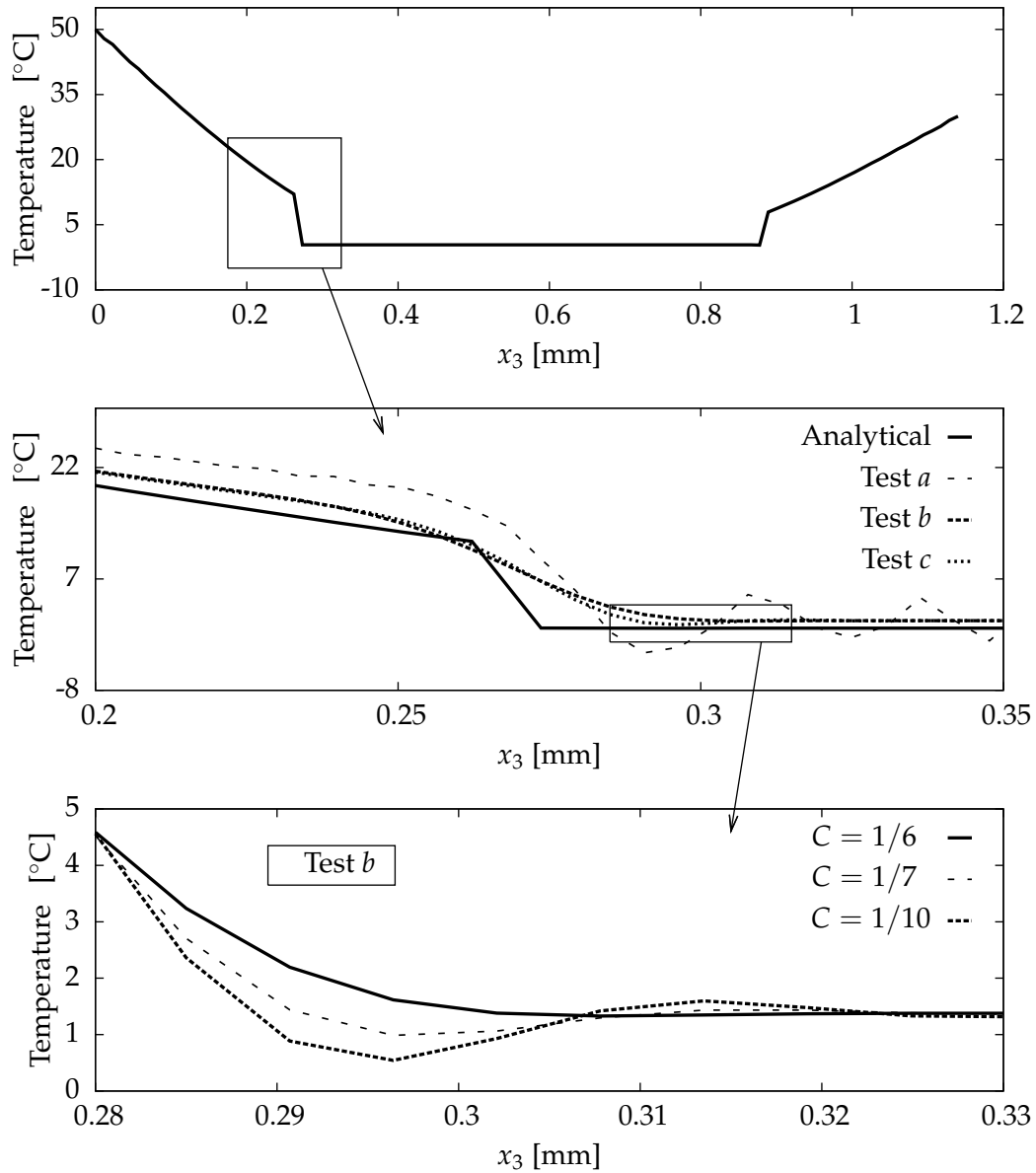


Figure 5.6: Analytical temperature solution for  $t = 0.06$ ,  $\tau_q = 0.02$  [s],  $C = 1/6$  (top). Different Newmark- $\beta$  and HHT parameters to study *Gibbs* phenomena (middle), see Table 5.2. Adjusting by trial and error the *Courant* number in Test b to avoid oscillations (bottom).

precise spectral analysis is not an objective of this thesis, a value  $C = 1/6$  is chosen, basing on a series of numerical tests. If smaller values of  $C$  (e.g.,  $1/10$  and consequently smaller  $\Delta t$ ) are used the oscillation appear again, as seen in Figure 5.6 (bottom). Larger values of  $C$  will artificially smear the distribution at the front itself.

In order to evaluate the performance of the time integration scheme, *Newmark- $\beta$*  and HHT algorithms are compared using parameters that produce different spectral radii  $\bar{\rho}$ , see Table 5.2 and Chapter 4.

Test	Algorithm	$\bar{\rho}$	$\bar{\beta}$	$\bar{\gamma}$	$\bar{\alpha}$
<i>a</i>	<i>Newmark-<math>\beta</math></i>	1	1/4	1/2	-
<i>b</i>	<i>Newmark-<math>\beta</math></i>	0	1	3/2	-
<i>c</i>	HHT	1/2	4/9	5/6	2/3

Table 5.2: *Newmark- $\beta$*  and HHT parameters used for the numerical testing

Figure 5.6 (top) shows temperature versus length  $x_3$  for an assumed  $\tau_q = 0.02$  (as in most of this section) at  $t = 0.06$ ; for shorter times the comparison analytical solution does not converge; the numerical one does although with increasing *Gibbs* noise. The analytical solution (solid line) and the FE (dashed) are obtained with *Newmark- $\beta$*  and HHT algorithms (these are unconditionally stable for the parameters tested when applied to linear problems).

For *Newmark- $\beta$* , the use of standard parameters (test *a*) results in numerical oscillations since this algorithm is non-dissipative. The HHT algorithm (test *c*) slightly oscillates due to its low numerical damping. Therefore, in the remainder of the present chapter the parameters of test *b* will be used, since according to Hughes [1987] this choice results in the highest numerical dissipation.

Figure 5.7 shows the voltage (top) and temperature (bottom) distributions along the TE at several instants of time. In the first, it can be observed the transition from very small times and hyperbolic solution to higher ones and parabolic, the last with almost linear distribution between boundary values. Note that in the curve for  $t = 0.06$  the electric wave fronts from left and right at around 0.28 and 0.8 [mm], with a non-linear distribution inside the wave and linear between the fronts. For  $t = 0.13$  the both waves almost collide at around 0.63 [mm], point shifted to the right. This is so since the temperature boundary condition is higher in the left: the energy and consequently velocity are also higher in the left wave.

In the temperature distribution a similar transition from hyperbolic to parabolic can be seen. The collision between the thermal waves is again clear for  $t = 0.13$  at the same TE point, a logical result since the thermal and electric waves are coupled. For  $t = 0.06$ , it can be appreciated that inside the wave zone the slope of the distribution is higher than

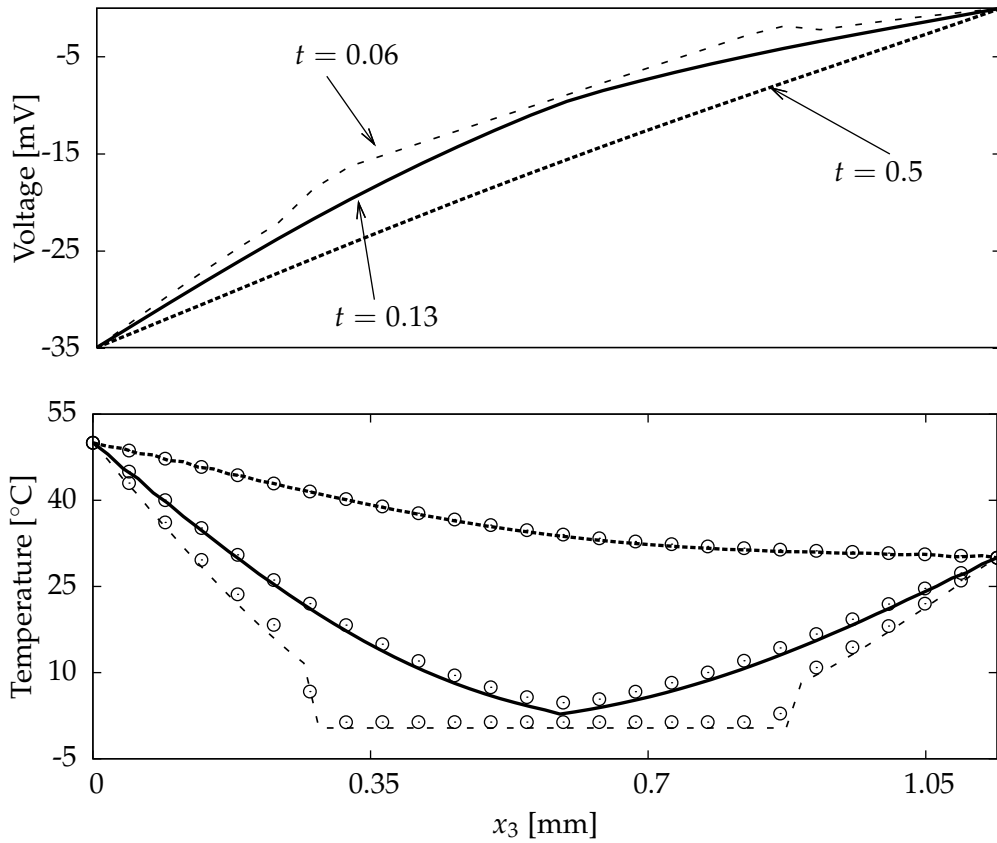


Figure 5.7: Voltage (top) and temperature (bottom) versus thermoelement length for several time instants. For voltage, only finite element results. For temperature, analytical results are shown with different line types and corresponding finite element results with circles.

the obtained with a parabolic model, with the consequence of a higher energy confined in a smaller volume. The agreement between analytical and numerical results is very good, except for a small region around the wave front at  $t = 0.06$ ; this is due to the intrinsic oscillations from the discrete time integration scheme and is very difficult to avoid.

Figure 5.8 compares the semi-analytical and FEM thermal fluxes for  $t = 0.06$ . Two peaks due to the discontinuous boundary conditions at the wave front are evident, representing the propagation of this wave. Even if a nil flux at the TE center could be expected, it has a constant negative value. The reason is found in (5.1)–top: the first right-term is zero due to a constant  $T$  distribution where the wave is not present (see Figure 5.7), distribution that is due to the electric coupling, see the last term in (5.1)–bottom. But the second term in (5.1)–top will be negative due to the prescribed  $j$ . The agreement is again very good, even at the peak maximums, although it has to be considered that both maximums can be affected by the respective choices of the numerical parameters.

As mentioned before, the behavior is hyperbolic in the initial instants and becomes parabolic later. This is clearly seen in Figure 5.9 (top), where the heat flux is plotted for several times. For  $t < 0.06$  the peaks described in the previous figure are visible, but for larger times they become smoother. At  $t = 0.13$  both waves collide, and after that the flux



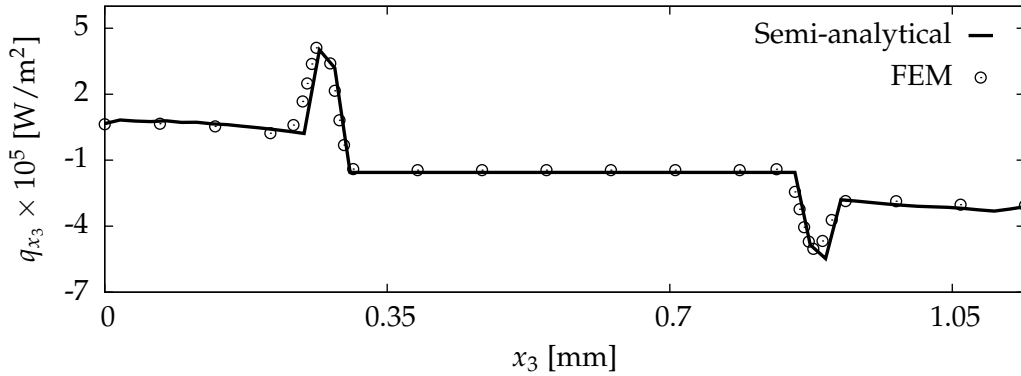


Figure 5.8: Thermal flux versus thermoelement length at  $t = 0.06$ . Semi-analytical result represented by solid line and finite element by circles.

will be linear as in Figure 5.5. The mathematical explanation of this attenuation can be seen in (5.1)–top: the last term on the left-hand side is hyperbolic and the first on the right-hand parabolic. In the initial instants the hyperbolic term is dominant; physically this can be interpreted as a ballistic motion of either electrons or holes. The wave is constantly attenuated up to a time in which the influence of the  $\tau_q$  terms vanish, and the first time derivative is the dominant term.

The last attenuation is obviously affected by the value of the constant  $\tau_q$ , see Figure 5.8 (bottom), where it can be seen that for larger  $\tau_q$  the behavior will be more hyperbolic (more difficult to simulate) and vice-versa. This figure is a test for the robustness of the finite element performance, but even for  $\tau_q = 0.06$  the simulation is satisfactory as long as the ratio  $\Delta t \leq Ch/v$  is used.

#### 5.4 A complete three-dimensional simulation

There are in the literature several studies aimed to the optimization of the TE geometry, see Hoyos et al. [1977] and Cheng and Lin [2005] and the following chapter for example. However, these studies use 1-D models (at most 2-D), not being able to observe 3-D effects. The aim of this section is to study the 3-D temperature propagation inside a TE by means of the hyperbolic model validated in the previous section. Note that the propagation of voltage is proportional to that of temperature through the thermoelectric interaction, and therefore will not be included here.

The function of a cooling thermoelectric device is to transport heat from the hot to the cold faces. As mentioned before, inside the device there are three heat fluxes (*Peltier*, *Joule*, *Fourier*), the first being the most interesting from a performance standpoint; *Joule* and *Fourier* fluxes are bulk effects while *Peltier* is a surface one. For this reason, Hoyos et al. [1977] recommends to optimize the TE geometry widening the hot face section, to increase the *Peltier* flux and thus the device performance.

To study the validity of this solution, this section analyzes a truncated pyramid TE, see Figure 5.10. Sections at hot and cold faces are 1.96 and 1.58 [mm<sup>2</sup>] respectively, the length

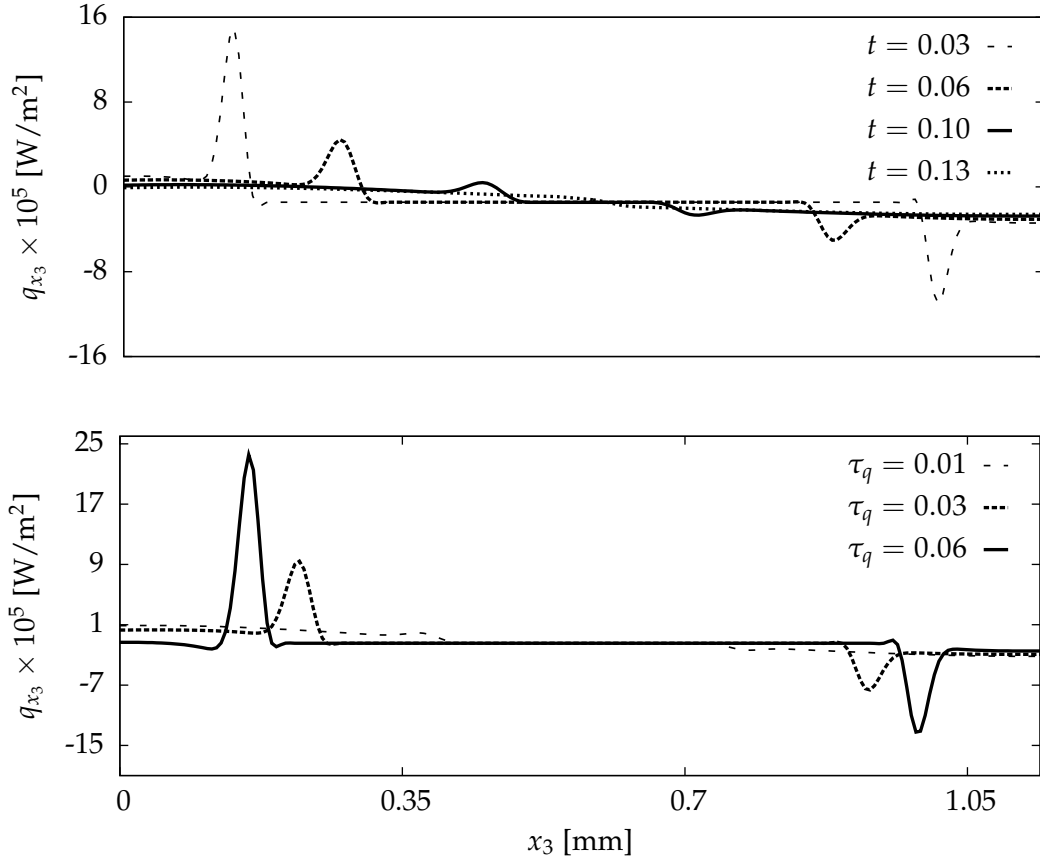


Figure 5.9: Thermal flux versus thermoelement length for several time instants with  $\tau_q = 0.02$  (top) and relaxation time influence in the wave shape (bottom) at  $t = 0.06$ . Only finite element results represented.

$L_{x_3} = 0.28$  [mm] and the prescribed vertical flux  $j_{x_3} = 2.65 \times 10^6$  [A/m<sup>2</sup>]. The temperatures at the hot and cold faces are fixed to  $T_h = 50$ ,  $T_c = 30$  [°C], respectively. Initially ( $t = 0$ ), the temperature is  $T_0 = 0$  [°C] everywhere. From an FE point of view, the element sizes and time steps are the ones optimized in the previous section.

Figure 5.11 shows the temperature propagation using the parabolic (left,  $\tau_q = 0$ ) and hyperbolic (right,  $\tau_q = 0.02$  [s]) models for four representative instants. The temperature propagation velocity is larger from the hot face than that from the cold, since in the former the prescribed temperature and the area are both larger and therefore the applied energy is higher.

There are significant differences between both models. For parabolic, a temperature diffusion from hot to cold faces is observed that could easily be simulated by a 1-D model, except for small, non-relevant variations at the edges. For hyperbolic, many non-uniformities at several sections are observed, requiring a 3-D model. The main differences between both models are:

- ▷ At initial  $t = 7.74 \times 10^{-3}$  [s]. For parabolic, the velocity of propagation is infinite, instantly increasing temperature by 3.47 [°C] in all the domain except the faces. In

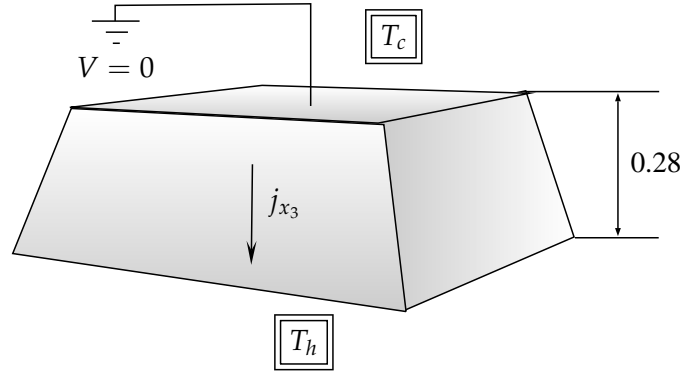


Figure 5.10: Truncated pyramid thermoelement dimensions for three-dimensional simulation. At hot face, surface  $1.96 \text{ [mm}^2\text{]}$  and  $T_h = 50 \text{ [}^\circ\text{C]}$ ; at cold  $1.58$ ,  $T_c = 30$  with constant prescribed vertical flux  $j_{x_3} = 2.65 \times 10^6 \text{ [A/m}^2\text{]}$ .

addition, the vertical distribution is linear and constant at every section. For hyperbolic, the wavefront increases the temperature only in the wave front, while the rest of the domain stays at the initial  $T_0$ . Furthermore, temperature at the inclined edges increases due to wave reflection at these edges, reaching a value of  $53.3 \text{ [}^\circ\text{C]}$ . This increase will reduce the performance of the truncated geometry TE

- ▷ At medium  $t = 3.44 \times 10^{-2} \text{ [s]}$ . For parabolic, the lower half increases its temperature and the rest reaches  $25 \text{ [}^\circ\text{C]}$  all due to thermal conduction. The vertical distribution is still constant at every section, except near the edges where concentrations occur. For hyperbolic, the wavefront from the hot face progresses upwards to more than half the TE, while the wavefront from the cold face does only one quarter. At this instant, the edge overheating is progressing with the front, and it also extends across the bottom of the TE due to the constant supply of energy. In the rest of the front section the temperature decreases to fulfill the conservation of total energy
- ▷ At medium  $t = 6.51 \times 10^{-2} \text{ [s]}$ . For parabolic, the system has clearly reached the steady-state with an almost linear distribution between  $T_h$  and  $T_c$ . For hyperbolic, both wavefronts have already met. The concentration at the edges is now more evident, due to the multiple bounces that occur in the inclined edge
- ▷ For larger times and hyperbolic model, the wavefront reflected at the cold face returns to the hot one, reaching the steady-state temperature distribution, that as expected is similar to that predicted by the parabolic

Although the geometry of this example is meso, these results could be relevant in the design and optimization of thermoelectric micro-devices under fast operation modes. For instance, an electron-phonon thermal mismatch due to different thermal and electrical carriers was reported in da Silva and Kaviany [2004] for cooling micro-thermoelectrics. This

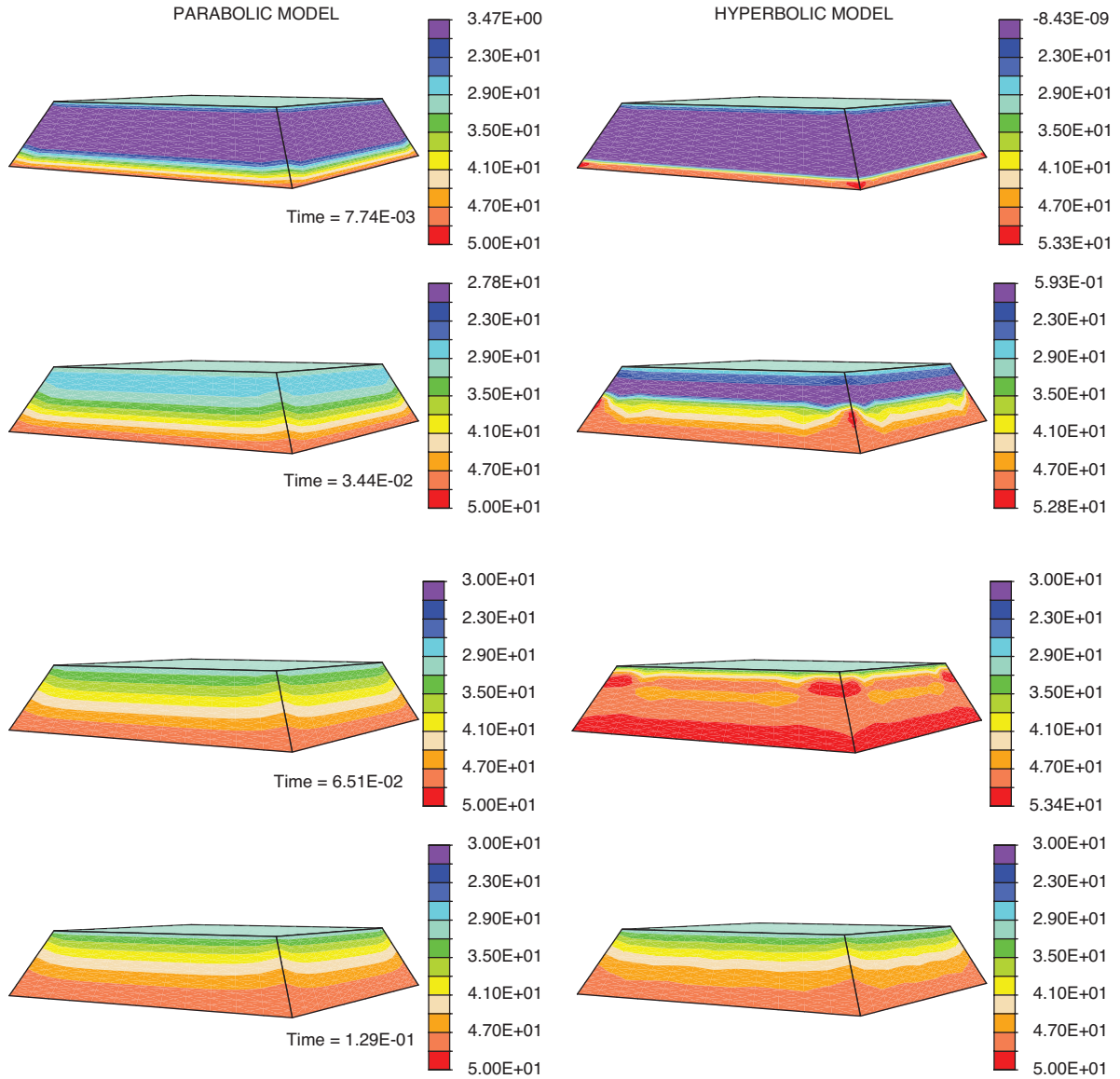


Figure 5.11: Temperature distribution inside the truncated pyramid thermoelment for the parabolic (left) and hyperbolic (right) models and for several time instants. For parabolic model  $\tau_q = 0$ , for hyperbolic  $\tau_q = 0.02$  [s] are assumed. Boundary conditions and geometry shown in Figure 5.10.

non-equilibrium has until now been modeled by molecular dynamics or Monte Carlo techniques; however, the present combined parabolic-hyperbolic model could simulate these effects through the introduction of the empirical values of relaxation times.

## 5.5 Conclusions

This chapter has presented a non-linear and transient finite element formulation to simulate thermoelectric interactions under hyperbolic model or second sound.

Numerically, non-linearities and transient hyperbolicity have been addressed by *Newton-Rhaphson* and by *Newmark- $\beta$*  and HHT algorithms, respectively. Analytically, four 1-D solutions have been obtained to validate the finite element results; the first three solve parabolic problems and both result types agree very well, using standard parameters of *Newmark- $\beta$* .

The fourth validation consists of a hyperbolic problem with discontinuous initial boundary conditions. In this example, voltage and temperature distributions present sharp discontinuities, and the numerical results numerical oscillations. To mitigate this *Gibbs* phenomena three numerical test have been developed: *Newmark- $\beta$*  with standard parameters, HHT and *Newmark- $\beta$*  with  $\bar{\beta} = 1$ ,  $\bar{\gamma} = 3/2$ . The last test provides the best results since this parametrization gives the highest numerical dissipation. In addition, the time steps and element sizes have been regularized using a linear relationship with a *Courant* number  $C = 1/6$ . This  $C$  has been chosen by means of trial and error, since the problem is highly non-linear and a spectral analysis is not one of the thesis objectives.

Physically, the obtained results show a wave propagation of temperature, of thermal flux and of voltage (due to the thermoelectric coupling). This numerical tool can be applied to the design of micro-devices for novel applications with fast processes, where the second sound effect could be relevant.

To steal ideas from one person is plagiarism, to steal ideas from many is research.

Anonymous

# 6

## Elasto–thermoelectric interactions



Thermoelectric materials submitted to electric pulses are denominated Pulsed Thermoelectric (PT). PT's enhance the cooling power since the *Joule* heat takes a longer time to reach the cold face than the *Peltier* one, reducing the minimum temperature respects to those obtained in steady–state situations. Note that the *Peltier* and *Joule* effects are surface (concentrated at the junctions) and bulk effects (distributed throughout the TE volume), respectively.

PT's are applied in electronic devices that need to be cold for a short interval of time. For example, they are included in laser gas sensor (Figure 6.1) that are used in compliance monitoring and process control.

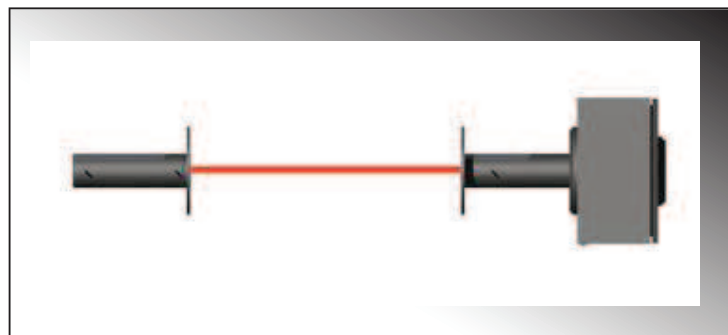


Figure 6.1: Pulsed thermoelectrics are included in electronic devices such as the gas sensor, shown in this figure. Picture taken from <http://www.tdlsensors.co.uk>.

The first study on PT's was developed by Stilbans and Fedorovich [1958]. At present, there are many experimental, analytical and numerical works in the literature. For example, experimental investigations were developed in Buist and Lau [1996] and Snyder et al. [2002]. Analytically, the pulse shape effects on the cooling power were studied in Landecker and Findlay [1961] considering constant material properties. In addition, a temperature–entropy diagram based on thermodynamic considerations was developed in Chakraborty and Ng [2006b]. Numerically, the influence of the pulse shape and of the TE length on the PT variables was studied in Thonhauser and Mahan [2004] and Yang et al. [2005], respectively. In the first work, a commercial FE software that uses constant material properties (avoiding the *Thomson* effect) was utilized; in the second, the finite difference method was employed. Furthermore, elasto–thermoelectric interactions in TE's have been addressed using commercial FE softwares: ANSYS (Huang et al. [2008], Clin et al. [2009] and Gao et al. [2011]) and COMSOL (Jaegle et al. [2008], Jaegle et al. [2008]). However, these works study TE's in steady–state situations: works on elasto–thermoelectric interactions in PT's have not been developed.

In the present chapter a PT is modeled by the multi–coupled FE to study the influence of geometry, of pulse shapes and of relaxation times on the PT variables. In addition, the mechanical responses of the PT's due to the thermal stresses are also addressed.

Section 6.1 describes the experimental study developed by Snyder et al. [2002]. Section 6.2 extracts the elasto–thermoelectric assembled FE matrix from the multi–coupled one (4.28). Finally, Sections 6.3 and 6.4 show the numerical results and the conclusions, respectively.

## 6.1 Experimental procedure

An experimental study for the determination of the main variables involved in the operation of a PT was developed in Snyder et al. [2002], investigating the responses of a thermocouple under applied square pulses of electric current. The thermocouple consists of two (n–Bi<sub>2</sub>Te<sub>2.85</sub>Se<sub>0.15</sub> and p–Bi<sub>0.4</sub>Sb<sub>1.6</sub>) TE's and of two copper foils. Figure 6.2 shows the main PT variables, which are defined in the following items:

- ▷  $I_{app}^{max}$  is the applied electric current to obtain a maximum cooling under steady–state situations
- ▷  $I_{app} = P I_{app}^{max}$  is the applied electric current
- ▷  $P$  is the amplification factor of the pulse
- ▷  $t_p$  is the pulse duration
- ▷  $\Delta T_{max} = T_h - T_c$  is the maximum temperature difference reached in steady–state
- ▷  $\Delta T_p$  is the maximum “transient” temperature difference reached at  $t_{min}$  due to the presence of the electric pulse

▷  $\Delta T_{pp}$  is the maximum post-pulse temperature difference

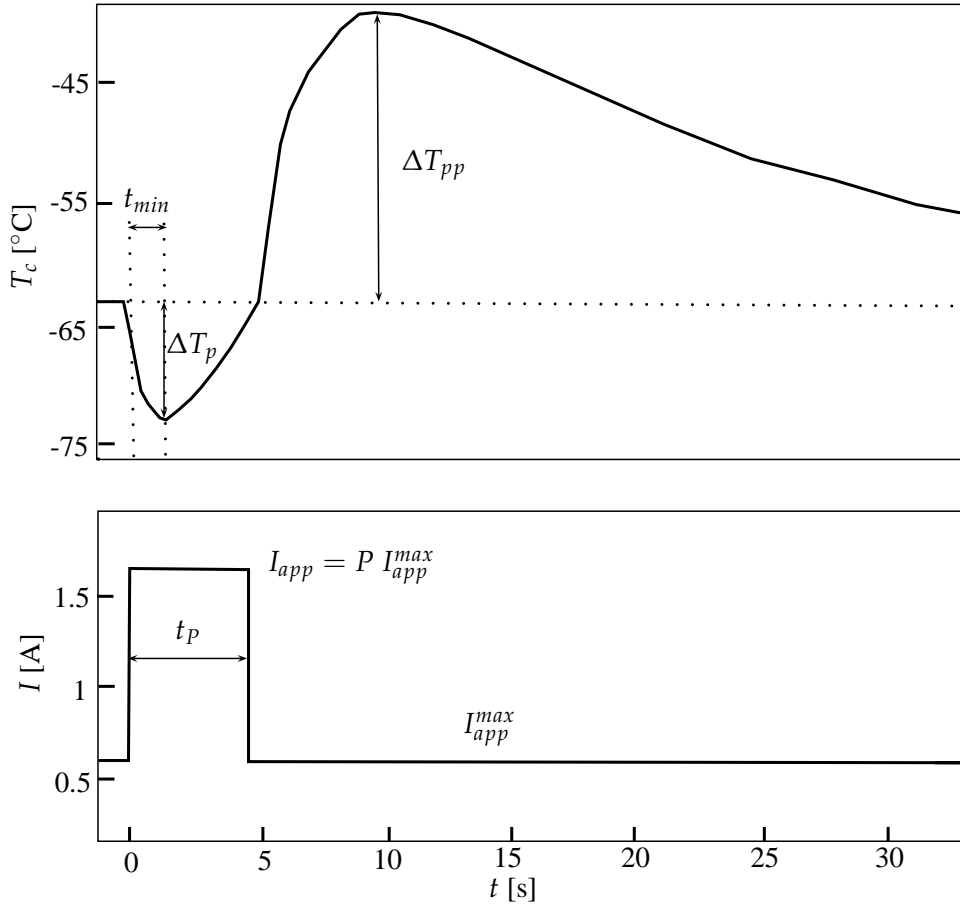


Figure 6.2: Main variables involved in a pulsed thermoelectric. Measured temperature at the cold face (top) and applied electric pulse (bottom) versus time for the experiment developed in Snyder et al. [2002].

The experiment developed in Snyder et al. [2002] consists of three steps, see Figure 6.2 (bottom):

- i) For each TE type, the  $I_{app}^{max}$  is determined representing the temperature at the cold face versus the applied current
- ii)  $I_{app}^{max}$  is applied to reach the steady-state situation
- iii) When the steady-state is achieved, a square pulse  $I_{app} = P I_{app}^{max}$  is applied

Figure 6.2 (top) shows the evolution of the temperature at the cold face. Starting from the steady-state temperature, the current pulse  $I_{app} = P I_{app}^{max}$  ( $P = 2.5$ ) is applied at  $t = 0$ . The maximum temperature difference  $\Delta T_p$  is reached at  $t_{min}$ . When  $I_{app} = I_{app}^{max}$  again, the temperature at the cold face is warmed up to  $\Delta T_{pp}$ . Finally, the steady-state temperature is recovered approximately at  $t = 60$  [s].



This experiment were repeated several times, characterizing  $\Delta T_p$  by means of the following empirical relationship:

$$\Delta T_p = \frac{\Delta T_{max}}{4} \left(1 - e^{1-p}\right) \quad (6.1)$$

where  $\Delta T_{max}$  depends on  $\alpha$ ,  $\gamma$  and  $\kappa$ .

## 6.2 Finite element equations

Five degrees of freedom are required to study elasto–thermoelectric interactions: three displacements, temperature and voltage. Therefore and from (4.28) the assembled matrix is:

$$\begin{bmatrix} c_1 \mathcal{K}^{uu} + c_3 \mathcal{M}^{uu} & c_1 \mathcal{K}^{ut} & c_1 \mathcal{K}^{uv} \\ c_2 \mathcal{C}^{tu} + c_3 \mathcal{M}^{tu} & c_1 \mathcal{K}^{tt} + c_2 \mathcal{C}^{tt} + c_3 \mathcal{M}^{tt} & c_1 \mathcal{K}^{tv} + c_2 \mathcal{C}^{tv} \\ \mathbf{0} & c_1 \mathcal{K}^{vt} + c_2 \mathcal{C}^{vt} & c_1 \mathcal{K}^{vv} \end{bmatrix} \quad (6.2)$$

The time–integration algorithm is regularized to avoid *Gibbs* phenomena by means of the procedure described in Chapter 5.

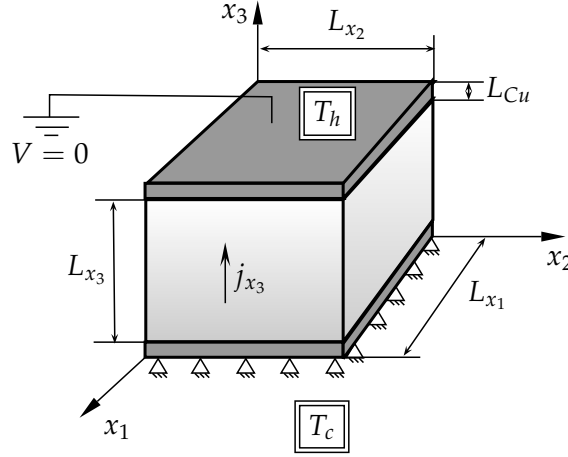


Figure 6.3: Model and boundary conditions used to simulate a pulsed thermoelectric. Only a thermoelement is used to reduce the calculation time.

## 6.3 Numerical results

The aim of the present section is to simulate the experimental procedure described in Section 6.1. For this purpose, the FE model, see Figure 6.3, consists of a p– $\text{Bi}_2\text{Te}_3$  TE, which dimensions are  $L_{x_1} = L_{x_2} = 1$ ,  $L_{x_3} = 5.8$  [mm], and of two cooper foils of thickness  $25$  [ $\mu\text{m}$ ]. Mechanical and thermal material properties are given in the Appendix B. Note that the properties of the TE are different from that used in the experiment, since there are no temperature–dependent properties available in the literature for n– $\text{Bi}_2\text{Te}_{2.85}\text{Se}_{0.15}$  or p– $\text{Bi}_{0.4}\text{Sb}_{1.6}$  semiconductors. Furthermore, only a TE is modeled to reduce the calculation time.

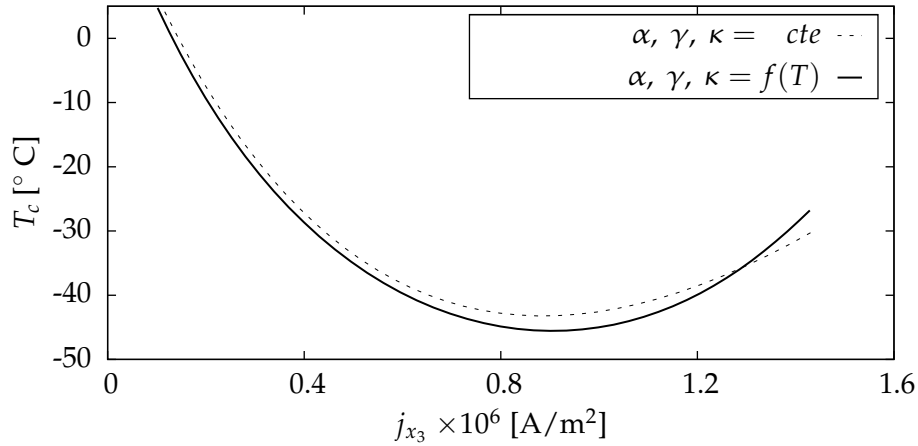


Figure 6.4: Temperature at the cold face versus prescribed electric flux for the determination of the electric current for maximum cooling under steady-state situations. Two simulations are represented considering constant and variable properties. Only finite element results are shown.

From a simulation point of view, the mesh consists of 1000 elements and the boundary conditions are:  $V = 0$  [V],  $T_h = 25$  [°C] at the hot face and the sample is mechanically attached at the cold face. For the calculation of the thermal stresses, the reference temperature is set to be  $T_0 = 25$  [°C]. In addition, two simulations are performed considering variable (temperature-dependent) and constant thermoelectric properties. The last are obtained by the procedure described in the Chapter 5 and the Appendix B. The following studies are performed:

- ▷ Calculation of the electric current that permits a maximum cooling in steady-state
- ▷ Calculation of the maximum transient temperature difference
- ▷ Effects of the pulse shape on the PT variables
- ▷ Effects of the TE geometry on the PT variables
- ▷ Effects of the relaxation time  $\tau_{qj}$  on the PT variables

### 6.3.1 Electric current for maximum cooling

The first step for the simulation of the experiment is to find  $I_{app}^{max}$  by mean of the procedure described in Snyder et al. [2002]. The applied electric current is numerically prescribed applying an electric flux  $j_{x_3}$  using the special interface element developed in the Chapter 4.

Figure 6.4 shows the results considering constant and variable properties. The maximum currents are those that minimize the temperature at the cold face:  $I_{app}^{max} = 0.87, 0.9$  [A] for constant and variable properties, respectively. Therefore, a difference of approximately 3% between both results is achieved. Temperature at the cold face is lower with variable properties since the fraction of both *Fourier* and *Joule* heating is reduced by the *Thomson* effect. These results agree with those reported in Huang et al. [2005].

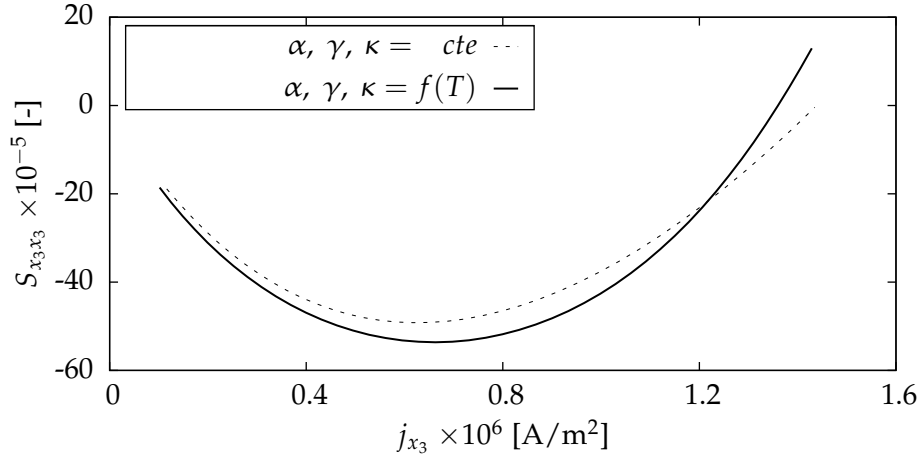


Figure 6.5: Strain along vertical  $x_3$  direction versus applied electric flux. Two simulations are represented considering constant and variable properties. Only finite element results are shown.

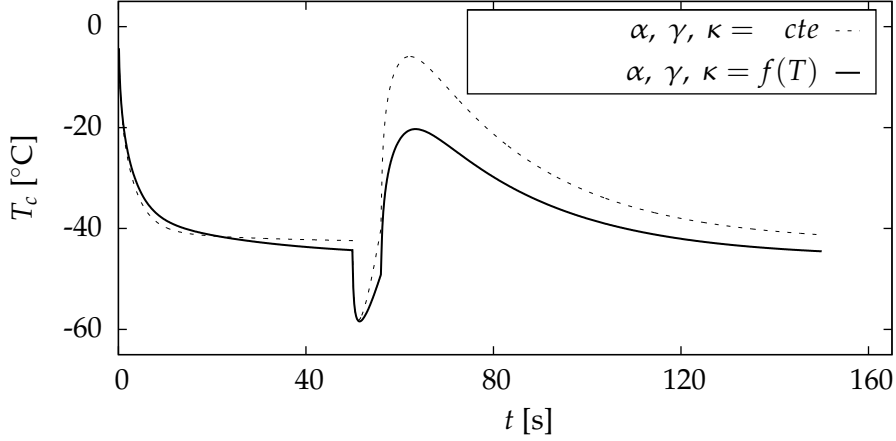


Figure 6.6: Evolution of the temperature at the cold face when a square pulse of electric current is prescribed. Temperature at the hot face is fixed to be  $T_h = 25$  [°C]. Two simulations are represented considering constant and variable properties. Only finite element results.

For the study of the thermal stresses along the vertical  $x_3$  direction, the strain  $S_{x_3x_3}$  is represented versus the applied electric flux  $j_{x_3}$  in Figure 6.5. Again, constant and variable properties are considered. For low fluxes, the thermoelectric is contracted due to its cooling mode; for high fluxes, it is expanded (heating mode). In addition, the electric current that minimize  $S_{x_3x_3}$  and  $T_c$  does not coincide since the strain is proportional to  $(T_0 - T_c)$ .

### 6.3.2 Maximum transient temperature difference

The second step consists of the simulation of the experimental results shown in Figure 6.2. For this purpose, the temperature at the hot face  $T_h = 25$  [°C] is fixed and the maximum applied electric current ( $I_{app}^{max} = 0.87$  or  $I_{app}^{max} = 0.9$  [A], for constant or variable properties, respectively) at  $t = 0$  is prescribed. The steady-state is reached at  $t \approx 50$  [s]. At this moment, an square pulse of  $I_{app} = 2.5 I_{app}^{max}$  and of  $t_p = 6$  [s] is prescribed.

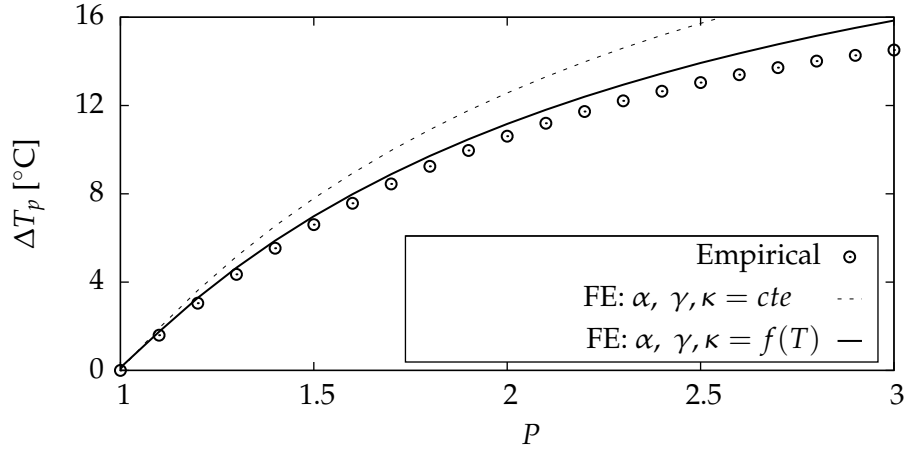


Figure 6.7: Maximum transient temperature difference versus pulse amplification. Finite element results using constant and variables properties (circles) and empirical ones (lines) are compared.

Figure 6.6 shows the evolution of the temperature at the cold face using variable and constant properties. A similar evolution was experimentally observed in Snyder et al. [2002], see Figure 6.2. For constant and variable properties,  $\Delta T_p$  (3% of difference) and  $t_{min} \approx 51.2$  [s] are very similar. However, about a 70% of relative error is found in  $\Delta T_{pp}$  due to the presence of the *Thomson* effect when variable properties are considered. Note that the *Joule* effect is reduced by the *Thomson* one. Finally, the steady-state is reached at  $t \approx 180$  [s].

In order to study the differences between constant and variable properties, Figure 6.7 compares the FE results for both types of properties with the empirical results obtained by Snyder et al. [2002] and given in (6.1). Note that according to Snyder et al. [2002], the empirical results are only applicable for  $P < 3$  due to the high standard deviations achieved in the measurements for higher values of  $P$ . The maximum transient temperature versus the amplification factor is represented in Figure 6.7, observing that FE results with variable properties agree best than the ones with constant properties. Therefore, variable properties are used in the remainder of the present chapter.

The electric pulse influence on the elastic response of the TE is studied in the Figures 6.8 and 6.9. Figure 6.8 shows the strain along the vertical direction  $x_3$  versus the time  $t$  for the case with variable properties represented in Figure 6.6. Four stages can be distinguished:

- I. From  $t = 0$  to  $t = 50$  [s], the TE is compressed since it is working in cooling mode
- II. From  $t = 50$  to  $t = 56$  [s] (pulse duration), it is compressed even more
- III. At  $t = 56$  [s], the TE quickly begins to expand due to the overheating  $\Delta T_{pp}$
- IV. At  $t > 56$  [s], the TE is compressed until the steady-state is reached

Figure 6.9 shows the stress distribution along  $x_3$  at  $t = 56$  [s]. At this time, the maximum stress reaches a value of 23.8 [MPa] due to the  $\Delta T_{pp}$ . This maximum stress will increase with

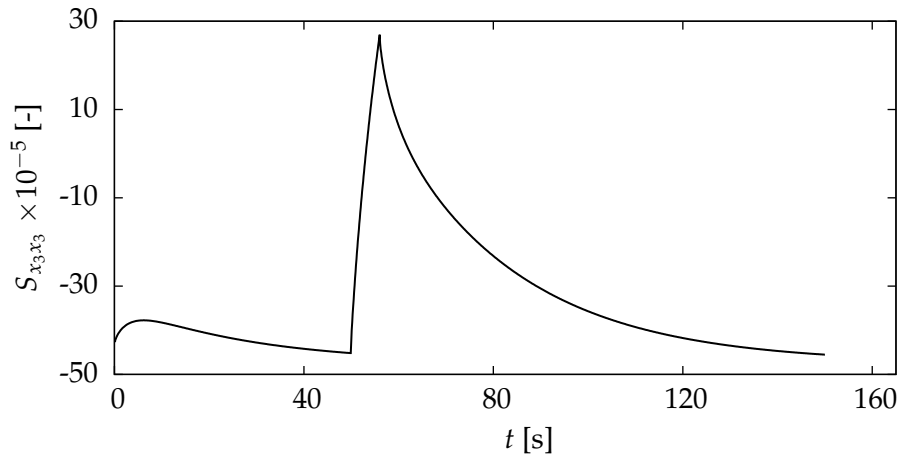


Figure 6.8: Electric pulse influence on elastic response of a thermoelement: strain along vertical  $x_3$  direction versus time. Only finite element results are shown.

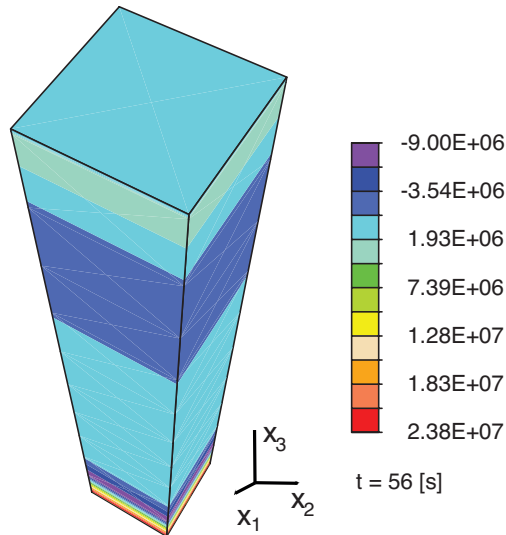


Figure 6.9: Stress distribution along  $x_3$  direction inside the thermoelement at  $t = 56$  [s]. At this time instant, the maximum stress is reached since the maximum post-pulse temperature is achieved.

the increasing of the amplification factor. Therefore, an elastic study must be performed since the thermoelectric materials have a low mechanical strength, see Gao et al. [2011].

### 6.3.3 Effects of the pulse shape on the pulsed thermoelectric variables

The study of the influence of the pulse shape on the PT variables could be considered as a starting point for the PT's optimization.

Again, the FE model is that given in Figure 6.3:  $T_h = 25$  [°C],  $P = 2.5$ . Now, the pulse duration is  $t_p = 2$  [s] and variable properties are only considered. Four different shapes of the electric current pulse are studied, which are shown in Figure 6.10 (bottom):  $t^0$ ,  $t^{-3}$ ,  $t^1$  and  $t^3$ .

Figure 6.10 (top) shows the temperature at the cold face versus the time. According to the results reported in Thonhauser and Mahan [2004],  $\Delta T_p$  increases and  $\Delta T_{pp}$  decreases

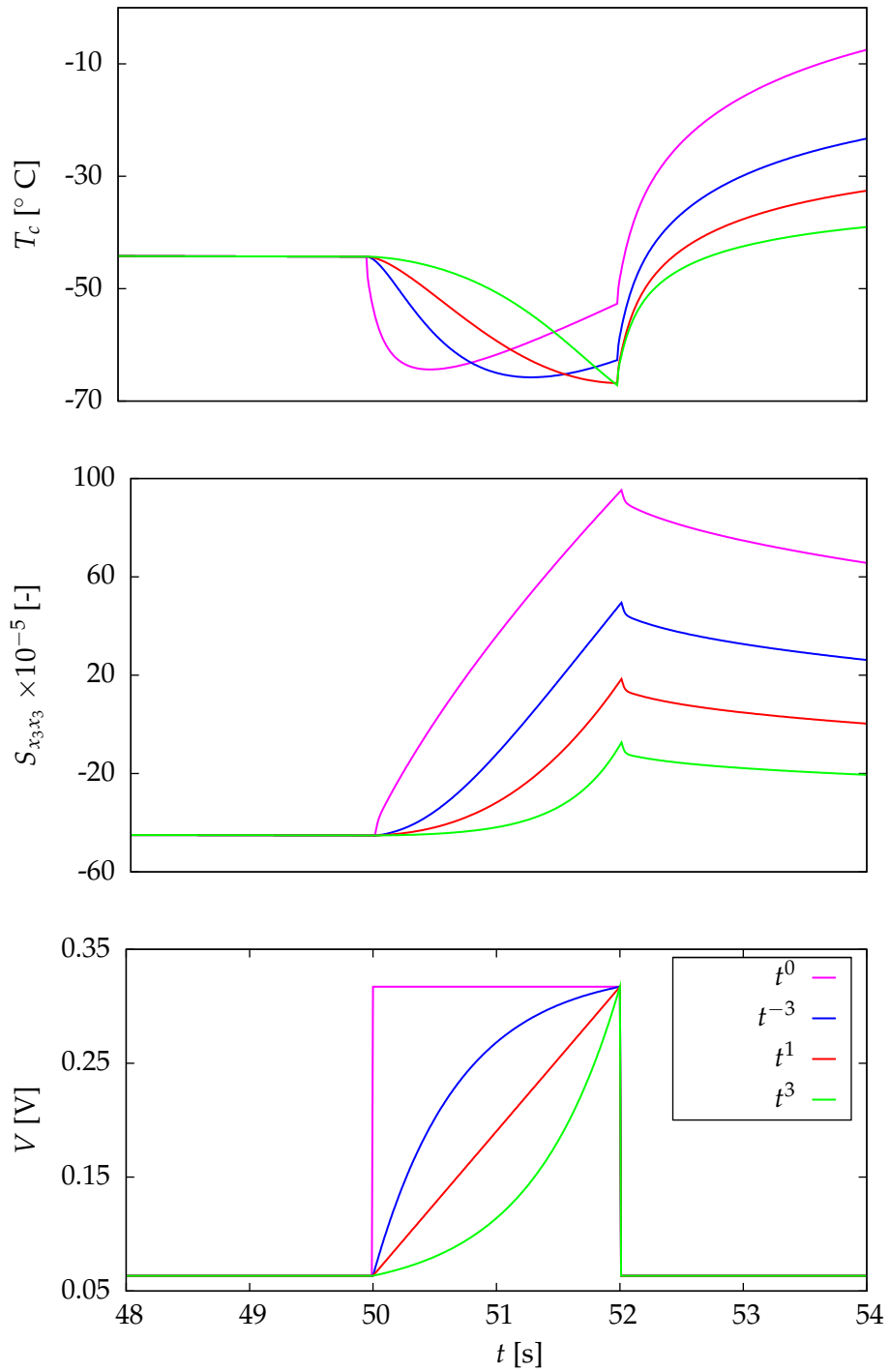


Figure 6.10: Effects of different current pulse shapes on pulsed thermoelectric variables. Temperature at the cold face (top), strain along vertical direction  $x_3$  (middle) and applied voltage (bottom) versus time. Only finite element results using variable properties are shown.

from  $t^0$  to  $t^3$ . In addition, the required time to reach the steady-state decreases from  $t^0$  to  $t^3$ , since the energy (proportional to pulse area) supplied to the TE decreases. Mechanically, the strain decreases from  $t^0$  to  $t^3$ , see Figure 6.10 (middle), since it is proportional to the temperature. Therefore, the optimal pulse is  $t^3$ , since  $\Delta T_p$  is maximum and  $\Delta T_{pp}$  minimum.

The holding time, which is defined as the time to remain at minimum temperature, is greater for  $t^{-3}$  due to the spatial difference between the *Peltier* and *Joule* effects.

#### 6.3.4 Effect of the thermoelement geometry on the pulsed thermoelectric variables

The influence of TE length  $L_{x_3}$  on the PT variables was studied in Yang et al. [2005] using the finite difference method, reporting that  $\Delta T_{max}$  does not depend on  $L_{x_3}$ . However, the influence of  $L_{x_1}$  or  $L_{x_2}$  have not been studied since, probably, most of the numerical studies are one-dimensional (an axisymmetric model is studied in Yang et al. [2005]). In this section, the 3-D influence is studied since the *Peltier* and *Joule* effects strongly depend on the geometry. For this purpose, three different geometries are tested, considering  $L_{x_3} = 5.8 \times 10^{-3}$ ,  $L_{x_1} = 1 \times 10^{-3}$  [m] and modifying  $L_{x_2}$ . The three tests A), B) and C) are shown in Figure 6.11.

Test	Electric current for maximum cooling [A]
A)	0.9
B)	0.32
C)	1.25

Table 6.1: Dependency of the geometry on the electric current for maximum cooling. Test notation is given in Figure 6.11.

From a numerical point of view, a square pulse with  $t_p = 6$  [s] and  $P = 2.5$  is used.  $I_{app}^{max}$  is calculated for each geometry by the procedure described in the previous section. Results are shown in Table 6.1: the test B) holds the lower intensity, which is applied for all the tests in order to prevent alterations in the comparisons. Again, variable properties are only considered.

Figure 6.12 shows the temperature at the cold face  $T_c$  (top) and the strain along the vertical direction  $S_{x_3x_3}$  (bottom) versus the time for the three geometries shown in Figure 6.11. Several observations:

- ▷ The A) geometry exhibits a intermediate behavior between B) and C)
- ▷ The minimum  $\Delta T_p$  is achieved for the B) geometry. This result agrees with the experimental one observed in Hoyos et al. [1977]

▷ The maximum holding time is given for C)

These results are due to the competition between the *Joule* heats: on one hand, the *Joule* heat tends to go to the regions of largest area; on the other, more *Joule* heat is generated at regions of smaller area.

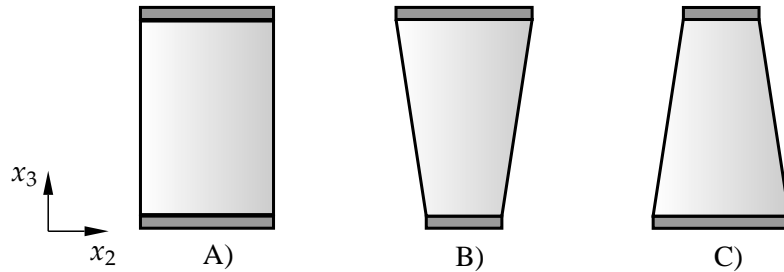


Figure 6.11: Three different geometries used to study the influence of thermoelement shape on pulsed thermoelectric variables.

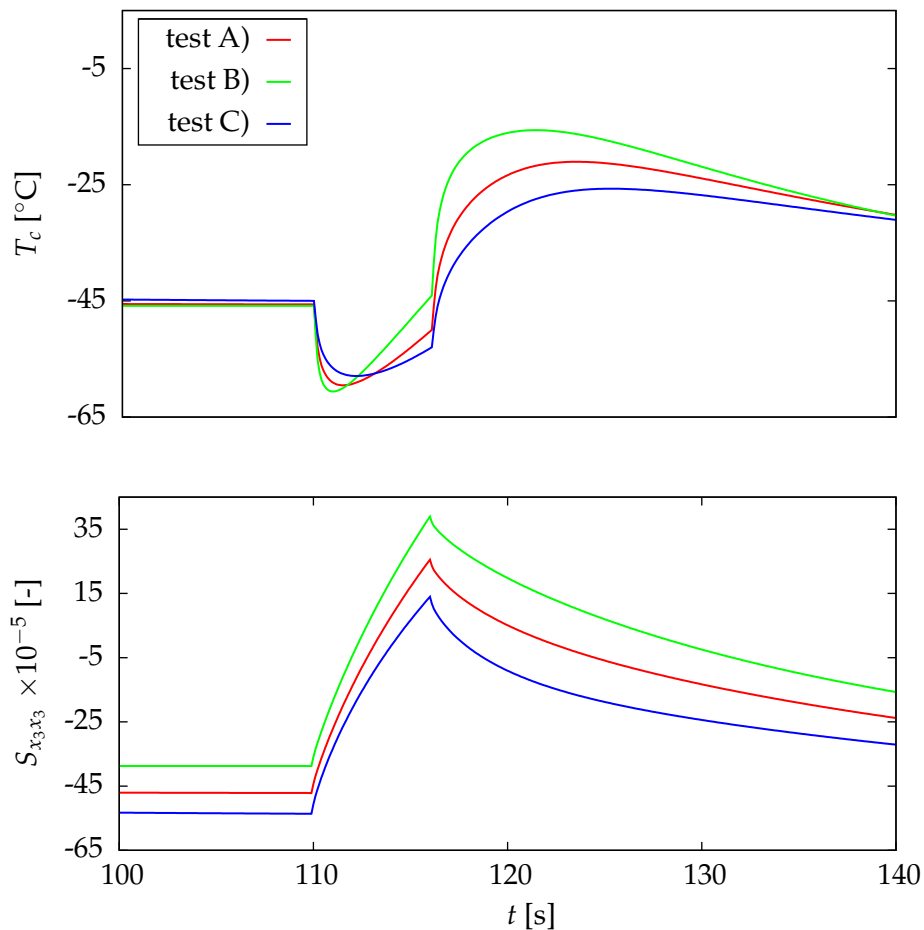


Figure 6.12: Temperature at the cold face (top) and strain along vertical direction  $x_3$  (bottom) versus time for the three geometries shown in Figure 6.11. For all the geometries the same square pulse of electric current is applied. Only finite element results using variable properties are shown.



### 6.3.5 Effect of the relaxation time on the pulsed thermoelectric variables

The purpose of this section is to study the influence of the relaxation time  $\tau_{qj}$  on the pulsed thermoelectric variables  $\Delta T_p$  and  $\Delta T_{pp}$ . From the governing equations for non-equilibrium interactions (3.20), (3.24), (3.25), assuming  $\tau_q = 0$ ,  $\mathbf{q} = \dot{\mathbf{Q}} = \mathbf{0}$  and for the configuration given in Figure 6.3, the relationship between temperature and voltage differences is:

$$\Delta T = \frac{\alpha \gamma T}{\kappa + \alpha^2 \gamma T} (\Delta V + \tau_{qj} \Delta \dot{V}) \quad (6.3)$$

Therefore, the ENET introduces a new term that is closely related to the relaxation time  $\tau_{qj}$ . In addition, the prescribed electric current must be satisfy  $\Delta \dot{V} \neq 0$ .

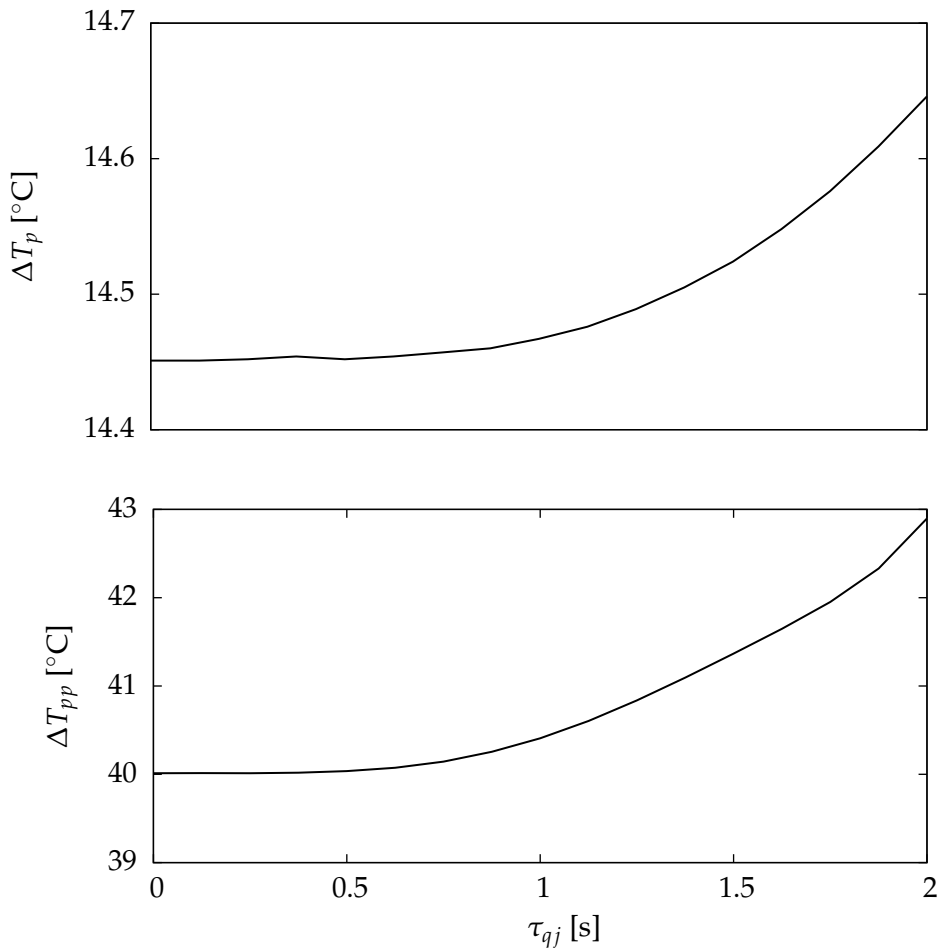


Figure 6.13: Maximum transient (top) and post-pulse (bottom) temperature differences versus the relaxation time  $\tau_{qj}$ . Only finite element results using variable properties are shown.

A  $t^3$  pulse type as that shown in Figure 6.10 (bottom) is prescribed in order to study the influence of  $\tau_{qj}$  on  $\Delta T_p$  and  $\Delta T_{pp}$ . Note that this pulse satisfy the requirement  $\Delta \dot{V} \neq 0$ . From a numerical point of view, the time integration algorithm must be regularized by the procedure described in Chapter 5 to obtain accurate results. Again, variable properties are only considered.

Figure 6.13 shows the maximum transient (top) and post-pulse (bottom) temperature differences versus the relaxation time  $\tau_{qj}$ . Both temperature differences increase with increasing  $\tau_{qj}$ . In addition, a cubic dependency is obtained fitting these curves, which corresponds to the type of applied pulse. For instance, the temperature at the cold face decreases 0.2 [°C] with  $\tau_{qj} = 2$  respects to those obtained with  $\tau_{qj} = 0$ . However, a detrimental result is obtained since  $\Delta T_{pp}$  increases approximately 2 [°C]. The holding time and  $t_{min}$  do not depend on  $\tau_{qj}$ .

In conclusion, the temperature at the cold face can be decreased applying pulses with strong slope and considering the relaxation time  $\tau_{qj}$ . This decreasing could be higher in microelectronic devices for which the relaxation times are more significative according to da Silva and Kaviany [2004].

## 6.4 Conclusions

In the present chapter, the multi-coupled finite element has been used to study the elasto-thermoelectric interactions in pulsed thermoelectric devices. This study can be understood as a first step for an optimization of these devices since it has been taken into account the pulse shape, the thermoelement geometry and the relaxation times. Several conclusions have been stated:

- ▷ The temperature dependence of the thermoelectric properties must be considered in the simulations since the *Thomson* effect reduces the overheating. For this reason, the numerical and experimental results agree better with variable than with constant properties
- ▷ The electric pulse causes high thermal stresses due to the overheating. Therefore, thermal stresses must be considered in the design of pulsed thermoelectric devices since thermoelectric materials have a low mechanical strength
- ▷ The shape of the electric pulse could improve the efficiency of these pulsed devices, increasing the maximum transient temperature and decreasing the maximum post-pulse differences. In addition, the geometry of the thermoelement also influences on the efficiency
- ▷ The performance of these pulsed devices depends on the relaxation time  $\tau_{qj}$  and the slope of the applied pulse. Note that the relaxation time could be an important variable to optimize in micro-devices



*There ain't no rules around here! We're trying to accomplish something!*

**Thomas Alva Edison**  
(1847–1931)

# 7

## Hysteretic behavior in thin–film photovoltaic materials



Thin–film semiconductors have taken great attention in the last two decades due to their capacity to be used in solar energy applications as solar cells, see Figure 1.3. Semiconductors are completely characterized by their figure–of–merit that depends on thermal and electric conductivities and on *Seebeck* coefficient. These transport properties must be determined experimentally to characterize the semiconductors and to design the solar cells.

An experimental study for the measurement of the *Seebeck* coefficient in thin–film semiconductors has recently been performed in Ferrer et al. [2006], reporting a hysteretic behavior that prevents correct measurement of this coefficient. In Galushko et al. [2005], a similar hysteretic behavior was observed in hornet cuticles that work as a thermoelectric heat pump for cooling the hornet body. Two challenges emerge from these works:

- ▷ Physical interpretation of the hysteretic behavior
- ▷ Measuring of the *Seebeck* coefficient

The first challenge was undertaken in Ferrer et al. [2006] and Galushko et al. [2005], concluding that the reason of this behavior could be arise from some ferroelectric properties (polarization phenomena). Pyroelectric interactions were discarded in Ferrer et al. [2006]. For the second challenge, an empirical procedure without theoretical basis that consists of fitting experimental curves was proposed in Ferrer et al. [2006].

According to Hernández-Lemus and Orgaz [2002], hysteretic behavior is due to the presence of multiple metastable configurations accessible to the system and is closely related with the relaxation times. Therefore, ENET could explain this behavior from a theoretical point of view.

The aims of the present chapter are: to provide a theoretical explanation for the hysteretic behavior using the ENET and to propose a method for the proper characterization of the *Seebeck* coefficient using the multi-coupled FE. For these purposes, the experiment developed in Ferrer et al. [2006] is simulated and two studies are performed:

- i) A Sensitivity Analysis (SA) to determine that properties affect to the hysteretic behavior
- ii) An Inverse Problem (IP) to calibrate and to determine the material properties of the model

This FE-IP combination could be employed for the characterization of the *Seebeck* coefficient and for the optimization of the efficiency in solar cells.

Section 7.1 introduces the experimental study, developing a theoretical interpretation of the results. Section 7.2 presents the FE equations and Section 7.3 calibrates the FE model solving the IP. Section 7.4 executes three numerical simulations to design new experiments that could be developed for the verification of the theoretical interpretation proposed in the present thesis. Finally, Section 7.5 reports the conclusions.

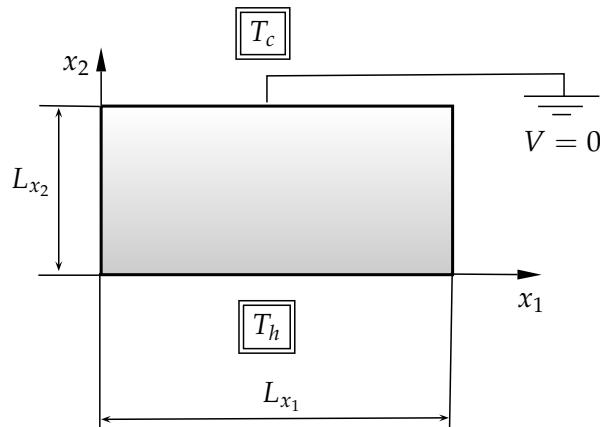


Figure 7.1: Experimental configuration for the measurement of the *Seebeck* coefficient.

## 7.1 Physical interpretation of the hysteretic behavior

The aim of the current section is to find a theoretical explanation of the hysteretic behavior using the ENET. Before, the experimental procedure and empirical results reported in Ferrer et al. [2006] are described.

### 7.1.1 Experimental procedure

The experimental configuration for measuring the *Seebeck* coefficient usually involves placing the sample between the hot  $T_h$  and cold  $T_c$  faces and fixing the voltage at the cold face, as in Figure 7.1. Removing the relaxation times, the classical electric transport equation is extracted from (3.22)–bottom. Assuming  $j = \mathbf{0}$ , a linear relationship between the applied temperature and the measured voltage is obtained:

$$\left. \begin{array}{l} j = -\gamma \nabla V - \alpha \gamma \nabla T \\ j = \mathbf{0} \end{array} \right\} \Rightarrow \nabla V = -\alpha \nabla T \Rightarrow \Delta V = -\alpha \Delta T \quad (7.1)$$

From (7.1), the *Seebeck* coefficient is determined plotting the measured voltage  $\Delta V$  versus the applied temperature  $\Delta T$  and calculating the slope  $\alpha$  of this linear relationship. The sign of  $\alpha$  depends on the semiconductor type: n or p.

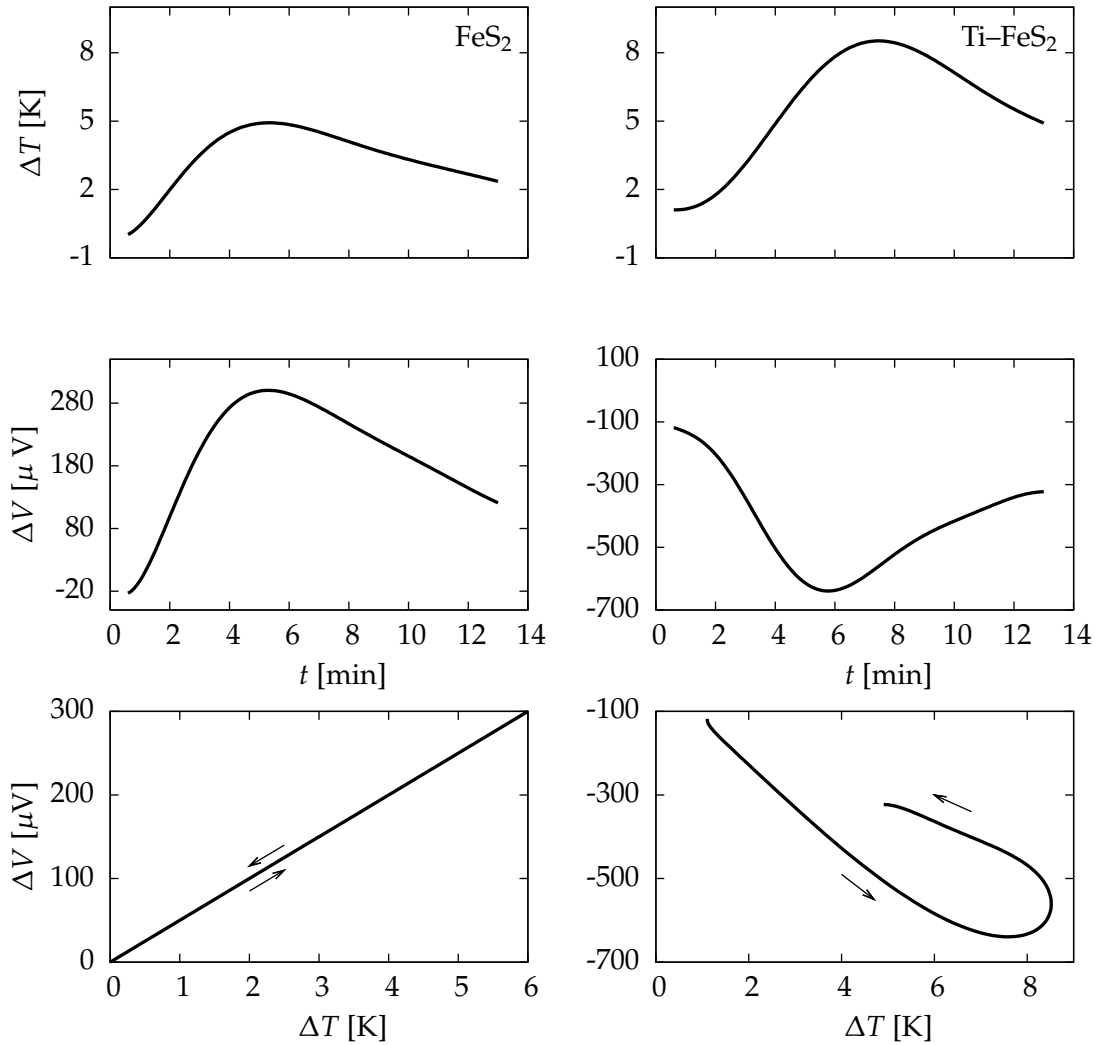


Figure 7.2: Experimental results reported in Ferrer et al. [2006] for FeS<sub>2</sub> (left) and Ti-doped FeS<sub>2</sub> (right) thin films. Top: applied temperature difference  $\Delta T(t)$ ; middle: measured voltage  $\Delta V$ ; bottom:  $\Delta V$  versus  $\Delta T$ .

In Ferrer et al. [2006], two samples of thin-film materials (FeS<sub>2</sub> and Ti-doped FeS<sub>2</sub>) of dimensions  $L_{x_2} = 15$ ,  $L_{x_1} = 25$  [mm] were investigated applying  $\Delta T(t)$  and measuring  $\Delta V$ . Depending on the sample, two very different results were observed:

- ▷ For FeS<sub>2</sub>, the linear relationship between  $\Delta V$  and  $\Delta T$  shown in Figure 7.2 (left)
- ▷ For Ti-doped FeS<sub>2</sub>, the hysteretic behavior shown in Figure 7.2 (right)

As has been discussed, for samples that present a hysteretic behavior is difficult to assign a constant *Seebeck* coefficient:  $\alpha$  was calculated from the heating branch in Galushko et al. [2005] and from the common slope to different loops obtained applying different  $\Delta T$  in Ferrer et al. [2006].

An empirical explanation, without theoretical basis, on the hysteretic behavior was reported in Ferrer et al. [2006] fitting the experimental results:

$$\Delta V = -\alpha \Delta T - \alpha K_{emp} \frac{d(\Delta T)}{dt} \quad (7.2)$$

where  $K_{emp}$  is an empirical magnitude that has dimension of time. Therefore, the loop shape and its slope (Figure 7.2) were determined by the second and by the first terms on the right side of (7.2), respectively.

### 7.1.2 Theoretical explanation

The motivation to provide a theoretical explanation using the ENET is due to the dependency on  $d\Delta T/dt$  and on  $K_{emp}$  of the empirical relation (7.2). These two magnitudes are closely related with those introduced by the ENET: dissipative fluxes and relaxation times, respectively. In addition,  $K_{emp}$  holds dimension of time.

From the electric transport equation (3.25) and assuming  $\mathbf{j} = \mathbf{0}$ :

$$\nabla V = -\alpha \nabla T - \alpha \tau_{jq} \frac{\partial(\nabla T)}{\partial t} \quad (7.3)$$

Contrasting (7.3) and (7.2), the equality  $K_{emp} = \tau_{jq}$  is achieved. Therefore, the loop shape, i.e. hysteresis, depends on  $\tau_{jq}$ . This conclusion agrees with the theoretical one given in Hernández-Lemus and Orgaz [2002]: the hysteresis depends on the ratio  $\tau_{jq}/T_{ob}$ , where  $T_{ob}$  is the observation time. This ratio depends on the properties of the material, observing linear or hysteretic behavior when:

- ▷  $\tau_{jq}/T_{ob} \ll 1 \rightarrow$  Linear
- ▷  $\tau_{jq}/T_{ob} \approx 1 \rightarrow$  Hysteresis

Summarizing, a statistical physics explanation could be that microscopic equilibration time  $\tau_{jq}$  increases when the material is doped with Ti. Therefore,  $\tau_{jq}/T_{ob} \approx 1$  and a hysteretic behavior is observed.

## 7.2 Finite element equations

In order to simulate the hysteretic behavior, the multi-coupled FE formulation only requires two degrees of freedom: temperature and voltage. Therefore and from (4.28), the assembled matrix is:

$$\begin{bmatrix} c_1 \mathcal{K}^{TT} + c_2 \mathcal{C}^{TT} + c_3 \mathcal{M}^{TT} & c_1 \mathcal{K}^{TV} + c_2 \mathcal{C}^{TV} \\ c_1 \mathcal{K}^{VT} + c_2 \mathcal{C}^{VT} & c_1 \mathcal{K}^{VV} \end{bmatrix} \quad (7.4)$$

In addition, the time-integration algorithm is regularized to avoid *Gibbs* phenomena by the procedure described in Chapter 5. For obvious reasons, the 3-D multi-coupled FE is used, although the hysteretic behavior is one-dimensional in the present study.

## 7.3 Calibration of the numerical model: inverse problem

Material properties are required for the numerical simulation of the experiment developed in Ferrer et al. [2006]. However, these properties are not reported. In addition, note that the relaxation time is not considered in the experimental work (it is empirically fitted). Therefore, the numerical model is calibrated using two steps:

- i) A SA to obtain the material properties more relevant in the hysteretic behavior
- ii) An identification IP to find the material properties

Random variables	SRC notation
$\alpha$	$\Theta_{\alpha}$
$\gamma$	$\Theta_{\gamma}$
$\kappa$	$\Theta_{\kappa}$
$c$	$\Theta_c$
$\rho_m$	$\Theta_{\rho_m}$
$\tau_q$	$\Theta_{\tau_q}$
$\tau_{jq}$	$\Theta_{\tau_{jq}}$

Table 7.1: Random variables and the standardized regression coefficient (SRC) notation.



### 7.3.1 Sensitivity Analysis

The SA is developed by the procedure described in the Appendix A. The dependent variable is the cost function (7.5) and the independent or random variables are those shown in Table 7.1. The notation of the Standardized Regression Coefficient (SRC) is also included in Table 7.1.

The cost function is defined as the quadratic difference between the voltages or potential drops obtained experimentally  $\Delta V^{EXP}$  and numerically  $\Delta V^{NUM}$  (Figure 7.2 bottom-right):

$$f = \frac{1}{N} \sum_{i=1}^N \left( \Delta V_i^{EXP} - \Delta V_i^{NUM} \right)^2 \quad (7.5)$$

where  $N$  is the number of measurement points (nodes). The random variables are assumed to be normally distributed: mean values are those reported in Appendix B and standard deviations assumed to be 25%.

An optimized sample of size  $m = 1000$  to reduce the CPU cost and to guarantee the convergence was calculated by the procedure developed in Palma et al. [2009]. The sample is of *Latin Hypercube* type since the convergence is faster than using random techniques, see Palma et al. [2009].

Figure 7.3 shows the SRC's in absolute value obtained from the SA. The cost function is most sensitive to the relaxation time  $\Theta_{\tau_{jq}}$  and the *Seebeck* coefficient  $\Theta_{\alpha}$ . These results agree with the theoretical one given in Section 7.1.2: the loop shape and its slope depend on  $\tau_{jq}$  and on  $\alpha$ , respectively. Note that the highest sensitivity is  $\Theta_{\tau_{jq}}$ , suggesting a strongly hysteretic dependency on  $\tau_{jq}$ . Other sensitivities, such as  $\Theta_{\kappa}$ ,  $\Theta_c$  and  $\Theta_{\rho_m}$ , are relevant since the electric energy generated by the *Seebeck* effects depends on the thermal properties of the material as shown in equation (7.7). Finally,  $\Theta_{\gamma}$ ,  $\Theta_{\tau_q}$  are not relevant since  $j = \mathbf{0}$  and probably  $\tau_q/T_{ob} \ll 1$ , respectively.

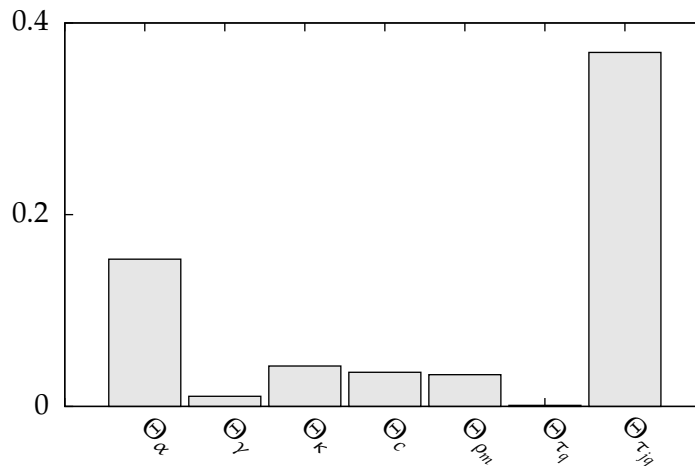


Figure 7.3: Standardized regression coefficient in absolute value, see notation in Table 7.1.

### 7.3.2 Inverse problem

The identification IP is solved by means of the procedure describe in Appendix A, defining a set of output variables (parametrization), a cost function and a minimization method.

#### PARAMETRIZATION

In the IP framework, model parametrization means to characterize the sought solution by a set of parameters (material properties for the present problem), which are the working variables and the IP output. As will reported in the Appendix A, the choice of parametrization is not obvious, being a critical step in the problem setup. In the present thesis and according to the SA results shown in Figure 7.3, the set of parameters is composed of:

$$parameters = \{\alpha, \kappa, c, \rho_m, \tau_{jq}\}$$

#### COST FUNCTION

The cost function (7.5) is redefined as:

$$f^L = \log(f + \varepsilon) \quad (7.6)$$

where  $\varepsilon = 10^{-16}$  is a small non-dimensional value that ensures the existence if  $f$  tends to zero. Furthermore and according to Gallego and Rus [2004], this redefinition usually increases the minimization algorithm convergence.

Parameter	Value
Population size	30
Crossover ratio	0.8
Mutation ratio	0.02
Number of generations	200

Table 7.2: Values of genetic algorithm parameters.

#### MINIMIZATION

Standard Genetic Algorithms (GA), which are described in the Appendix A, are employed for the minimization of (7.6) and for obtaining the IP output (*parameters*). Other optimization techniques such as gradient-based algorithms could be applied. However and according to Rus et al. [2009], GA's guarantee convergence, whereas gradient-based algorithms strongly depend on the initial guess that needs to be provided.

Table 7.2 shows the intrinsic GA parameters. The selected population size should guarantee to find a global optimum under an adequate computational cost. Mutation and crossover parameters inject genetic diversity, ensuring that the solution does not fall in a local minima.

*IP RESULTS*

The IP has been executed ten times in order to ensure accurate results. Calculated means and standard deviations are shown in Table 7.3. Standard deviations are approximately 2%, except for the most sensitivity parameters  $\alpha$ ,  $\tau_{jq}$ .

Parameter	Mean	Standard deviation %
$\alpha$	-68	3
$\kappa$	1.66	1.8
$c$	534	1.9
$\rho_m$	7428	1.3
$\tau_{jq}$	93	3

Table 7.3: Means and standard deviations obtained solving ten times the inverse problem.

Parameter	Empirical	Inverse problem	Relative error
$\alpha$ [ $\mu\text{V}/\text{K}$ ]	-65.8	-68	3%
$\tau_{jq}$ [s]	95	93	2%

Table 7.4: Comparison between inverse problem results and those empirically obtained in Ferrer et al. [2006].

Figure 7.4 shows the GA convergence that is reached about 50 generations. This fast convergence evidences that the GA parameters (shown in Table 7.2) were correctly chosen.

The values of  $\alpha$  and  $\tau_{jq}$  calculated by the resolution of the IP and those empirically fitted in Ferrer et al. [2006] are compared in Table 7.4. Note that  $\tau_{jq}$  is an empirical parameter (without theoretical basis) denoted by  $K_{emp}$  in Ferrer et al. [2006]. The relative errors between the IP results and the empirical values are approximately equals that the standard

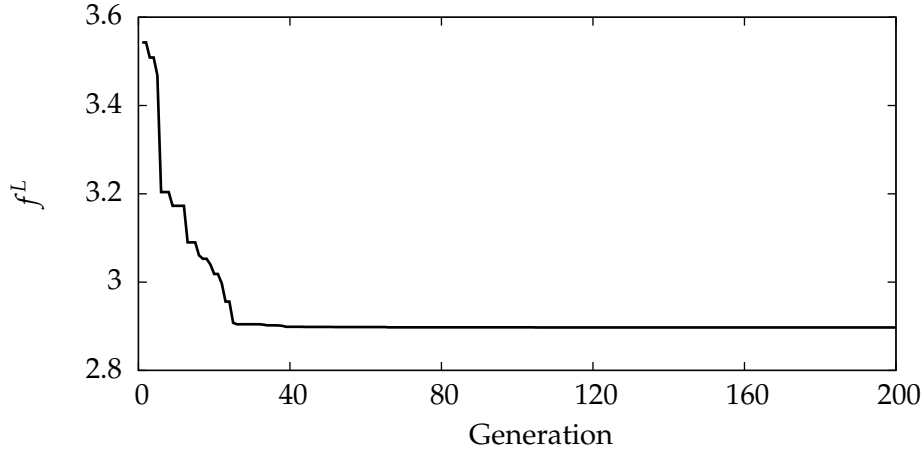


Figure 7.4: Genetic algorithm convergence. Cost function versus number of generations.

deviations obtained minimizing the problem with GA. Therefore, the proposed FE–IP combination is able for the correctly calibration of the model and would be a technique for the characterization of materials from experimental curves.

Experimental and FE results are compared in Figures 7.5 and 7.6 for two samples of n- and p-type of Ti-doped FeS<sub>2</sub>, respectively. Material properties for both simulations have been calculated from the IP solution.

Figure 7.5 shows  $\Delta V$  versus time (top) and  $\Delta V$  versus  $\Delta T$  (bottom). The FE model correctly reproduces the experimental results once the properties have been characterized by the IP. Figure 7.6 represents  $\Delta V$  versus  $\Delta T$  for a p-type sample, showing that the agreement between experimental and numerical results is very good. Ten IP's have been executed to calculate the material properties, obtaining  $\alpha = 55.5$  [ $\mu\text{V}/\text{K}$ ],  $\tau_{jq} = 30.6$  [s]. These material properties significantly change respect to those obtained for a n-type sample. This change may be due to difference in the doped process. Furthermore, the *Seebeck* coefficient has the opposite sign.

#### 7.4 Design of experiments for the validation of the theoretical explanation

The aim of the current section is to present three experimental designs that could validate the theoretical explanation for the hysteretic behavior. From the multi-coupled energy balance (4.5) and assuming  $\mathbf{j} = \mathbf{0}$ ,  $\tau_q = 0$ , the following *Poisson* equation for the voltage distribution is obtained:

$$\nabla^2 V = -\alpha \frac{\rho_m c}{\kappa} \dot{T} - \tau_{jq} \alpha \frac{\rho_m c}{\kappa} \ddot{T} \quad (7.7)$$

where the sources (terms on the right side) depend on the material properties  $\alpha$ ,  $\kappa$ ,  $\rho_m$ ,  $c$  and on  $\dot{T}$ ,  $\ddot{T}$ ,  $\tau_{jq}$ . From this equation and according to the theoretical explanation proposed in this chapter:

$$\tau_{jq} = 0 \text{ or } \ddot{T} = 0 \Rightarrow \text{No hysteresis}$$

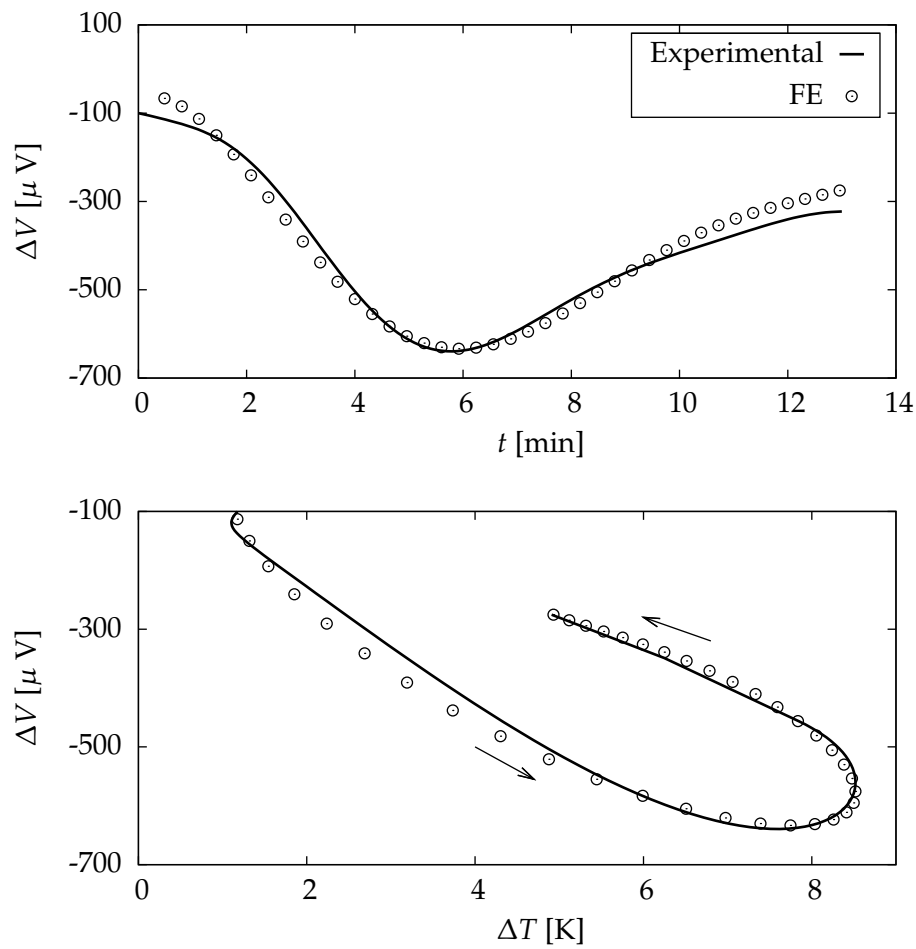


Figure 7.5: Experimental (solid line) and finite element (circles) results obtained for a n-type sample of Ti-doped  $\text{FeS}_2$ . Top: measured voltage versus time, bottom: measured voltage versus applied temperature.

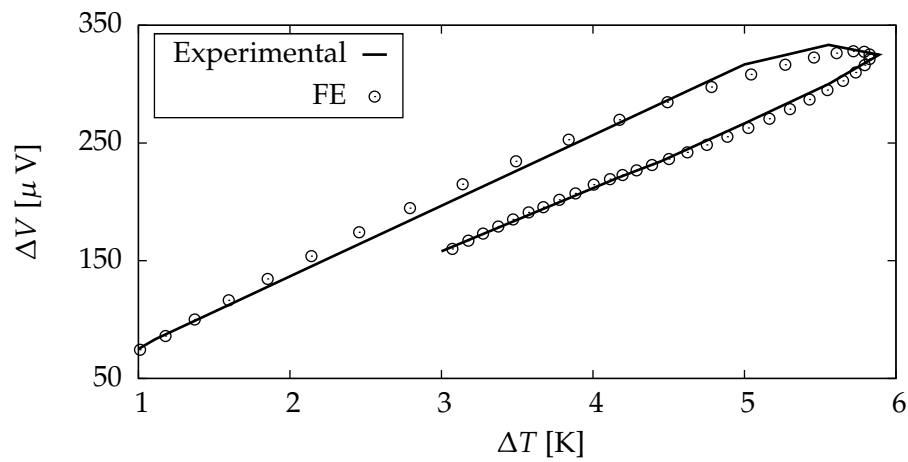


Figure 7.6: Measured voltage versus applied temperature. Experimental (solid line) and finite element (circles) results obtained for a p-type sample of Ti-doped  $\text{FeS}_2$ .

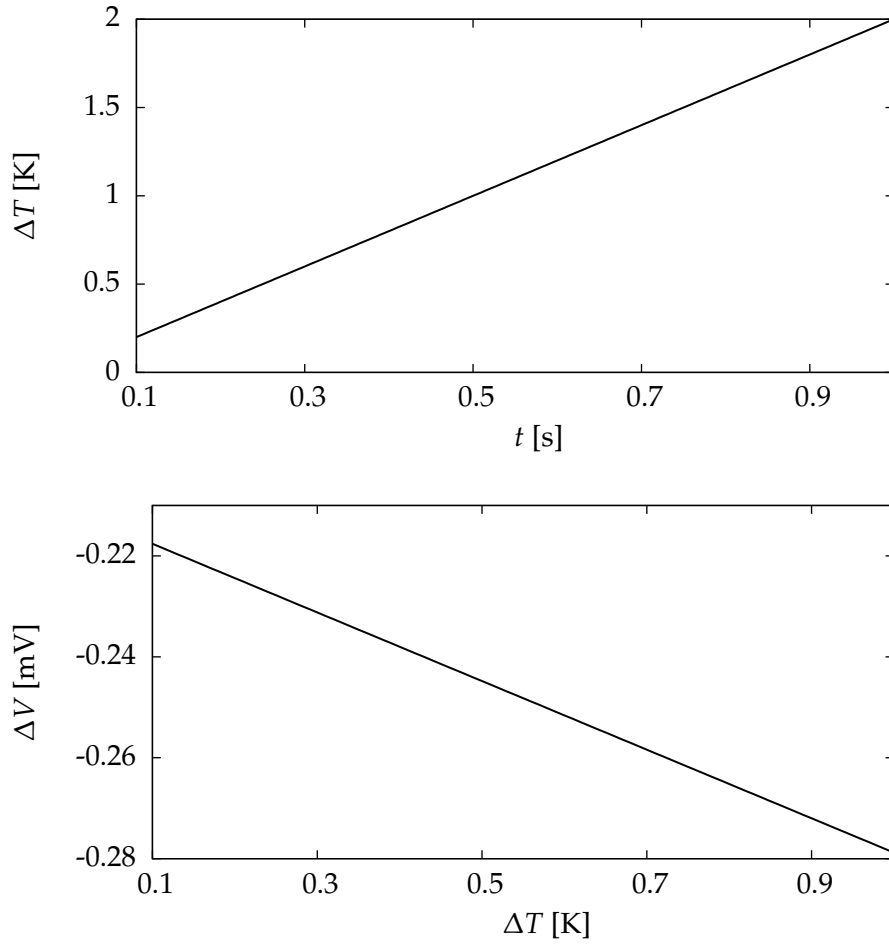


Figure 7.7: Numerical experiment consisting of the application of a linear temperature signal (top) and of the calculation of the generated voltage. Calculated voltage versus applied temperature (bottom). Only finite element results are shown.

As has been verified, there is no hysteretic behavior if  $\tau_{jq} = 0$ . For  $\ddot{T} = 0$ , three experimental designs are proposed:

- A. The applied temperature satisfy  $\ddot{T} = 0$
- B. Influence of the applied temperature frequency on the hysteresis
- C. Influence of the applied temperature amplitude on the hysteresis

All the designs are simulated by the multi-coupled FE, considering a n-type sample of Ti-doped  $\text{FeS}_2$ . Material properties are those obtained by the resolution of the IP and shown in Table 7.3. Nevertheless,  $\tau_{jq} = 1.55$  [s]; note that  $\tau_{jq}$  is given in [min] in Table 7.3.

*DESIGN A.*

The linear temperature signal shown in Figure 7.7 (top) is considered for the application of a  $\Delta T$  satisfying  $\ddot{T} = 0$ . A linear behavior is observed by plotting  $\Delta V$  versus  $\Delta T$ , see Figure 7.7

(bottom). Therefore, the hysteretic behavior depends on  $\tau_{jq}$  and on the applied temperature, which must satisfy  $\ddot{T} \neq 0$  as is shown in (7.7).

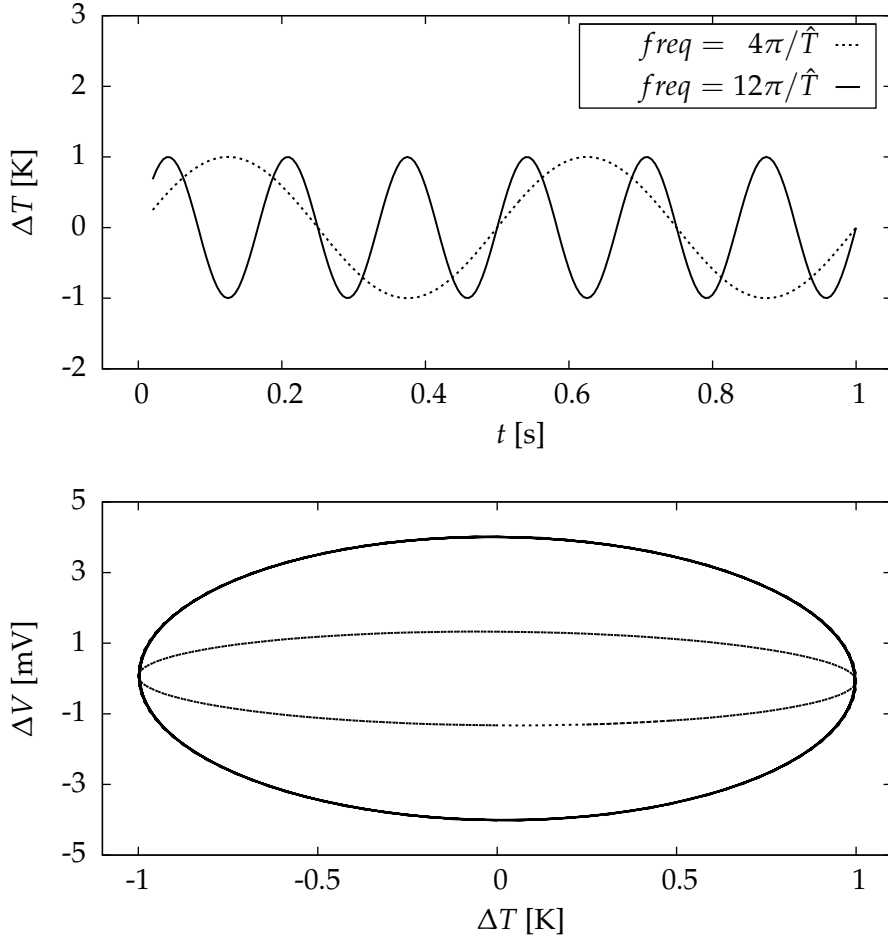


Figure 7.8: Numerical experiment consisting of the application of two sinusoidal temperature signals with different frequencies (top) and of the calculation of the generated voltages. Calculated voltage versus applied temperature (bottom). Again, finite element results are only shown.

#### DESIGN B.

For this design, two sinusoidal temperature signals with different frequencies ( $freq = 4\pi/\hat{T}$ ,  $12\pi/\hat{T}$ ) are applied, see Figure 7.8 (top). Figure 7.8 (bottom) shows the generated voltage versus the applied temperature. For both frequencies, hysteretic behaviors are achieved, since  $\tau_{jq} \neq 0$ ,  $\ddot{T} \neq 0$ . Three observations:

- ▷ At  $\Delta T = \pm 1$  [K] both potential drops are the same, since  $\ddot{T} = 0$
- ▷ At  $\Delta T = 0$  [K] the maximum difference is achieved since  $\ddot{T}$  is maximum
- ▷ The increasing of the potential drop is proportional to the signal frequency since  $\ddot{T} \propto dfreq/dt$ . Therefore and as argued in Chapter 1, the influence of relaxation times is higher for fast effects such as ultrasound

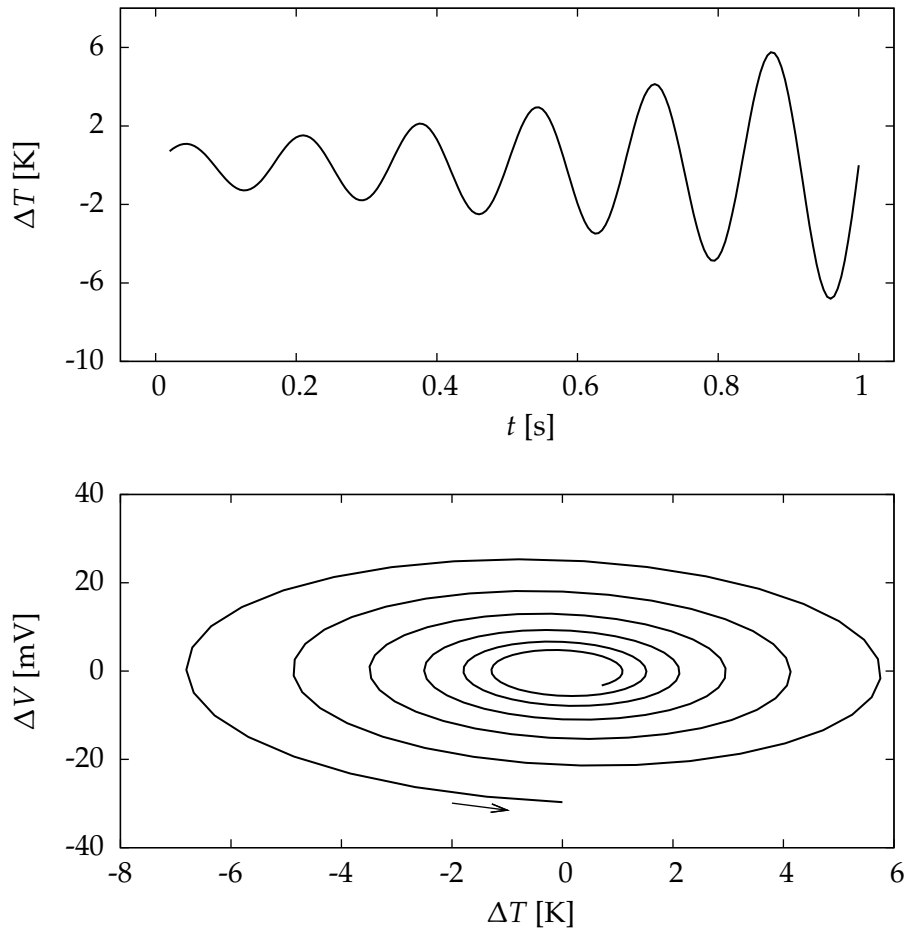


Figure 7.9: Numerical experiment consisting of the application of an exponentially increasing sinusoidal temperature signal (top) and of the calculation of the generated voltage. Calculated voltage versus applied temperature (bottom). Again, finite element results are only shown.

### DESIGN C.

For this design an exponentially increasing sinusoidal  $\Delta T$  is applied, see Figure 7.9 (top). The response, Figure 7.9 (bottom), consists of an upward spiral for which the slope of its axis is the *Seebeck* coefficient. Again, the explanation is found in the relationship  $\ddot{T} \propto \text{amplitude}$ .

## 7.5 Conclusions

This chapter has presented a theoretical explanation using the ENET for the understanding of the hysteretic behavior in thin-film photovoltaic materials, concluding that this behavior depends on the relaxation time  $\tau_{jq}$  and on the acceleration of the prescribed temperature signal  $\ddot{T}$ . The last dependency could explain the influence of relaxation times on fast effects. Experimental results have been simulated by the multi-coupled finite element, validating the theoretical explanation. In addition, three experimental designs have been proposed and numerically simulated in order to fully validate our theoretical explanation.



An identification inverse problem has been performed for the characterization of the *Seebeck* coefficient and of the relaxation time  $\tau_{jq}$ . The combination of the inverse problem and of the finite element permits a proper characterization of thin-film material properties from experimental curves.

*In every branch of knowledge  
the progress is proportional to  
the amount of facts on which  
to build, and therefore to the  
facility of obtaining data.*

**James Clerk Maxwell**  
(1831–1879)

# 8

## Galvanomagnetic and thermo–magnetic interactions



Galvanomagnetic and thermo–magnetic interactions are consequence of the *Lorentz* forces that a magnetic field exerts on moving charges, see Landau and Lifshitz [1984], de Groot and Mazur [1984], Callen [1985], Rowe [1995], Newnham [2005] and Tinder [2008]. These interactions are widely applied in transducers and sensors, Stefanescu [2011]; engineering and medical applications (biosensors as that shown in Figure 8.1), Johnstone [2008]; optimization of thermoelectric devices, Newnham [2005]; chemical processes and in cell–stimulant interactions, Johnstone [2008].

Several analytical solutions for these magnetic interactions are available in the literature, for example Chaplik [2000] and Delves [1964]. However and according to Rowe [1995], Okumura et al. [1998] and Johnstone [2008], these interactions are very sensitive to the sample geometry and to the material properties. In addition, these interactions show strong distortion of the electric and thermal fluxes. Therefore, analytical solutions, which assume simple geometries, are far from being able to use in sophisticated applications. For this reason, several numerical formulations have emerged in the two last decades:

- ▷ The finite difference method was applied in Okumura et al. [1998] and Okumura et al. [1999]

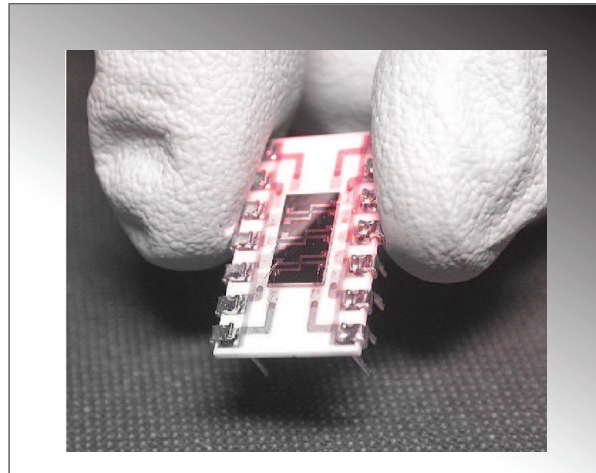


Figure 8.1: Biosensor based on the *Hall* effect and used for molecule recognition. Picture taken from <http://bme240.eng.uci.edu/>.

- ▷ The FE was used to study the *Hall* effect in Brauer et al. [1995]. However, this FE formulation is very simple, consisting of an electric element with anisotropic conductivity. The magnetic-dependency on the electric conductivity tensor was introduced as data: it is not a fully coupled element

The objective of the present chapter is to simulate the galvanomagnetic and thermo-magnetic interactions using the multi-coupled FE, assuming steady-state situations. For this purpose, three degrees of freedom (voltage, temperature and magnetic scalar potential) are only required. In addition, the transport properties (*Seebeck* coefficient, thermal and electric conductivities) become tensor entities.

Section 8.1 describes the galvanomagnetic and thermo-magnetic interactions from a physical point of view. Section 8.2 extracts the terms from the multi-coupled assembled matrix, incorporating two new terms to study these interactions. FE validations are performed in Section 8.3 using simple analytical solutions. Finally, Section 8.4 presents the conclusions.

## 8.1 Physical interpretation of galvanomagnetic and thermo-magnetic interactions

Thermal and electric fluxes interact with the magnetic field due to the thermal and electric energies that carry the moving charges. Therefore, in the presence of a magnetic field:

- ▷ Galvanomagnetic interactions involve voltage gradients and electric fluxes, Figure 8.2 (left)
- ▷ Thermo-magnetic interactions involve temperature gradients and thermal fluxes, Figure 8.2 (right)

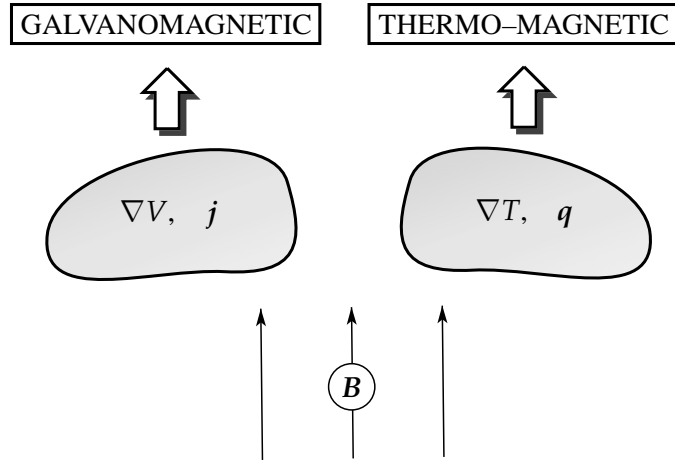


Figure 8.2: Physical magnitudes involved in the galvanomagnetic and thermo-magnetic interactions.

These interactions depend on the isotropy or anisotropy of the media. Second-order interactions such as piezo-resistance or magnetoresistance emerge in anisotropic media since the properties depend on the magnetic field strength, Tinder [2008]. Anisotropic media are not considered in the present thesis.

Galvanomagnetic	Thermo-magnetic
<i>Hall effect</i>	<i>Righi-Leduc effect</i>
<i>Ettingshausen effect</i>	<i>Nernst effect</i>

Table 8.1: Galvanomagnetic and thermo-magnetic first-order transverse interactions.

Considering an isotropic medium and, therefore, neglecting second-order interactions, four transverse interactions due to the presence of a magnetic field are present. These transverse interactions are shown in Table 8.1.

Assuming a magnetic field along  $x_3$  and from Figure 8.3, the transverse interactions or effects can be interpreted as:

- **Hall**: Electric fluxes along  $x_1$  (cause) induce voltage gradients along  $x_2$  (effect)
- **Ettingshausen**: Electric fluxes along  $x_1$ ; temperature gradients along  $x_2$
- **Righi-Leduc**: Temperature gradients along  $x_1$ ; temperature gradients along  $x_2$
- **Nernst**: Temperature gradients along  $x_1$ ; voltage gradients along  $x_2$

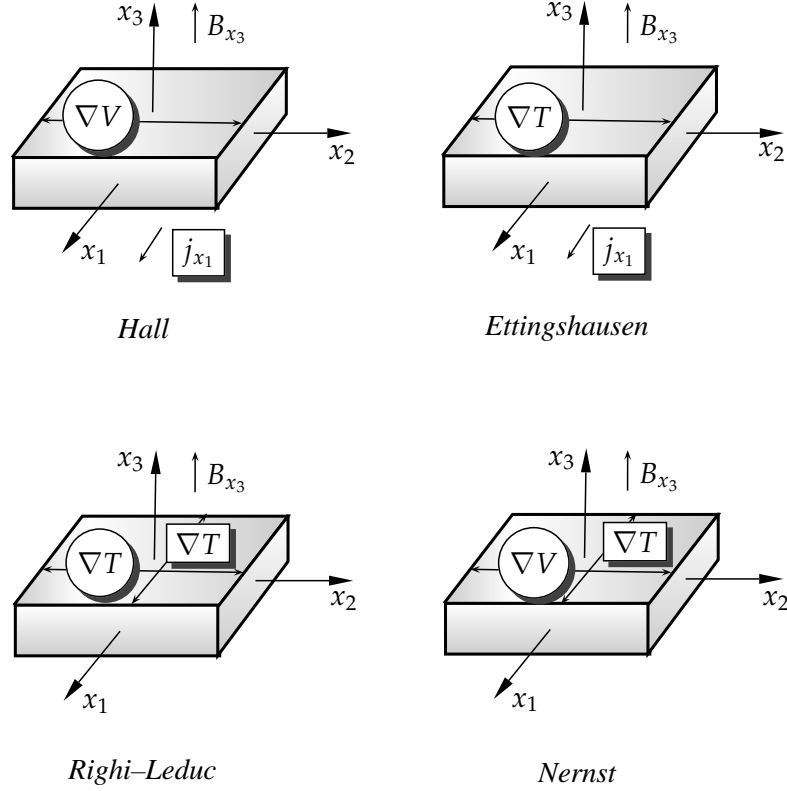


Figure 8.3: Sketch of the four transverse galvanomagnetic and thermo-magnetic interactions. Following the convection of Figure 1.5, causes are represented by rectangles and effects by circles.

Neglecting relaxation times since this chapter assumes steady-state situations, the transport equations are:

$$\begin{aligned}
 \mathbf{q} &= -\kappa \nabla T + \alpha T \mathbf{j} \quad ; \\
 \mathbf{j} &= -\gamma \nabla V - \alpha \gamma \nabla T
 \end{aligned}
 \tag{8.1}$$

According to Landau and Lifshitz [1984], these transport equations are modified in presence of a magnetic field:

$$\begin{aligned}
 \mathbf{q} &= -\kappa \nabla T + \alpha T \mathbf{j} + \bar{N} T \mathbf{B} \times \mathbf{j} + \kappa \bar{M} \mathbf{B} \times \nabla T \quad ; \\
 \mathbf{j} &= -\gamma \nabla V - \alpha \gamma \nabla T - \bar{R} \gamma \mathbf{B} \times \mathbf{j} - \bar{N} \gamma \mathbf{B} \times \nabla T
 \end{aligned}
 \tag{8.2}$$

where  $\bar{N}$ ,  $\bar{M}$  and  $\bar{R}$  are the *Nernst*, *Righi-Leduc* and *Hall* coefficients. The third terms on the right side in (8.2) (top and bottom) represent the *Ettingshausen* and *Hall* effects, respectively; the fourth terms the *Righi-Leduc* and *Nernst* effects. Note that *Ettingshausen* and *Nernst* effects are due to the same coefficient:  $\bar{N}$ .

Combining (8.1) and (8.2), the transport properties or phenomenological coefficients ( $\alpha$ ,  $\kappa$ ,  $\gamma$ , scalar entities) in (8.1) can be converted into tensor entities ( $\boldsymbol{\alpha}$ ,  $\boldsymbol{\kappa}$ ,  $\boldsymbol{\gamma}$ ):

$$\mathbf{q} = -\boldsymbol{\kappa} \cdot \nabla T + T \boldsymbol{\alpha} \cdot \mathbf{j} \quad ; \quad (8.3)$$

$$\mathbf{j} = -\boldsymbol{\gamma} \cdot \nabla V - \boldsymbol{\alpha} \boldsymbol{\gamma} \cdot \nabla T$$

Using the identity matrix  $\mathbf{I}$  and the *Levi-Civita* symbol  $\varepsilon$  (a tensor of rank 3), the transport properties can be expressed in tensor notation:

$$\boldsymbol{\kappa} = \kappa \mathbf{I} - \kappa \bar{M} \boldsymbol{\varepsilon} \cdot \mathbf{B} \quad ;$$

$$\boldsymbol{\gamma} = (\rho \mathbf{I} + \bar{R} \boldsymbol{\varepsilon} \cdot \mathbf{B})^{-1} \quad ; \quad (8.4)$$

$$\boldsymbol{\alpha} = \alpha \mathbf{I} + \bar{N} \boldsymbol{\varepsilon} \cdot \mathbf{B}$$

Also, these properties can be written in matrix notation:

$$[\boldsymbol{\kappa}] = \begin{bmatrix} \kappa & \kappa \bar{M} B_{x_3} & -\kappa \bar{M} B_{x_2} \\ -\kappa \bar{M} B_{x_3} & \kappa & \kappa \bar{M} B_{x_1} \\ \kappa \bar{M} B_{x_2} & -\kappa \bar{M} B_{x_1} & \kappa \end{bmatrix} \quad (8.5)$$

$$[\boldsymbol{\alpha}] = \begin{bmatrix} \alpha & -\bar{N} B_{x_3} & \bar{N} B_{x_2} \\ \bar{N} B_{x_3} & \alpha & -\bar{N} B_{x_1} \\ -\bar{N} B_{x_2} & \bar{N} B_{x_1} & \alpha \end{bmatrix} \quad (8.6)$$

$$[\boldsymbol{\rho}] = \begin{bmatrix} \rho & -\bar{R} B_{x_3} & \bar{R} B_{x_2} \\ \bar{R} B_{x_3} & \rho & -\bar{R} B_{x_1} \\ -\bar{R} B_{x_2} & \bar{R} B_{x_1} & \rho \end{bmatrix} \quad (8.7)$$

where relationship  $\gamma = \rho^{-1}$  has been used.

## 8.2 Finite element equations

The multi-coupled FE formulation only requires three degrees of freedom (temperature, voltage and magnetic scalar potential) to simulate the galvanomagnetic and thermo-magnetic interactions. Furthermore, capacity and mass matrices in the assembled matrix (4.28) are avoided since this chapter assumes steady-state situations. Therefore and from (4.28), the assembled matrix is:

$$\begin{bmatrix} \mathcal{K}^{TT} & \mathcal{K}^{TV} & \mathcal{K}^{T\varphi} \\ \mathcal{K}^{VT} & \mathcal{K}^{VV} & \mathcal{K}^{V\varphi} \\ \mathbf{0} & \mathbf{0} & \mathcal{K}^{\varphi\varphi} \end{bmatrix} \quad (8.8)$$

Three observations:

- ▷  $\mathcal{K}^{\varphi T} = \mathbf{0}$  since pyromagnetic interactions have been neglected by mean of the **Simplification 1**
- ▷  $\mathcal{K}^{\varphi V} = \mathbf{0}$  is an approximation. The electric flux modifies the magnetic field according to the *Maxwell* law:  $\nabla \times \mathbf{B} = \mu_0 \mathbf{j} + \epsilon_0 \mu_0 (\partial \mathbf{D} / \partial t)$ . However,  $(\partial \mathbf{D} / \partial t) = \mathbf{0}$  (steady-state and **Simplification 3**) and  $\mu_0$  is so small that the modification can be neglected. Note that this approximation was also assumed in Okumura et al. [1998] and Okumura et al. [1999]
- ▷  $\mathcal{K}^{T\varphi} \neq \mathbf{0}$ ,  $\mathcal{K}^{V\varphi} \neq \mathbf{0}$  since the transport properties depend on the magnetic field now. Therefore, the derivatives (4.21) and (4.22) are modified for taking into account this magnetic dependency

Assuming not temperature-dependency of the transport properties, the new matrices  $\mathcal{K}^{T\varphi}$ ,  $\mathcal{K}^{V\varphi}$  are obtained from the residual (4.16):

$$\begin{aligned} \mathcal{K}_{AB}^{T\varphi} &= -\frac{\partial \mathcal{R}_A^T}{\partial a_B^\varphi} = \int_{\Omega} \mathcal{B}_A^t \frac{\partial q}{\partial a_B^\varphi} d\Omega - \int_{\Omega} \mathcal{N}_A \frac{\partial j}{\partial a_B^\varphi} \mathcal{B}_A^V d\Omega \quad ; \\ \mathcal{K}_{AB}^{V\varphi} &= -\frac{\partial \mathcal{R}_A^V}{\partial a_B^\varphi} = \int_{\Omega} \mathcal{B}_A^t \frac{\partial j}{\partial a_B^\varphi} d\Omega \end{aligned} \quad (8.9)$$

where the derivatives are obtained from (8.3), (8.4) and applying the chain rule:

$$\boxed{\begin{aligned} \frac{\partial q}{\partial a_B^\varphi} &= -\kappa \bar{M} \varepsilon \mu_0 \mathcal{B}_B^2 a_B^T - \bar{N} \varepsilon \mu_0 \mathcal{B}_B T j_B + T \alpha \frac{\partial j}{\partial a_B^\varphi} \quad ; \\ \frac{\partial j}{\partial a_B^\varphi} &= -\bar{R} \gamma^2 \varepsilon \mu_0 \mathcal{B}_B^2 a_B^V + \bar{N} \varepsilon \mu_0 \gamma \mathcal{B}_B^2 a_B^T - \bar{R} \alpha \gamma^2 \varepsilon \mu_0 \mathcal{B}_B^2 a_B^T \end{aligned}} \quad (8.10)$$

### 8.3 Results

The multi-coupled FE is used to simulate the galvanomagnetic and thermo-magnetic interactions using simple cases for which analytical solutions are calculated. Furthermore, the influence of the boundary conditions on these interactions is also studied using two TE geometries: one representing a typical TE (denominated finite domain) and one increasing ten times the length along the  $x_3$  direction (semi-infinite domain). Note that complex distortions of the fluxes appear from the boundary conditions, as was reported in Rowe [1995]. The material properties are those given in the Appendix B for the indium antimonide semiconductor.

#### 8.3.1 Hall and Righi-Leduc effects

Simple analytical solutions for the *Hall* and *Righi-Leduc* effects can be extracted from (8.2)–bottom and (8.2)–top, respectively. For this purpose, consider the parallelepipeds of dimensions  $L_{x_1} = L_{x_2} = 1.4$ ,  $L_{x_3} = 11.4$  [mm] shown in Figure 8.4. Note that  $L_{x_3}$  is 10 times greater than a typical TE, to avoid boundary phenomena: semi-infinite domain. The boundary conditions for the simulation of both effects are:

- ▷ For the *Hall* effect, Figure 8.4 (left):  $V = 0$  [V] at top,  $j_{x_3} = -2.65 \times 10^6$  [A/m<sup>2</sup>] and  $B_{x_1} = 0.5 \times 10^{-2}$  [T]
- ▷ For the *Righi-Leduc* effect, Figure 8.3 (right):  $T_c = 30$  at top,  $T_h = 50$  [°C] at bottom and  $B_{x_1} = 1$  [T]

Assuming the semi-infinite domain, voltage distributions and temperature gradients can be calculated from (8.2):



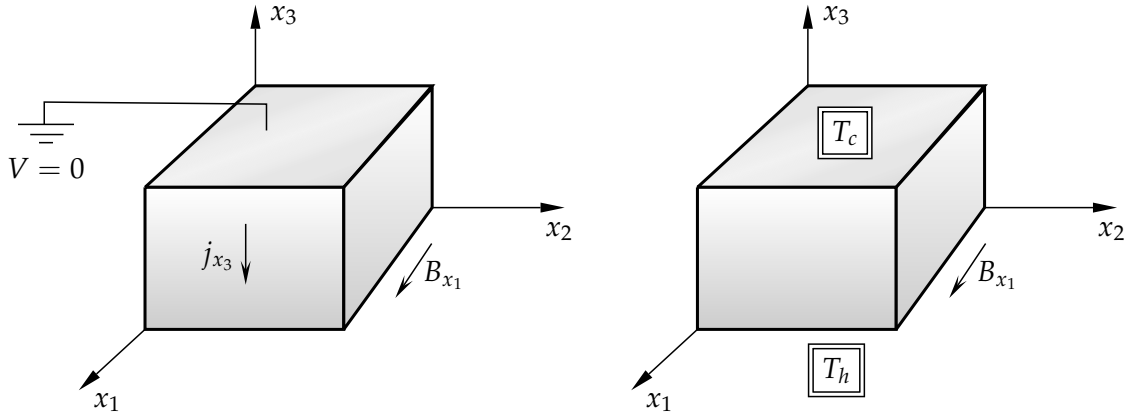


Figure 8.4: Geometry, boundary conditions and prescribed fluxes for the validation of the: *Hall* (left) and *Righi-Leduc* (right) effects.

Hall effect

$$\left. \begin{aligned}
 \alpha &= \bar{N} = 0 \\
 \bar{R} &= -2.34 \times 10^{-4} \text{ [m}^3\text{A}^{-1}\text{s}^{-1}\text{]} \\
 \gamma &= 9.12 \times 10^4 \text{ [V/K]}
 \end{aligned} \right\} \Rightarrow \quad (8.11)$$

$$\boxed{\frac{\partial V}{\partial x_2} = \bar{R} B_{x_1} j_{x_3} = 3.10 \text{ [V/m]}}$$

Righi-Leduc effect

$$\left. \begin{aligned}
 \alpha &= \bar{N} = 0 \\
 \bar{M} &= 5 \times 10^{-2} \text{ [m}^2\text{V}^{-1}\text{s}^{-1}\text{]} \\
 \kappa &= 1.57 \text{ [W/mK]}
 \end{aligned} \right\} \Rightarrow \quad (8.12)$$

$$\boxed{\frac{\partial T}{\partial x_2} = -\bar{M} B_{x_1} \frac{(T_c - T_h)}{L_{x_3}} = 87.72 \text{ [K/m]}}$$

Numerically, FE simulations are performed using a structured mesh composed of 1100 elements with eight node per element. Each node has two degree of freedom: voltage and magnetic scalar potential for the simulation of the *Hall* effect and temperature and magnetic

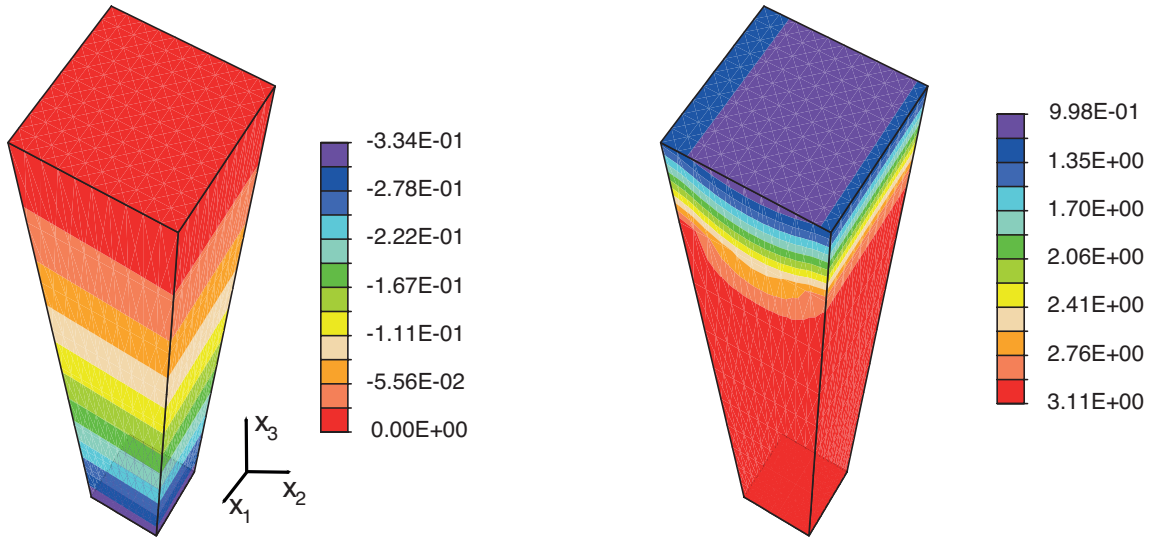


Figure 8.5: Voltage distribution (left) and gradient of voltage along the  $x_2$  direction (right) for the validation of the *Hall* effect. The vertical length of the thermoelement is magnified 100 times ( $L_{x_3} = 11.4$  [mm]): semi-infinite domain.

scalar potential for the *Righi-Leduc*. The magnetic field is prescribed using the interface element developed in Chapter 4. The consumed CPU time for the calculation is 1.8 [s], using a computer with 2 [Gb] of RAM. Table 8.2 shows the analytical and numerical results; relative errors are also included. As expected, very good FE approximations are obtained for these simple cases.

Effect	Analytical	Numerical	Relative error [%]
<i>Hall</i>	3.10 [V/m]	3.10	0
<i>Righi-Leduc</i>	87.72 [K/m]	87.72	0

Table 8.2: Comparison between analytical and numerical voltage and temperature gradients along the  $x_2$  direction for the validation of the *Hall* and of the *Righi-Leduc* effects, respectively.

Figure 8.5 shows the voltage distribution (left) and the gradient of voltage along  $x_2$  (right) for the *Hall* effect. The voltage distribution presents a linear behavior since the prescribed electric flux is constant:  $j_{x_3} = \text{cte}$ . However, this distribution is distorted by the presence of the magnetic field, although it can not be appreciated in this figure due to the color scale. The gradient of voltage is practically constant, although boundary phenomena can be observed on the top. These phenomena decrease whit increasing the vertical length  $L_{x_3}$  of the TE.

The typical TE length  $L_{x_3} = 1.14$  [mm] (finite domain) is recovered to study these boundary phenomena. Figure 8.6 shows the voltage distributions without (left) and with (right) magnetic field applied. The presence of the magnetic field disturbs the voltage distribution and a gradient of voltage appears along the  $x_2$  direction. Note that a similar distortion was reported in Brauer et al. [1995].

Figure 8.7 shows the voltage gradient along the  $x_2$  direction (left) and electric flux along the  $x_3$  direction (right) for a finite domain. Now, boundary phenomena are more relevant and analytical solutions are far to estimate the exact solution. The distortion of the electric flux  $j_{x_3}$  modifies the performance of *Peltier* devices, as will be calculated in Chapter 9.

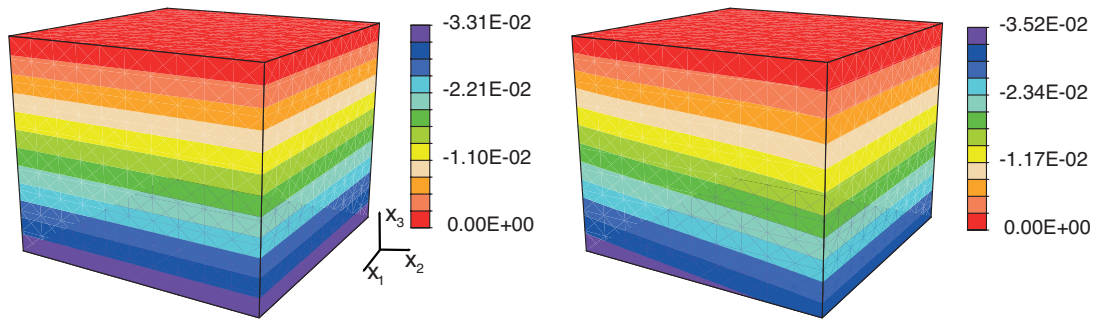


Figure 8.6: Voltage distributions with (left) and without (right) magnetic field applied. A finite domain  $L_{x_3} = 1.14$  [mm] is considered. Magnetic field disturbs the voltage distribution due to the *Hall* effect.

Figure 8.8 shows the temperature distribution (left) and gradient of temperature along the  $x_2$  direction (right) for the *Righi-Leduc* effect and infinite domain. Again, the temperature distribution is distorted by the magnetic field and the gradient of temperature is practically constant. However, boundary phenomena on both edges are now observed.

### 8.3.2 Ettingshausen and Nernst effects

The simulation of the *Ettingshausen* and *Nernst* effects separately by means of the multi-coupled FE formulation is very difficult since both effects depend on  $\bar{N}$ . Note that these

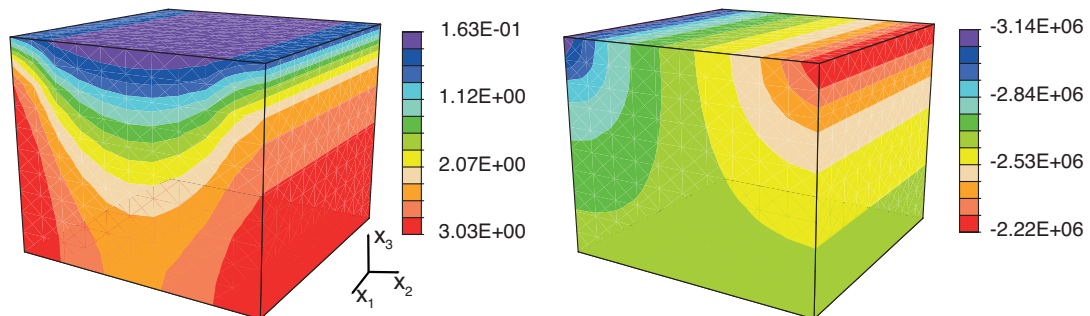


Figure 8.7: Gradient of voltage along the  $x_2$  direction (left) and electric flux along the  $x_3$  direction (right) due to the *Hall* effect. A finite domain  $L_{x_3} = 1.14$  [mm] is considered.

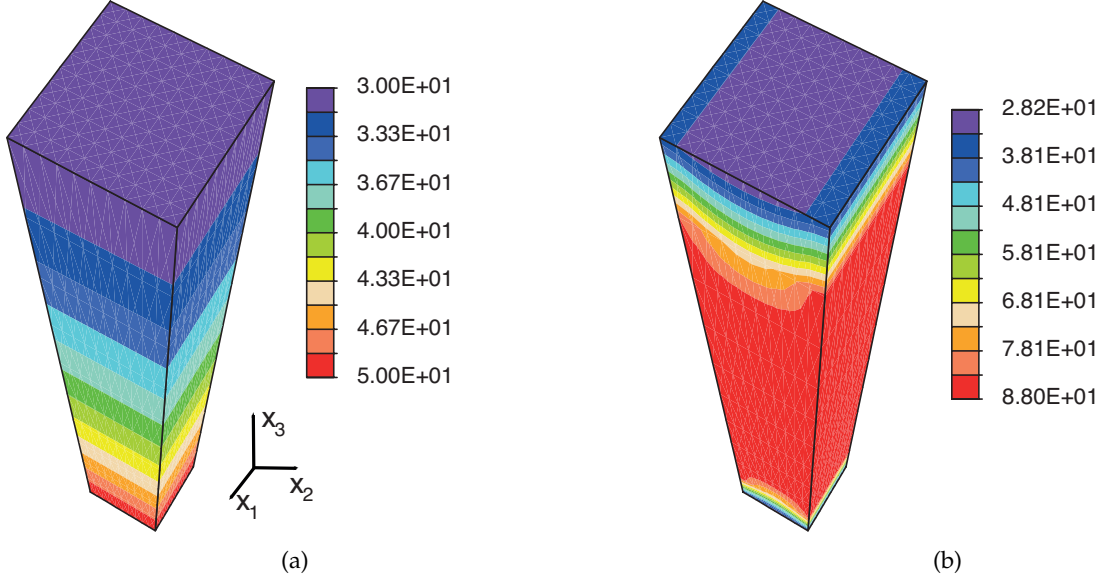


Figure 8.8: Temperature distribution (left) and gradient of temperature along the  $x_2$  direction (right) for the validation of the *Righi-Leduc* effect. The vertical length of the thermoelement is magnified 100 times ( $L_{x_3} = 11.4$  [mm]): semi-infinite domain.

effects are reported as *Ettingshausen-Nernst* effect in the literature due to their intrinsic coupling from a physical point of view. For this reason, the FE implementation has been modified by removing the following terms on the right side in (8.2):

- ▷ The last term in (8.2)–bottom for the simulation of the *Ettingshausen* effect
- ▷ The third term in (8.2)–top for the simulation of the *Nernst* effect

For the simulation of the *Ettingshausen* and *Nernst* effects, the parallelepipeds of dimensions  $L_{x_1} = L_{x_2} = 1.4$ ,  $L_{x_3} = 11.4$  [mm] shown in Figure 8.9 are considered. Now, the boundary conditions are:

- ▷ For the *Ettingshausen* effect, Figure 8.9 (left):  $V = 0$  [V] at the top,  $T_c = T_h = 20$  [°C],  $j_{x_3} = -2.65 \times 10^6$  [A/m<sup>2</sup>] and  $B_{x_1} = 0.5 \times 10^{-2}$  [T]
- ▷ For the *Nernst* effect, Figure 8.9 (right):  $T_c = 30$  [°C] at the top,  $T_h = 50$  [°C] at the bottom,  $V = 0$  [V] at the top and  $B_{x_1} = 1$  [T]

Analytical expressions for temperature and voltage gradients are obtained from (8.2), assuming  $\alpha = \bar{M} = 0$ ,  $\bar{N} = -6.28 \times 10^{-5}$  [m<sup>2</sup>/sK],  $\gamma = 9.12 \times 10^4$  [V/K] and  $\kappa = 1.57$  [W/mK] for both effects:

*Ettingshausen* effect

$$\boxed{\frac{\partial T}{\partial x_2} = -\frac{\bar{N}TB_{x_1}j_{x_3}}{\kappa} = -155.29 \text{ [K/m]}} \quad (8.13)$$

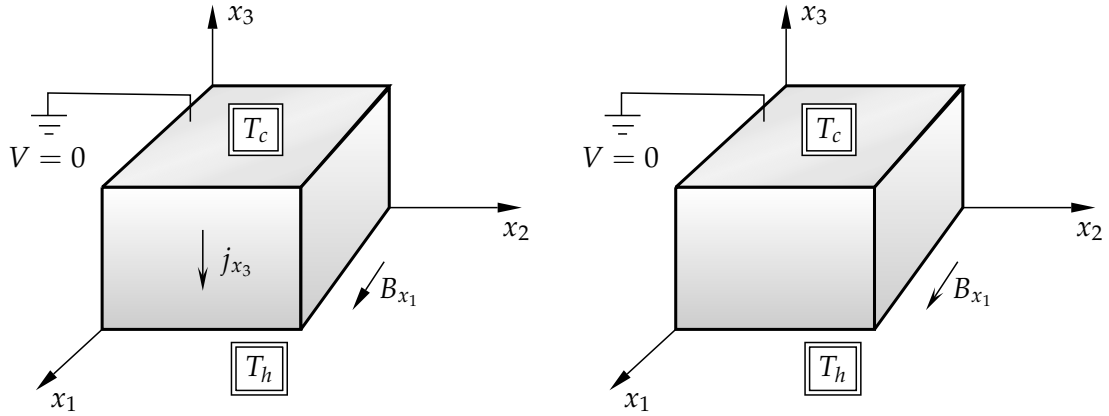


Figure 8.9: Geometry, boundary conditions and prescribed fluxes for the validation of the *Ettingshausen* (left) and *Nernst* (right) effects.

Nernst effect

$$\frac{\partial V}{\partial x_2} = \bar{N} B_{x_1} \frac{(T_c - T_h)}{L_{x_3}} = 0.11 \text{ [V/m]} \quad (8.14)$$

Both simulations are performed using the structured mesh described in the previous section. However, three d.o.f. per node (temperature, voltage and magnetic scalar potential) are considered for these simulations since *Ettingshausen* and *Nernst* effects are coupled. Table 8.3 shows the analytical and numerical results and the relative errors. Again, very good FE approximations are achieved.

Effect	Analytical	Numerical	Relative error [%]
<i>Ettingshausen</i>	-155.30 [K/m]	-155.29	0
<i>Nernst</i>	0.11 [V/m]	0.11	0

Table 8.3: Comparison between analytical and numerical temperature and voltage gradients along the  $x_2$  direction for the validation of the *Ettingshausen* and *Nernst* effects, respectively.

Figure 8.10 shows the voltage (left) temperature (right) gradients along the  $x_2$  direction for the validation of the *Ettingshausen* and *Nernst* effects, respectively. Again, the boundary phenomena are observed.

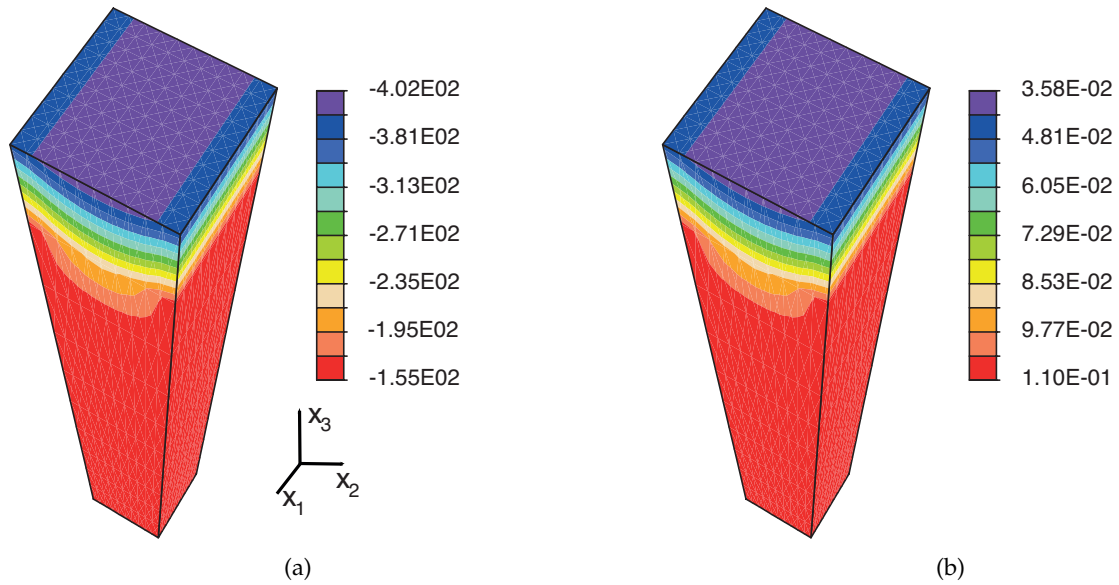


Figure 8.10: Voltage (left) and temperature (right) gradients along  $x_2$  for the validation of the *Ettingshausen* and the *Nernst* effects, respectively. The vertical length of the thermoelement is magnified 100 times ( $L_{x_3} = 11.4$  [mm]): semi-infinite domain.

## 8.4 Conclusions

Galvanomagnetic and thermo-magnetic (*Hall*, *Ettingshausen*, *Righi-Leduc* and *Nernst*) interactions or effects have been described and simulated using the multi-coupled FE formulation in the present chapter. Two new terms have been incorporated into the multi-coupled assembled matrix for taking into account these interactions. Strong dependency on the boundary conditions has been observed using simple geometries. From a physical point of view, the presence of a magnetic field causes strong alteration on thermal and on electric fluxes. Summarizing, the multi-coupled FE could be employed to model complex geometries and material properties that depend on the temperature. Therefore, this numerical tool could be used in micro-electronic devices since the performance of these devices is altered by the presence of magnetic fields. For instance, a performance study will be developed in the Chapter 9.



*Heat can never pass from a colder to a warmer body without some other change, connected therewith, occurring at the same time.*

**Rudolf Julius Emmanuel  
Clausius (1822–1888)**

# 9

## Elasto–magneto–thermo–electric study of commercial Peltier coolers



*Peltier* thermoelectric cells are devices composed of several thermocouples thermally connected in parallel and electrically in series, see Figure 1.3 (top–left). In turn, thermocouples are formed by pairs of n– and p–type TE’s. *Peltier* devices can be used in two ways: heat pumps (working in cooling or heating modes) and electric generators. The present chapter studies the *Peltier* cooler that is energetically not efficient but has several advantages such as compactness, simplicity and reliability (lack of moving parts). For this reason, these coolers are applied for the temperature stabilization in laser diodes, for cooling infrared detectors and small–scale refrigeration, see Riffat and Ma [2003] for a full revision on applications.

The Coefficient–Of–Performance (COP) is defined as the cooling capacity divided by the consumed electric power. It depends on the geometrical and material properties of the *Peltier* cooler, on the thermal and electrical contacts and on the presence of magnetic fields. Many works study the COP analytically and numerically; from an analytical point of view, in Rowe [1995] there is an expression of the COP using two main simplifications: the *Thomson* effect is not considered and any material properties are not function of the temperature. The first simplification was addressed in Chen et al. [1997], where it was analytically (with rather simple formulae) concluded that the influence of *Thomson* on COP is about 2%. This influence was further explained in Huang et al. [2005], reporting qualitatively that the fraction of both *Fourier* and *Joule* heating at the cold face is reduced by *Thomson*. The second simplification was studied in Yamashita [2009], concluding that it is very important



to consider temperature-dependent properties to design high-performance *Peltier* coolers. From a numerical point of view, Gavela and Pérez-Aparicio [1998] and Pérez-Aparicio et al. [2007] developed a steady-state and non-linear (including material and *Joule* heating) 3-D FE to study the thermal, voltage and flux distributions inside a TE. Recently, Antonova and Looman [2005] and Ebling et al. [2009] implemented thermoelectric elements into FE commercial softwares. These works were validated by analytical and experimental results, respectively. Furthermore, the FE used by Antonova and Looman [2005] included a standard interface element to model heat convection. The COP is reduced when convection and radiation are elevated, according to the 3-D finite difference model developed by Cheng et al. [2010] and when the thermal and electrical contacts are considered, Ju and Ghoshal [2000] and Ju [2008]. The previous works considered deterministic material and geometrical properties, therefore not their inherent randomness. In this sense, Oden et al. [2003] reported the treatment of physical uncertainties is a research area of great importance for the *Continuum Mechanics* community.

According to Landau and Lifshitz [1984], Rowe [1995] and Newnham [2005], the presence of a magnetic field could increase the COP since the cooling capacity is modified by the magnetic field. Specifically, the magnetic field modifies the figure-of-merit of the material and causes that the cooling capacity strongly depends on the TE geometry. Therefore, the COP can be improved optimizing the TE geometry in presence of a magnetic field without the need to enhance the material properties.

Thermal stresses inside a thin-film thermoelectric was studied in Huang et al. [2008] by means of a FE commercial software, reporting that the TE is deformed in the direction of its thickness and near its ends. FE commercial softwares were also used to calculate the thermal stresses inside thermocouples in Gao et al. [2011], Clin et al. [2009], Jaegle et al. [2008] and Jaegle et al. [2008]. Furthermore, the last work considered temperature-dependent material properties.

In the current chapter the multi-coupled FE and the interface FE are used to simulate a commercial *Peltier* cooler fabricated by MELCOR [2000]. The objectives are:

- ▷ To obtain temperature, voltage and flux distributions within the devices taking into account the radiation and convection phenomena. In addition, thermal and electric contacts are simulated using a modified circular *a*-spot model reported in Braunovic [2007]. The numerical results are compared with those given by the manufacturer
- ▷ To study the influence of an applied magnetic field on the COP due to the galvanomagnetic and thermo-magnetic interactions. This study permits to obtain the applied magnetic field that optimizes the figure-of-merit and, therefore, the COP
- ▷ To calculate the thermal stresses inside a thermocouple, considering temperature-dependent material properties. In addition, thermal stresses in presence of a magnetic

field are also calculated. These calculation gives the *Von Mises* stresses that can be used to mechanically optimize the *Peltier* device

- ▷ To obtain uncertainties and sensitivities for the COP using the combined Monte Carlo–FE technique developed in Palma et al. [2009] and described in Appendix A. This probabilistic study permits the selection of the most relevant design variables, which could be taken into account to fabricate *Peltier* devices and to optimize their performance

Section 9.1 describes a *Peltier* cooler and its simple analytical equations. Section 9.2 summarizes the multi–coupled assembled matrix, avoiding the capacity and mass matrices since the present chapter only study steady–state situations. The FE model and the results are given in Section 9.3 and 9.4, respectively. The SA is performed in Section 9.5 and Section 9.6 studies the temperature–dependency of the material properties on the *Peltier* cooler performance.

## 9.1 *Peltier* coolers

*Peltier* coolers or cells are usually composed of many special thermocouples of the type from Figure 9.1. Thermocouples are connected electrically in series by copper bars and tin solders, to form a circuit fed by a source  $V_{af}$  with intensity  $I_{tec}$ . Thermally, they are connected in parallel with external plate–shaped alumina  $Al_2O_3$  with a reasonable thermal conductivity, which is used to electrically isolate the thermocouple.

In the cooling mode studied in this chapter, the device takes heat from the cold face at  $T_c$  and transports it to the hot face at  $T_h$ , for which the *Seebeck* coefficients must be as different as possible. The same device can act in heating mode if the electric current is driven from the p– to the n–type TE.

Two main detrimental effects (irreversibilities) have to be taken into consideration:

- i) Heat conduction from the hot face to the cold face
- ii) Internal heat generated by the *Joule* effect

For the latter, in analytical formulae it is assumed (sometimes with little accuracy) that half the heat goes to the hot face and the other half to the cold face. From Rowe [1995], the approximate expressions for the total heat taken from the cold face  $Q_c$  and that given to the hot face  $Q_h$  are:

$$\begin{aligned}
 Q_h &= (\alpha_p - \alpha_n) I_{tec} T_h - \frac{\kappa A}{L} (T_h - T_c) + \frac{L}{2 \gamma A} I_{tec}^2 \quad ; \\
 Q_c &= (\alpha_p - \alpha_n) I_{tec} T_c - \frac{\kappa A}{L} (T_h - T_c) - \frac{L}{2 \gamma A} I_{tec}^2
 \end{aligned}
 \tag{9.1}$$

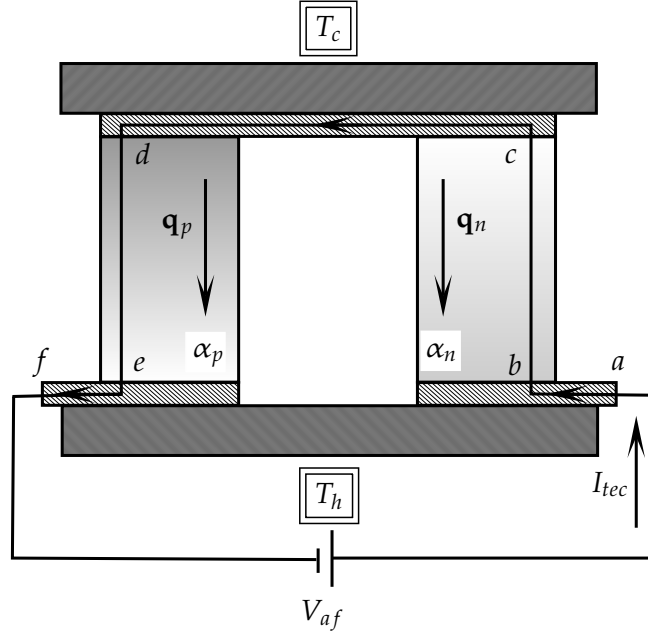


Figure 9.1: *Peltier* cooling thermocouple, thermal fluxes and electric magnitudes. Hot and cold faces temperatures.

where the three terms represent the *Peltier*, *Fourier* and *Joule* effects, and  $A$ ,  $L$  are the areas and TE lengths. In this simplified expression the *Thomson* effect is not included; however, Chen et al. [1997], Yamashita [2009] reported analytical expressions that take it into account. These works concluded that the influence on (9.1) (not necessarily on the real experimental response) of *Thomson* is of only about 2%.

If perfect performance is assumed, the difference between  $Q_h$  and  $Q_c$  must be equal to the electric power, as in (9.2)–top. The maximum intensity that can pass the *Peltier* cell is calculated from the minimum of  $Q_c$  with respect to  $I_{tec}$ , giving the middle equation. Finally, in the bottom the maximum increment of temperature  $\Delta T_{max} = T_h - T_c$  is obtained from  $Q_c(I_{max}) = 0$ :

$$V_{af} I_{tec} = (\alpha_p - \alpha_n) I_{tec} (T_h - T_c) + \frac{L}{\gamma A} I_{tec}^2 ;$$

$$I_{max} = \frac{\kappa A}{L (\alpha_p - \alpha_n)} \left( \sqrt{1 + 2 T_h Z} - 1 \right) ; \quad (9.2)$$

$$\Delta T_{max} = T_h - \frac{\sqrt{1 + 2 T_h Z} - 1}{Z}$$

where the material figure of merit is  $Z = \alpha^2 \gamma / \kappa$ . As defined before, the COP is given by:

$$\text{COP} = \frac{Q_c}{V_{af} I_{tec}} \quad (9.3)$$

### 9.1.1 Carnot equivalence

In a first analysis, it could seem that the *Peltier* cooling violates the thermodynamic laws, but in reality it follows the *Carnot* cycle of refrigeration, neglecting the two mentioned irreversibilities for now. To understand this cycle, the path of a charge carrier from point  $c$  to  $d$  in Figure 9.1 is studied. In  $c, d$  the carrier is approximately at temperature  $T_c$ , while in  $b, e$  is at a higher  $T_h$ . On the other hand, in  $b, c$  the entropy ( $\alpha_n$ ) is lower than that of  $d, e$ . This situation can be represented in the classical simplified  $T$ - $s$  Carnot cycle of Figure 9.2 (top), in which the following processes can be distinguished:

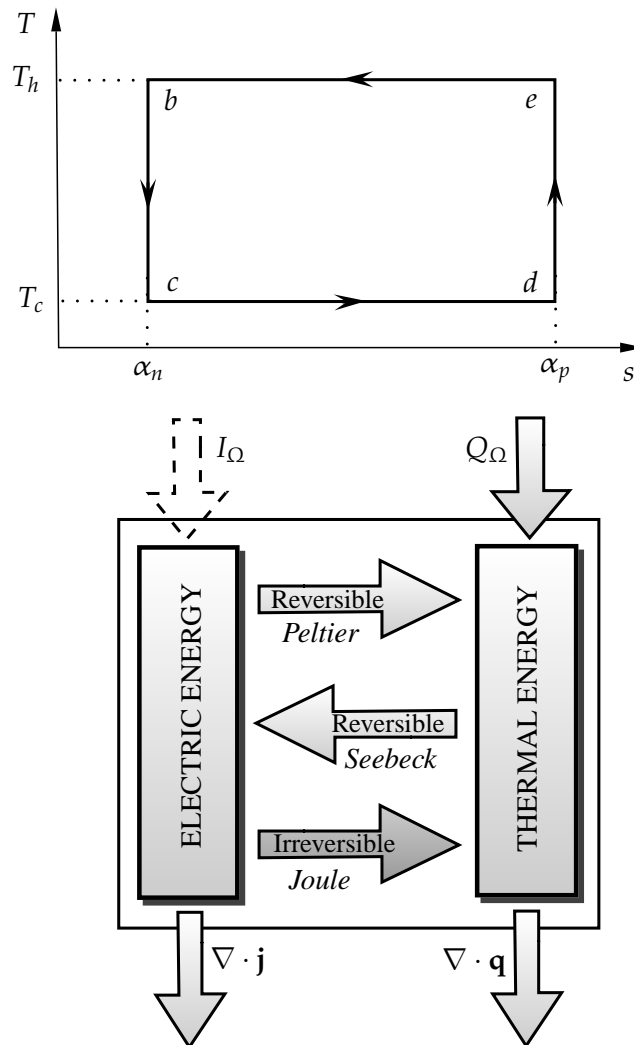


Figure 9.2: Simplified  $T$ - $s$  diagram of a charge carrier in thermoelectric materials (top). Balance of energies per unit volume (bottom). The non-physical term  $I_\Omega$  is included for numerical procedures.

- ▷ Isentropic expansion  $b$ - $c$  along the n-type TE. Not an expansion as in gases but of similar effect: the charge carrier performs a work (electric energy generated by *Seebeck*) under a constant entropy

- ▷ Isothermal heat absorption  $c-d$  along the cold face. The carrier absorbs heat (*Peltier*) from the cold face at constant temperature incrementing its entropy
- ▷ Isentropic compression  $d-e$  along the p-type TE. The entropy remains constant but the carrier absorbs electric work
- ▷ Isothermal heat transfer  $e-b$  along the hot face. At constant  $T_h$ , the carrier releases heat decreasing its entropy

The expansion and compression would be not isentropic (a heat exchanged would exist) if *Thomson* is considered. See Arenas et al. [2000], that includes it, and Chua et al. [2002] that includes *Thomson*, *Fourier* and *Joule*.

## 9.2 Finite element equations

The present chapter studies the global performance of *Peltier* coolers but also the details of displacements, temperature, voltage, stresses, electric and heat fluxes, magnetic field that can affect the accuracy of the approximated expressions (9.1) to (9.3).

In *Peltier* coolers, usually the thermocouple are arranged very closely, to allow the vertical heat transfer to be uniform. Due to the trend towards miniaturization in electronic and other devices, this tendency has recently been reinforced. Temperatures can also reach very high values not usual in traditional mesoscale applications. The interchange of heat flux between TE's of the same or different thermocouple can be important.

Therefore, the multi-coupled and the special interface 2-D (to simulate radiation and convection heat fluxes through the air) FE's are used in the present chapter. Note that the six d.o.f. will be used. However, all the calculations are in steady-state, avoiding the capacity and mass matrices in (4.28):

$$\begin{bmatrix} \mathcal{K}^{UU} & \mathcal{K}^{UT} & \mathcal{K}^{UV} & \mathcal{K}^{U\varphi} \\ \mathbf{0} & \mathcal{K}^{TT} & \mathcal{K}^{TV} & \mathcal{K}^{T\varphi} \\ \mathbf{0} & \mathcal{K}^{VT} & \mathcal{K}^{VV} & \mathcal{K}^{V\varphi} \\ \mathbf{0} & \mathbf{0} & \mathbf{0} & \mathcal{K}^{\varphi\varphi} \end{bmatrix} \quad (9.4)$$

In addition and taking into account the galvanomagnetic and thermo-magnetic effects, the material properties  $\alpha$ ,  $\gamma$ ,  $\kappa$  are assumed to be tensor entities as in (8.3). Therefore, the terms  $\mathcal{K}^{T\varphi}$ ,  $\mathcal{K}^{V\varphi}$  are incorporated into the assembled FE matrix (9.4).

## 9.3 Finite element model

Using the two FE's, a CP1.4-127-045 *Peltier* cooler manufactured by MELCOR [2000] will be simulated. This cooler was chosen as representative of practical applications and is composed of 127 thermocouples electrically connected in series, as in Figure 9.3. One of them

was carefully measured to give the dimensions of Figure 9.4, where the upper alumina is in contact with the cold face and the lower with the hot. The maximum intensity of the thermocouple is 8.7 [A] (above that the irreversible *Joule* is prevalent) and under  $T_h = T_c = 50$  [°C] it can extract a heat power  $Q_{ctec} = 82.01$  [W] with voltage drop  $V_{tec} = 15.33$  [V] according to the manufacturer, see Table 9.2.

Only half of the thermocouple needs to be studied if it is assumed that the  $T_c$  and  $T_h$  distributions are constant, that is a reasonable hypothesis for medium and small devices. This is indicated by the symmetry line in the left view of Figure 9.4. If the temperature varies significantly, a mesh including more thermocouples can be studied although at a higher computational cost; in any case the variation will depend on the media the cooling device refrigerates, not on the thermocouple itself. Assuming the conservation of charge hypothesis ( $I_{tec}$  is the same everywhere in the *Peltier* cooler), only one thermocouple needs to be studied, fact which is represented by periodicity lines in Figure 9.4.

On a surface of symmetry, the *Neumann* boundary conditions for electric and heat fluxes will be automatically set to zero, while on the two periodicity copper “cuts” (connections in the following), the prescribed flux  $j_c \equiv j_{cfe} = I_{tec}/A_{con}$  is directly applied within the interface element (see Figure 9.5 and next section) to the connection area  $A_{con}$ . Given that air and alumina are good electric isolators, no other electric flux condition is necessary. On the other hand and in order to take into account galvanomagnetic and thermo-magnetic effects, a magnetic field  $B$  is applied along the  $x_3$  direction by means of the interface element.

Periodicity “cuts” are also present in the alumina mid-faces, represented in Figure 9.4 by sawed lines. An alternative to the use of the interface element for the prescription of

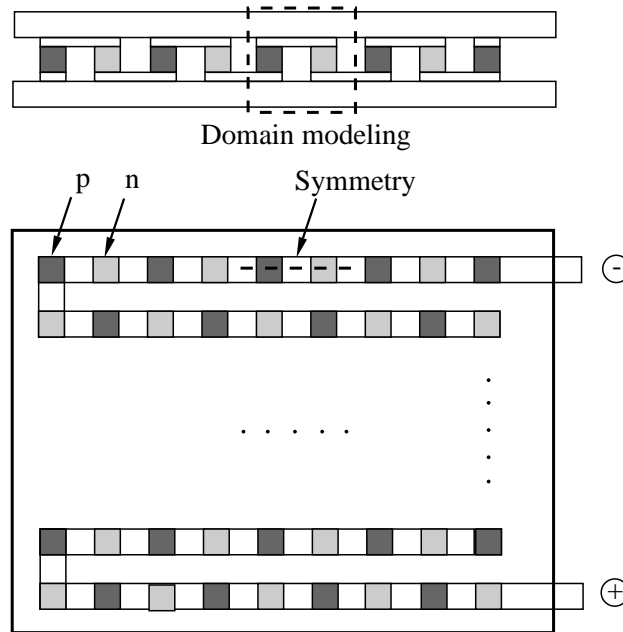


Figure 9.3: Top view scheme of the CP1.4-127-045 thermoelectric cell. Periodicity (top) and symmetry (bottom).

intensity is the term  $I_{\Omega} \equiv I_{tec}/\Omega_e$  ( $\Omega_e$  would be the chosen element volume) in the adjacent 3-D elements, but with this solution some flux concentrations locally appear.

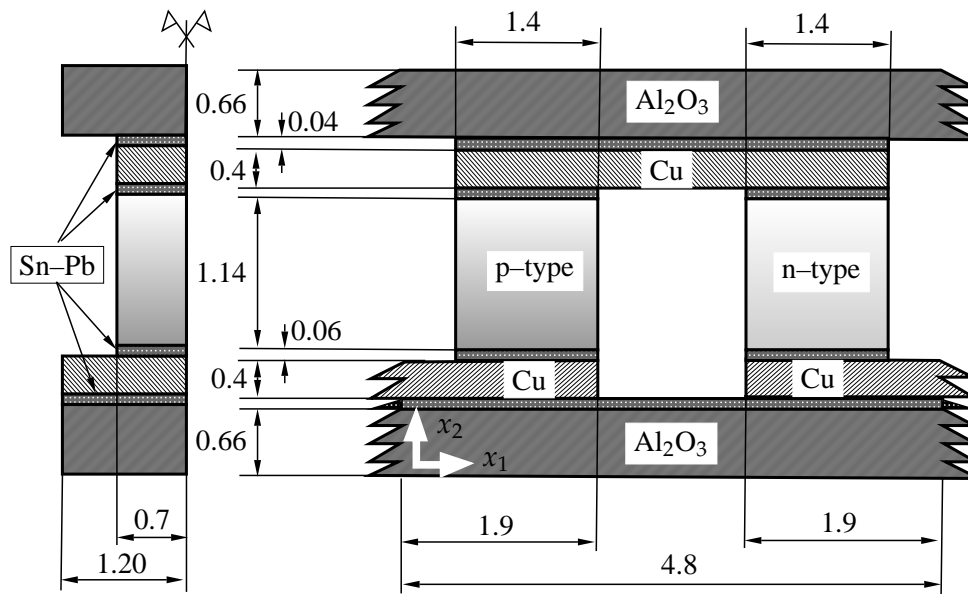


Figure 9.4: Dimensions [mm] of a CP1.4-127-045 thermocouple, materials and origin of coordinates. Symmetry represented by flags, periodicity by sawed lines.

The interface element is also used in the cold and hot faces to force convection and radiation with air. The influence of other contact fluids, such as water, could be easily simulating by changing  $h$ .

The *Dirichlet* boundary conditions are applied at a surface of voltage reference  $V = 0$  [V], chosen to be in the middle of the upper copper to preserve symmetry of the electric results, and in the cold and hot face surfaces to the corresponding  $T_c$  and  $T_h$  (Figure 9.5). Note that in spite of prescribing both *Neumann* and *Dirichlet* conditions in these surfaces, the problem is not of a mixed type, the interface element will only modify the related external unknown fluxes. Finally, the thermocouple is fixed at the cold and hot faces to study the mechanical interactions.

From the prescribed  $T_h, T_c, I_{tec}$ , at any point of the domain the unknown volumetric variables  $T, V, j, q$  as a function of space are found. From the difference between the  $V$  values at each of the connections, the potential drop  $V_{fe}$  (numerical counterpart of  $V_{af}$  in Figure 9.1) in a single thermocouple can be easily computed. Similarly, from the addition of "reactions" (using the mechanical analogy) in the upper surface or cold face, the numerical total heat extracted  $Q_{cfe}$  is calculated.

An optimal mesh size is now found using the parametrization of all dimensions from Figure 9.4. In Figure 9.6, the potential drop between connexions  $V_{fe}$  and the extracted heat  $Q_{cfe}$  are plotted versus the total number of finite elements. The variables  $V_{fe}$  and  $Q_{cfe}$  have been normalized to their maximum values (coarse mesh) to show both convergences. With the restriction of conformity and similarity of finite element sizes, the converging mesh is composed of 12,670 elements showed in Figure 9.5. It is interesting to note that  $V_{fe}$  reaches

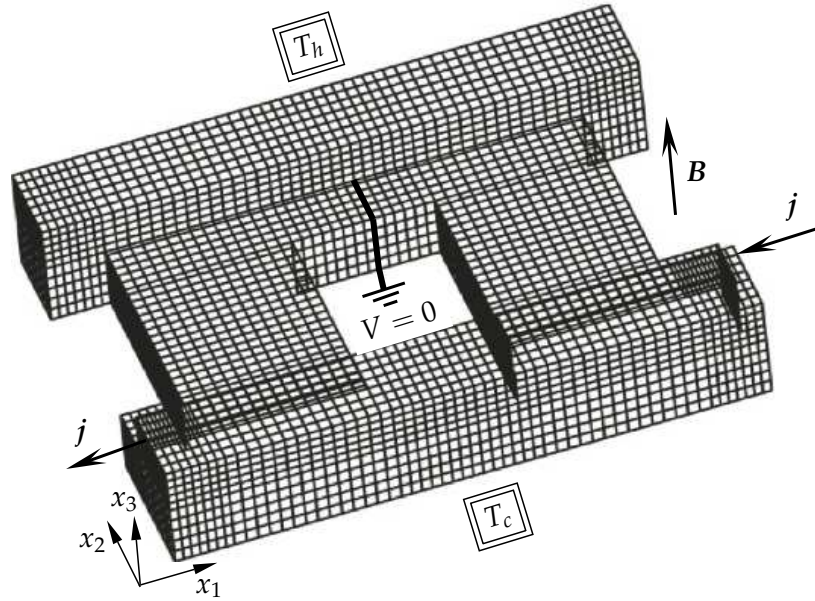


Figure 9.5: Mesh of 12,670 elements for half thermocouple. Prescribed voltage, temperature, magnetic field and electric flux.

the correct value with very few elements (about 320) but the power  $Q_{cfe}$ , proportional to a first derivative, needs a substantial higher number of at least 10,000.

In order to obtain accurate results (the problem is highly non-linear), the residual norm  $\|\mathcal{R}\|$  must exhibit a quadratic convergence, Zienkiewicz et al. [2005]. The order of convergence is obtained from the expression  $\ln \|\mathcal{R}_{k+1}\| = \ln \mu + m_r \ln \|\mathcal{R}_k\|$ , where  $k$  and  $k + 1$  are two successive iterations,  $\mu$  is a parameter of about half of the CPU precision and  $m_r$  is the ratio of convergence. Table 9.1 shows the residual norms for each iteration; the ratio of convergence is  $m_r \approx 2$ , therefore the quadratic convergence is attained in only four iterations.

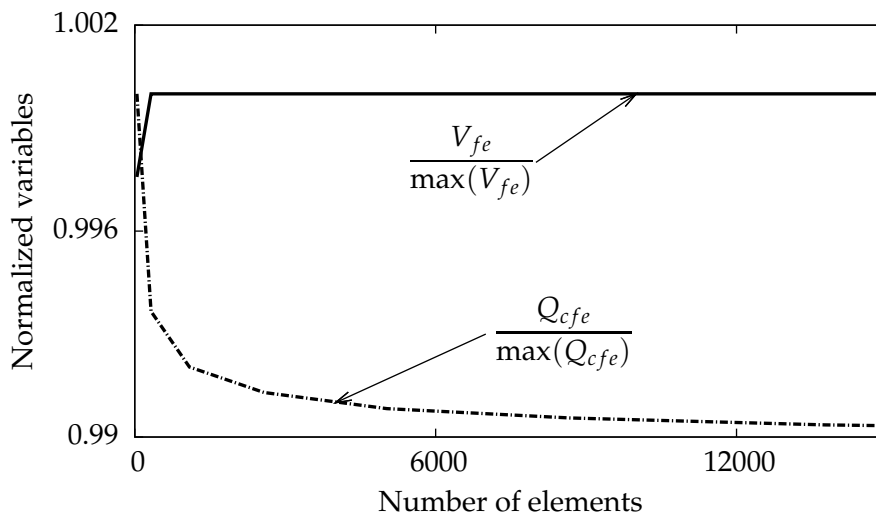


Figure 9.6: Convergence of normalized voltage drop and extracted heat versus number of elements.



Iteration	$  \mathcal{R}  $
1	1.0002
2	0.0631
3	0.0029
4	0.00001

Table 9.1: Quadratic residual norm convergence.

	Analytical	FEM	Melcor
$Q_{ctec}$ [W]	91.94	85.57	82.01
$V_{tec}$ [V]	14.71	16.74	15.33
$T_{max}$ [°C]	-	78.5	-
$I_{max}$ [A]	7.99	8.7	8.7
COP [-]	0.78	0.59	0.61

Table 9.2: Thermoelectric cell performance for  $T_h = T_c = 50$  [°C],  $I_{tec} = 8.7$  [A].

### 9.3.1 Modeling thermal and electrical contacts

As has been commented in the introduction, thermal and electrical contacts affect to the performance of the *Peltier* coolers. Several procedures can be found in the specialized literature to model these contacts:

- i) The use of special thermal contact FE, see Soba and Denis [2009]
- ii) The addition of a fictitious layer of infinitesimal thickness, considering the thermal and electrical conductances as in Ju [2008]

The multi-coupled FE developed in the present thesis can not simulate these contacts. For this reason and for the sake of brevity, the present thesis proposes a combined procedure, involving the modification of electric and thermal conductivities of the Sn-Pb layer and

taking into account the temperature–dependence of the contact conductivities between this and the Cu. For this purpose, two steps are used:

1. A circular  $a$ -spot model, Braunovic [2007], writing the thermal  $\kappa_c$  and electric  $\gamma_c$  contact conductivities as:

$$\begin{aligned}\kappa_c &= 4\eta_c \left( \frac{\kappa_{Cu} \kappa}{\kappa + \kappa_{Cu}} \right) \quad ; \\ \gamma_c &= 4\eta_c \left( \frac{\gamma_{Cu} \gamma}{\gamma + \gamma_{Cu}} \right)\end{aligned}\tag{9.5}$$

where  $\kappa_{Cu}, \gamma_{Cu}$  are the conductivities of the Cu given in Appendix B and  $\eta_c$  the ratio between real and total interface contact surfaces. For example, if  $\eta_c = 1$  the complete interface is in contact but in reality  $\eta_c < 1$  due to roughness, misalignment, etc.

2. From the series–circuit theory, effective Sn–Pb conductivities  $\kappa_{eff}^{Sn}, \gamma_{eff}^{Sn}$  are expressed by:

$$\begin{aligned}\kappa_{eff}^{Sn} &= \frac{\kappa_{Sn} \kappa_c}{\kappa_{Sn} + \kappa_c} \quad ; \\ \gamma_{eff}^{Sn} &= \frac{\gamma_{Sn} \gamma_c}{\gamma_{Sn} + \gamma_c}\end{aligned}\tag{9.6}$$

where  $\kappa_{Sn}, \gamma_{Sn}$  are the Sn–Pb conductivities also given in the Appendix B. Finally, to feed the FE code with the conductivities' variation, results from equation (9.6) are fitted to quadratic functions of  $T$ :

$$\begin{aligned}\kappa_{eff}^{Sn} &= \frac{1.54 \times 10^4 \eta_c (52050 - 112 T + T^2)}{1.21 \times 10^7 - 112 T + T^2 + \eta_c (1.67 \times 10^6 - 3.6 \times 10^3 T + 32 T^2)} \quad ; \\ \gamma_{eff}^{Sn} &= \frac{2.32 \times 10^9 \eta_c (43875 - 224 T + T^2)}{2.33 \times 10^7 - 224 T - T^2 + \eta_c (2.17 \times 10^6 - 1.11 \times 10^4 T + 49 T^2)}\end{aligned}\tag{9.7}$$

It will be calculated in following section that the influence of  $\eta_c$  is very small unless the contact is very imperfect,  $\eta_c < 0.6$ . The contact  $\text{Al}_2\text{O}_3$ –Cu is not modeled in the present thesis since it is considered from the beginning irrelevant for the global results.

## 9.4 Results

In this section, the two FE's and the mesh from Figure 9.5 have been used to simulate the thermocouple. The parameters calculated, directly or indirectly from the FE results are:

- ▷ Potential drop in the thermocouple, taken directly from the difference of nodal values at both connectors,  $V_{fe}$
- ▷ Potential drop in the *Peltier* cooler,  $V_{tec} = 127 V_{fe}$
- ▷ Maximum and minimum  $T_{max}$  and  $T_{min}$  temperatures in the thermocouple, also from nodal values

- ▷ Heat taken from the cold face of a thermocouple,  $Q_{cfe}$
- ▷ Heat taken from the cold face  $Q_{ctec} = 2 \cdot 127 Q_{cfe}$  by the *Peltier* device
- ▷ Coefficient of performance,  $COP = Q_{ctec}/(V_{tec} I_{tec})$

#### 9.4.1 Study of thermoelectric interactions

The thermocouple is simulated here for  $I_{tec} = 8.7$  [A] and  $T_h = T_c = 50$  [°C]. These boundary conditions are chosen to maximize the studied effects, behaving the thermocouple as a heat pump that takes heat from the cold face (in fact a source) and gives it to the hot face (a sink).

Figure 9.7 top-left shows the voltage distribution that decreases more or less linearly in the TE, while is constant in the other materials, good conductors or isolators. Inside the copper and closer to the cold face, an antisymmetric horizontal distribution is observed, due to the prescription of the reference zero potential. The total potential drop is 0.1318 [V], that for the 127 *Peltier* cooler gives 16.74 [V] (see Table 9.2). This number is to be compared with 15.33 [V] given in the catalog, with a 9% difference. The drop occurs only in the TE, in the copper and even in the solders is very small due to their relatively high (two orders of magnitude for the first) electric conductivity. The analytical numbers in the table are computed using the simplified equations (9.1) to (9.3).

In the top-right figure, the temperature distribution shows a parabolic distribution inside the TE, due to the *Joule* effect. This is a very important fact, since the maximum temperature in the center is 78.5 [°C], a 57% higher than the nominal  $T_h$ . Obviously, this increment substantially affects the heat calculated from (9.1), see next paragraph. The alumina and copper close to the cold face are at a temperature similar to  $T_h$ ; the value of 47.9 [°C] in the surface, different from the prescribed  $T_h$ , is due to the discrete palette of colors used in the FE interpolation. In any case a slight gradient appears, close to the hot face to allow the transfer of heat power to it.

These distributions strongly depend on the boundary conditions. In Figure 9.8,  $I_{tec}$  and  $T_h$  are maintained but  $T_c$  decreases through the functioning limits of the catalog. The distributions of voltage (top) and temperature (bottom) are drawn along a  $x_2$  vertical line at the center of the p-type TE. As mentioned, voltage is linear or constant in all materials except in the TE where it varies linearly for  $T_c = 50$  [°C] and slightly non-linearly for the other values. It also varies in the solders, although it can not be appreciated due to scale. The  $V$  drop decreases with the increase of  $T_c$ , since *Seebeck* is directly proportional to the temperature difference and, therefore, the conversion of thermal energy into electricity is reduced with this difference.

About the temperature, the prescription of  $T_c$  forces the final value in the left part of the plot. *Joule* is very clear inside the TE, specially for the heat pump mode  $T_c = 50$ , and temperature is non-linear for all choices of  $T_c$ . Inside the copper and alumina *Joule* is not

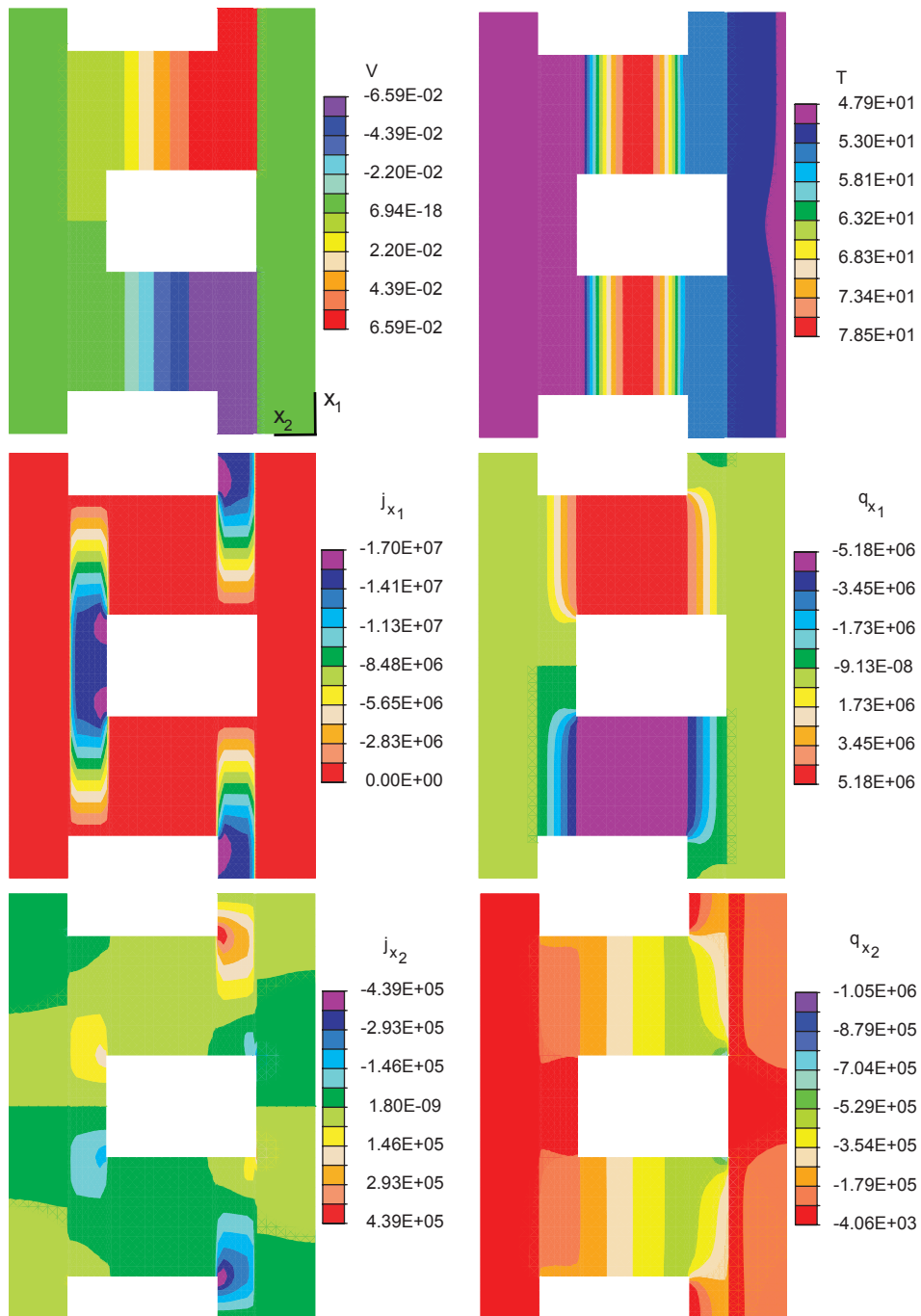


Figure 9.7: Contour plot distributions from the finite element analyses, electric magnitudes in left and thermal in right column. Top: Voltage and temperature. Middle: Horizontal fluxes. Bottom: Vertical fluxes, all for  $I_{tec} = 8,7$  [A],  $T_c = T_h = 50$  [°C].

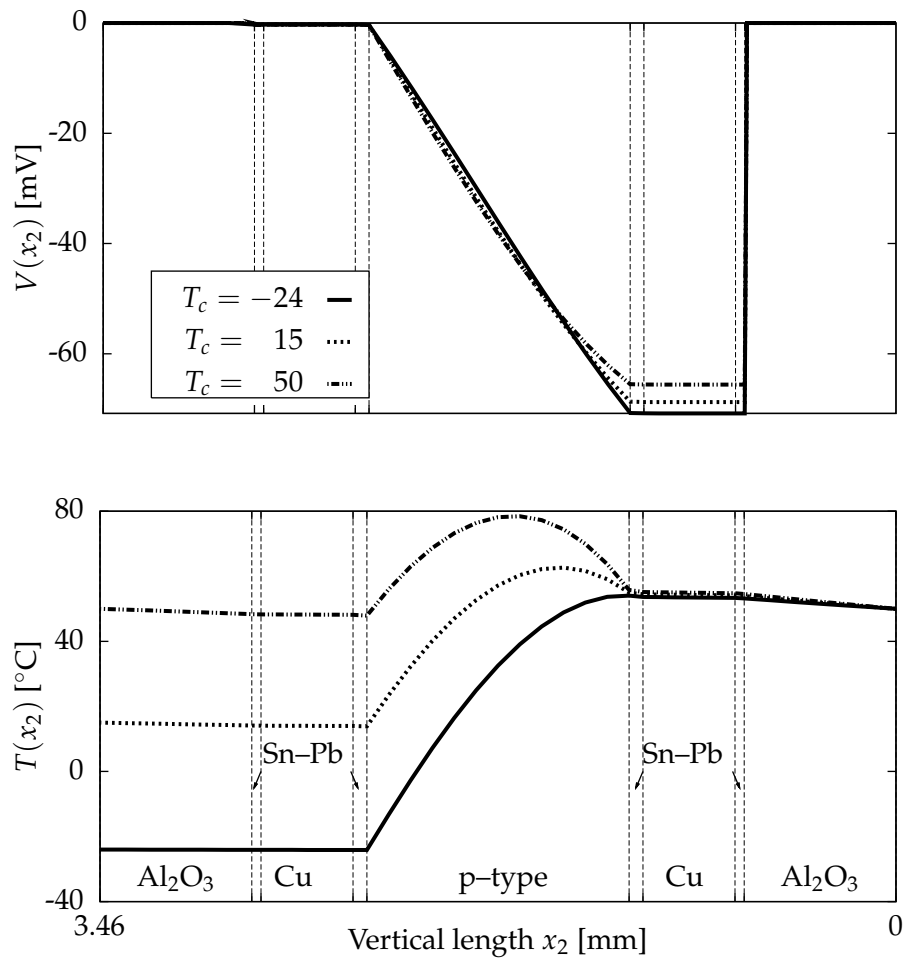


Figure 9.8: Vertical temperature and voltage distributions for  $T_h = 50$  [°C] and several  $T_c$ . Origin at the thermoelement bottom-left.

present, in the first due to its high electric conductivity and in the second to the absence of electric current (very low electric conductivity), therefore temperature is almost linear or even constant due to the lack of internal heat sources. At the copper-TE interface close to the hot face, temperature almost coincides in all cases. Again the variation of the distribution in the Sn-Pb solders is too small to be appreciated within the scale of the figures.

In the left column, middle and bottom Figure 9.7, the horizontal and vertical electric fluxes are shown. Since the electric intensity is constant, the maximum flux occurs in both coppers, where the conductive area is smaller, and zero in the alumina (an electric isolator). The flux is unidirectional (both horizontal and vertical in the copper and vertical but with different sign in the TE) except around some corners where a significant change of direction is represented by the concentration in both materials. In the TE's this flux is constant, in the copper around the area by the TE is mostly vertical while in the rest mostly horizontal, with an abrupt change in the corners. This implies that the typical "rectangular" shape of the copper components is not optimal in the sense of electric conduction. Smaller fluxes than

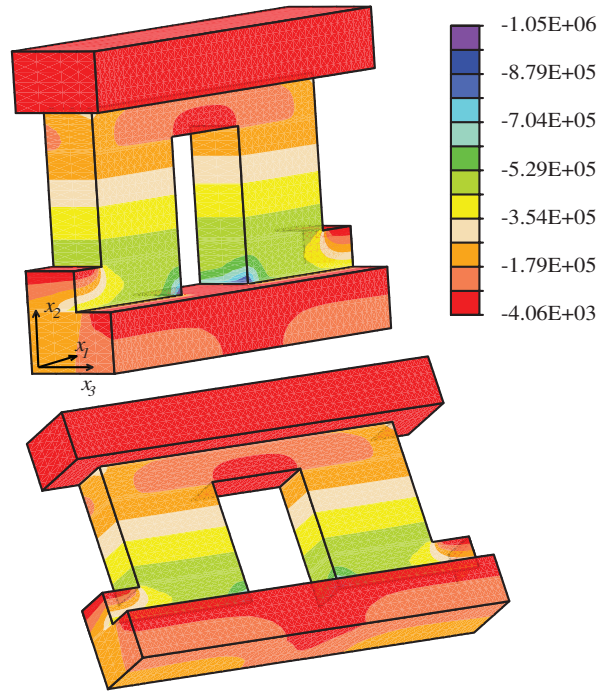


Figure 9.9: Three-dimensional view of the vertical heat flux  $q_{x_2}$  for  $I_{tec} = 8,7$  [A],  $T_c = T_h = 50$  [°C].

that of copper are present in the solders of copper and TE, due to their lower electric conductivity. Note that the application of the prescribed current  $I_{tec}$  with the interface FE at the end of the external cut copper section (“connectors”) does not produce any concentration.

The heat flux is shown in the second column, middle and bottom figures. The most interesting is the latter, vertical against  $x_2$  (from the cold to the hot face), the direction along which the heat pumping occurs. In the TE, the flux is more intense closer to the hot face, due to the electric energy that is transformed into thermal and that is directed against the direction of thermal conduction (towards the hot face). In the middle figure again a strong concentration in the internal corners of the copper–alumina connection is appreciated, that will be quantified in the next paragraph. These concentrations are due to the sudden increment of the copper area, that forces the field lines to change direction towards the whole of the hot face and are antisymmetric with respect to the  $x_1$  direction. The value  $Q_{ctec} = 85.57$  [W] in Table 9.2 is taken from the FE reactions of the alumina external surface in the cold face.

In spite of the 3D nature of the analysis, Figure 9.7 is represented in the  $x_1$ – $x_2$  plane, since the distributions are mostly 2–D. But there are some exceptions, in Figure 9.9 the 3–D view of the vertical flux shows that the mentioned concentration corner also happens in the perpendicular plane. Also, in the hot face the flux is higher in the area vertical to the TE, which means that even if  $T_h$  is forced to be constant the flux will be variable. This lack of uniformity also happens in the cold face, but is not visible due to the scale.

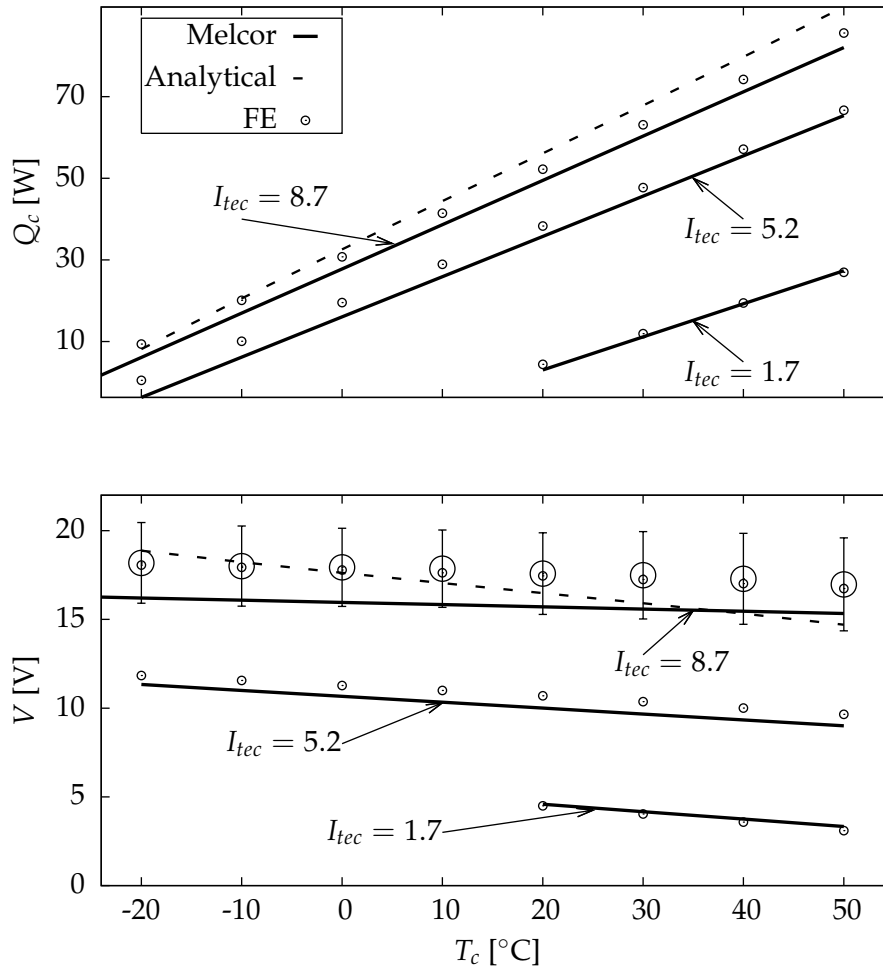


Figure 9.10: Comparison of analytical formulae (Rowe [1995]), current finite element and manufacturer (MELCOR [2000]). Heat extracted and voltage drop for the functioning range of  $I_{tec}$ ,  $T_c$  and for  $T_h = 50$  [°C].

#### 9.4.2 Comparison between numerical and experimental results

The FE is used to simulate the thermocouple for three values of  $I_{tec}$ , the maximum and minimum and another intermediate, and for  $T_h = 50$  [°C], all with variable  $T_c$ . These values are chosen to maximize the *Peltier* and *Joule* and to cancel *Fourier*. *Thomson* is directly included in the FE formulation with all its non-linearities and terms, although not in (9.1).

In Figure 9.10 the distributions for  $Q_{ctec}$  (top) and  $V_{tec}$  (bottom) are shown. For the first, the correlation between the results, both in value and slope, given by the Melcor catalog and those of the current FE are very close for the extracted heat, even for the maximum intensity  $I_{tec} = 8.7$  [A], that maximizes the irreversible *Joule*. For the voltage drop  $V_{tec}$ , the agreement is perfect and good for the first two intensities and differs an almost constant 8.4% for the highest.

In any case this result is very sensitive to material properties and boundary conditions: for the high  $I_{tec}$ , standard deviations bars (see Section 9.5) show that with a small variation

results almost coincide in the lower bound with those from the manufacturer. The simplified equation (9.1) gives values of  $Q_{ctec}$  and specially  $V_{tec}$  (plotted only for the maximum intensity) not that similar to those of the manufacturer. For the latter, the slope is different probably due to the absence of *Thomson*, that is based on the temperature-dependency of the *Seebeck* coefficient.

#### 9.4.3 Study of galvanomagnetic and thermo-magnetic interactions

The influence of the galvanomagnetic and thermo-magnetic interactions on the COP is studied in the present subsection using the thermocouple described in Section 9.3. Nevertheless, the  $\text{Bi}_2\text{Te}_3$  TE's are replaced by indium antimonide InSb ones since there are no magnetic properties in the literature for the former. Indium antimonide properties are given in the Appendix B. In addition, constant properties are considered and obtained using the average temperature between the external faces,  $T_m = (T_c + T_h)/2$ .

According to Landau and Lifshitz [1984], Rowe [1995] and Newnham [2005] the presence of a magnetic field changes the figure-of-merit of the TE's and the cooling capacity of the *Peltier* coolers. Specifically, the *Nernst* and *Ettingshausen* effects are the transverse analogues of the *Seebeck* and *Peltier* ones. Therefore, the *Nernst* and *Ettingshausen* effects could be used in the generation of electricity and in cooling applications, respectively. In addition, the COP could be increased optimizing the TE shape since the cooling capacity strongly depends on the geometrical parameters.

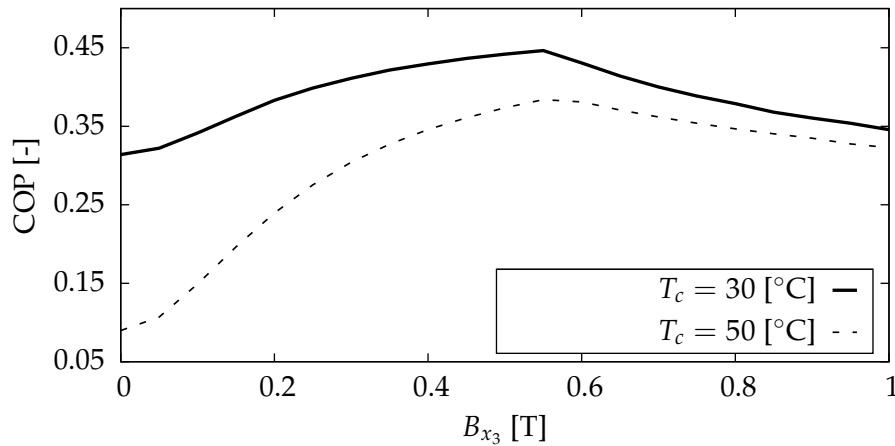


Figure 9.11: Coefficient-of-performance versus magnetic field along the  $x_3$  direction, maintaining  $T_h = 50$  [°C],  $I_{tec} = 7.5$  [A].

In order to study the influence of a magnetic field on the COP, a magnetic field along the  $x_3$  direction  $B_{x_3}$  (perpendicular to the electric and thermal fluxes, which are along the  $x_1$  direction) is applied using the special interface FE. Two different cases are considered:  $T_c = 30$ ,  $T_c = 50$  [°C], fixing the temperature at the hot face:  $T_h = 50$  [°C]. Again, an electric current  $I_{tec} = 7.5$  [A] is applied by means of the interface FE.



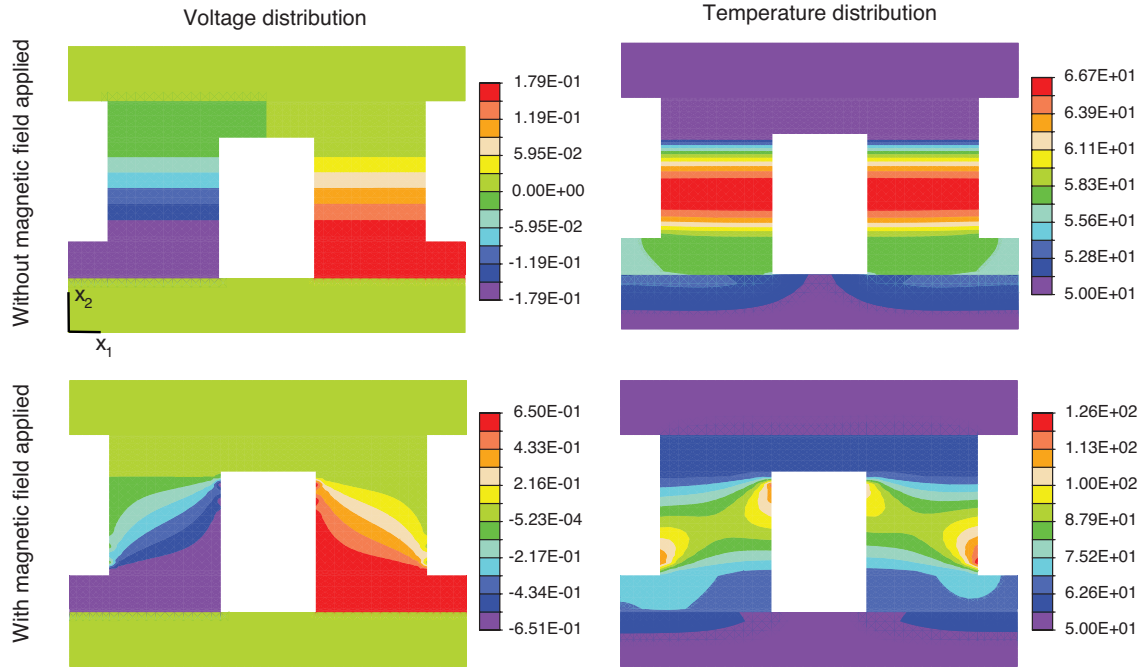


Figure 9.12: Voltage (left) and temperature (right) distributions without (top) and with (bottom) applied magnetic field  $B_{x_3} = 0.55$  [T].  $T_h = 50$ ,  $T_c = 50$  [°C] and  $I_{tec} = 7.5$  [A].

Figure 9.11 shows the COP versus the applied magnetic field  $B_{x_3}$  for the two cases previously commented. Both curves show a maximum COP at  $B_{x_3} = 0.55$  [T]. Note that a ferrite or ceramic magnets typically exhibit fields of 0.5 to 1 [T]. The magnetic field increases the *Seebeck* coefficient and decreases the thermal and electric conductivities. Therefore, the figure-of-merit exhibits a maximum, which is  $B_{x_3} = 0.55$  [T] in the InSb material. Note that this maximum agrees with that given in Rowe [1995] for the  $\text{Bi}_{0.88}\text{Sb}_{0.12}$  material. For this optimum, the COP is enhanced approximately 41% and 260% for the cases  $T_c = 30$  and  $T_c = 50$  [°C], respectively.

Figure 9.12 shows the voltage (left) and temperature (right) distributions without (top) and with (bottom) prescribed magnetic field  $B_{x_3} = 0.55$  [T],  $T_h = 50$ ,  $T_c = 30$  [°C] and  $I_{tec} = 7.5$ [A]. These distributions has been previously discussed in Figure 9.7 (top) (when  $B_{x_3} = 0$ ,  $T_c = T_h = 50$  [°C] and the material is  $\text{Bi}_2\text{Te}_3$ ). The presence of the magnetic field alters the distributions, increasing the potential drop and the maximum temperature up to 126 [°C] due to the *Lorentz* forces exerted by the magnetic field. Although this increasing may seem detrimental to device performance, the *Ettingshausen* effect permits the evacuation of more heat from the cold face.

Figure 9.13 shows the COP versus the angle  $\theta$  between the magnetic field and the fluxes for the two cases ( $T_c = 30, 50$  [°C]) in order to study the influence of the magnetic field direction on the COP. The maximum values correspond to the perpendicular fields and the minimum to the parallel ones. Therefore, applying a parallel field is the same as not applying magnetic field.

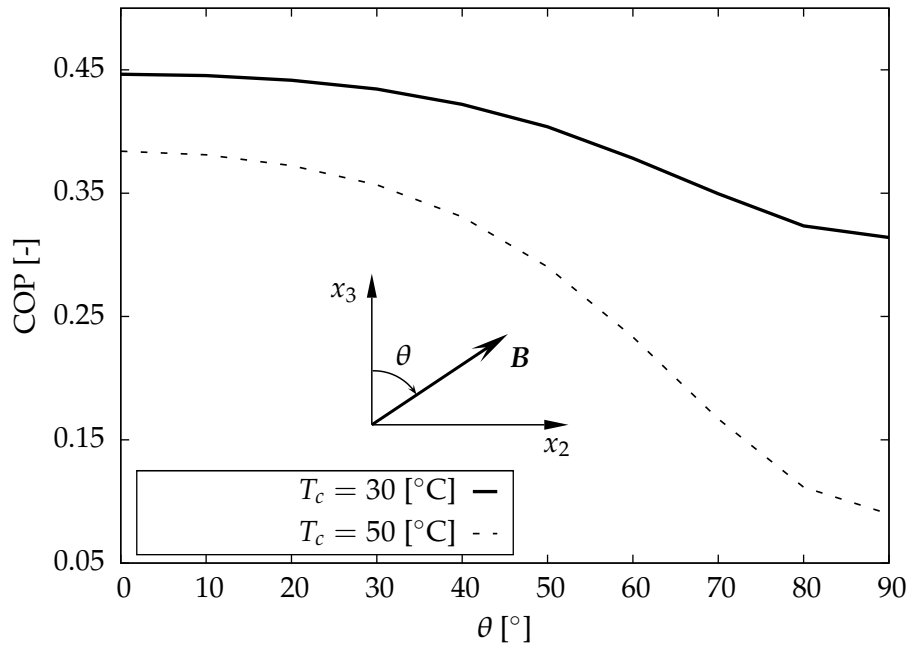


Figure 9.13: Coefficient-of-performance versus angle between magnetic field and electric and thermal fluxes, maintaining  $T_h = 50$  [°C],  $I_{tec} = 7.5$  [A] and  $B = 0.55$  [T]. Note that electric and thermal fluxes are prescribed along the  $x_2$  direction.

#### 9.4.4 Study of thermal stresses

The aim of the present section is to perform an analysis of the thermal stresses due to the elasto-thermo-electric and elasto-magneto-thermo-electric interactions. For this purpose, the model described in Section 9.3, assuming temperature-dependent properties, is used. Mechanical properties and thermal expansion coefficients for all materials are given in the Appendix B. The reference temperature  $T_0$  is assumed to be 25 [°C]. Finally and as was commented before, the thermocouple is mechanically fixed at the cold and hot faces.

The displacements along the  $x_1$ ,  $x_2$  and  $x_3$  directions are shown in Figure 9.14 (top-left), (top-right) and (bottom), respectively. As expected, all the displacement distributions are symmetric. The order of magnitude of these displacements is  $10^{-7}$  [m]. In addition, they show an expansion along the  $x_1$ - $x_2$  directions and a compression along  $x_3$  since the final temperature distributions (see Figure 9.7 top-right) are greater than  $T_0$ . This mechanical response can be observed in the Figure 9.16, where the undeformed (red line) and deformed meshes are shown. The deformed one is magnified by a factor 200 for clarity.

Two 3-D views of the *Von Mises* stresses within thermocouple are plotted in the Figure 9.15. *Von Mises* stresses are computed from the second deviatoric stress invariant and give a measure of the stresses that could cause plastic deformation if their values are greater than the yield strength of the material. From Figure 9.15:

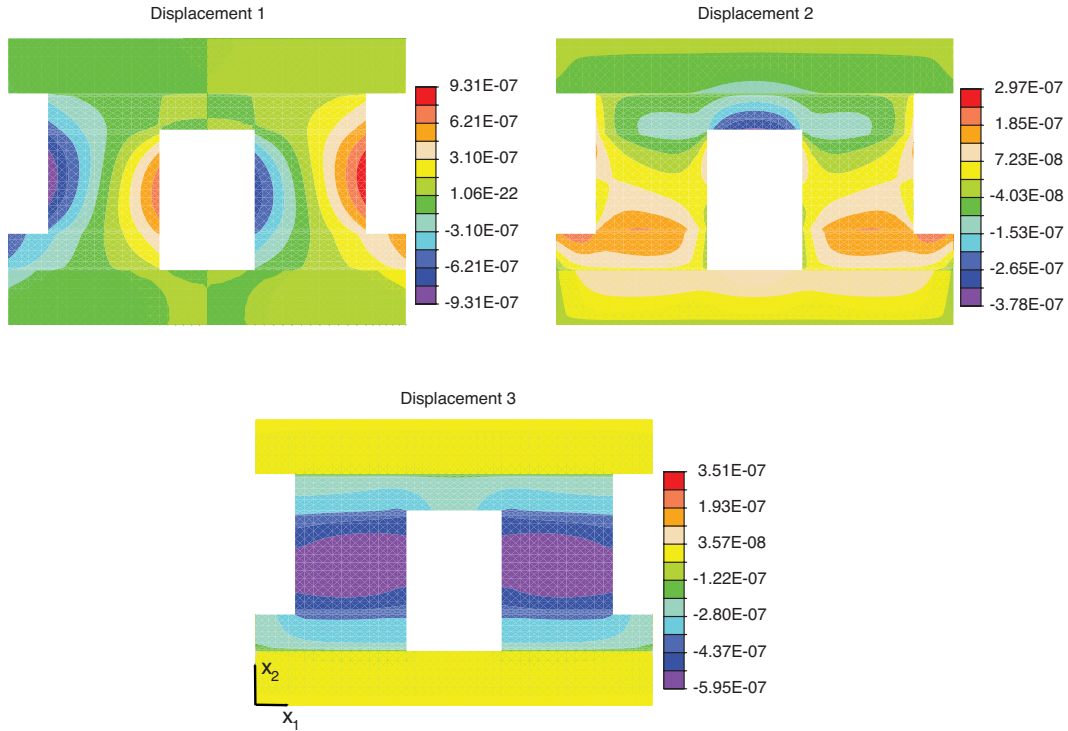


Figure 9.14: Contour plot distributions of the displacements along the  $x_1$  (top-left),  $x_2$  (top-right) and  $x_3$  (bottom) directions for  $I_{tec} = 7.5$  [A],  $T_c = T_h = 50$  [°C].

- ▷ The maximum stress is about 93 [MPa] and is localized at the corners of the thermocouple (inside the alumina at the cold face). This result agrees with that reported in Clin et al. [2009]
- ▷ A stress of 60 [MPa] (yellow in the figure) is reached at the four corners of the hot side (inside the TE's). Similar results, 64.2 and 50 [MPa], were reported in Gao et al. [2011] and Clin et al. [2009], respectively

For the study of the elasto-magneto-thermo-electric interaction, Figure 9.17 shows the *Von Mises* stresses for a model as that shown in Figure 9.15 but prescribing a magnetic field  $B_{x_3} = 0.55$  [T]. Note that the deformed mesh is also shown in this figure. Now, the stresses inside the TE's increase due to the presence of the *Lorentz* forces: voltage and temperature distributions are disturbed by the magnetic field, see Figure 9.12 (right). For this applied magnetic field, the stress increases from 60 to 220 [MPa]; the COP from 0.1 to 0.45, see Figure 9.11.

Figure 9.18 plots the maximum *Von Mises* stresses inside the TE's versus the applied magnetic field  $B_{x_3}$  for the cases shown in Figure 9.11. The stresses increase with increasing the magnetic field. Therefore, the increasing of COP is limited by the maximum TE stresses. Note that the ultimate tensile strength for the TE's is approximately 65 [MPa], according to Clin et al. [2009].

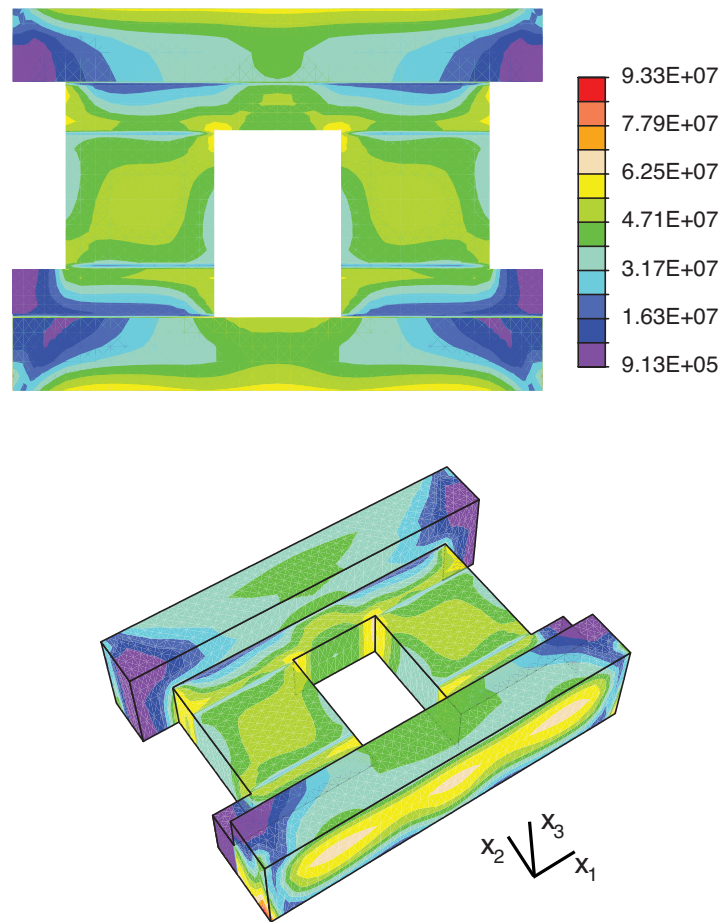


Figure 9.15: Two views of the *Von Mises* stresses for  $I_{tec} = 7.5$  [A],  $T_c = T_h = 50$  [°C].

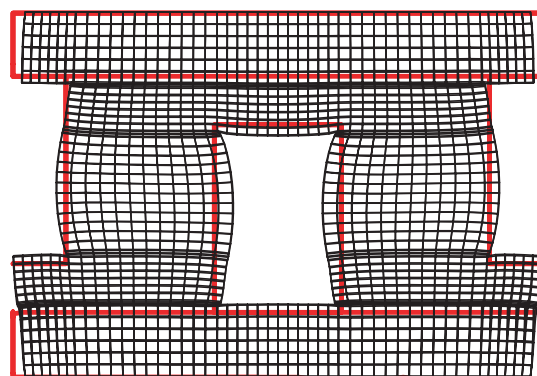


Figure 9.16: Undeformed mesh (red line) and deformed one due to the thermal stresses. For clarity, the deformed mesh is magnified by a factor 200.

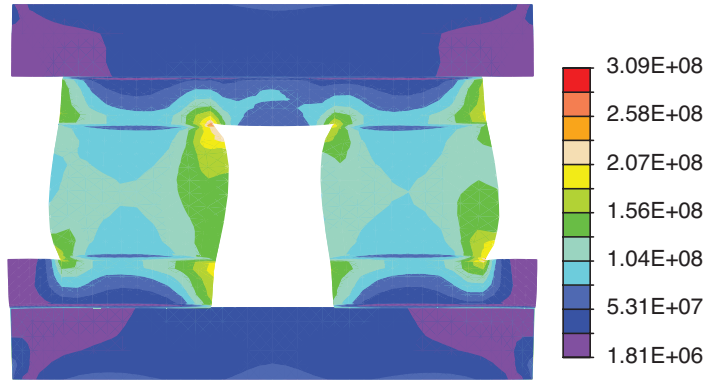


Figure 9.17: View of the *Von Mises* stresses for  $I_{tec} = 7.5$  [A],  $T_c = T_h = 50$  [°C] and  $B_{x_3} = 0.55$  [T].

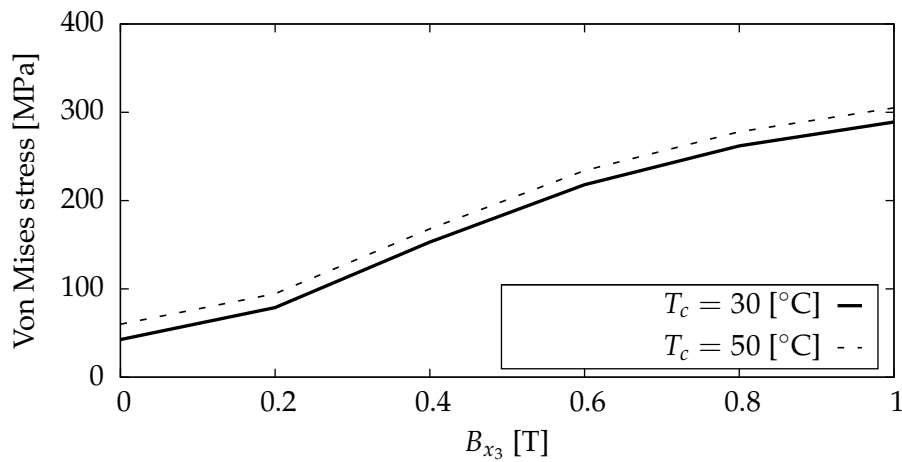


Figure 9.18: Maximum *Von Mises* stresses inside the thermoelement versus prescribed magnetic field along the  $x_3$  direction, maintaining  $T_h = 50$  [°C] and  $I_{tec} = 7.5$  [A].

Summarizing, stresses inside the TE's must be considered for the optimization of the COP using magnetic fields.

## 9.5 Sensitivity Analysis

The aim of this section is to study the influence of the design or random variables on the COP. For this purpose, a Sensitivity Analysis (SA) is performed combining the Monte Carlo (MC) and the FE analyses. The SA output permits to identify and quantify the main variables affecting the COP, with the intention to improve this performance variable. Appendix A describes the SA, which combines the MC and the FE.

### 9.5.1 Problem definition

The main task in developing a SA is the choice of the design variables and their distribution functions, often from experimental considerations, Saltelli et al. [2004]. In the present thesis, the design variables are:

- a) Geometric dimensions

b) Material properties of all materials

c) Prescribed  $I_{tec}$ ,  $T_c$ ,  $T_h$

Their distribution functions are not reported by the manufacturer and they are assumed to be normally distributed. The mean of the design variables are also assumed to be those give in the Appendix B, while the Standardized Regression Coefficient (SRC) notation and the standard deviation are given in Table 9.3. These are assumed to be:

- ▷ 5% for the geometric parameters
- ▷ 1% for the prescribed variables, mostly due to variations in the temperature distributions and errors in the electric source
- ▷ 5% for the material parameters measurement error, Smith and Wolfe [1962]

In Table 9.3 the TM properties  $\alpha$ ,  $\gamma$ ,  $\kappa$  are represented by three variables, corresponding to the three polynomial coefficients of given in Appendix B.

In order to generate the sample of the random variables, the *Latin hypercube* technique is used since the convergence is faster than that of the standard random technique, see Palma et al. [2009]. Finally, an optimized (to reduce the CPU cost and guarantee the convergence) sample of size  $m = 100$  was calculated by the procedure also from Palma et al. [2009]. To sum up, there are 22 design variables normally distributed, three responses,  $V_{tec}$ ,  $Q_{ctec}$ , COP, and the model  $M_d$  is solved by the FE.

### 9.5.2 SA Results

The results obtained by the Uncertainty Analysis (UA) are shown in Figure 9.19, where the probability distribution functions of the responses for the case studied in subsection 9.4.1 are presented. The means agree well with the deterministic results showed in Figures 9.10 and Table 9.2, implying that the UA results are accurate. The type of distribution functions are obtained using the *Jarque-Bera* test, Jarque and Bera [1987]; concluding that the responses  $V_{tec}$ ,  $Q_{ctec}$  are not normally distributed but the COP is. This distribution types are expected since both voltage and extracted heat are non-linear (due to *Joule* and material nonlinearities) while the COP is a normalized variable.

In Figure 9.10 (bottom and  $I_{tec} = 8.7$  [A]) the voltage value was shown with error-bars. The mean (large circle) calculated here agrees well (only 1.4% error) with the deterministic results (small circle) while the lower end of the standard deviations (straight bars) slightly overlaps the manufacturer curves. Therefore, the probabilistic model with reasonable values of standard deviations agrees with the manufacturer results.

The SRC's obtained from the SA are shown in Figures 9.20. The top one shows that  $V_{tec}$  is most sensitive to the design variables  $\Theta_4$  (TE length) and  $\Theta_{13}$ ,  $\Theta_{14}$ ,  $\Theta_{15}$ , the electric conductivities. This is predictable, since *Joule* is a bulk effect that depends on the length and since the potential drop is proportional to the resistivity (inverse of  $\gamma$ ). The least relevant

Property	Standard deviation	Notation
Al <sub>2</sub> O <sub>3</sub> thickness	5%	Θ <sub>1</sub>
Sn-Pb thickness (lower)	5%	Θ <sub>2</sub>
Cu length	5%	Θ <sub>3</sub>
TE length	5%	Θ <sub>4</sub>
Sn-Pb thickness (upper)	5%	Θ <sub>5</sub>
$T_h$	1%	Θ <sub>6</sub>
$T_c$	1%	Θ <sub>7</sub>
$I_{tec}$	1%	Θ <sub>8</sub>
$\kappa$ (Al <sub>2</sub> O <sub>3</sub> )	5%	Θ <sub>9</sub>
$\alpha_0, \alpha_1, \alpha_2$ (TE)	5%	Θ <sub>10,11,12</sub>
$\gamma_0, \gamma_1, \gamma_2$ (TE)	5%	Θ <sub>13,14,15</sub>
$\kappa_0, \kappa_1, \kappa_2$ (TE)	5%	Θ <sub>16,17,18</sub>
$\gamma$ (Cu)	5%	Θ <sub>19</sub>
$\kappa$ (Cu)	5%	Θ <sub>20</sub>
$\gamma$ (Sn-Pb)	5%	Θ <sub>21</sub>
$\kappa$ (Sn-Pb)	5%	Θ <sub>22</sub>

Table 9.3: Standard deviations and standardized regression coefficient notation for the design variables. Upper solder between Cu-Al<sub>2</sub>O<sub>3</sub>, lower between Cu-Bi<sub>2</sub>Te<sub>3</sub>.

coefficient of the electric conductivity is  $\gamma_2$ , since the dependence on temperature of  $\gamma$  is practically linear in the studied range.

The SRC's for  $Q_{ctec}$  are in Figure 9.20 (middle). Now the most sensitive design variable is  $\Theta_{10}$  corresponding to  $\alpha_0$ , since the *Peltier* heat strongly depends on *Seebeck*. Again,  $\alpha_2$  is not very relevant since the material property is fairly linear. Again  $\Theta_{4,13,14,15}$  are relevant for the

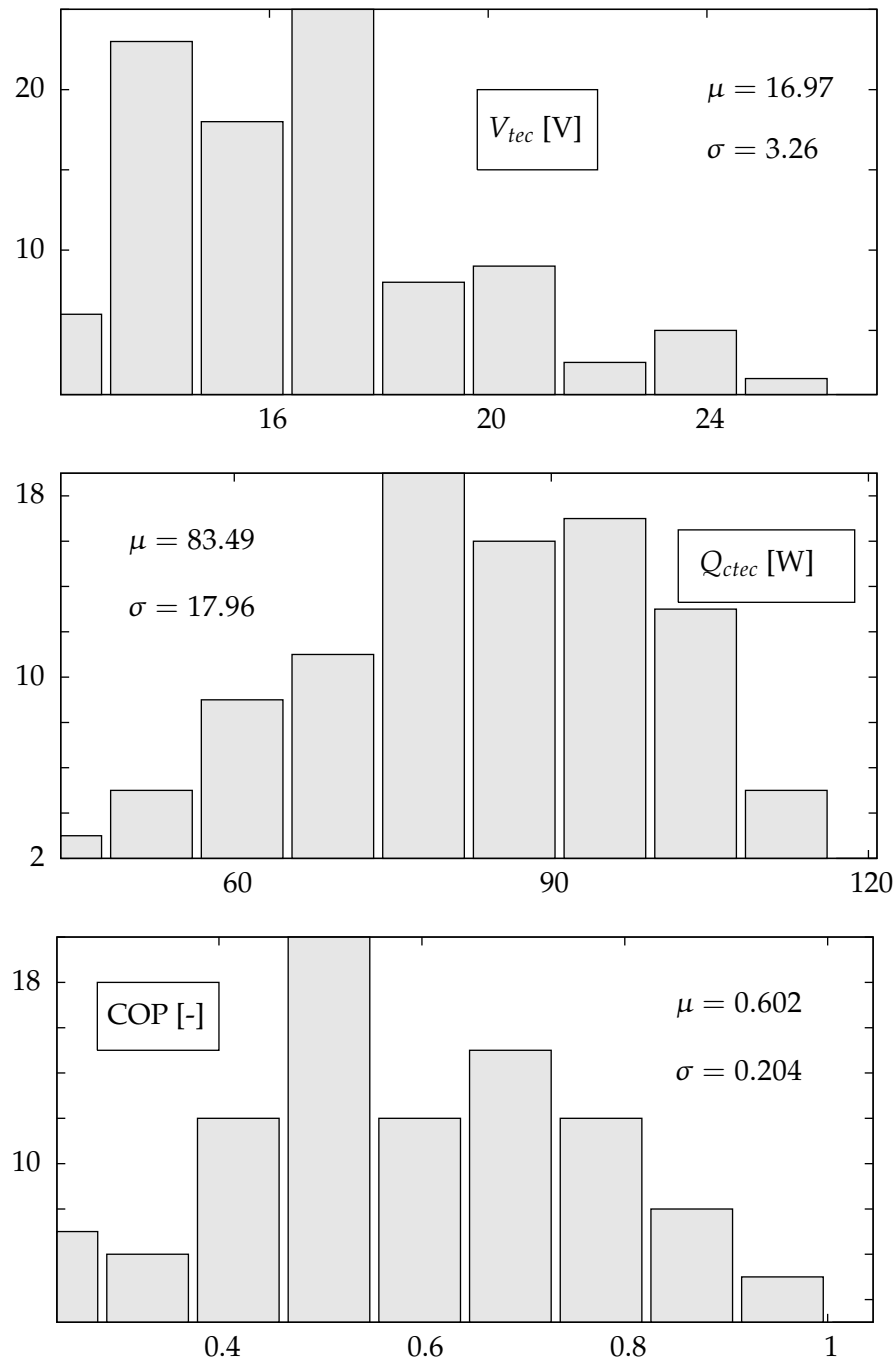


Figure 9.19: Probability distribution function for potential drop, extracted heat and coefficient-of-performance for  $T_c = T_h = 50$  [°C],  $I_{tec} = 8.7$  [A]. Mean and standard deviation indicated in each figure.



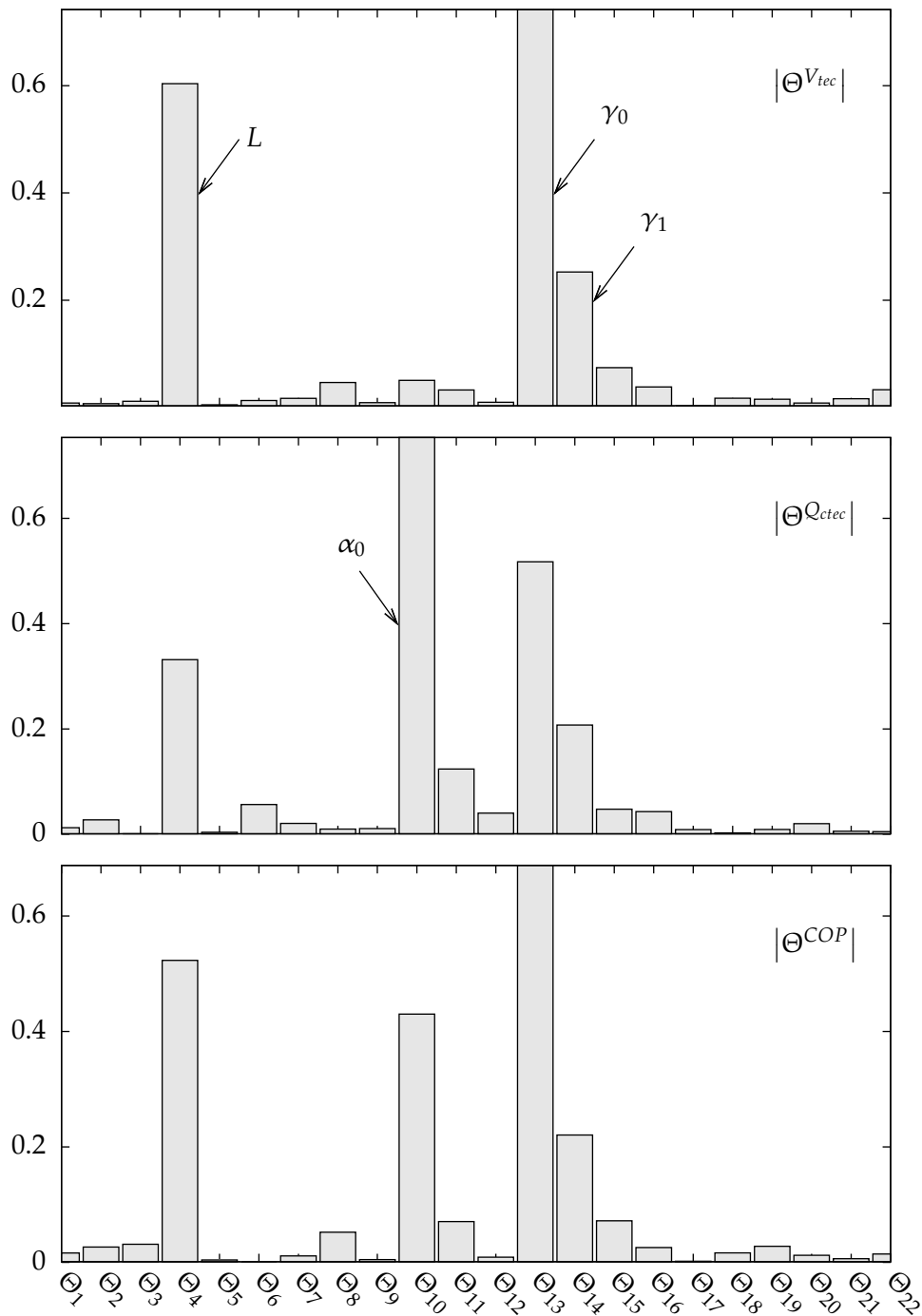


Figure 9.20: Standardized regression coefficients in absolute value for  $T_c = T_h = 50$  [°C],  $I_{tec} = 8.7$  [A]. Notation in Table 9.3.

same reasons as those of  $V_{tec}$ . Finally, since the COP is a relation of the previous responses, its sensitivities are the same, as shown in the bottom figure. Among the rest, input current  $\Theta_8$  is the only one slightly sensitive; in particular the SRC of the thermal conductivity is not relevant since conduction is cancelled by the choice  $T_h = T_c = 50$  [°C].

To study now the  $\kappa$  influence on the COP, Figure 9.21 compares the sensitivities of the TE material properties, i.e.,  $\Theta_{10}$  to  $\Theta_{18}$  for a different  $T_c = 15$  [°C]. The trend is similar but

as expected the SRC's  $\Theta_{10}$  and  $\Theta_{16}$  increase their importance, since both potential drop and thermal conduction depend on  $T_h - T_c$ . But the effect of  $\gamma_1$  is still much more relevant than that of  $\kappa_0$ :  $\Theta_{14} > \Theta_{16}$ . Therefore, for this type of material the temperature-dependency of electric conductivity should be considered in future works, while that of thermal conductivity is much less important.

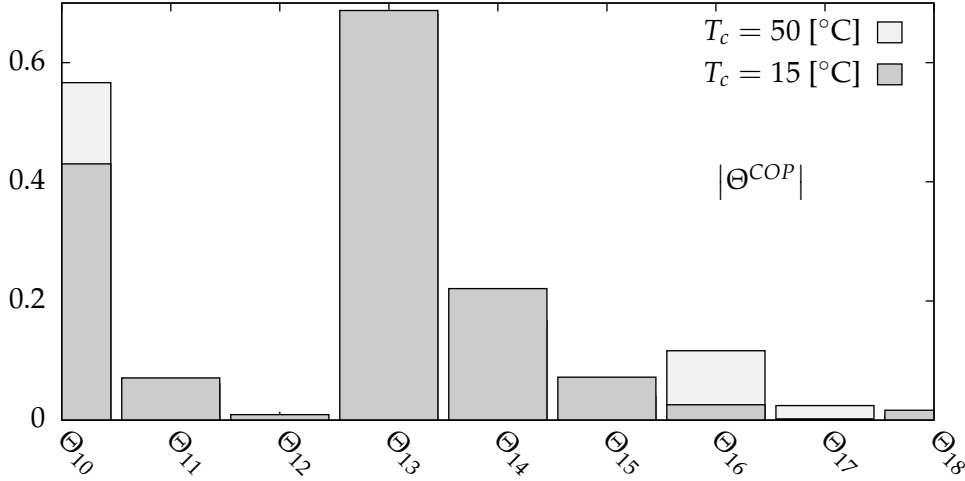


Figure 9.21: Standardized regression coefficients in absolute value for  $T_h = 50$  [°C],  $I_{tec} = 8.7$  [A] and two values of  $T_c$ . Notation in Table 9.3.

The contact effects described in Section 9.2 are included in the effective properties of Sn–Pb ( $\Theta_{5,21,22}$ ) as a function of  $\eta_c$  in (9.5). Under a perfect contact,  $\eta_c = 1$ , the sensitivities affected by contact  $\Theta_{21,22}$  are again much lower than those of the material temperature-dependency,  $\Theta_{11,14}$ . Nevertheless, as it was reported in Ju [2008] these contact effects could be much more pronounced in micro-thermoelectric devices. Now, to study the influence of  $\eta_c$  on the thermoelectric performance, Figure 9.22 shows the the COP relative decrease with respect to  $\eta_c = 1$  versus  $\eta_c$  itself, for  $T_h = 50$  [°C],  $I_{tec} = 1.7$  [A] and  $T_c = 50$  [°C] (no conduction, solid line) and for  $T_c = 15$  [°C] (heat conduction, dashed line). The COP reduction decreases with  $\eta_c$  since thermal and electric losses are lower. For the first boundary condition a very small 3% is calculated even for an unrealistic 25% real contact surface; furthermore, for a more realistic 60% contact the losses are already practically nil. The situation is different if conduction is present in the second boundary condition: the maximum reduction is more than 11% and the reduction is progressive. Note that the reduction will be even larger for the minimum  $T_c = -24$  [°C].

## 9.6 Study of the temperature-dependency of material properties on the Peltier cooler performance

The design variables that need to be controlled to design a good thermoelectric cell are: TE length, electrical conductivity and Seebeck coefficient. These three results from Section 9.5 agree with the already known facts: a good TM needs a high  $\alpha$  to maximize Peltier, also a high  $\gamma$  to reduce Joule and a low  $\kappa$  to reduce heat transfer. The variability of  $\kappa$  is

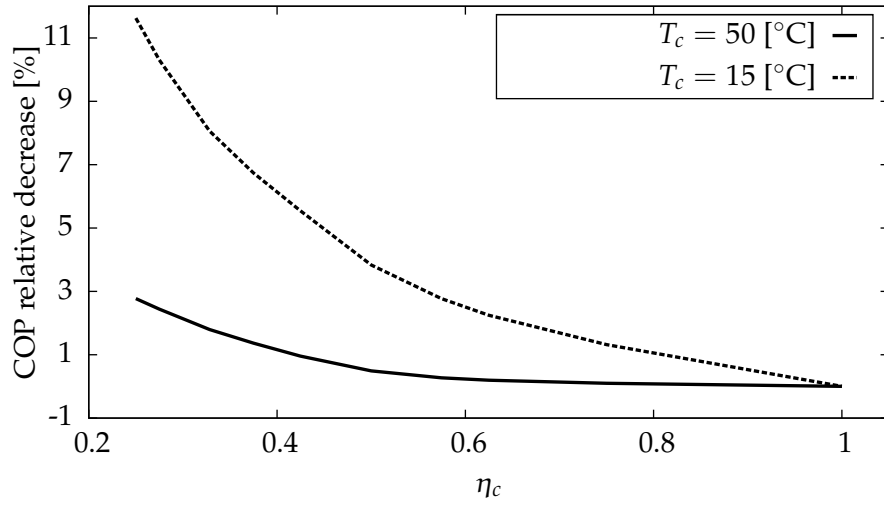


Figure 9.22: Effect of thermal and electric conductivities reduction due to contact in soldering. Coefficient-of-performance versus ratio between real and total contact surfaces.  $T_h = 50$  [°C],  $I_{tec} = 1.7$  [A].

		$Q_{ctec}$ [W]	$V_{tec}$ [V]	COP [-]
	Melcor	82.01	15.33	0.61
i)	$\alpha(T_m), \kappa(T_m), \gamma(T_m)$	83.073	15.798	0.604
ii)	$\alpha(T), \kappa(T), \gamma(T)$	85.577	16.738	0.587
iii)	$\alpha(T), \kappa(T), \gamma(T_m)$	88.742	15.824	0.644
iv)	$\alpha(T_m), \kappa(T), \gamma(T)$	79.362	16.738	0.545

Table 9.4: Finite element calculated thermoelectric cell performance for  $T_h = T_c = 50$  [°C],  $I_{tec} = 8.7$  [A].

not influential as shown in Figure 9.20, therefore its variation will not be considered in the following.

The objective of this section is to discuss the influence of the temperature-dependency of the material properties in the *Peltier* cooler performance. For that, two cases are performed to compute with the FE the extracted heat  $Q_{ctec}$  and the necessary potential drop  $V_{tec}$ : first with fixed  $T_c = T_h = 50$  [°C],  $I_{tec} = 8.7$  [A] (Table 9.4), and second with  $T_c = 15$ ,  $T_h = 50$  [°C] and varying  $I_{tec}$  (Figure 9.23).

Four cases are contemplated for the material properties:

- i) constant  $\alpha(T_m), \gamma(T_m), \kappa(T_m)$  as in Rowe [1995]
- ii) temperature-dependency of  $\alpha(T), \gamma(T), \kappa(T)$

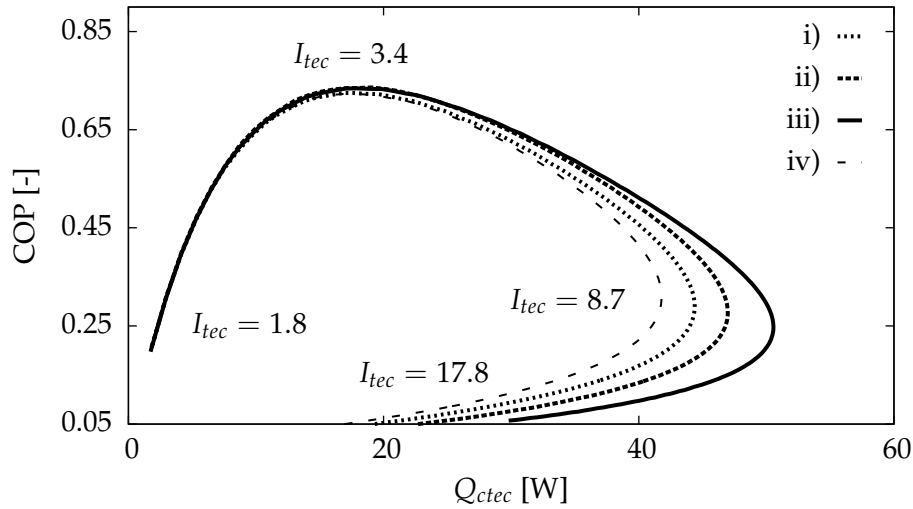


Figure 9.23: Coefficient-of-performance versus extracted heat for increasing electric intensity,  $T_h = 50$  [°C],  $T_c = 15$  [°C]. Thermal conductivity  $\kappa$  temperature dependent.

iii) idem for  $\alpha(T)$ ,  $\kappa(T)$  and constant for  $\gamma(T_m)$

iv) idem for  $\gamma(T)$ ,  $\kappa(T)$  and constant for  $\alpha(T_m)$

In Table 9.4 the results from the four cases and for comparison purposes those from the manufacturer are listed. The COP increases from iv) to ii) by 7.7%. This result approximately agrees with that reported in Chakraborty and Ng [2006a], where it was concluded that the inclusion of *Thomson* increases the calculated COP by 5 to 7%. The COP decreases from iii) to ii) by 8.8%. This is due to the decreasing temperature-dependence of conductivity, which will be lower considering 78 [°C] in the TE middle than considering  $T_m = 50$  [°C]. Therefore, *Joule* is increased, forcing the potential drop to be larger and the COP lower. In Table 9.4 and in Figure 9.20, it can be appreciated that  $V_{tec}$  is sensible to the temperature-dependency of the electric conductivity, but not to that of  $\alpha$ . Finally,  $Q_{ctec}$  is sensible to the dependence of both *Seebeck* coefficient and electric conductivity.

In Figure 9.23, COP (vertical axis) and  $Q_{ctec}$  (horizontal) values are represented for prescribed increasing intensities and again for the four cases. Starting with a small  $I_{tec} \approx 1.8$  [A], both COP and  $Q_{ctec}$  increase since *Peltier* is predominant over *Joule*. When  $I_{tec} \approx 3.4$  [A], *Peltier* is still predominant, but the required electric power  $V_{tec}I_{tec}$  (denominator in (9.3)) is higher. The consequence is that  $Q_{ctec}$  keeps increasing but COP decreases. However, at  $I_{tec} \approx 8.7$  [A], (the maximum recommended by the manufacturer) the value of *Joule* becomes larger than that of *Peltier*, and both variables decrease. Note that for a constant COP, for instance  $\approx 0.3$ , two intensities are possible: one with a low extracted heat but also low electric power used, and another with a high heat but consequently high electric power.

For  $I_{tec} \leq 3.4$  and for  $I_{tec} \geq 17.8$  [A] the differences between the four mentioned cases are small since *Peltier* and *Joule* are very dominant, respectively. This conclusion agrees with the one reported in Chakraborty et al. [2006]. The current FE cannot produce results for

intensities larger than 17.8 [A] due to numerical overflows. Between 3.4 and 17.8 [A], there are relevant differences among the cases: for iv), and given a COP value,  $Q_{ctec}$  has the lowest value due to *Thomson*. For iii),  $Q_{ctec}$  is highest, since the  $V$  drop is also highest due to the increase in *Joule*.

## 9.7 Conclusions

A commercial *Peltier* cooler has been simulated in this chapter using the multi-coupled FE and considering the elasto-magneto-thermo-electric interactions. Summarizing, the most important conclusions obtained in the present chapter are:

- ▷ An applied magnetic field perpendicular to the electric and thermal fluxes increases the COP due to the galvanomagnetic and thermo-magnetic effects. In particular, *Nernst* and *Ettingshausen* effects increase the *Seebeck* and *Peltier* effects, enhancing the figure-of-merit and the cooling capacity, respectively. In conclusion, the COP can be increased up to 260% applying a perpendicular magnetic field of 0.55 [T]. Note that the FE could be used to optimize the TE shape since the cooling capacity strongly depends on the geometrical parameters
- ▷ Maximum thermal stresses are concentrated at the corners of the thermocouple (inside the alumina). In addition, strong concentrations are reached at the four corners on the hot face of the TE's. These stress concentrations increase with increasing the prescribed magnetic field due to the *Lorentz* forces
- ▷ For the studied thermoelectric cell the decreasing temperature-dependency of electric conductivity is more relevant for the COP than that of *Seebeck* coefficient and specially of thermal conductivity and of the consideration of reduced contact in the soldering connections
- ▷ The COP decreases with the thermal and electric contacts due to interface losses

*I'm just guardian of my balance  
and my truth.*

**Manolo García**

# 10

## Conclusions and future works

### 10.1 Conclusions

This thesis has presented a non-linear finite element formulation for non-equilibrium interactions that couple up to four fields: mechanical, thermal, electric and magnetic.

From a theoretical point of view, the assumption of two simplifications has permitted the distinction between equilibrium and non-equilibrium interactions. Two further simplifications have been stated to obtain the governing equations for non-equilibrium interactions using the Extended Non-equilibrium Thermodynamic formalism. This formalism introduces empirical parameters denominated relaxation times that can be interpreted as thermal and electric viscous phenomena.

Numerically, standard eight-node isoparametric elements with six degrees of freedom (displacements, temperature, voltage and magnetic scalar potential) per node has been used. Non-linearities due to temperature-dependency of the material properties and non-linear interactions such as the *Joule* effect have been addressed with the *Newton-Raphson* algorithm. For the dynamic problem, HHT and *Newmark- $\beta$*  algorithms have been compared to obtain accurate results, since numerical oscillations (*Gibbs* phenomena) are present when the relaxation times are considered. The regularization of the last algorithm by relating time steps and element sizes using the *Courant* number provides the best results.

Finally, the finite element implementation has been validated using practical applications, testing the numerical algorithms and obtaining significative conclusions that are reported at the end of each chapter of results.

## 10.2 Future works

This thesis may be regarded as the starting point for future research topics:

- ▷ Theoretically, the elimination of the simplifications could enable a single coupled formulation including equilibrium and non-equilibrium interactions. For this elimination, a thermodynamic formulation using the Extended Non-Equilibrium Thermodynamics must be performed
- ▷ Experimentally, the development of experiments to verify that the hysteresis-like behavior in photovoltaic materials is due to the relaxation times. In addition, the finite element implementation could be used for designing new experiments taking into account these relaxation times
- ▷ Numerically, the development of spectral analyses to study the stability of the time integration algorithms. *Staggered* and mixed finite element formulation will be developed to reduce the CPU times and to obtain more accurate results, respectively. In addition, the numerical techniques for the resolution of viscoelastic problems could be extrapolated to solve the multi-coupled transport equations when the relaxation times are present.
- ▷ The current finite element implementation will be used for the optimization of electronic devices and for the characterization of material properties using inverse problems



## Outline of the sensitivity analysis and inverse problem techniques



This appendix describes the Sensitivity Analysis (SA) and the Inverse Problem (IP), which have been used in the present thesis. In addition, the Monte Carlo Technique (MCT) and Genetic Algorithm (GA) are also described since they are required in SA and IP, respectively. Part of this description has been published in Rus et al. [2009], Palma et al. [2009], Rus et al. [2012] and Rus et al. [2011].

### A.1 Sensitivity Analysis

In the present thesis the SA is performed using the MCT, which has been applied in many research areas such as *Geophysics*, Tarantola [2005], or *Structural Mechanics*, Charnpis and Scheller [2006]. The idea behind the MCT (an allusion to the famous *Casino*) is old, but its application to the solution of scientific problems is closely connected to the advent of modern computers.

Consider a physical model represented by:

$$\phi_i = M_d(\xi_j) \tag{A.1}$$

where  $\phi_i$  are the  $i$  dependent or observable variables,  $\xi_j$  are the  $j$  independent variables, model parameters or random variables (this last denomination is the form used in the remainder of this appendix) and  $M_d$  is a mathematical operator that describes the model.



MCT consists of performing multiple evaluations of a sample of the random variables using the following five steps, see Figure A.1:

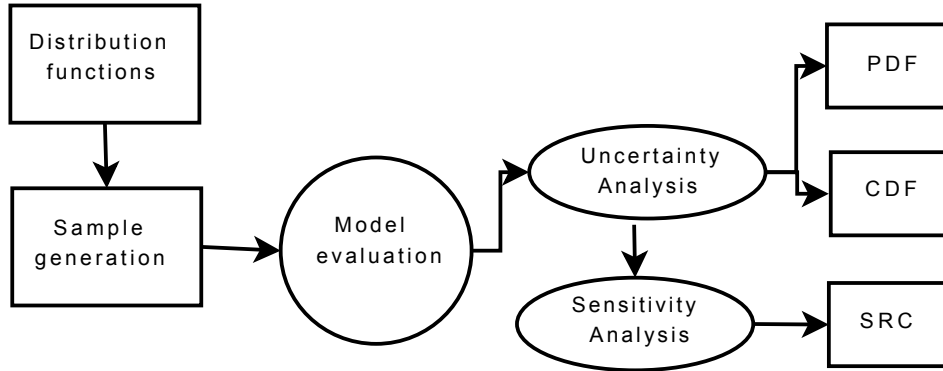


Figure A.1: Flowchart to compute the probability distribution function (PDF), cumulative distribution function (CDF) and standardized regression coefficients (SRC) using the Monte Carlo technique.

- I. Selection of distribution functions for the random variables  $\xi_j$ . Distribution functions are chosen depending on the type of problem, see Clemen and Winkler [1999] for a revision of the selection and calibration of the models
- II. Generation of the sample. In the literature there are many sampling procedures. However, the two most important types are:
  - a) Random sampling is easy to implement and provides unbiased estimates for means, variances and distribution functions. This procedure is preferred when sufficiently large samples can be evaluated
  - b) Latin hypercube sampling, Cochran [1977], is used when large samples are not computationally practicable
- III. Evaluation of the model. The model  $M_d$  is executed using numerical or analytical techniques. These can be understood by the MCT as a *black box*.
- IV. Uncertainty Analysis (UA). The purpose of UA is to determinate the uncertainty in  $\phi_i$  when the uncertainties in  $\xi_j$  are known. Thus, the Probability Distribution Function (PDF) and Cumulative Distributions Function (CDF) are obtained. They allow an easy extraction of the probabilities of having values in different subsets of the range of  $\phi_i$ . Furthermore, two scalar variables (mean  $\mu$  and standard deviation  $\sigma$ ) can summarize the uncertainties in scalar-valued results. These scalar variables are calculated by, Saltelli et al. [2000]:

$$\mu = \frac{1}{m} \sum_{i=1}^m \phi_i \quad ; \quad \text{Variance} = \frac{1}{m-1} \sum_{i=1}^m (\phi_i - \mu)^2 \quad (\text{A.2})$$

where  $m$  is the number of executions of the model or sample size.

- V. SA. The objective of SA is the determination of the relationships between the uncertainties in  $\xi_j$  and  $\phi_i$ . This is a method for checking the quality of a given model. There are many available procedures to develop the SA. However, the multiple linear regression procedure, Montgomery and Runger [1999], is used in the present thesis. This procedure provides a relationship between  $\xi_j$  and  $\phi$  approximating  $M_d$  by means of:

$$\phi \approx \sum_{j=1}^{N_\xi} \theta_{r_j} \xi_j + \Psi \quad (\text{A.3})$$

where  $N_\xi$  is the number of random variables,  $\theta_{r_j}$  are the regression coefficients, which can be used to indicate the importance of individual random variables  $\xi_j$  with respect to the uncertainty in the output  $\phi$ , and  $\Psi$  is the error of the approximation. The multiple linear regression is aimed at finding the  $\theta_{r_j}$  parameters that minimize  $\Psi$ . For this purpose, at least  $N_\xi$  observations or simulations are required. The degree to which random variables are related to the dependent variable is expressed by the correlation coefficient:  $R$ . Thus, the closer  $R^2$  is to unity, the better is the model performance. Standardized regression coefficients are defined in Mayer and Younger [1974] as:

$$\Theta_j = \theta_{r_j} \frac{\sigma_{\xi_j}}{\sigma_\phi} \quad (\text{A.4})$$

and, when the  $\xi_j$  are independent, their absolute value can be used to provide a measure of variable importance. Calculating  $\Theta_j$  is equivalent to perform the regression analysis with the input and output variables normalized to mean zero and standard deviation one.

## A.2 Inverse Problem

An IP can be defined in opposition to the forward problem. If a forward problem aims at finding the response of a system given a known model, an IP consists of retrieving unknown information of the model given the response as known input data. IP's have recently been applied to study and to characterize damages or properties of materials, providing the general framework for reconstructing an unknown part of a system model.

The model-based IP is the most advanced approach for the IP solution. From Figure A.2, it consists of:

- I. Obtaining a set of experimental measurements given a specific experimental design, which interrogates the system by propagating some physical magnitude that interacts with the unknown part of the system and manifests on an accessible part of it
- II. Solving computationally a mathematical model that is generated by assuming some physical assumptions. The unknown part of the model to be reconstructed depend

on some defined parameters. This model simulates the measurements given a set of parameter values

III. Defining a Cost Function (CF) by means of some metrics. The CF represents the discrepancy between experimental and simulated measurements

IV. Finding the values of the parameters that minimize the CF

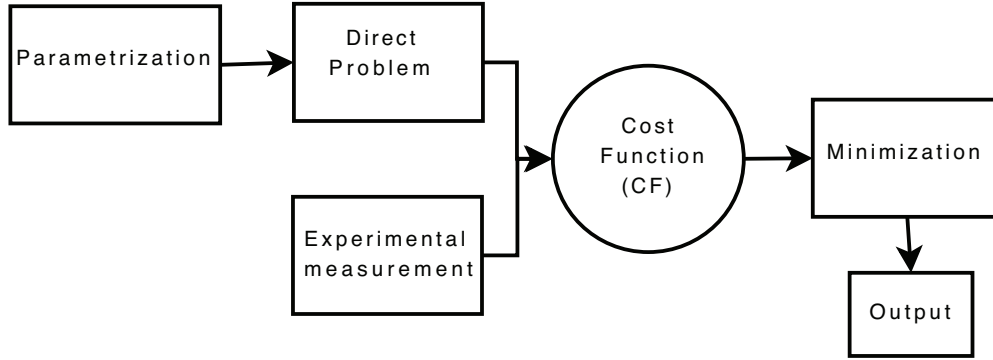


Figure A.2: Flowchart of the model-based inverse problem.

IP's are ill-conditioned problems, in the sense that the solution may not be unique, may not exist and may be unstable and divergent. This ill-conditioning is rooted in the physical meaning of the problem, and cannot be completely avoided by purely mathematical manipulations. Instead, some physical pieces of a priori information have to be incorporated into the formulation. This is the basis of a set of techniques called regularization that were formally introduced by Tikhonov and Arsénine [1974], Tikhonov and Arsenin [1979] and extended by Menke [1984] and Aster et al. [2005].

### A.2.1 Cost function

The CF, also denominated objective function, is usually defined as a L-2 norm of the difference between the experimental measurements  $\psi^{EXP}$  and those simulated by the numerical procedure  $\psi^{NUM}$ :

$$f = \frac{1}{2N} \sum_{i=1}^N \left( \psi_i^{EXP} - \psi_i^{NUM} \right)^2 \quad (\text{A.5})$$

Other alternatives such as the L-1 norm are also possibles.

When GA or other heuristic search algorithms are used for the minimization, an alternative form of the CF that improves the convergence of the algorithm is defined, Gallego and Rus [2004]:

$$f^L = -\log(f + \varepsilon) \quad (\text{A.6})$$

where  $\varepsilon$  is a small non-dimensional constant (here  $\varepsilon = 10^{-16}$ ) that ensures the existence of the logarithm when  $f$  vanishes.

### A.2.2 Parametrization

In the context of the IP, parametrization of the model means to characterize the sought solution by a set of parameters, which are the working variables and the output of the IP. The choice of parametrization is not obvious and is a critical step in the problem setup. Note that the IP is a badly conditioned one, in the sense that the solution may not be stable, exist or be unique. In particular, a reduced set of parameters is chosen to facilitate the convergence of the search algorithm, and it is also defined to avoid coupling between them.

### A.2.3 Search algorithm

The CF minimization can be performed by two alternative families of methods:

- ▷ Gradient based methods: *Gauss–Newton* algorithms, BFGS or simulated annealing are some of the most popular, see Dennis et al. [1996]
- ▷ Random search algorithms: GA, Goldberg [1989], particle swarm algorithms, etc.

The latter family requires significantly small amount of data in dealing with complex problems, while attaining global convergence as opposed to gradient-based methods, which in opposition are much less computationally expensive.

The IP can be mathematically formalized as a minimization problem that starts from a measuring system from which the response is recorded. Then, a computational idealization of the system simulates the measurements (forward problem) depending on the unknown characterization (parametrization) and defining a CF as above. Finally, the solution of the IP is obtained by solving:

$$\min_{p_i} f(\mathbf{p}) \quad (\text{A.7})$$

where  $\mathbf{p}$  is the set of  $p_i$  parameters.

## A.3 Genetic Algorithm

The GA is a heuristic optimization technique based on the rules of natural selection and genetics, Goldberg [1989]. It simulates the mechanism of survival competitions: *the superiors survive while the inferiors are eliminated*. The GA has been applied in different research topics due to its simple implementation procedure.

Figure A.3 shows the flowchart of the GA. A population of individuals (denominated chromosomes) is randomly generated. The population comprises a group of chromosomes to represent possible solutions in a problem domain. Each solution is generated by computing the CF, for which one forward problem is solved independently. Genetic operators such as crossover and mutation are applied to obtain other population. Then, the child chromosomes with higher fitness replace some of their parent chromosomes. The process runs until a stopping criterion (such as the number of generations) is reached.

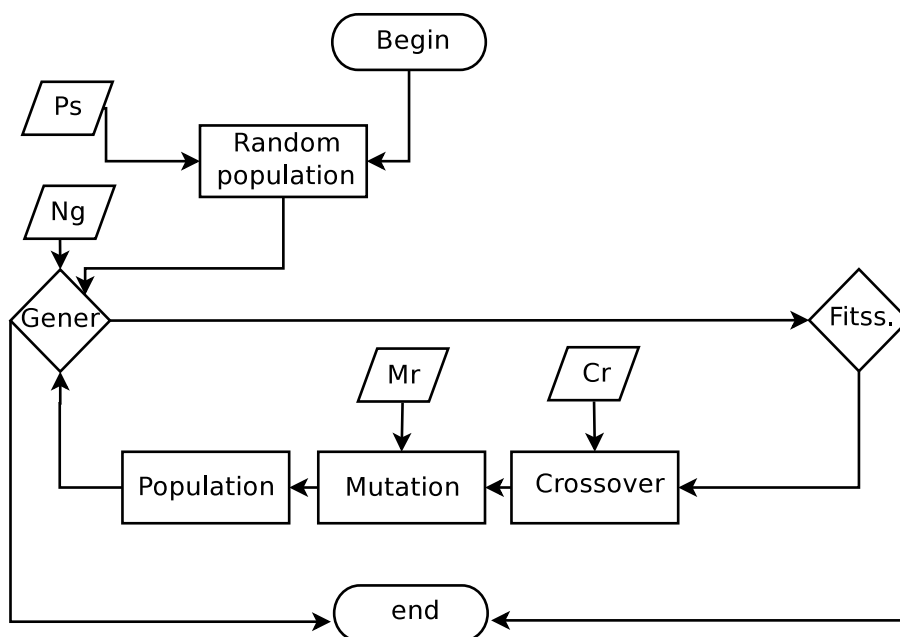


Figure A.3: Flowchart of the inverse problem solution by genetic algorithms. Gener., Fits., Mr, Cr, Ps and Ng denote generations, cost function, mutation ratio, crossover ratio, population size and number of generations, respectively.

# B

## Material properties



This appendix presents the material properties for bismuth telluride ( $\text{Bi}_2\text{Te}_3$ ) and indium antimonide (InSb) thermoelements, copper (Cu), tin–lead (Sn–Pb) and alumina ( $\text{Al}_2\text{O}_3$ ), which have been used to obtain the numerical results of this thesis.

### THERMOELECTRIC PROPERTIES

The thermoelectric properties of the  $\text{Bi}_2\text{Te}_3$ , a metal–metalloid alloy showing a high *Seebeck* coefficient although with a strong dependency on temperature, as well as thermal and electric conductivities, are taken from Rowe [1995] and depicted in Figure B.1. These properties can be fitted to quadratic polynomial:

$$\begin{aligned}\alpha &= \underbrace{1.99 \times 10^{-4}}_{\alpha_0} + \underbrace{3.35 \times 10^{-7} T}_{\alpha_1} - \underbrace{7.52 \times 10^{-10} T^2}_{\alpha_2} ; \\ \kappa &= \underbrace{1.66}_{\kappa_0} - \underbrace{3.58 \times 10^{-3} T}_{\kappa_1} + \underbrace{3.19 \times 10^{-5} T^2}_{\kappa_2} ; \\ \gamma &= \underbrace{1.09 \times 10^5}_{\gamma_0} - \underbrace{5.59 \times 10^2 T}_{\gamma_1} + \underbrace{2.49 T^2}_{\gamma_2}\end{aligned}\tag{B.1}$$

where the temperature is introduced in *Celsius* degrees.

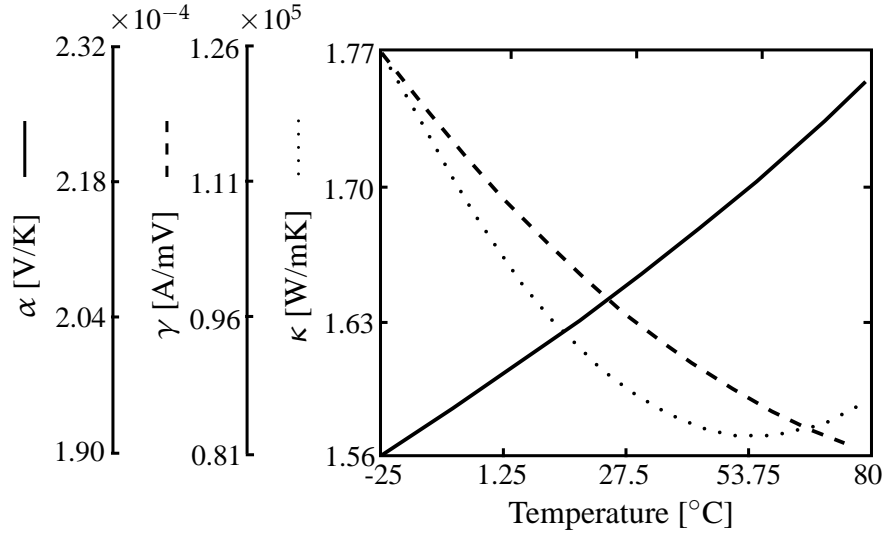


Figure B.1: Thermoelectric material property variations with temperature for the bismuth telluride material.

The thermoelectric properties of the InSb semiconductors are taken from Okumura et al. [1998] and fitted to quadratic polynomial:

$$\begin{aligned}
 \alpha &= -3.2 \times 10^{-4} + 1.0 \times 10^{-6} T - 2.9 \times 10^{-22} T^2 ; \\
 \kappa &= 13 - 7.8 \times 10^{-2} T + 2.8 \times 10^{-4} T^2 ; \\
 \gamma &= 1.2 \times 10^4 + 2.2 \times 10^2 T + 2.6 T^2
 \end{aligned}
 \tag{B.2}$$

Again, the temperature is introduced in *Celsius* degrees.

#### GALVANOMAGNETIC AND THERMO-MAGNETIC PROPERTIES

The thermo-magnetic and galvanomagnetic properties for the *InSb* semiconductors are also taken from Okumura et al. [1998] and are mathematically represented by:

$$\begin{aligned}
 \bar{R} &= (-5.6 e^{-0.034 T} - 0.9) \times 10^{-4} ; \\
 \bar{N} &= -5.7 e^{-T/65} - 3.2) \times 10^{-5} ; \\
 \bar{M} &= 5 \times 10^{-2}
 \end{aligned}
 \tag{B.3}$$

Again, the temperature is introduced in *Celsius* degrees. Note that the magnetic properties for  $\text{Bi}_2\text{Te}_3$  have not been found.

Finally, the constant properties for  $\alpha$ ,  $\gamma$ ,  $\kappa$ ,  $\bar{R}$  and  $\bar{N}$  are obtained from (B.1), (B.2) and (B.3) using an average temperature  $T_m = (T_h + T_c)/2$ . Furthermore, p- and n-type properties are the same by changing the sign of *Seebeck* and *Nernst* coefficients.

### MECHANICAL PROPERTIES

The mechanical properties of the Bi<sub>2</sub>Te<sub>3</sub> p- and n- thermoelements, which have been taken from Clin et al. [2009], are shown in Table B.1. Thermal, mechanical and electric properties of the Cu, Sn-Pb and Al<sub>2</sub>O<sub>3</sub> are shown in Tables B.2, B.3 and B.3, respectively.

Property	Value	Unit
$\mu$	16.78	[GPa]
$\lambda$	67.14	[GPa]
$c$	544	[J/Kg K]
$\rho_m$	7530	[Kg/m <sup>3</sup> ]
$\alpha_T$	16.8	$\times 10^{-6}$ [K <sup>-1</sup> ]
Ultimate strength	60	[MPa]

Table B.1: Mechanical properties for bismuth telluride p- and n- thermoelements.

Property	Value	Unit
$\mu$	43.89	[GPa]
$\lambda$	71.61	[GPa]
$\alpha_T$	17	$\times 10^{-6}$ [K <sup>-1</sup> ]
$\alpha$	0	$\times 10^{-4}$ [V/K]
$\kappa$	386	[W/mK]
$\gamma$	581	$\times 10^5$ [A/mV]
Ultimate strength	250	[MPa]

Table B.2: Mechanical, thermal and electric properties of the copper.



Property	Value	Unit
$\mu$	16.79	[GPa]
$\lambda$	32.47	[GPa]
$\alpha_T$	27	$\times 10^{-6}$ [K <sup>-1</sup> ]
$\alpha$	0	$\times 10^{-4}$ [V/K]
$\kappa$	48	[W/mK]
$\gamma$	47	$\times 10^5$ [A/mV]
Ultimate strength	41	[MPa]

Table B.3: Mechanical, thermal and electric properties of the tin-lead.

Property	Value	Unit
$\mu$	150.8	[GPa]
$\lambda$	163.3	[GPa]
$\alpha_T$	5.	$\times 10^{-6}$ [K <sup>-1</sup> ]
$\alpha$	0	$\times 10^{-4}$ [V/K]
$\kappa$	35.3	[W/mK]
$\gamma$	0	$\times 10^5$ [A/mV]
Ultimate strength	-	[MPa]

Table B.4: Mechanical, thermal and electric properties of the alumina.

## References

- M. Abraham. Sull'elettrodinamica di Minkowski. *Rend. Circ. Matem*, XXX:33–46, 1910.
- M. Alata, M.A. Al-Nimr, and M. Naji. Transient behaviour of a thermoelectric device under the hyperbolic heat conduction model. *International Journal of Thermophysics*, 24(6):1753–1768, 2003.
- H. Allik and T.J.R. Hughes. Finite element method for piezoelectric vibration. *International Journal for Numerical Methods in Engineering*, 2:151–157, 1970.
- E.E. Antonova and D.C. Looman. Finite elements for thermoelectric device analysis in ANSYS. In *International Conference on Thermoelectrics*, 2005.
- A. Arenas, J. Vázquez, M.A. Sanz-Bobi, and R. Palacios. Performance of a thermoelectric module using the thermodynamic relationship temperature-entropy (T-S). In *XIX International Conference of Thermoelectrics*, 2000.
- R.C. Aster, B. Borchers, and C.H. Thurber. *Parameter Estimation and Inverse Problems*. Elsevier, USA, 2005.
- J. Atulasimha and A.B. Flatau. A review of magnetostrictive Iron-Gallium alloys. *Smart Materials and Structures*, 20:1–15, 2011.
- A. Ballato. Piezoelectricity: Old effect, new thrusts. *IEEE Transactions on Ultrasonics, Ferroelectrics and Frequency Control*, 42(5):916–926, 1995.
- S. Baoyuan, W. Jiantong, Z. Jun, and Q. Min. A new model describing physical effects in crystals: the diagrammatic and analytic methods for macro-phenomenological theory. *Journal of Materials Processing Technology*, 139:444–447, 2003.
- S. Bargmann and P. Steinmann. Finite element approaches to non-classical heat conduction in solids. *Computer Modeling in Engineering and Sciences*, 9(2):133–150, 2005.
- S. Bargmann and P. Steinmann. Theoretical and computational aspects of non-classical thermoelasticity. *Computer Methods in Applied Mechanics and Engineering*, 196:516–527, 2006.
- S. Bargmann and P. Steinmann. Modeling and simulation of first and second sound in solids. *International Journal of Solids and Structures*, 45:6067–6073, 2008.
- S.M. Barnett. Resolution of the Abraham-Minkowski dilemma. *Physical Review Letters*, 104:070401, 2010.
- M.H. Benbouzid, G. Reyne, and G. Meunier. Nonlinear finite element modelling of giant magnetostriction. *IEEE Transactions on Magnetics*, 29(6):2467–2469, 1993.

- M.H. Benbouzid, G. Meunier, and G. Meunier. Dynamic modelling of giant magnetostriction in Terfenol-D rods by the finite element method. *IEEE Transactions on Magnetics*, 31(3):1821–1824, 1995a.
- M.H. Benbouzid, G. Reyne, and G. Meunier. Finite element modelling of magnetostrictive devices: investigations for the design of the magnetic circuit. *IEEE Transactions on Magnetics*, 31(3):1813–1816, 1995b.
- M. Besbes, Z. Ren, and A. Razek. Finite element analysis of magneto-mechanical coupled phenomena in magnetostrictive materials. *IEEE Transactions on Magnetics*, 32(3):1058–1061, 1996.
- M.A. Biot. Thermoelasticity and irreversible thermodynamics. *Journal of Applied Physics*, 27(3):240–253, 1956.
- J. Bonet and R.D. Wood. *Nonlinear Continuum Mechanics for Finite Element Analysis*. Cambridge University Press, 1997.
- P. Bowyer. The momentum of light in media: the Abraham-Minkowski controversy, 2005.
- J.R. Brauer, J.J. Ruehl, B.E. MacNeal, and F. Hirtenfelder. Finite element analysis of Hall effect and magnetoresistance. *IEEE Transactions on Electron Devices*, 42(2):328–333, 1995.
- M. Braunovic. Current and heat transfer across the contact interface. *Electric and Computer Engineering*, 132:149–204, 2007.
- R.J. Buist and P.G. Lau. Theoretical analysis of thermoelectric cooling performance enhancement via thermal and electric pulsing. In *Fifteenth International Conference on Thermoelectrics*, 1996.
- H.B. Callen. The application of Onsager's reciprocal relations to thermoelectric, thermomagnetic, and galvanomagnetic effects. *Physical Review*, 73(11):1349–1358, 1948.
- H.B. Callen. *Thermodynamics and an Introduction to Thermostatistics*. John Wiley and Sons, Inc., 1985.
- J.P. Carter and J.R. Booker. Finite element analysis of coupled thermoelasticity. *Computer and Structures*, 31(1):73–80, 1989.
- C. Cattaneo. Sulla conduzione del calore. *Atti Seminario Mat. Fis. University Modena*, 3:83–1013, 1938.
- A. Chakraborty and K.C. Ng. Thermodynamic formulation of temperature-entropy diagram for the transient operation of a pulsed thermoelectric cooler. *International Journal of Heat and Mass Transfer*, 49:1845–1850, 2006a.
- A. Chakraborty and K.C. Ng. Thermodynamic formulation of temperature-entropy diagram for the transient operation of a pulsed thermoelectric cooler. *International Journal of Heat and Mass Transfer*, 49:1845–1850, 2006b.
- A. Chakraborty, B.B. Saha, S. Koyoma, and K.C. Ng. Thermodynamic modelling of a solid state thermoelectric cooling device: Temperature-entropy analysis. *International Journal of Heat and Mass Transfer*, 49:3547–3554, 2006.
- A.V. Chaplik. Some exact solutions for the classical Hall effect in an inhomogeneous magnetic field. *JETP Lett.*, 72:503, 2000.

- D. Charmpis and G. Scheller. *Using Monte Carlo simulation to treat physical uncertainties in structural reliability: Coping with Uncertainty*. Springer, 2006.
- J. Chen, Z. Yan, and L. Wu. Nonequilibrium thermodynamic analysis of a thermoelectric device. *Energy*, 22(10):979–985, 1997.
- C.H. Cheng, S.H. Huang, and T.C. Cheng. A three-dimensional theoretical model for predicting transient thermal behavior of thermoelectric coolers. *International Journal of Heat and Mass Transfer*, 53:2001–2011, 2010.
- Y.H. Cheng and W.K. Lin. Geometric optimization of thermoelectric coolers in a confined volume using genetic algorithms. *Applied Thermal Engineering*, 25:2983–2997, 2005.
- H.T. Chua, K.C. Ng, X.C. Xuan, C. Yap, and J.M. Gordon. Temperature-entropy formulation of thermoelectric thermodynamic cycles. *Physical Review E*, 65:056111, 2002.
- R. Ciegis. Numerical solution of hyperbolic heat conduction equation. *Mathematical Modelling and Analysis*, 14(1):11–24, 2009.
- R. T. Clemen and R.L. Winkler. Combining probability distributions from expert in risk analysis. *Risk Analysis*, 2:187–203, 1999.
- Th. Clin, S. Turenne, D. Vasilevskiy, and R.A. Masut. Numerical simulation of the thermomechanical behavior of extruded bismuth telluride alloy module. *Journal of Electronic Materials*, 38(7):994–1001, 2009.
- W. Cochran. *Sampling Techniques*. John Wiley & Sons, 1977.
- B.D. Coleman. Thermodynamics of materials with memory. *Archive for Rational Mechanics and Analysis*, 17:1–46, 1964.
- R. Courant, K. Friedrichs, and H. Lewy. Uber die partiellen differenzgleichungen der mathematischen physik. *Mathematische Annalen*, 100:32–74, 2007.
- L.W. da Silva and M. Kaviany. Micro-thermoelectric cooler: Interfacial effects on thermal and electrical transport. *International Journal of Heat and Mass Transfer*, 47:2417–2435, 2004.
- S.R. de Groot. Non-equilibrium thermodynamics of systems in an electromagnetic field. *Journal of Nuclear Energy C: Plasma Physics*, 2:188–194, 1961.
- S.R. de Groot and P. Mazur. *Non-equilibrium Thermodynamics*. Dover, 1984.
- P. Debye. Ver. deut. phys. Geseww, 777, 1913.
- L.F. del Castillo and L.S. García-Colín. Thermodynamic basis for dielectric relaxation in complex materials. *Physical Review B*, 33(7):4944–4951, 1986.
- R.T. Delves. Figure of merit for Ettingshausen cooling. *British Journal of Applied Physics*, 15: 105–106, 1964.
- J.E. Dennis, B. Robert, and B. Schnabel. *Numerical Methods for Unconstrained Optimization and Nonlinear Equations*. SIAM, Philadelphia, 1996.
- D. Ebling, M. Jaegle, M. Bartel, A. Jacquot, and H. Bottner. Multiphysics simulation of thermoelectric systems for comparison with experimental device performance. *Journal of Electronic Materials*, 38(7):1456–1461, 2009.
- A.C. Eringen. *Mechanics of Continua*. Robert E. Krieger Publishing Company, 1980.

- A.C. Eringen and G.A. Maugin. *Electrodynamics of Continua I*. Springer-Verlag New York, Inc., 1990.
- Y. Ersoy. A new nonlinear constitutive theory for conducting magnetoelastothermoelastic solids. *International Journal of Engineering Science*, 22(6):683–705, 1984.
- Y. Ersoy. A new nonlinear constitutive theory of electric and heat conductions for magnetoelastothermo-electrical anisotropic solids. *International Journal of Engineering Science*, 24(6):867–882, 1986.
- I.J. Ferrer, P. Díaz-Chao, A. Pascual, and C. Sánchez. Hysteresis-like behaviour of the thermoelectric voltage in photovoltaic materials. *Thin Solid Films*, 511-512:177–181, 2006.
- T.C. Fung. Numerical dissipation in time-step integration algorithms for structural dynamic analysis. *Progress in Structural Engineering and Materials*, 5:167–180, 2003.
- R. Gallego and G. Rus. Identification of cracks and cavities using the topological sensitivity boundary integral equation. *Computational Mechanics*, 33, 2004.
- D. Galushko, N. Ermakov, M. Karpovski, A. Palevski, J.S. Ishay, and D.J. Bergman. Electrical, thermoelectric and thermophysical properties of hornet cuticle. *Semiconductor Science and Technology*, 20:286–289, 2005.
- J.L. Gao, Q.G. Du, X.D. Zhang, and X.Q. Jiang. Thermal stress analysis and structure parameter selection for a Bi<sub>2</sub>Te<sub>3</sub>-based thermoelectric module. *Journal of Electronic Materials*, 40(5):884–888, 2011.
- P. Gaudenzi and K.J. Bathe. An iterative finite element procedure for the analysis of piezoelectric continua. *Journal of Intelligent Material Systems and Structures*, 6:266–273, 1995.
- D. Gavela and J.L. Pérez-Aparicio. Peltier pellet analysis with a coupled, non-linear 3D finite element model. In *4th European Workshop on Thermoelectrics*, 1998.
- D. Goldberg. *Genetic Algorithms in Search, Optimization and Machine Learning*. Addison-Wesley Publ, Reading, Massachusetts, etc., 1989.
- D.J. Griffiths. *Introduction to Electrodynamics*. Prentice-Hall, Inc., 1999.
- L. Gros, G. Reyne, C. Body, and G. Meunier. Strong coupling magneto mechanical methods applied to model heavy magnetostrictive actuators. *IEEE Transactions on Magnetics*, 34(5):3150–3153, 1998.
- E. Hernández-Lemus and E. Orgaz. Hysteresis in nonequilibrium steady states: the role of dissipative couplings. *Revista Mexicana de Física*, 48:38–45, 2002.
- H.M. Hilber, T.J.R. Hughes, and R.L. Taylor. Improved numerical dissipation for time integration algorithms in structural dynamics. *Earthquake Engineering and Structural Dynamics*, 5:282–292, 1977.
- E.A. Hinds. Momentum exchange between light and a single atom: Abraham or Minkowski? *Physical Review Letters*, 102:050403, 2009.
- L. Hirsinger and R. Billardon. Magneto-elastic finite element analysis including magnetic forces and magnetostriction effects. *IEEE Transactions on Magnetics*, 31(3):1877–1880, 1995.
- G.E. Hoyos, K.R. Rao, and D. Jerger. Fast transient response of novel Peltier junctions. *Energy Conversion*, 17:23–29, 1977.

- M.J. Huang, R.H. Yen, and A.B. Wang. The influence of the Thomson effect on the performance of a thermoelectric cooler. *International Journal of Heat and Mass Transfer*, 48:413–318, 2005.
- M.J. Huang, P.K. Chou, and M.C. Lin. An investigation of the thermal stresses induced in a thin-film thermoelectric cooler. *Journal of Thermal Stresses*, 31:438–454, 2008.
- T.J.R. Hughes. *The Finite Element Method. Linear Static and Dynamic Finite Element Analysis*. Prentice-Hall, Inc., 1987.
- IEEE Standard on Piezoelectricity*. IEEE Standards Board, 1987.
- IEEE Standard on Magnetostrictive Materials: Piezomagnetic Nomenclature*. IEEE Standards Board, 1990.
- J.D. Jackson. *Classical Electrodynamics*. John Wiley and Sons, Inc., 1962.
- M. Jaegle. Multiphysics simulation of thermoelectric systems - modeling of Peltier - cooling and thermoelectric generation. In *Proceedings of the COMSOL*, 2008.
- M. Jaegle, M. Bartel, D. Ebling, A. Jacquot, and H. Bottner. Multiphysics simulation of thermoelectric systems. In *European Conference on Thermoelectrics ECT2008*, 2008.
- C.M. Jarque and A.K. Bera. A test for normality of observations and regression residuals. *International Statistical Review*, 16(2):1–10, 1987.
- J.L. Jiménez and I. Campos. *Advanced Electromagnetism: Foundations, Theory and Applications*, chapter The balance equations of energy and momentum in classical electrodynamics. World Scientific Publishing Co. Pte. Ltd., 1996.
- S. Johnstone. Is there potential for use of the Hall effect in analytical science? *Analyst*, 133: 293–296, 2008.
- D. Jou and G. Lebon. *Extended Irreversible Thermodynamics*. Springer-Verlag Berlin Heidelberg, 1996.
- Y.S. Ju. Impact of interface resistance on pulsed thermoelectric cooling. *Journal of Heat Transfer*, 130:1–3, 2008.
- Y.S. Ju and U. Ghoshal. Study of interface effects in thermoelectric microrefrigerators. *Journal of Applied Physics*, 88:4135–4139, 2000.
- M. Kaltenbacher, M. Meiler, and M. Ertl. Physical modeling and numerical computation of magnetostriction. *International Journal for Computation and Mathematics in Electrical and Electronic Engineering*, 28(4):819–832, 2009.
- M. Kaltenbacher, B. Kaltenbacher, T. Hegewald, and R. Lerch. Finite element formulation for ferroelectric hysteresis of piezoelectric materials. *Journal of Intelligent Material Systems and Structures*, 21:773–785, 2010.
- M. Kamlah and U. Bohle. Finite element analysis of piezoceramic components taking into account ferroelectric hysteresis behavior. *International Journal of Solids and Structures*, 38: 605–633, 2001.
- K.S. Kannan and A. Dasgupta. A nonlinear Galerkin finite-element theory for modeling magnetostrictive smart structures. *Smart Materials and Structures*, 6:341–350, 1997.

- J. Kiang and L. Tong. Nonlinear magneto-mechanical finite element analysis of Ni-Mn-Ga single crystals. *Smart Materials and Structures*, 19:1–17, 2010.
- P. Kinsler, A. Favaro, and M.W. McCall. Four Poynting theorems. *European Journal of Physics*, 30:983–993, 2009.
- S. Klinckel and K. Linnemann. A phenomenological constitutive model for magnetostrictive materials and ferroelectric ceramics. In *Proceedings in Applied Mathematics and Mechanics*, volume 8, pages 10507–10508, 2008.
- T. Lahmer. *Forward and Inverse Problems in Piezoelectricity*. PhD thesis, Universität Erlangen-Nürnberg, 2008.
- L.D. Landau and E.M. Lifshitz. *Mechanics*. Butterworth-Heinemann, 1982.
- L.D. Landau and E.M. Lifshitz. *Electrodynamics of Continuous Media*. Pergamon Press Ltd., 1984.
- K. Landecker and A.W. Findlay. Study of the fast transient behaviour of Peltier junction. *Solid-State Electronics*, 3:239–260, 1961.
- C.M. Landis. A new finite-element formulation for electromechanical boundary value problems. *International Journal for Numerical Methods in Engineering*, 55:613–628, 2002.
- G. Lebon, D. Jou, and J.Casas-Vázquez. *Understanding Non-equilibrium Thermodynamics*. Springer-Verlag, 2008.
- K. Linnemann and S. Klinkel. A constitutive model for magnetostrictive materials - theory and finite element implementation. In *Proceedings in Applied Mathematics and Mechanics*, volume 6, pages 393–394, 2006.
- K. Linnemann, S. Klinkel, and W. Wagner. A constitutive model for magnetostrictive and piezoelectric materials. *International Journal of Solids and Structures*, 46:1149–1166, 2009.
- J.E. Llebot, D. Jou, and J. Casas-Vázquez. A thermodynamic approach to heat and electric conduction in solids. *Physica*, 121(A):552–562, 1983.
- X. Lu and V. Hanagud. Extended irreversible thermodynamics modeling for self-heating and dissipation in piezoelectric ceramics. *IEEE Transactions on Ultrasonics, Ferroelectrics and Frequency Control*, 51(12):1582–1592, 2004.
- B. Maruszewski and G. Lebon. An extended irreversible thermodynamic description of electrothermoelastic semiconductors. *International Journal of Engineering Science*, 24(4):583–593, 1986.
- L.S. Mayer and M.S. Younger. Procedures for estimating standardized regression coefficients from sample data. *Sociological Methods and Research*, 2(4):431–453, 1974.
- R.M. McMeeking, C.M. Landis, and M.A. Jimenez. A principle of virtual work for combined electrostatic and mechanical loading of materials. *International Journal of Non-Linear Mechanics*, 42:831–838, 2007.
- MELCOR. *Thermoelectric Handbook*. Melcor, a unit of Laird Technologies, 2000. <http://www.lairdtech.com>.
- MELCOR. Application notes for thermoelectric devices. Technical report, Melcor: Laird Technologies, <http://www.lairdtech.com>, 2010.

- W. Menke. *Geophysical data analysis, Discrete Inverse Theory*. Academic Press INC., 1984.
- H. Minkowski. *Nachr. ges. wiss. Gottingen*, 53, 1908.
- D.C. Montgomery and G.C. Runger. *Applied Statistics and Probability for Engineers*. John Wiley and Sons, 1999.
- R.E. Nettleton and S.L. Sobolev. Applications of extended thermodynamics to chemical, rheological, and transport processes: A special survey part I. approaches and scalar rate processes. *Journal of Non-Equilibrium Thermodynamics*, 20:205–229, 1995a.
- R.E. Nettleton and S.L. Sobolev. Applications of extended thermodynamics to chemical, rheological, and transport processes: A special survey part II. vector transport processes, shear relaxation and rheology. *Journal of Non-Equilibrium Thermodynamics*, 20:297–331, 1995b.
- R.E. Nettleton and S.L. Sobolev. Applications of extended thermodynamics to chemical, rheological, and transport processes: A special survey part III. wave phenomena. *Journal of Non-Equilibrium Thermodynamics*, 21:1–16, 1996.
- R.E. Newnham. *Properties of Materials: Anisotropy, Symmetry, Structure*. Oxford University Press, 2005.
- A.E. Nour, N. Abd-Alla, and G.A. Maugin. Nonlinear equations for thermoelastic magnetizable conductors. *International Journal of Engineering Science*, 27(7):589–603, 1990.
- A. Nowacki. *International Series of Monographs in Aeronautics and Astronautics*. Pergamon Press, 1962.
- J.T. Oden, T. Belytschko, I. Babuska, and T.J.R. Hughes. Research directions in computational mechanics. *Computer Methods in Applied Mechanics and Engineering*, 192:913–922, 2003.
- H. Okumura, S. Yamaguchi, H. Nakamura, K. Ikeda, and K. Sawada. Numerical computation of thermoelectric and thermomagnetic effects. In *17th International Conference on Thermoelectrics*, 1998.
- H. Okumura, Y. Hasegawa, H. Nakamura, and S. Yamaguchi. A computational model of thermoelectric and thermomagnetic semiconductors. In *18th International Conference on Thermoelectrics*, 1999.
- X. Oliver and C. Agelet. *Mecánica de Medios Continuos para Ingenieros*. Edicions UPC, 2000.
- R. Palma, G. Rus, and R. Gallego. Probabilistic inverse problem and system uncertainties for damage detection in piezoelectrics. *Mechanics of Materials*, 41:1000–1016, 2009.
- J.L. Pérez-Aparicio and D. Gavela. 3D, non-linear coupled, finite element model of thermoelectricity. In *4th European Workshop on Thermoelectrics*, 1998.
- J.L. Pérez-Aparicio and H. Sosa. A continuum three-dimensional, fully coupled, dynamic, non-linear finite element formulation for magnetostrictive materials. *Smart Materials and Structures*, 13:493–502, 2004.
- J.L. Pérez-Aparicio, R.L. Taylor, and D. Gavela. Finite element analysis of nonlinear fully coupled thermoelectric materials. *Computational Mechanics*, 40:35–45, 2007.
- A.D. Polyanin. *Handbook of Linear Partial Differential Equations for Engineers and Scientist*. Chapman & Hall CRC, 2002.



- H. Qi, D. Fang, and Z. Yao. FEM analysis of electro-mechanical coupling effect of piezoelectric materials. *Computational Materials Science*, 8:283–290, 1997.
- J.R. Reitz and F.J. Milford. *Foundations of Electromagnetic Theory*. Addison-Wesley Publishing Company, Inc., 1960.
- Z. Reng, B. Ionescu, M. Besbes, and A. Razek. Calculation of mechanical deformation of magnetic materials in electromagnetic devices. *IEEE Transactions on Magnetics*, 31(3):1873–1876, 1995.
- L. Restuccia. On a thermodynamic theory for magnetic relaxation phenomena due to n microscopic phenomena described by n internal variables. *Journal of Non-Equilibrium Thermodynamics*, 35:379–413, 2010.
- L. Restuccia and G.A. Kluitenberg. On generalizations of the Debye equation for dielectric relaxation. *Physica A*, 154:157–182, 1988.
- L. Restuccia and G.A. Kluitenberg. On the heat dissipation function for dielectric relaxation phenomena in anisotropic media. *International Journal of Engineering Science*, 30(3):305–315, 1992.
- S.B. Riffat and X. Ma. Thermoelectrics: a review of present and potential applications. *Applied Thermal Engineering*, 23:913–935, 2003.
- D.M. Rowe, editor. *CRC Handbook of Thermoelectrics*. CRC Press, 1995.
- G. Rus, R. Palma, and J.L. Pérez-Aparicio. Optimal measurement setup for damage detection in piezoelectric plates. *International Journal of Engineering Science*, 47:554–572, 2009.
- G. Rus, R. Palma, and J. Suárez. *Piezoelectric Ceramics*, chapter Characterization of properties and damage in piezoelectric. Ed. Sciyo, 2011.
- G. Rus, R. Palma, and J.L. Pérez-Aparicio. Experimental design of dynamic model-based damage identification in piezoelectric ceramics. *Mechanical System and Signal Processing*, 26:268–293, 2012.
- A. Saltelli, K. Chan, and E. M. Scott. *Sensitivity Analysis*. John Wiley and Sons, 2000.
- A. Saltelli, S. Tarantola, F. Campolongo, and M. Ratto. *Sensitivity Analysis in Practice. A Guide to Assessing Scientific Models*. John Wiley and Sons Ltd., 2004.
- W. Seiffert, M. Ueltzen, and E. Muller. One-dimensional modelling of thermoelectric cooling. *Physica Status Solidi A*, 194(1):277–290, 2002.
- A.S. Semenov, H. Kessler, A. Liskowsky, and H. Balke. On a vector potential formulation for 3D electromechanical finite element analysis. *Communications in Numerical Methods in Engineering*, 22:357–375, 2006.
- E. Serra and M. Bonaldi. A finite element formulation for thermoelastic damping analysis. *International Journal for Numerical Methods in Engineering*, 78(6):671–691, 2008.
- J.C. Simo and T.J.R. Hughes. *Computational Inelasticity*, volume 7 of *Interdisciplinary Applied Mathematics*. Springer-Verlag New York, Inc., 1998.
- G.E. Smith and R. Wolfe. Thermoelectric properties of bismuth-antimony alloys. *Journal of Applied Physics*, 33(3), 1962.

- G.J. Snyder, J.P. Fleurial, and T. Caillat. Supercooling of Peltier cooler using a current pulse. *Journal of Applied Physics*, 92(3):1564–1569, 2002.
- A. Soba and A. Denis. Contacto intermitente y localizado entre dos superficies. Aplicación al caso de la interacción pastillas-vaina (PCI) en un combustible nuclear de potencia. *Revista Internacional Métodos Numéricos para Cálculo y Diseño en Ingeniería*, 25:79–89, 2009.
- A.K. Soh and J.X. Liu. On the constitutive equations of magnetoelastic solids. *Journal of Intelligent Material Systems and Structures*, 16:597–602, 2005.
- D.M. Stefanescu. *Handbook of Force Transducers: Principles and Components*. Springer-Verlag Berlin Heidelberg, 2011.
- L.S. Stilbans and N.A. Fedorovich. The operation of refrigerating thermoelectric elements in nonstationary conditions. *Sov. Phys. Tech. Phys.*, 3:460, 1958.
- K.K. Tamma and R.R. Namburu. An effective finite element modeling/analysis approach for dynamic thermoelasticity due to second sound effects. *Computational Mechanics*, 9:73–84, 1992.
- T. Tang and W. Yu. Micromechanical modeling of the multiphysical behavior of smart materials using the variational asymptotic method. *Smart Materials and Structures*, 18:1–14, 2009.
- A. Tarantola. *Inverse Problem Theory*. SIAM, 2005.
- R.L. Taylor. *FEAP A Finite Element Analysis Program: User Manual*. University of California, Berkeley, 2010. <http://www.ce.berkeley.edu/feap>.
- T. Thonhauser and G.D. Mahan. Improved supercooling in transient thermoelectrics. *Applied Physics Letters*, 85(15):3247–3249, 2004.
- R.N. Thurston. Warren p. Mason (1900-1986) physicist, engineer, inventor, author, teacher. *IEEE Transactions on Ultrasonics, Ferroelectrics and Frequency Control*, 41(4):425–434, 1994.
- X. Tian, Y. Shen, C. Chen, and T. He. A direct finite element method study of generalized thermoelastic problems. *International Journal of Solids and Structures*, 43:2050–2063, 2006.
- A. Tikhonov and V. Arsenine. *Méthodes de Résolution de Problèmes mal Posés*. Editions Mir, Moscou, 1974.
- A.N. Tikhonov and V.J. Arsenin. *Methods for Solving Ill-posed Problems*. Nauka, Moscow, 1979.
- R.F. Tinder. *Tensor Properties of Solids: Phenomenological Development of the Tensor Properties of Crystals*. Morgan and Claypool Publishers, 2008.
- C. Truesdell. *Thermodynamics for Beginners, in Irreversible Aspects of Continuum Mechanics*. Springer, Berlin Heidelberg New York, 1968.
- O. Yamashita. Effect of linear and non-linear components in the temperature dependences of thermoelectric properties on the cooling performance. *Applied Energy*, 86:1746–1756, 2009.
- R. Yan, B. Wang, Q. Yang, F. Liu, S. Cao, and W. Huang. A numerical model of displacement for giant magnetostrictive actuator. *IEEE Transactions on Magnetics*, 14(2):1914–1917, 2004.

- R. Yang, G. Chen, A.R. Kumar, G.J. Snyder, and J.P. Fleurial. Transient cooling of thermoelectric coolers and its applications for microdevices. *Energy Conversion and Management*, 46:1407–1421, 2005.
- B. Yoo, M. Hirano, and K. Hirata. Fully coupled electro-magneto-mechanical analysis method of magnetostrictive actuator using 3D finite element method. In *Proceedings of the 2008 International Conference on Electrical Machines*, 2008.
- H.M. Youssef. Theory of two-temperature-generalized thermoelasticity. *IMA Journal of Applied Mathematics*, 71(383-390), 2006.
- H.M. Youssef and A.A. El-Bary. Two-temperature generalized thermoelasticity with variable thermal conductivity. *Journal of Thermal Stresses*, 33:187–201, 2010.
- N. Yu, S. Imatani, and T. Inoue. Hyperbolic thermoelastic analysis due to pulsed heat input by numerical solution. *JSME International Journal Series A*, 49(2):180–187, 2006.
- X. Zeng and R.K.N.D. Rajapakse. Effects of remanent field on an elliptical flaw and a crack in a poled piezoelectric ceramic. *Computational Materials Science*, 30:433–440, 2004.
- L. Zhou, D.W. Tang, and N. Araki. Coupled finite element analysis of generalized thermoelasticity in semi-infinite medium. *JSME International Journal Series A*, 49(2):195–200, 2006.
- O.C. Zienkiewicz, R.L. Taylor, and J.Z. Zhu. *The Finite Element Method: The Basis*. Elsevier Butterworth-Heinemann, 2005.